On growth processes and motion of particles in protoplanetary disks

Von der Fakultät für Physik der Universität Duisburg-Essen
genehmigte Dissertation von

Tim Husmann
(né Jankowski)

zur Erlangung des akademischen Grades

Dr. rer. nat.

1. Gutachter Prof. Dr. Gerhard Wurm
2. Gutachter Prof. Dr. Jürgen Blum
Disputation: 18. Mai 2017

for everyone

"There's always been a quote which is worth quoting"

unknown

Abstract

The process of planet formation is defined by a multiplicity of physical and chemical effects. Observations show that – starting from sub-micrometer sizes – particles have to reach planetesimal sizes in approximately three million years. This implies growth over at least thirty decades in mass. Within this work, two aspects are treated in detail: the collisional dynamics of dust particles and their motion in protoplanetary disks.
The material properties and their influence on the collisional behaviour as well as the effect of reaccretion of ejecta in small impactor - large target collisions are investigated. It is shown that both aspects can have significant impact on the growth process in certain areas of the disk.
The motion of particles in protoplanetary disks is caused by different forces. A new analytic formula for photophoretic forces affecting irradiated particles in a gaseous environment with temperatures deviating from the surrounding gas is presented. Applying this formula to particles in pre-transitional disks results in a self-sustained recycling mechanism which is established within the inner parts of those disks. Hence, this process can explain the stability of the inner dust disk while no material is replenished by the outer disk through the gap.

Der Prozess der Planetenentstehung wird bestimmt von einer Vielzahl physikalischer und chemischer Effekte. Aus Beobachtungen folgt, dass Partikel ausgehend von submikrometer Größe in etwa drei Millionen Jahren zu Planetesimalen wachsen müssen. Dies impliziert Wachstum über mindestend dreißig Massendekaden. Innerhalb dieser Arbeit werden zwei Aspekte im Detail behandelt: Die Kollisionsdynamiken von Staubpartikeln sowie ihre Bewegung in protoplanetaren Scheiben.
Die Materialeigenschaften und ihr Einfluss auf das Kollisionsverhalten sowie der Effekt der Reakkretion von Auswurfmaterial in Kollisionen von unterschiedlich großen Körpern wird untersucht. Dabei zeigt sich, dass beide Aspekte einen signifikanten Einfluss auf die Wachstumsprozesse in bestimmten Bereichen der Scheibe haben können.
Die Bewegung von Partikeln in Protoplanetaren Scheiben wird durch verschiedene Kräfte verursacht. Es wird eine neue analytische Formel für photophoretische Kräfte vorgestellt, welche auf bestrahlte Partikel wirken und eine Temperatur besitzen, die von der des umgebenden Gases abweicht. Durch die Anwendung dieser Formel auf Partikel in Pre-Transitional Disks wird gezeigt, dass sich ein selbsterhaltener Recyclingprozess in den inneren Teilen dieser Scheiben etabliert. Dieser Prozess kann daher die Stabilität der inneren Staubscheibe erklären, während kein Material aus der äußeren Scheibe durch die Lücke nachgeliefert wird.

Publications

Articles (peer reviewed)

- **T. Jankowski**, G. Wurm, T. Kelling, J. Teiser, W. Sabolo, P. J. Gutiérrez, and I. Bertini *Crossing barriers in planetesimal formation: The growth of mm-dust aggregates with large constituent grains.* Astronomy & Astrophysics, 542, 2012

- C. de Beule, T. Kelling, G. Wurm, J. Teiser, and **T. Jankowski** *From planetesimals to dust: Low gravity experiments on recycling solids in inner protoplanetary disks.* The Astrophysical Journal, 763, 2013.

- C. de Beule, G. Wurm, T. Kelling, M. Küpper, **T. Jankowski**, and J. Teiser *The martian soil as planetary gas pump.* Nature Physics, 10, 2014

- G. Musiolik, J. Teiser, **T. Jankowski**, and G. Wurm *Collisions of CO_2 Ice Grains in Planet Formation.* The Astrophysical Journal, 818, 2016

- C. Lösche, G. Wurm, **T. Jankowski**, and M. Küpper *Photophoresis on particles hotter/colder than the ambient gas in the free molecular flow.* Journal of Aerosol Science, 97, 2016

- G. Musiolik, J. Teiser, **T. Jankowski**, and G. Wurm *Ice Grain Collisions in Comparison: CO_2, H_2O, and Their Mixtures.* The Astrophysical Journal, 827, 2016

- **T. Husmann**, C. Lösche, and G. Wurm *Self-sustained Recycling in the Inner Dust Ring of Pre-transitional Disks.* The Astrophysical Journal, 829, 2016

- C. Lösche and **T. Husmann** *Photophoresis on particles hotter/colder than the ambient gas for the entire range of pressures.* Journal of Aerosol Science, 102, 2016

Proceedings

- C. de Beule, T. Kelling, G. Wurm, J. Teiser, and **T. Jankowski** *Light Induced Dust Lifting on Mars: 0g Experiments.* EPSC-DPS Joint Meeting 2011, p. 201, 2011

- **T. Jankowski**, T. Kelling, and G. Wurm *Steps in Planet formation: Collisions of mm sized dust aggregates in the cm/s regime.* EPSC-DPS Joint Meeting 2011, p. 1822, 2011

- C. de Beule, T. Kelling, G. Wurm, J. Teiser, and **T. Jankowski** *Light induced erosion of dusty planetesimals and mars: μg experiments.* Journal of Physics: Conference Series, 327, 2011

Conference contribution

- **T. Jankowski**, T. Kelling, and G. Wurm. EPSC-DPS Joint Meeting, Nantes, 02-07.10.2011, *Steps in Planet formation: Collisions of mm sized dust aggregates in the cm/s regime.* Poster
- **T. Jankowski**, G. Wurm, and J. Teiser. Protostars and Planets VI, Heidelberg, 15-20.07.2013, *Reaccretion Efficiencies in Small Impactor - Large Target Collisions.* Poster
- **T. Jankowski**, G. Wurm, and J. Teiser. 45th Annual Meeting of DPS, Denver, 06-11.10.2013, *Reaccretion Efficiencies in Small Impactor - Large Target Collisions.* Talk

Invited Talks

- Astroseminar, Westfälische Wilhelms-Universität Münster, *Astrophysik im Labor - Ein Einblick in den Experimentieralltag*, 2013

Contents

1

Motivation - How planets form

The question of our origin is a matter of great human concern. What was the beginning? Where do we come from? How did and how will the universe evolve? Undoubtedly life would not be possible without planets orbiting a star which drives chemical processes and supplies the planet with energy. While the research concerning the human evolution has already advanced far, the question how our solar system has formed is still not answered satisfactorily since the process of forming a planetary system can be qualified as highly complex.

It is widely accepted that the earliest stages start with the accumulation of so called interstellar medium (Reipurth et al., 2007; Dobbs et al., 2014). This primarily consists of light gases, mainly Hydrogen ($\sim$ 74 %) and Helium ($\sim$ 26 %). At the beginning, external high-energetic irradiation prevents the formation of molecules and therefore clouds develop consisting of atomic gas. Once the density increases, the outer layers of the cloud absorb the external irradiation and allow the gas in the inner parts to form molecules (Fukui and Kawamura, 2010). Clouds in this state are called molecular clouds.

The first stars ever formed consisted exclusively of Hydrogen and Helium gas which burned in fusion processes to Lithium. It is assumed that these stars were very massive, resulting in large supernova explosions at the end of their lifetime and thus providing material to later generations of stars and clouds. These and later supernovae have led to the presence of heavier elements in molecular clouds. For example Carbon-oxides have been observed by Lada (1976) and Kutner et al. (1977) in the cloud M17 although in a smaller proportion compared to Hydrogen and Helium (Sanders et al., 1984; Solomon et al., 1987). Besides the distinction between light and heavy elements, especially in later stages of cloud evolution one differs between gaseous and solid material (often simply called “dust”).

Molecular clouds can have enormous sizes up to $\sim$ 200 pc and masses up to $\sim 10^7$ $M_\odot$ (Oka et al., 2001; Murray, 2011). The larger ones, called Giant Molecular Clouds, contain most of the material present in the universe with number densities (number of H_2

molecules per volume) of $n_{H_2} = 2 - 8 \times 10^8$ m^{-3} (Roman-Duval et al., 2010), which equals a density of $\rho_{H_2} \approx 10^{-18}$ kg m^{-3}.
Self-gravitation as well as externally triggered perturbations lead to turbulences and to local increases in density (McKee and Ostriker, 2007). Therefore parts of these clouds start to collapse into localised aggregations with non-zero angular momentum.
Once the gas and dust start to accrete onto these denser cores, they are called Young Stellar Objects (YSO). YSOs evolve through four different stages and are classified according to the slope of their spectral energy distribution in the infrared domain (Lada and Wilking, 1984; André and Montmerle, 1994). Whilst the first class (class 0 YSO) is associated with the very beginning of the accretion phase, the later evolution leads to a central protostar with a diffuse ring of gas ($\gtrapprox 99\%$) and dust ($\lessapprox 1\%$) orbiting around it (class I YSO). Since *ab initio* a net angular momentum exists, gravitational effects lead to a disk-like shape of the surrounding gas and dust – the so called protoplanetary disk (PPD). Generally its mass is much less then the mass of the central star. The whole object is than identified with a class II YSO. Once the disk starts to disperse e.g. because of the formation of planetary candidates, the object is labelled class III YSO. A more detailed scheme of the different classes of young stellar objects is depicted in fig. 1.1.

Even though the basic formation processes of YSOs and PPDs seems quite simple on the outside, in detail plenty of different physical effects have to be considered. Some aspects are well understood since there has been major progress in the past decades. Nevertheless, other issues are still object to research. A model capable of explaining the entire process of forming planetary systems as observed in nature still has to be developed. Within this work, different aspects and effects are investigated aiming for a contribution to a better understanding of the physical processes in and the evolution of PPDs in class II and class III YSOs. The motion and coagulation of dust particles is focussed since they dominate the growth characteristics and therefore the timescales of the planet formation process. Furthermore, it is investigated how observationally determined disk models for later stages of protoplanetary disks can be explained using computer simulations with suitable models for these aspects.

Class 0

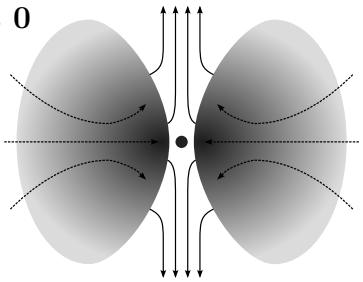

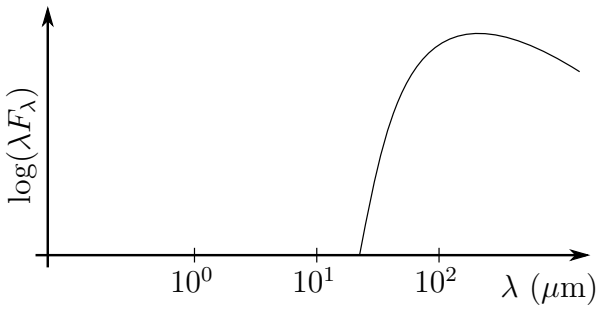

Main accretion phase: The cloud is slowly collapsing, leading to material being accreted onto the star. The SED equals the spectrum of a cold black body.

Class I

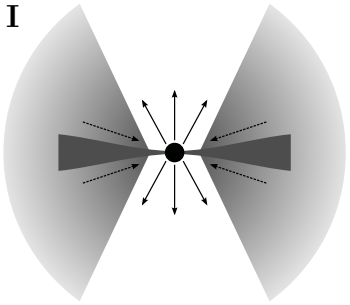

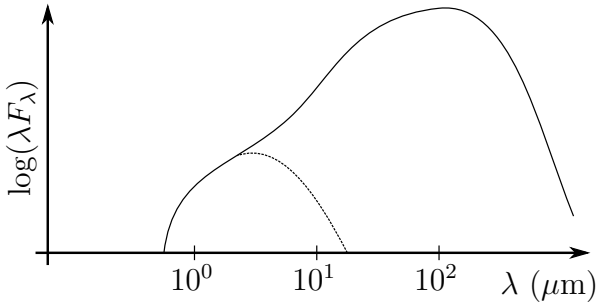

Late accretion phase: A disk-like shape is evolving, the protostar is already visible inside the SED (dashed line), though the star is still far away from its final temperature.

Class II

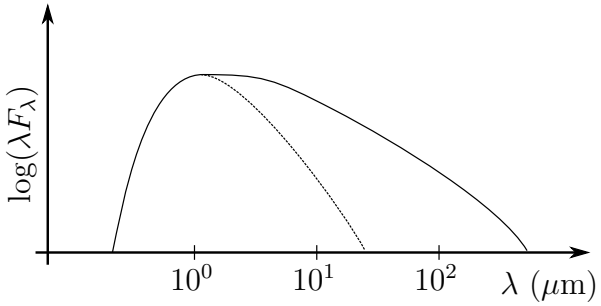

Optically thick disk: The disk has developed, the star is in its final state. The SED show signatures from the star (dashed line) with far-infrared radiation from the disk.

Class III

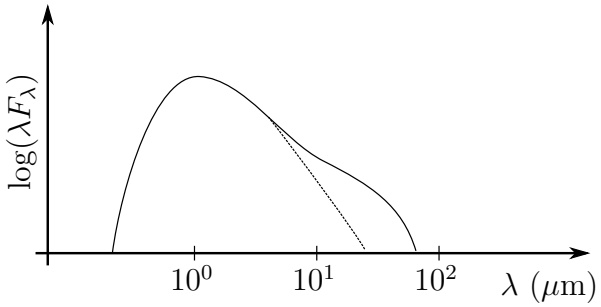

Optically thin disk: The protoplanetary disk has evolved further into an optically thin dust disk. The graph therefore flattens in the far-IR region and the star is more and more dominating the SED.

Figure 1.1: Classification of Young Stellar Objects via their spectral energy distribution (SED). On the basis of André (1994) and Armitage (2010).

1.1 Protoplanetary Disks (PPDs)

The basic structure of an idealised PPD as described earlier is depicted in fig. 1.2. As shown there, PPDs have a bowl-like shape which means that the disk height above the midplane – called "scale-height"– h increases with increasing distance to the central star r. Although the underlying ideas and theoretical considerations of PPDs have existed quite long (e.g. Lynden-Bell and Pringle, 1974; Weidenschilling, 1977b; Hayashi, 1981) modern observations confirm these models very well (see fig. 1.3). The solid and gaseous material is mixed within the disk. However, in the description of disk models one treats them separately and distinguishes between a gaseous disk and a solid or dust disk. Note here that the evolution of and the physical processes in the gaseous and solid parts are closely linked to each other and that this linkage has to be considered all the time.
The differences in the model for the solid and gaseous disk become clear when getting into more details: The dust disk has an inner edge at the sublimation distance r_{sub}, where the temperature reaches the sublimation temperature T_{sub} of the solid material, often set as $T_{\mathrm{sub}} = T_{\mathrm{sub,silicate}} = 1500$ K (e.g. in Baillié et al., 2015)). In the following if not otherwise stated the sublimation radius is always connected with the sublimation radius of silicates. Gaseous material on the other hand exists further inwards as well.
The gaseous disk as well as the dust disk do not have sharp edges in vertical direction. Thus, the scale height h is only a parametrisation of the disks height. Furthermore, the scale-height for the gaseous disk h is not necessarily the same as the scale-height for the dust disk h_{dust}.
The aspect ratio h/r can be derived by balancing the forces caused by the vertical component of the star's gravity and the pressure gradient (Armitage, 2010), omitting the disk's self-gravitation due to the much lower mass of the disk compared to the stellar mass ($m_{\mathrm{disk}} \ll m_*$). This leads to

$$\frac{h}{r} = \frac{c_{\mathrm{s}}}{v_{\mathrm{k}}} \propto r^{\phi} \ , \tag{1.1}$$

where ϕ is the flaring angle with $\phi = \frac{1}{4}$ describing a disk in hydrostatic equilibrium and $\phi = 0$ leads to a flat disk ($h/r = \mathrm{const}$). The Keplarian velocity v_{k} is given by

$$v_{\mathrm{k}} = \Omega_{\mathrm{k}}\, r = \sqrt{\frac{G M_*}{r}} \quad , \tag{1.2}$$

where Ω_{k} is the Keplarian frequency, G is the gravitational constant and M_* is the mass of the central star. The isothermal sound speed c_{s} is given via

$$c_{\mathrm{s}} = \sqrt{\frac{k_{\mathrm{B}}\, T}{\mu\, \mathrm{u}}} \quad . \tag{1.3}$$

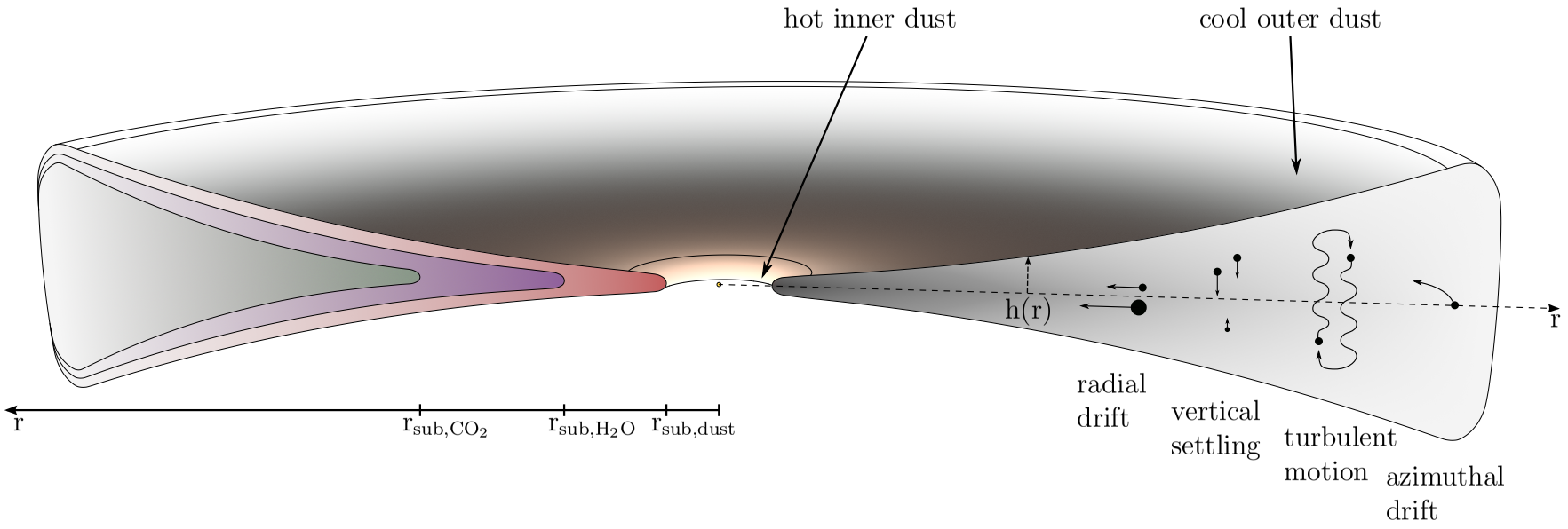

Figure 1.2: Schematic cut through a protoplanetary disk (PPD). The star is placed in the disk's centre, the disk (not to scale) has a bowl-like shape with a disk height above the midplane h dependent on the distance to the central star r. The dust temperature close to the star reaches the sublimation temperature while the dust further outwards or closer to the disks mid-plane can be much cooler. On the left-hand side, the different sublimation radii for silicates, H_2O and CO_2 are depicted (see chapter 3 for details). On the right-hand side different types of motion of solid particles are displayed (see chapter 2 for details). The different brightness levels correspond to different densities inside the disk – close to the star the density is the highest, further outwards the density decreases.

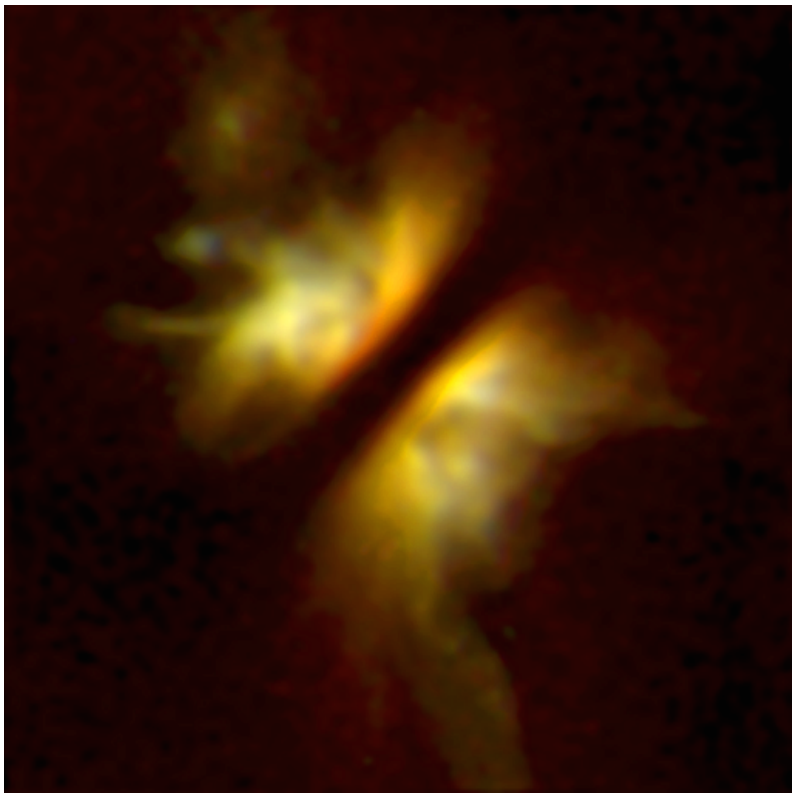

Figure 1.3: Sideview of a protoplanetary disk (Iras 04302+2247) in near infrared spectrum. Due to its optical thickness, the disk (black) hides the star and only scattered light from higher, diffuse dust is visible. The disk diameter is about 0.014 ly. Original image by D. Padgett (IPAC/Caltech), W. Brandner (IPAC), K. Stapelfeldt (JPL) and NASA/ESA.

Here, $\mu = 2.34$ is the mean molecular weight of gas of cosmic composition in units of the atomic mass u and k_B is the Boltzmann constant.
The height of the dust disk h_dust is not necessarily the same as the gas disk height h and might even depend on the particle size. For simplicity, the dust scale height will be described using a factor χ_dust via

$$h_\mathrm{dust} = \chi_\mathrm{dust}\, h \quad . \tag{1.4}$$

A more detailed discussion on the calculation of χ_dust and the assumed simplifications is elaborated in section 5.2.3.
Especially in the early stages of disk evolution where growth of particles has not yet advanced far, PPDs are optically thick which means that radiation cannot pass through the disk without getting absorbed and reemitted. This leads to different temperatures of the mid-plane and the surface of the PPDs.
Using radiative heat transfer modelling one can determine the temperature distribution of different disk models in detail if the exact disk structure is known (see e.g. Chiang

and Goldreich, 1997; D'Alessio et al., 1998; Min et al., 2011). A simple approach links the mid-plane temperature to the aspect ratio h/r via the flaring angle ϕ. A general description can be made by

$$T = T_0 \left(\frac{r}{r_0} \right)^{2\phi - 1} \quad , \tag{1.5}$$

where T_0 is the temperature at a distance r_0 to the central star. The actual surface temperature of the disk and therefore the temperature distribution inside the disk can be influenced by several different factors like emissions from the protostar itself or other protostars or from hot clouds in the environment and is therefore not trivial to predict.
Due to the decreasing temperature inside the disk for increasing distances to the central star, different materials exist in different aggregation states within the disk. While silicates are solid in the whole disk ($r > r_{\mathrm{sub}}$), more volatile materials can exist in solid state only further outwards. Two important radii where solid materials change their state are depicted in fig. 1.2: the snow-line for water ice ($r_{\mathrm{sub,H_2O}}$) and the snow-line for CO_2 ice ($r_{\mathrm{sub,CO_2}}$).
The distribution of the gas has – as mentioned – no sharp borders. Moreover, for thin disks the density of the gas can be approximated via

$$\rho_{\mathrm{gas,3d}} = \rho_{\mathrm{gas}} \exp\left(-\frac{z^2}{2\,h^2} \right) \tag{1.6a}$$

$$\rho_{\mathrm{gas}} = \frac{1}{\sqrt{2\,\pi}} \frac{\Sigma_{\mathrm{gas}}}{h} \quad , \tag{1.6b}$$

where Σ_{gas} is the surface density of the gas which is defined as the surface projected density in units of mass per square-size. Correspondingly, the density of solid material, hereafter as well referred to as dust density, can be described via

$$\rho_{\mathrm{dust,3d}} = \rho_{\mathrm{dust}} \exp\left(-\frac{z^2}{2\,(\chi_{\mathrm{dust}} \cdot h)^2} \right) \tag{1.7a}$$

$$\rho_{\mathrm{dust}} = \frac{1}{\sqrt{2\,\pi}} \frac{\Sigma_{\mathrm{dust}}}{\chi_{\mathrm{dust}} \cdot h} \quad . \tag{1.7b}$$

The resulting gas pressure at a given distance to the central star can be calculated via

$$P = \rho_{\mathrm{gas}}\, T\, \frac{\mathrm{N_A}\, k_{\mathrm{B}}}{\mu} \quad , \tag{1.8}$$

where $\mathrm{N_A}$ is Avogadros constant.

1.2 Evolution and dispersal of PPDs

In our solar system the protoplanetary disk has dispersed nearly completely and only remnants are left like for example the circumstellar disk at 30 – 50 AU, called Edgeworth-Kuiper belt. The process of the disk dispersal has neither happened instantaneously nor over a very long timescale. Following observations of extrasolar disks, the typical disk lifetime is estimated to be in the order of $3 - 5 \times 10^6$ yr for the dust as well as for the gaseous components (Haisch et al. (2001) and Hartmann et al. (1998)). Therefore, the dispersal of the disk has to happen on such timescales (see for example Andrews and Williams, 2005).

Furthermore, for a quick dispersal the angular momentum of the disk has to be dissipated as well. Since the gaseous hydrodynamical (molecular) viscosity is too low to explain this process, other sources of viscosity have to exist. Note here that without other sources the disks lifetime would be in the order of 10^{13} yr (Andrews and Williams, 2005). Generally it is accepted that turbulence inside the disk has a major influence on the dissipation process since the calculated turbulent viscosities ν_t are much higher than the molecular viscosity ν_mol. A discussion on the values of turbulent viscosity is given in sec. 2.3. The sources for these turbulences are still being discussed but so-called magneto-rotational instabilities (MRI) might play a crucial role (Johansen et al., 2014).

Due to this long-term process, another effect influences the dispersal of a PPD: photoevaporation. Stellar wind as well as heating by external radiation can lead to an acceleration acting on the material in the upper layers of PPDs. Especially the lighter gases are susceptible to this, leading to a loss of gaseous material influencing the dust in the disk as well.

The disk evolution includes the growth of (sub-)micrometer particles to sizes of several km, where gravitation starts to dominate. The question whether this is happening by pure coagulation or aided or even triggered by increasing particle concentration for example in turbulence eddies, pressure bumps or streaming instabilities is still object of research. Nonetheless, growth is always linked to collisions of dust grains and the collisional outcome determines the growth rates. Collision processes are highly complex since lots of parameters exist which influence particle-growth significantly.

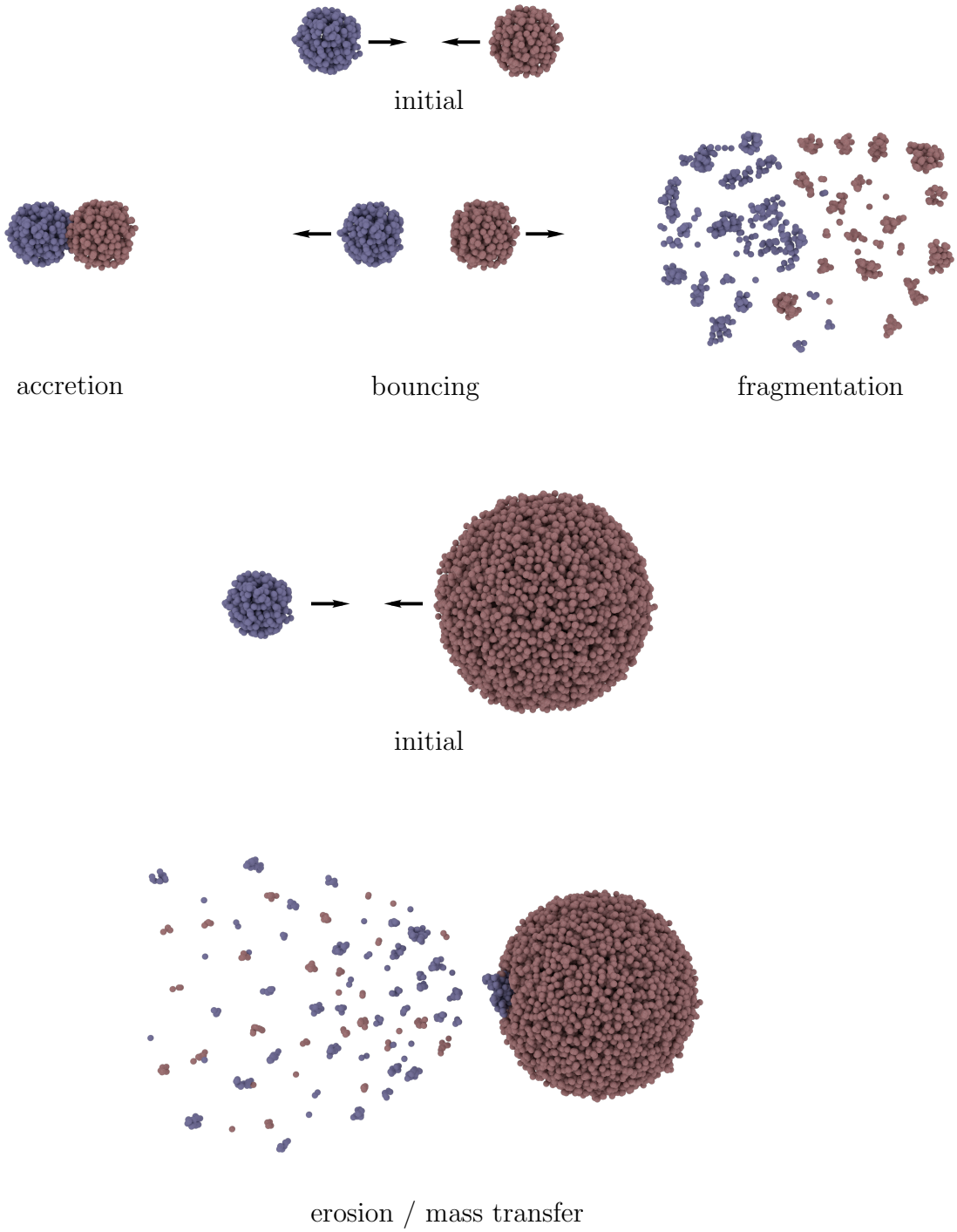

Figure 1.4: Collisional outcome. Top: Collisions of equal sized particles can lead to accretion (low collision velocities), bouncing or fragmentation (high collision velocities). Bottom: Collisions of different sized particles can in addition lead to erosion/mass transfer, where mass is transferred from the impactor to the target body and simultaneously mass can get eroded from the target body. Whether net growth of the larger body occurs highly dependends on the impactor size and collision velocity.

As shown in fig. 1.4, the collisional outcome can be divided into the following four categories (Güttler et al., 2010; Windmark et al., 2012b):

1. Accretion - If the collision velocity and therefore the collisional energy is low, the adhesive forces are strong enough to prevent a detachment and the collision energy can be dissipated.

2. Bouncing - Once the collision velocity increases bouncing occurs. This is often connected with slight restructuring but can also include mass transfer from one body to the other.

3. Erosion and Mass Transfer - During the collision of different sized particles with high collision velocities, the smaller body can get disrupted transferring mass onto the larger body while simultaneously the larger body gets eroded. Whether such a collision implies net growth (mass gain) or net erosion (mass loss) of the larger body mainly depen-dends on the mass differences and collisional velocities (Güttler et al., 2010; Windmark et al., 2012b). As shown in chapter 4, other effects like reaccretion of ejected particles can have a significant impact on the net growth rate.

4. Fragmentation - Once collision velocities get very high, particles with equal sizes can get disrupted completely.

As mentioned, in all four categories the outcome of a collision of dust particles is primarily dominated by their relative velocity and their sizes. Different extensions to these possibilities exist within models which also include mass transfer in bouncing collisions or growth via penetration of larger particles by smaller ones (Güttler et al. (2010), Kruss et al. (2016) and unpublished work by Kothe and Blum (2016)).
The collisional outcome does not only influence the growth timescales but also the amount and size of possible protoplanetary bodies. Later stages of disk dispersal are often influenced by the presence of these bodies since they might be capable of opening gaps in the disks. PPDs with gaps are called pre-transitional disks. Later on, when the inner dust disk has disappeared and only an outer dust disk remains they are labeled transitional disks. A scheme of these disks depicting the differences is shown in fig. 1.5.
The word “transitional” is linked to the disks opacity which transits from optically thick to optically thin. Once the disk transits into an optically thin disk, the particle movement is influenced heavily since radiation determined forces like radiation pressure or photophoresis can dominate the force balance even in the outer parts of the disk. One

has to note that while the gap is (nearly) dust free, gas is still present although in lower proportion compared to the original disk.

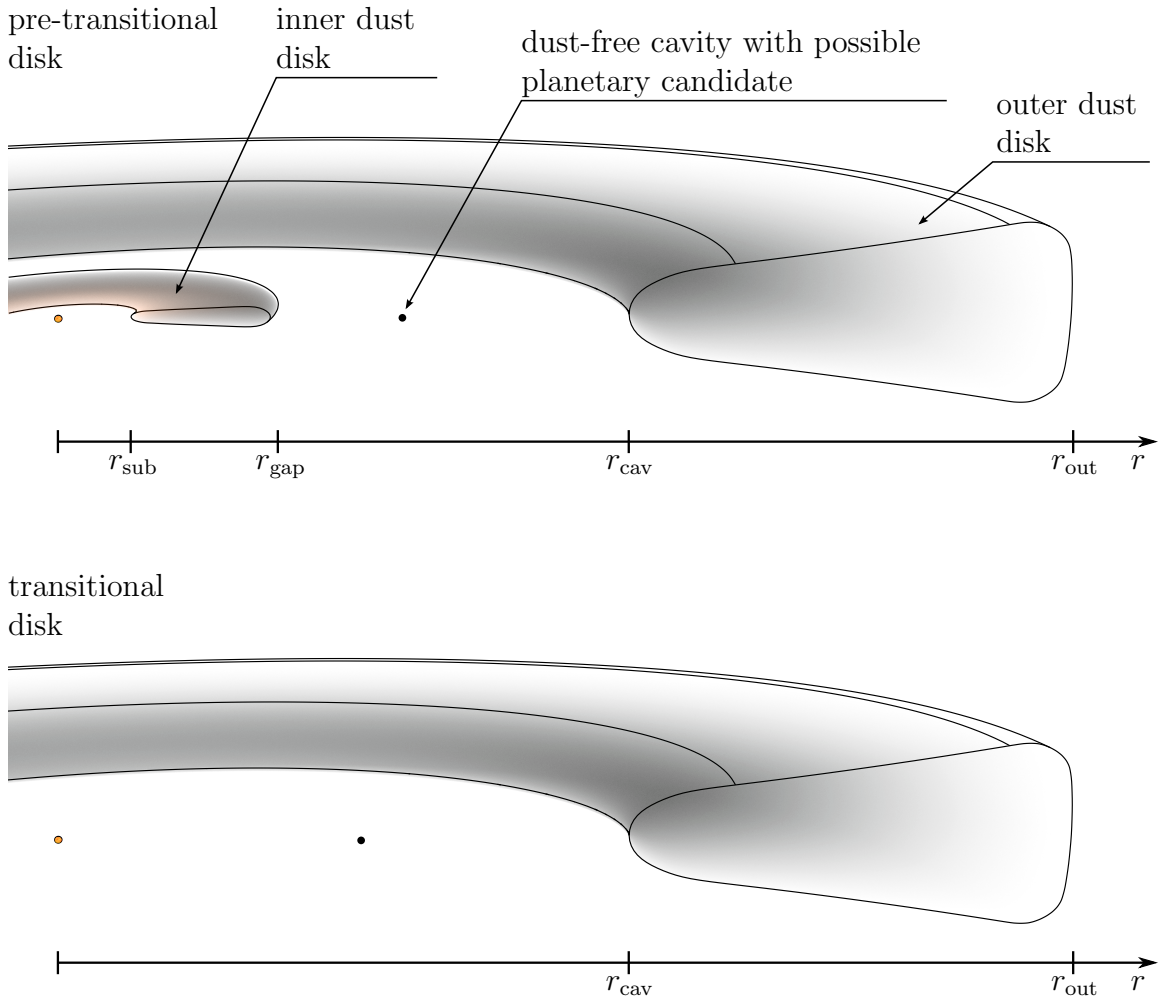

Figure 1.5: Cut through a pre-transitional disk (top) and a transitional disk (bottom). The disk evolution is assumed to be as follows: inside a protoplanetary disk (as seen in fig. 1.2) a gap is opened for example due to an planetary candidate. This happens because of runaway growth of the (proto-)planet, leading to a sweep up of mass around its orbit due to gravitation. Once a gap has opened, the disk is called "pre-transitional". Evolving in time, the inner dust ring begins to disappear and the disk is called "transitional".

1.3 The aim of this work

Within this work, the motion and growth of particles in PPDs are investigated. Therefore the classic, drag related sources of particle motion are presented in chapter 2, extended by radiation related forces with a special emphasis on a new analytic formula for the so-called photophoresis. This force acts on irradiated particles suspended in an gaseous environment. The derived formula presented within this chapter takes into account that the particle's mean temperature can deviate from the temperature of the surrounding gas. It is therefore suitable to describe the photophoretic force acting on the dust particles in protoplanetary disks over the full range of pressure.
Since particles in PPDs suffer from collisions with other bodies, a general review on the collisional outcome is given in chapter 3, supplemented by findings gained from new experimental approaches on the determination of the collisional behaviour of H_2O and CO_2 ices. The influence of the material properties on the growth behaviour is discussed, leading to an extended model of protoplanetary disks where regions exist which are favourable for growth.
Furthermore, another source of particle erosion besides the one caused by collisions is investigated in detail: light-induced erosion. This effect takes place when granular bodies are suspended in a gaseous environment and simultaneously are illuminated by a strong radiation source. Experimental studies on the gravity dependence of this effect are presented, showing that the amount of eroded mass can be significant, especially if the granular body is close to the star.
The collisional outcome model is extended in chapter 4 with simulations on an effect called "reaccretion": Assuming a collision of a larger target particle with a smaller impactor, the source for the relative velocity and therefore the reason for such collisions are the different couplings of the target and the impactor to the surrounding gas. In the reference frame of the target, the impactor approaches with a velocity which equals the relative gas velocity. The target therefore suffers from a headwind influencing the movement of the ejecta produced in the collision: they can get pushed back to the targets surface and reaccreted by the target body. This leads to an increase in mass gain which is quantified analytically for a specific disk model and which can significantly influence the growth of large particles.
An issue treated within chapter 5 is the explanation of the stability of the inner dust ring of pre-transitional disks: Using the forces on particles in PPDs as described in chapter 2, the motion of the dust particles inside the inner part of the pre-transitional disk is investigated in the cases of the disks LkCa15 and HD135344B. A self-sustained recycling mechanism can be established where dust is continuously distributed throughout the full inner dust disk. As shown there, this process is suitable to explain why this inner dust

disk does not disappear quickly in contrast to the prediction of classical models of dust motion. Besides using the collisional outcome model presented in chapter 3, the existing disk models by van der Marel et al. (2015) are extended by several parameters and aspects necessary for the realisation of single particle evolution simulations to characterise the recycling process in more detail.

2

Gas and Dust Motion in Protoplanetary Disks

In this chapter, the motion of dust in protoplanetary disks is focussed. One distinguishes two types of motion: In time-average, the first type does not result in a change of position like e.g. Brownian motion while the other one does like e.g. radial drift. Therefore, the former influences particle motion only on local scales, the latter is responsible for the global motion of the dust. The strength of both types of motion is highly dependent on the disk model which determines the physical background for particle motion and which therefore has to be specified first.
Moreover, both types of motion influence the collision velocities of particles. Note here that the relative velocity of particles with identical physical properties (size, mass, shape, opacity etc.) is caused only by local motion while the relative velocity for non-equally sized ones is influenced by the global motion as well. The forces leading to these motions can have different origins but are often linked to the interaction of the dust particles and the surrounding gas. The global gas motion therefore influences the particle motion as well. Furthermore, other radiation-related forces can be important as well. Photophoresis for example can dominate the motion of particles in certain disk setups. A new analytical approximation is given within this work suitable for particles with mean temperatures deviating from the temperature of the surrounding gas.
The quantification of the local and global dust motion is important not only for the outcome of collisions but furthermore for the evolution of the dust surface density and hence for the evolution of the complete disk. As mentioned, it is necessary to specify the disk model first before calculating the forces and the resulting motion of the dust.

2.1 Protoplanetary Disk Models

Since observations of protoplanetary disks do not favour a single model, a multiplicity of disk models exist capable of describing different disk types and evolutional stages. Two models for different stages of PPDs are depicted in detail here: the Minimum Mass Solar Nebular (MMSN, Hayashi (1981); Weidenschilling (1977b)) and a Pre-transitional Disk Model (PDM, Andrews et al. (2011b); van der Marel et al. (2015)).
The general physical properties of protoplanetary disk models are intuitive: the closer to the star, the hotter and denser the gas. The basic idea of the Minimum Mass Solar Nebular is to represent our early solar system by taking the minimum mass necessary to build a planet and spreading it around its orbit. The radial dependency of the resulting surface density is then approximated with a power-law function. The PDM focuses on reproducing the observations of pre-transitional disks made by e.g. ALMA (Atacama Large Millimeter/Submillimeter Array), following the viscosity disk model $\nu_{\text{mol}} \propto r^{\kappa}$ by Lynden-Bell and Pringle (1974) and Hartmann (1978). The dust disk has an "inner edge" at a distance r_{sub} to the central star at which the disk temperature equals the sublimation temperature of the dust ($T_{\text{sub}} = 1500$ K, see sec. 1.1). Furthermore pre-transitional disks - as mentioned in sec. 1.2 - may show gaps and gas drops leading to a non-monotone distribution function of gas and dust.
In general a protoplanetary disk can be described using the surface densities for gas (Σ_{gas}) and dust (Σ_{dust}) and either a formula for the aspect radio h/r (eq. 1.1) or the temperature profile (eq. 1.5). All other parameters can be calculated using these functions and values.

2.1.1 Minimum Mass Solar Nebular (MMSN)

The Minimum Mass Solar Nebular model (MMSN) was introduced by Weidenschilling (1977b) and described in more detail by Hayashi (1981). The gas surface density is given by

$$\Sigma_{\text{gas}} = \Sigma_0 \left(\frac{r}{1\,\text{AU}} \right)^{-3/2} \quad , \tag{2.1}$$

where $\Sigma_0 = 1.7 \times 10^4$ kg m^{-2} is the gas surface density at 1 AU. The dust surface density Σ_{dust} is described via

$$\Sigma_{\text{dust}} = \Delta_{\text{dust}}\, \Sigma_{\text{gas}} \tag{2.2}$$

$$\Delta_{\text{dust}} = \begin{cases} 4.18 \times 10^{-3}\,, & r < r_{\text{ice}} \\ 1.77 \times 10^{-2}\,, & r > r_{\text{ice}} \end{cases} \quad , \tag{2.3}$$

where r_{ice} is the sublimation radius of H_2O-ice (see section 3.2.2 and fig. 3.5). Both surface densities are valid for $r > r_{\mathrm{sub}}$.
The midplane temperature profile is given by

$$T = T_0 \left(\frac{r}{1\,\mathrm{AU}} \right)^{-\frac{1}{2}} \quad , \tag{2.4}$$

where T_0 is the temperature at 1 AU, often set to be 280 K (Weidenschilling, 1977b) or 200 K (Windmark et al., 2012a).
With the mass of the central star M_* which equals the mass of the sun $M_\odot$, the scale-height can be derived using the Keplerian velocity (eq. 1.2) and the isothermal sound speed (eq. 1.3) following eq. 1.1 as

$$h = \frac{c_{\mathrm{s}}}{v_{\mathrm{k}}} r = r^{\frac{5}{4}} \sqrt{\frac{k_{\mathrm{B}}\, T_0 \sqrt{\mathrm{AU}}}{\mu\, \mathrm{u}\, G\, M_\odot}} \quad , \tag{2.5}$$

where k_{B} is the Boltzmann constant, G the gravitational constant and $\mu = 2.34$ is the mean molecule weight of gas molecules of cosmic composition in units of u. The surface densities are plotted in fig. 2.1.

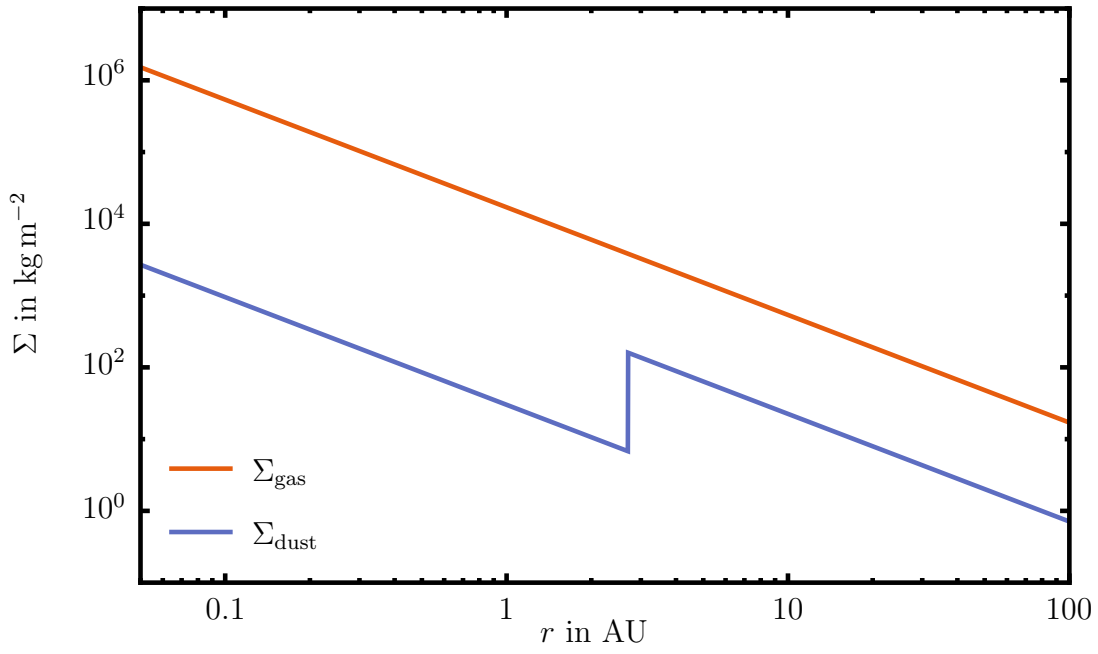

Figure 2.1: Dust and gas surface densities in the Minimum Mass Solar Nebular, $r_{\mathrm{sub,H_2O}}$ was set to 2.7 AU.

2.1.2 Pre-transitional Disk Model (PDM)

Andrews et al. (2011b) describe pre-transitional disks by using a gas surface density following

$$\Sigma_{\mathrm{gas}} = \Delta_{\mathrm{gas}} \Sigma_{\mathrm{c}} \left(\frac{r}{r_{\mathrm{c}}}\right)^{-\kappa} \exp\left(\left(-\frac{r}{r_{\mathrm{c}}}\right)^{2-\kappa}\right) \quad , \tag{2.6}$$

where Σ_{c} is the surface density at a critial radius r_{c}.
Since pre-transitional disks contain gaps and gas drops, Δ_{gas} is a function on the distance r. Several possibilities exist for the description of this function. Following Andrews et al. (2011b) and van der Marel et al. (2015) who applied this disk model to several pre-transitional disks and comparing the results to observations, Δ_{gas} can be simply specified to

$$\Delta_{\mathrm{gas}} = \begin{cases} \delta_{\mathrm{gas}}\,, & r < r_{\mathrm{gap}} \text{ with } 0 \leq \delta_{\mathrm{gas}} \leq 1 \\ 1\,, & r > r_{\mathrm{gap}} \end{cases} \quad . \tag{2.7}$$

The dust surface density Σ_{dust} is then described via

$$\Sigma_{\mathrm{dust}} = \Delta_{\mathrm{DGR}} \Delta_{\mathrm{dust}}\, \Sigma_{\mathrm{gas}} \tag{2.8}$$

$$\Delta_{\mathrm{dust}} = \begin{cases} \delta_{\mathrm{dust}}\,, & r < r_{\mathrm{gap}} \\ \delta_{\mathrm{dust}}\delta_{\mathrm{dustcav}}\,, & r_{\mathrm{gap}} < r < r_{\mathrm{cav}} \\ 1\,, & r > r_{\mathrm{cav}} \end{cases} \quad , \tag{2.9}$$

where Δ_{DGR} is the dust-to-gas ratio of 1:100. Other functions for Δ_{gas} and Δ_{dust} are possible since disks might have a larger inner gap up to several AU (e.g. SR21, van der Marel et al. (2015)) or even contain a much more complex substructure consisting of multiple rings and gaps (Andrews et al., 2016).
The description of the dimensionless aspect ratio $h\,r^{-1}$ follows eq. 1.1 and is given via

$$\frac{h}{r} = \frac{h_{\mathrm{c}}}{r_{\mathrm{c}}} \left(\frac{r}{r_{\mathrm{c}}}\right)^{\phi} \quad , \tag{2.10}$$

where h_{c} is the scale-height at r_{c}. The temperature profile can then be calculated to

$$T = T_{\mathrm{sub}} \left(\frac{r}{r_{\mathrm{sub}}}\right)^{2\phi-1} \quad . \tag{2.11}$$

The disk parameters for three different disks are shown in tab. 2.1 and the surface densities for the disk LkCa15 are plotted in fig. 2.2.

	r_c [AU]	Σ_c [kg/m^2]	h_c	ϕ	δ_{dust}	r_{cav}	r_{sub}	r_{gap}	δ_{gas}	$\delta_{dustcav}$	L_* [$L_\odot$]	M_* [$M_\odot$]
SR 21	15	4000	0.07	0.15	10^{-6}	25	0.18	1	10^{-2}	10^{-3}	10	1.0
HD135344B	25	2000	0.15	0.05	10^{-2}	40	0.18	0.25	10^{-1}	$< 10^{-4}$	7.8	1.6
LkCa15	85	340	0.06	0.04	10^{-5}	45	0.08	1	10^{-1}	$< 10^{-4}$	1.2	1.0

Table 2.1: Disk parameters for SR21, HD135344B and LkCa15 given by van der Marel et al. (2015). Note that SR21 does not contain gas and dust up to 7 AU.

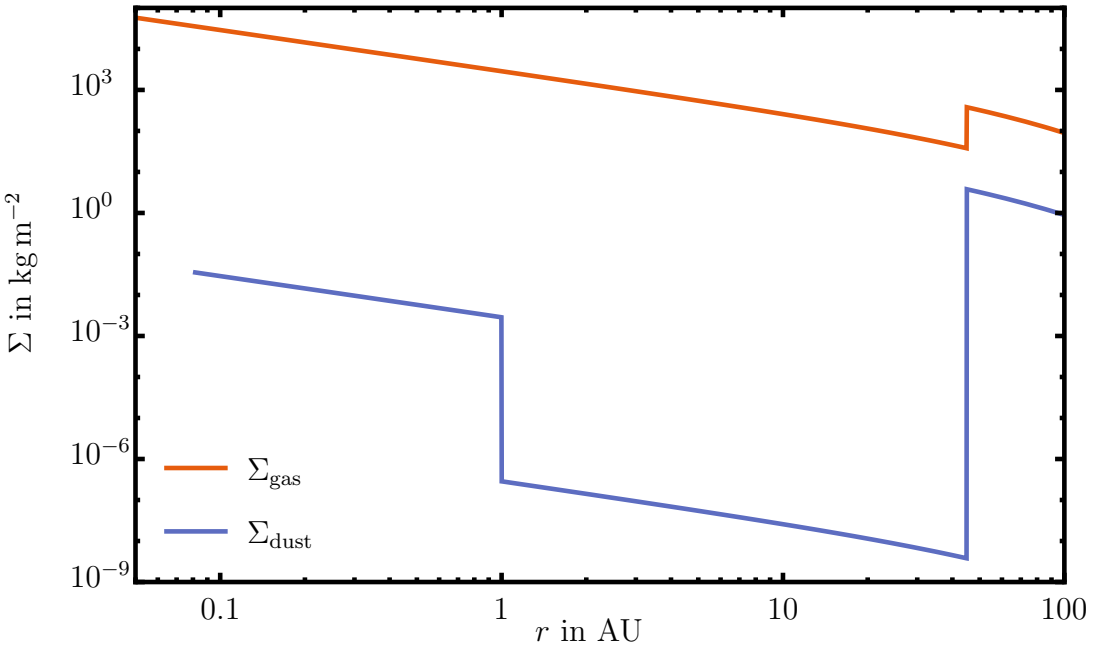

Figure 2.2: Dust and gas surface densities in the disk LkCa15.

2.2 Opacity of PPDs

The forces acting on illuminated particles are highly dependent on the intensity of the radiation. Since dust and gas in PPDs result in scattering and absorption of radiation (omitting re-emission of radiation), the intensity at a given distance to the central star r can be described via

$$I = I_0 \cdot \exp\left(-\int_{r_{sub}}^{r} \kappa_{med}(r')\rho_{dust}(r')\mathrm{d}r'\right) \quad . \tag{2.12}$$

Here, $I_0 = \frac{L_\star}{4\pi r^2}$ is the undisturbed initial intensity at a distance r with a luminosity (the net power emitted) of the star $L_\star$ and

$$\kappa_{med}(r) = \frac{\int B_\lambda(\lambda, T_{bb})\kappa_\lambda(T(r))\mathrm{d}\lambda}{\int B_\lambda(\lambda, T_{bb})\mathrm{d}\lambda} \tag{2.13}$$

is the mean opacity for radiation from a black body (Planck-)spectra of temperature T_{bb} and dust/gas mixture of temperature T.
The calculation of $\kappa_\lambda(r)$ is highly complex. Different approaches exist (for example by Semenov et al., 2003) but data for specific disks (dust distributions, temperatures, gas to dust ratios) are missing. For the simulations presented later on, κ_λ is simplified by assuming an independency on the temperature, leading to a constant κ_{med} and simplifying the integral from 2.12 as well. The resulting error is discussed later on.

2.3 Motion of gas in PPDs

As stated earlier, calculating particle motion in PPDs is heavily dependent on the gas motion. In general, a stable circular orbit of any body without external influences can be described by the azimuthal mean orbital speed (Keplerian velocity) v_{k} given by eq. 1.2. Gas molecules in PPDs are furthermore exposed to a pressure gradient pointing towards the central star ($\frac{\mathrm{d}P}{\mathrm{d}r} < 0$), reducing their azimuthal velocity. Treating the gas as ideal liquid the momentum equation can be reduced to (Whipple, 1972)

$$v_{\phi,\mathrm{gas}} = \sqrt{\frac{GM_*}{r} + \frac{r}{\rho_{\mathrm{gas}}}\frac{\mathrm{d}P}{\mathrm{d}r} + r\, v_{r,\mathrm{gas}}\frac{\mathrm{d}v_{r,\mathrm{gas}}}{\mathrm{d}r}} < v_{\mathrm{k}} \quad , \tag{2.14}$$

where $v_{r,\mathrm{gas}}$ is the radial velocity of the gas. It can be calculated following Lynden-Bell and Pringle (1974) via

$$v_{\mathrm{r,gas}} = -\frac{3}{\Sigma_{\mathrm{gas}}\sqrt{r}}\frac{\partial}{\partial r}\left(\Sigma_{\mathrm{gas}}\nu_{\mathrm{gas}}\sqrt{r}\right) \quad , \tag{2.15}$$

where ν_{gas} is the gas viscosity which consists on the one hand of the molecular viscosity ν_{mol} of the gas and on the other hand of the so-called turbulent viscosity ν_{T}. Shakura and Sunyaev (1973) introduced a formalism for the latter:

$$\nu_{\mathrm{T}} = \alpha_{\mathrm{t}}\, c_{\mathrm{s}}\, h \quad , \tag{2.16}$$

where α_{t} is the dimensionless Shakura-Sunyaev parameter which is often denoted as "turbulence parameter". Their considerations result from a specific problem in the evolution of a PPD: the loss of angular momentum. Since angular momentum is a conserved quantity, any changes in density are linked to the transfer of angular momentum. As shown earlier, molecular viscosity is not sufficient to explain the observed mass accretion rates. Therefore other sources for an "abnormal" viscosity are introduced like for example magneto-rotational instabilities caused by ionized molecules in the disk. Since the

detailed solution is highly dependent on the actual disk properties, Shakura and Sunyaev (1973) simplified this issue via the α_t-prescription which allows treating turbulent motion without knowing all properties exactly. Since turbulent viscosity ν_T is much larger than molecular viscosity ν_{mol}, the gas viscosity in eq. 2.15 is often set to be ν_T. Note here that for non-accreting disks, the radial velocity of the gas is often set to be zero.
Besides influencing the global motion of the gas in radial direction, turbulence leads to locally altering gas velocities which induces forces on particles as well.

2.4 Forces on Particles in PPDs

The main influence on particle motion is the drag force. All types of gas motion exert drag forces. This even includes - for very small dust particles - Brownian motion. If one is only interested in the radial drift of single particles, turbulent and Brownian motion can be neglected as these types are limited to local phenomenons only. Nonetheless, Brownian motion leads to diffusion which distributes particles inside the disk. For dust evolution via coagulation, all sources of drag have to be considered.
Other types of forces are those induced due to the radiation of the (proto-)star. This includes radiation pressure as well as photophoresis. Since the gas pressure in protoplanetary disks is non-zero, effects like the Poynting-Robertson drag are insignificant for dust motion. Nonetheless, in later disk stages (debris disk) this effect can influence the motion of particles heavily (Wyatt, 2005).

2.4.1 Drag forces

Suspended particles moving relative to the gas are subjected to drag forces pointing contrarily to the direction of motion. Generally, this force can be expressed via

$$F_D = \frac{m}{\tau_{fric}} \Delta v \quad , \tag{2.17}$$

where m is the particles mass, τ_{fric} is the gas-grain friction time (or "stopping time") and Δv is the velocity difference between the particle and the gas. This formula is valid for every particle regardless of its size, porosity, material or shape (note here that τ_{fric} itself can be dependent on Δv as well). To simplify calculations, particles in protoplanetary disks are characterised as spherical and quasi-solid (bulk density and porosity are often connected to an effective particle density). This simplification allows the treatment of dust motion and growth evolution without intensive studies on the particle properties. The drag on particles can then be described more easily without using correction factors (see e.g. Loth, 2008) or even simulating/measuring the interaction of single particles with

the gas. Nonetheless, the influence of shape effects on the collision velocities and the collisional outcome is still investigated (e.g. Kruss et al., 2016).
Different drag regimes exist, depending on the dimensionless quantities Knudsen Number and Particle Reynolds Number. The Knudsen Number Kn is defined as the ratio of the mean free path λ_{mfp} and a characteristic length which in the case of a spherical solid particle can be associated with the particle's radius s:

$$Kn = \frac{\lambda_{\mathrm{mfp}}}{s} \quad . \tag{2.18}$$

The Reynolds Number Re can generally be described as the ratio of momentum forces to viscous forces for a flow within a system with a characteristic length scale L and a characteristic velocity scale U:

$$\mathrm{Re} = \frac{L\,U}{\nu_{\mathrm{mol}}} \quad , \tag{2.19}$$

where ν_{mol} is the kinetic or molecular viscosity of the surrounding gas or fluid. In case of a spherical solid particle the characteristic length can be associated with its diameter $2\,s$ and the characteristic velocity is the velocity difference of the gas and the particle Δv:

$$\mathrm{Re_p} = \frac{2\,s\,\Delta v}{\nu_{\mathrm{mol}}} \tag{2.20}$$

Generally the Reynolds Number characterises the flow regime and is important not only in the treatment of flows around particles but furthermore for the determination of turbulent flows in protoplanetary disks.
Different drag regimes can be classified as follows (e.g. Weidenschilling, 1977a):

1. $Kn > 8/9$: Epstein Drag
2. $Kn < 8/9$: Stokes Drag
   (a) $\mathrm{Re_p} < 1$: laminar flow
   (b) $1 < \mathrm{Re_p} < 800$: transition flow
   (c) $\mathrm{Re_p} > 800$: turbulent flow

Epstein Drag: $Kn > 8/9$
Assuming subsonic movement of the spherical, solid particle in respect to the gas and large Knudsen Numbers, the drag force can be approximated by taking the collision frequency of the gas molecules and the particle and calculating the momentum transfer per collision:

$$F_{\mathrm{D,ep}} = \frac{4}{3}\pi\epsilon\rho_{\mathrm{gas}}s^2\overline{v}_{\mathrm{th}}\,\Delta v \quad , \tag{2.21}$$

where $\overline{v}_{\mathrm{th}}$ is the mean thermal velocity of the gas molecules, Δv is the relative (macroscopic) velocity of the particle and the gas and ϵ is an empirical factor which depends on the exact interaction of the impinging gas molecule and the particle surface. For air, experimental data revealed $\epsilon = 0.68 \pm 0.10$ (Blum et al., 1996) which is in good agreement with a simulated value of $\epsilon = 0.58$ (Meakin et al., 1989).

Stokes Drag and Rayleigh Formula: $Kn < 8/9$

Generally for small Knudsen Numbers the drag on spherical, solid particles can be described via

$$F_{\mathrm{D,full}} = \frac{\pi}{2} C_{\mathrm{D}} s^2 \rho_{\mathrm{gas}} \Delta v^2 \quad , \tag{2.22}$$

where C_{D} is the drag coefficient dependent upon the shape of the particle and the particle Reynolds Number. For a spherical particle C_{D} can be expressed as follows:

$$C_{\mathrm{D}} = \begin{cases} 24\,\mathrm{Re}_{\mathrm{p}}^{-1}\,, & \mathrm{Re}_{\mathrm{p}} < 1 \\ 24\,\mathrm{Re}_{\mathrm{p}}^{-0.6}\,, & 1 < \mathrm{Re}_{\mathrm{p}} < 800 \\ 0.44\,, & \mathrm{Re}_{\mathrm{p}} > 800 \quad . \end{cases} \tag{2.23}$$

Large Reynolds Numbers result in a drag force proportional to Δv^2 which is therefore called quadratic drag. This dependency was discovered by Rayleigh who observed the drag in turbulent flows. On the other hand, in protoplanetary disks small dust particles are subjected to laminar flows only and the drag can then be simplified to the equation given by Stokes:

$$F_{\mathrm{D,st}} = 6\pi \rho_{\mathrm{gas}}\, s\, \Delta v \quad . \tag{2.24}$$

Cunningham Correction

A general problem is the transition between Epstein and Stokes drag at $Kn = 8/9$. Although the transition is steady, the deviation is not. This can lead to issues in simulations of particle movements with coarse temporal resolution and is physically incomplete. Cunningham (1910) therefore provided an empirical function to modify the drag forces leading to smooth transition. The Cunningham corrected drag force can be expressed as

$$F_{\mathrm{D,cun}} = \frac{F_{\mathrm{D,st}}}{1 + \frac{Kn}{2}\left(A_1 + A_2 \exp\left(-\frac{2\,A_3}{Kn}\right)\right)} \tag{2.25}$$

with A_{i} being gas dependent values measured for example by Cunningham himself. Hutchins et al. (1995) and Rader (1990) provided the following values for He and H_2 Gas:

	H_2	He
A_1	1.141	1.277
A_2	0.506	0.370
A_3	-	2.0

Table 2.2: Values for Cunningham correction (Hutchins et al., 1995; Rader, 1990), note that $A_1 + A_2 \stackrel{!}{=} 1.647$.

Since gas of cosmic composition is a mixture of different gases with the main component H_2, the following values for A_i were used for the calculations presented later on: $A_1 = 1.2$, $A_2 = 1.647 - A_1 = 0.447$, and $A_3 = 2.0$.
The Cunningham corrected drag force $F_{D,cun}$ transitions into the Epstein drag $F_{D,ep}$ for $s \to 0$. With $F_{D,ep} = \epsilon \frac{8}{9\,Kn} F_{D,st}$ the following relation should be pointed out:

$$\lim_{s\to 0} F_{D,cun}(s) = \lim_{s\to 0} F_{D,ep}(s) \tag{2.26}$$

$$\Rightarrow \epsilon = \frac{9}{8\,(A_1 + A_2)} \tag{2.27}$$

which reveals $\epsilon = 0.68$ for the values found by Hutchins et al. (1995). This value is in good agreement with the value found by Blum et al. (1996).

2.4.2 Residual gravity

Assuming a gas-free disk, the gravitational acceleration due to the central star forces the particle onto an orbit with an azimuthal velocity equalling the Keplerian velocity. As mentioned earlier, the azimuthal velocity of the gas particles (see eq. 2.47) is lower than the Keplerian velocity $v_{\phi,kep}$, leading to a drag force onto the orbiting particles. The acceleration due to this residual gravity (Weidenschilling, 1977a) is given by

$$a_{res} = \frac{1}{\rho_{gas}} \frac{dP}{dr} \tag{2.28}$$

The residual gravity is used to calculate the force balance for particles at a specific distance to the central star. For detailed analysis of the particles motion, the equations of motion (see sec. 2.5.1 and eq. 2.45) have to be solved directly.

2.4.3 Radiation Pressure

Photons that are emitted from a radiation source transfer energy when impinging on a surface. Depending on the interaction with the surface, photons can get absorbed or reflected. The pressure exerted by the photons is described via

$$P_{\mathrm{rp}} = (1 + R_{\mathrm{surf}}) \frac{I}{\mathrm{c}} \cos^2 \vartheta \quad , \tag{2.29}$$

where I is the energy flux (intensity) given by eq. 2.12, c is the speed of light, ϑ is the angle between the surface normal and the direction of the impinging photons, and $R_{\mathrm{surf}} = \frac{\Phi_{\mathrm{refl}}}{I}$ is the surface reflectivity which is the ratio between the reflected energy flux Φ_{refl} and the received energy flux (intensity). This yields $R_{\mathrm{surf}} = 0$ for fully absorbing surface and $R_{\mathrm{surf}} = 1$ for a fully reflecting surface. A scheme on radiation pressure on a sphere is depicted in fig. 2.3.

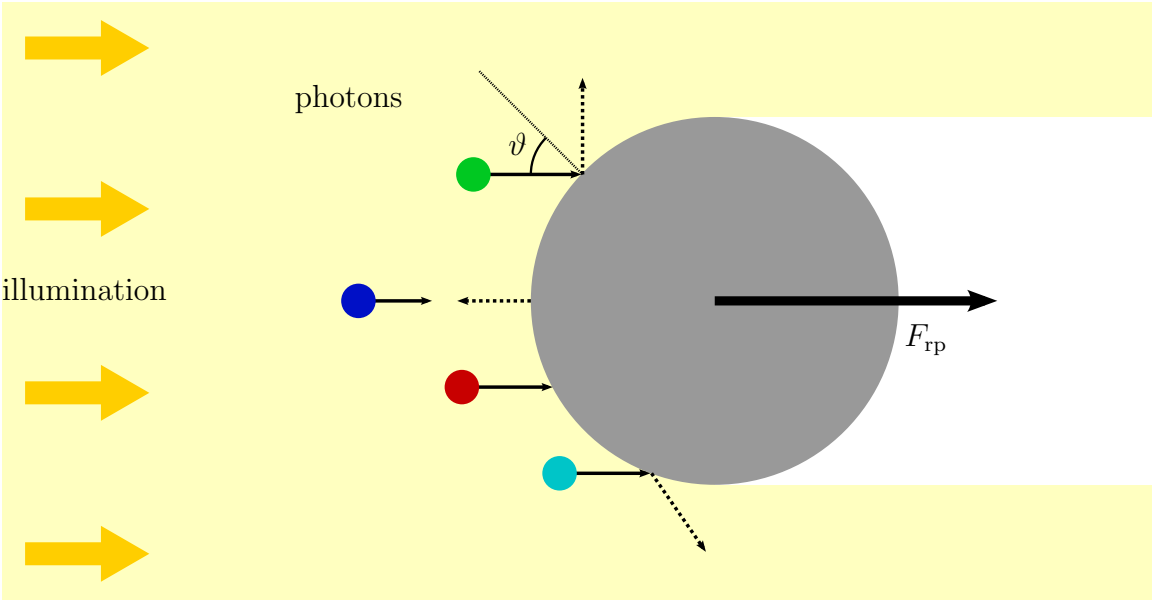

Figure 2.3: Scheme of radiation pressure. Photons impinging the particles surface can get reflected (blue, green, cyan) or absorbed (red). The incident angle ϑ in respect to the surface normal equals the reflection angle.

Assuming only geometrical reflection (particle circumference is much larger than the wavelength of the irradiation) and using eq. 2.29, the force acting on a spherical particle with radius s can be calculated by splitting the force in a normal and tangential component in respect to the surface normal. The net force in direction of illumination can then be calculated by integrating over the normal and tangential forces for every surface element. For a spherical particle, the resulting force is independent on the reflectivity, leading to

$$F_{\mathrm{rp}} = 2\pi s^2 \frac{I}{\mathrm{c}} \quad . \tag{2.30}$$

Since particles in protoplanetary disks are not ideal spherical bodies, the resulting force due to radiation pressure may differ for realistic particle shapes.

2.4.4 Photophoresis

Photophoresis is a force acting on an illuminated particle in a gaseous environment (Yalamov et al., 1976a,b; Rohatschek, 1995). A basic explanation is depicted in fig. 2.4.

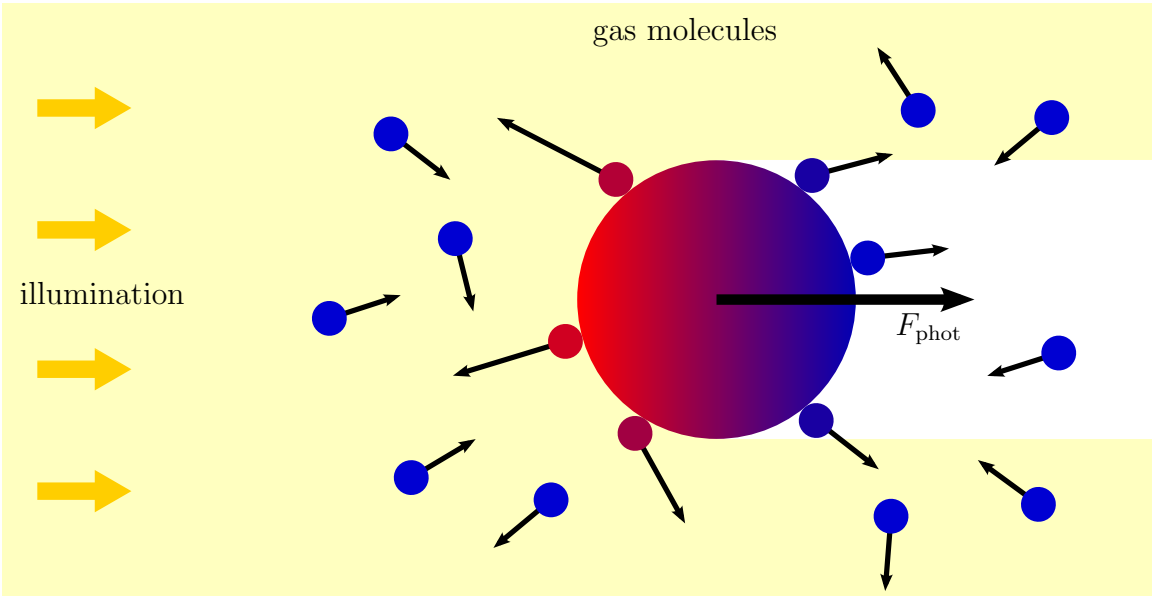

Figure 2.4: Scheme of phorotphoretic force. Gas molecules impinging the particles surface accommodate and leave the surface with a mean energy equal to the surface temperature at the collision point. If the surface is hotter at the illuminated side than on the non-illuminated side (positive photophoresis), a temperature gradient is established over the particle in opposition to the direction of illumination. This leads to a net momentum transfer (net force) in the direction of illumination.

Gas particles impinging the colder side transfer less momentum than those impinging the hotter side. This leads to a net force pointing from the hotter to the colder side (positive photophoresis). One has to note here that scenarios exist where particles have a high refractive index and simultaneously a high (or non-linear) opacity which can switch the temperature gradient and therefore the direction of the photophoretic force (negative phorophoresis). Photophoresis might be important for the movement of chondrules in protoplanetary disks (Krauss and Wurm, 2005; Wurm and Krauss, 2006a; Loesche et al., 2013, 2014) and might also influence the sorting of solid materials (Haack and Wurm, 2007; Wurm et al., 2013; Cuello et al., 2016). In general, photophoretic forces depend on a variety of parameters like for example thermal conductivities of the particle and the gas, illumination strength, Knudsen Number, gas pressure and more. Several studies exist in

experiments (Wurm and Krauss, 2008; Wurm et al., 2010; van Eymeren and Wurm, 2012; von Borstel and Blum, 2012; Kuepper et al., 2014; Loesche et al., 2014) as well as in theory (Yalamov et al., 1976a,b; Reed, 1977; Beresnev et al., 1993; Matthews et al., 2016) covering different pressure regimes and particle characteristics and describing the photophoretic force. One approach for the photophoretic force on spherical and homogeneous particles covering all pressure regimes was proposed by Rohatschek (1995). Using the calculated photophoretic forces in the free molecular (fm) flow ($Kn \gg 0$) as well as in the slip-flow (sf) regime ($Kn \ll 1$), Rohatschek (1995) firstly extrapolated the latter for $Kn \to 0$ to get a continuum formula (co) and then interpolated between the fm and co solutions using a function following

$$F_{\mathrm{ph}} = \frac{2\,F_{\mathrm{ph,max}}}{\frac{P}{\hat{P}} + \frac{\hat{P}}{P}} \quad , \tag{2.31}$$

where $\hat{P}$ is the pressure where the force has its maximum $F_{\mathrm{ph,max}}$. Both values, $\hat{P}$ as well as $F_{\mathrm{ph,max}}$ are non-trivial and certain approximations to the physical models have to be made. Hettner (1928) presented an interpolation for the latter following

$$\frac{1}{F_{\mathrm{ph}}} = \frac{1}{F_{\mathrm{ph}}^{\mathrm{co}}} + \frac{1}{F_{\mathrm{ph}}^{\mathrm{fm}}} \quad . \tag{2.32}$$

One major issue in most recent approximations is that the temperature difference between the gas and the particle has to be low. In protoplanetary disks - especially if they are optically thin - as well as in laboratory setups this is not necessarily the case (Loesche and Wurm, 2012; Loesche, 2015).

Loesche and Husmann (2016) therefore improved the model for photophoretic forces starting from the free molecular flow regime. Loesche et al. (2016) use a kinetic model for the gas-surface interaction and provide a solution for the heat transfer problem with the thermal radiation field of the particle balancing an external radiation field and a linearised boundary condition for the particles thermal radiation at the mean particle temperature $\overline{T}$. The photophoretic force in the free molecular flow regime can then be calculated via

$$F_{\mathrm{phot}}^{\mathrm{fm}} = \frac{\pi}{3}\,\alpha\,\alpha_{\mathrm{m}}\,\frac{P}{\sqrt{T_\infty^2 + T_\infty \alpha (A_0^{\mathrm{fm}} - T_\infty)}}\,s^2 \cdot \frac{I\,J_1}{\frac{k_{\mathrm{th}}}{s} + 4\sigma_{\mathrm{SB}}\varepsilon\,(A_0^{\mathrm{fm}})^3} \quad , \tag{2.33}$$

where α is the thermal accommodation coefficient, α_{m} is the momentum accommodation coefficient (for details on the accommodation coefficients see sec. 4.3.2), T_∞ the gas temperature, I the intensity of the irraditation, $J_1 = 1/2$ an asymmetry factor for spherical particles (Wurm et al., 2010; Rohatschek, 1995), k the thermal conductivity of the particle, $h_{\mathrm{fm}} = \frac{1}{2}\,\alpha_{\mathrm{m}}\,\alpha\,\frac{p}{T_\infty} v_{\mathrm{th}}$ the heat transfer coefficient for a thermal gas velocity v_{th}, ε the emissivity, k_{th} the thermal conductivity of the particle, and A_0^{fm} the evolution coefficient

(or mean particle temperature) in the fm case. The latter results from the ansatz for the particle temperature (dependent on the particle radius s and the azimuthal angle ζ)

$$T(s,\zeta) = \sum_{\nu=0}^{\infty} A_\nu P\nu(\cos(\zeta)) \tag{2.34}$$

and the median particle temperature

$$\overline{T} = \frac{1}{4\pi} \int_0^{2\pi} \int_0^{\pi} T(\zeta) \sin\zeta \, \mathrm{d}\zeta \, \mathrm{d}\xi = A_0^{\mathrm{fm}} \quad . \tag{2.35}$$

A_0^{fm} can be calculated via

$$A_0^{\mathrm{fm}} = \frac{\sigma_{\mathrm{SB}} \, \epsilon \, (3T_{\mathrm{bb}}^4 + T_{\mathrm{rad}}^4) + I_0 J_0}{4 \, \sigma_{\mathrm{SB}} \, \epsilon \, T_{\mathrm{bb}}^3} \quad , \tag{2.36}$$

which is a direct result from the boundary conditions including a background irradiation field and the above mentioned linearisation. A detailed derivation can be found in Loesche et al. (2016).

The slip-flow solution for photophoretic forces – presented by Loesche and Husmann (2016) with an included model for thermal creep, thermal stress as well as frictional gas slippage and a temperature jump at the gas-particle interface – was extrapolated for vanishing Knudsen Numbers. This leads to a continuum solution following

$$F_{\mathrm{phot}}^{\mathrm{co}} = 4\pi \, \kappa_{\mathrm{s}} \, \frac{\eta_{\mathrm{dyn}}^2}{\rho_{\mathrm{gas}} \, A_0^{\mathrm{co}}} \, \frac{I \, J_1}{\frac{k_{\mathrm{th}}}{s} + 2\frac{k_{\mathrm{gas}}}{s} + 4\sigma_{\mathrm{SB}} \varepsilon \, T_{\mathrm{bb}}^3} \quad , \tag{2.37}$$

where $\kappa_{\mathrm{s}} \simeq \frac{3}{4}(1+0.5\,\alpha_{\mathrm{m}})$ is the thermal creep coefficient, η_{dyn} is the dynamic gas viscosity, k_{gas} is the thermal conductivity for the gas, T_{bb} is the black-body temperature for a given intensity I and radiation field T_{rad}, and A_0^{co} is evolution coefficient (or mean particle temperature) in the continuum case. The latter results – similar to A_0^{fm} – from the ansatz for the particle temperature. Using an homogenisation in the heat transfer equation to cope with direct illumination and the boundary conditions at the particles surface including a temperature jump and radiation, the mean particle temperature can be calculated via

$$A_0^{\mathrm{co}} = \frac{\frac{k_{\mathrm{gas}}}{s} T_\infty + \sigma_{\mathrm{SB}} \, \epsilon \, (3T_{\mathrm{bb}}^4 + T_{\mathrm{rad}}^4) + I \, J_0}{\frac{k_{\mathrm{gas}}}{s} + 4 \, \sigma_{\mathrm{SB}} \, \epsilon \, T_{\mathrm{bb}}^3} \quad . \tag{2.38}$$

Since the thermal conductivity of the gas close to the particle surface k_{gas} depends on the gas temperature close to the surface (which equals A_0^{co} in the co case), eq. 2.38 has to be calculated iteratively using the black-body temperature T_{bb} as starting point.

A covering formula for all pressure regimes was found using eq. 2.31 by rewriting the fm and co solutions following

$$F_{\text{phot}}^{\text{fm}} \overset{2.33}{\simeq} 2\,\Xi\,\frac{P}{P^*}\,r_0^2\,\tau_{\text{fm}}\,\frac{J_1\,I}{k} \tag{2.39a}$$

$$F_{\text{phot}}^{\text{co}} \overset{2.37}{=} 2\,\Xi\,\frac{P^*}{P}\,r_0^2\,\tau_{\text{co}}\,\frac{J_1\,I}{k} \quad . \tag{2.39b}$$

Here, the dimensionless scaling coefficients τ_{fm} and τ_{co} are determined via

$$\tau_{\text{fm}} = \frac{\alpha}{2}\,\frac{\sqrt{A_0^{\text{co}}}}{\sqrt[4]{T_\infty^2 + T_\infty\alpha(A_0^{\text{fm}} - T_\infty)}}\,\frac{1}{\frac{k_{\text{th}}}{s} + h_{\text{fm}} + 4\sigma_{\text{SB}}\epsilon\left(A_0^{\text{fm}}\right)^3} \tag{2.40a}$$

$$\tau_{\text{co}} = \kappa_{\text{s}}\,\frac{\sqrt[4]{T_\infty^2 + T_\infty\alpha(A_0^{\text{fm}} - T_\infty)}}{\sqrt{A_0^{\text{co}}}}\,\frac{1}{\frac{k_{\text{th}}}{s} + 2\frac{k_{\text{gas}}}{s} + 4\sigma_{\text{SB}}\epsilon T_{\text{bb}}^3} \quad , \tag{2.40b}$$

the force coefficient Ξ via

$$\Xi = \frac{\pi}{2}\sqrt{\frac{\pi}{3}\kappa_{\text{s}}}\,\frac{v_{\text{th}}\,\nu_{\text{dyn}}}{\sqrt{A_0^{\text{co}}\,\sqrt{T_\infty^2 + T_\infty\alpha(A_0^{\text{fm}} - T_\infty)}}} \quad . \tag{2.41}$$

The pressure factor P^* can be calculated by

$$P^* = \frac{3}{\pi}\,\Xi\,\frac{\sqrt{A_0^{\text{co}}\,\sqrt{T_\infty^2 + T_\infty\alpha(A_0^{\text{fm}} - T_\infty)}}}{s} \quad . \tag{2.42}$$

Using eq. 2.32, the maximum photophoretic force can be calculated via

$$F_{\text{ph,max}} = \Xi\sqrt{\tau_{\text{fm}}\,\tau_{\text{co}}}\,s^2\,\frac{I\,J_1}{k_{\text{th}}} \tag{2.43}$$

and the pressure optimum $\hat{P}$ by

$$\hat{P} = \sqrt{\frac{\tau^{\text{co}}}{\tau^{\text{fm}}}}\,P^* \quad . \tag{2.44}$$

2.5 Motion and Velocity of Dust in PPDs

As mentioned in section 2.4 one can differentiate between two types of forces. Forces which are time-averaged zero on the one hand cause only local motion of particles. Forces which are time-averaged nonzero cause global motion of particles. Sources for local motion are for example Brownian motion and turbulence, sources for global motion are directed forces which influence radial or azimuthal motion like gas drag due to global gas motion, photophoresis or radiation pressure.

Most investigations of dust evolution in PPDs limit the motion of particles to one dimension - the radial direction. Nonetheless, when calculating collision velocities, all sources (global and local) are included.

2.5.1 Two-dimensional dust motion

In general, the equations of motion for solid particles in radial (v_r) and azimuthal (v_ϕ) direction can be expressed via

$$\frac{\mathrm{d}v_r}{\mathrm{d}t} = \frac{v_\phi^2}{r} - \frac{GM_*}{r^2} - \frac{(v_r - v_{\mathrm{r,gas}})}{\tau_{\mathrm{fric}}} + \frac{F_{\mathrm{radial}}}{m} \tag{2.45a}$$

$$\frac{\mathrm{d}}{\mathrm{d}t}(r\,v_\phi) = -\frac{r}{\tau_{\mathrm{fric}}}(v_\phi - v_{\phi,\mathrm{gas}}) \quad , \tag{2.45b}$$

where F_{radial} represents additional forces acting on the particles in radial direction (e.g. radiation pressure or photophoresis) and $\tau_{\mathrm{fric}} = \frac{m_{\mathrm{p}}}{F_{\mathrm{D}}}\Delta v$ is the gas grain friction time, calculated from the drag force F_{D} acting on the particle with mass m_{p}. The gas velocity in radial direction $v_{\mathrm{r,gas}}$ is defined by (Lynden-Bell and Pringle, 1974)

$$v_{\mathrm{r,gas}} = -\frac{3}{\Sigma_{\mathrm{gas}}\sqrt{r}}\frac{\mathrm{d}\left(\Sigma_{\mathrm{gas}}\nu\rho_{\mathrm{gas}}^{-1}\sqrt{r}\right)}{\mathrm{d}r} \tag{2.46}$$

and $v_{\phi,\mathrm{gas}}$ is the gas velocity in azimuthal direction defined via

$$v_{\phi,\mathrm{gas}} = \sqrt{\frac{G\,M_*}{r} + \frac{r}{\rho_{\mathrm{gas}}}\frac{\mathrm{d}P}{\mathrm{d}r}} \tag{2.47}$$

Although solutions exist for special cases (Weidenschilling, 1977a) in the general case numerical methods have to be used, especially for large forces F_{radial}.

2.5.2 Relative Velocities of Dust

Five sources for relative velocities exist:

1. radial motion
2. azimuthal motion
3. turbulent motion
4. Brownian motion
5. vertical motion .

Other sources might exist as well (e.g. motion of charged particles in magnetic or electric fields) but are often not considered to be significant.

Relative radial and azimuthal velocities

Using eq. 2.45 and assuming $F_{\text{radial}} = 0$, particles spiral inwards. Introducing the dimensionless Stokes Number

$$\text{St} = \tau_{\text{fric}} \sqrt{\frac{GM_*}{R^3}} \tag{2.48}$$

the steady state solution for the radial drift velocity can be calculated to (Weidenschilling, 1977a)

$$v_r = \frac{v_{\text{r,gas}}}{1 + \text{St}^2} - \frac{2\, v_{\text{n}}}{\text{St} + \text{St}^{-1}} \quad , \tag{2.49}$$

where $v_{\text{r,gas}}$ is the radial gas velocity (eq. 2.46) and v_{n} as the maximum drift velocity, described by

$$v_{\text{n}} = -\frac{\partial P}{\partial r} \frac{\tau_{\text{fric}}}{2\, \rho_{\text{gas}}\, \text{St}} \quad . \tag{2.50}$$

The steady state solution for the azimuthal motion can be calculated to

$$v_\phi = v_{\phi,\text{gas}} + \frac{v_{\text{n}}}{1 + \text{St}^2} \quad , \tag{2.51}$$

where $v_{\phi,\text{gas}}$ is the azimuthal gas velocity (eq. 2.47). Using eq. 2.49 and eq. 2.51, the resulting relative velocities between two particles with Stokes Numbers St_1 and St_2 can be written as

$$\Delta v_r = \left| v_{r,\text{gas}} \left(\frac{1}{1 + \text{St}_1^2} - \frac{1}{1 + \text{St}_2^2} \right) - 2\, v_{\text{n}} \left(\frac{1}{\text{St}_1 + \text{St}_1^{-1}} - \frac{1}{\text{St}_2 + \text{St}_2^{-1}} \right) \right| \tag{2.52a}$$

$$\Delta v_\phi = \left| v_{\text{n}} \left(\frac{1}{1 + \text{St}_1^2} - \frac{1}{1 + \text{St}_2^2} \right) \right| \tag{2.52b}$$

The gas-grain friction time τ_{fric} can be calculated using either the general equation for drag forces eq. 2.17 with the domain-specific drag (eq. 2.21, eq. 2.22 or eq. 2.24) or the Cunningham drag eq. 2.25.

Relative turbulent velocities

Calculating relative turbulent velocities is not trivial. Voelk et al. (1980) introduced a formalism to describe turbulent motions which was improved by Markiewicz et al. (1991). Their model is based on a theory of smallest and largest eddies in PPDs. While the period

of the largest eddies $\tau_{\mathrm{ed,L}}$ are identified with the local orbital period, the smallest eddies period $\tau_{\mathrm{ed},\eta}$ can be calculated via the turbulent Reynolds Number $\mathrm{Re_t}$:

$$\tau_{\mathrm{ed},\eta} = \mathrm{Re_t}^{-1/2}\,\tau_{\mathrm{ed,L}} \tag{2.53}$$

The Reynolds Number for turbulent motion can be expressed using eq. 2.16 to

$$\mathrm{Re_t} = \frac{\nu_\mathrm{t}}{\nu_\mathrm{mol}} = \alpha_\mathrm{t}\frac{c_\mathrm{s}^2}{\nu_\mathrm{mol}\,\Omega} \quad . \tag{2.54}$$

Dependent on the gas-grain coupling time τ_{fric}, particles are influenced most by the smallest eddies or by the largest ones. This leads to relative velocities which in general are not trivial to calculate. Ormel and Cuzzi (2007) derived a closed-form expression for the relative velocities in an α_t-parameterised turbulent disk. They distinguish between different regimes with different resulting relative velocities Δv. With the particles gas-grain friction times $\tau_1 \geq \tau_2$ this results in:

a) Tightly coupled particles, $\tau_1,\ \tau_2 < \tau_{\mathrm{ed},\eta}$

I) $\tau_1 \ll \tau_{\mathrm{ed},\eta}$: $\quad \Delta v^2 = V_\mathrm{g}^2\,\mathrm{Re_t}^{1/2}\,(\mathrm{St}_1 + \mathrm{St}_2)^2$

II) else: $\quad \Delta v^2 = V_\mathrm{g}^2\,\dfrac{\mathrm{St}_1 - \mathrm{St}_2}{\mathrm{St}_1 + \mathrm{St}_2}\left(\dfrac{St_1^2}{\mathrm{St}_1 + \mathrm{Re_t}^{-1/2}} - \dfrac{St_2^2}{\mathrm{St}_2 + \mathrm{Re_t}^{-1/2}}\right)$

b) intermediate regime, $\tau_{\mathrm{ed},\eta} \leq \tau_1 \leq \tau_{\mathrm{ed,L}}$

$$\Delta v^2 = V_\mathrm{g}^2\,\mathrm{St}_1\left[2\,y_\mathrm{a} - \epsilon - 1 + \frac{2}{1+\epsilon}\left(\frac{1}{1+y_\mathrm{a}} + \frac{\epsilon^3}{y_\mathrm{a}+\epsilon}\right)\right]$$

$$\epsilon = \frac{\tau_2}{\tau_1}$$

$$y_\mathrm{a} \approx 1.6 \text{ for } \tau_1 \ll \tau_{\mathrm{ed,L}}$$

V_g can be expressed via

$$V_\mathrm{g} = \sqrt{\frac{3}{2}\,V_{\mathrm{ed,L}}^2} \quad , \tag{2.55}$$

where $V_{\mathrm{ed,L}} = \sqrt{\alpha_\mathrm{t}}c_\mathrm{s}$ is the largest eddy velocity.

Relative velocities due to Brownian motion

Brownian motion of gas particles can influence the motion of dust particles as well (Blum et al., 1996). For small particles the momentum transfer of the randomly colliding gas-molecules does not vanish for specific timescales. This leads to a relative velocity depen-

dent on the particle masses m_1 and m_2 and the distance to the central star r according to

$$\Delta v_{\mathrm{brown}}(m_1, m_2, r) = \sqrt{\frac{8\, k_{\mathrm{b}}\, T(r)\, (m_1 + m_2)}{\pi\, m_1 m_2}} \quad . \tag{2.56}$$

Note here that although the mean (three-dimensional) velocity due to Brownian motion is zero, the mean relative velocity of two particles is not.

Vertical settling

Particles above the midplane are subjected to gravitation with a net component larger than zero in the disks normal direction. Therefore, the resulting motion of these particles leads to relative velocities. Birnstiel et al. (2010) introduced a formalism and showed that the relative velocity peaks if the particles have different sizes and one particle has a Stokes number of unity. Since the relative velocity due to vertical settling is mostly much lower than the relative velocities due to the other sources (especially if the turbulence value α_{t} is large), it is neglected in several papers (e.g. Windmark et al., 2012a) and is therefore omitted in further calculations presented in later chapters.

3

Growth of Dust in PPDs: Models and Material Dependencies

Forming planets implies dust growth of at least twelve orders of magnitude starting with sizes of several micrometer or even nanometer. As mentioned earlier, this growth has to be caused by collisions between the dust particles, which can lead to different outcomes depending on a variety of parameters. The exact process of forming large bodies is highly complex and can involve billions of particle collisions in the disk. Dust evolution simulations require suitable models for the collisional outcome. These models are based on empirical, experimental studies and simulations of dust collisions. To keep the computational timescales acceptable these models have to be simplified that way that the amount of parameters influencing the collisional outcome are conveniently reduced to only a few significant ones, e.g. the particle masses and the collision velocity. In this chapter the outcome of dust collisions is treated in detail and the collisional outcome model as depicted in Windmark et al. (2012a) is presented. Within section 3.2, experimental studies are presented dealing with the material dependency of the collisional outcome and possible influences on growth in PPDs. Besides collisions, another effect can influence influence particle growth in disks where the intensity of the solar irradiation is high: light-induced erosion. Experimental studies determining the influence of gravity on the erosion of particles due to this effect are presented in the last subsection.

3.1 Collisional outcome in detail

Collisions between dust particles are always between a larger particle with radius r_t (called "target") and a smaller particle with radius r_p (called "impactor") although collisions of particles with mass differences less than a specific value are often called "equally sized" collisions (e.g. Güttler et al., 2010). Recent models do not explicitly differentiate between

equally sized and non-equally sized particles but use the particle masses for the determination of the collisional outcome. As mentioned earlier, lots of different parameters exist influencing the outcome of a collision, for example the porosity, the inclination of the collision or the particle circularities (Teiser et al., 2011a,b; Jankowski et al., 2012). The aim of creating a collisional outcome model is to reduce the set of parameters to only a few significant ones. The model by Windmark et al. (2012a) for silicate particles uses only the masses of the bodies and the collision velocity to determine the collisional outcome which is either accretion, bouncing, fragmentation or mass transfer/erosion.

3.1.1 Accretion, Bouncing Regime and Transition

The most effective way of growth is via hit & stick, when the mass gain of the target equals the mass of the impactor

$$\Delta m_\mathrm{t} = m_\mathrm{p} \quad . \tag{3.1}$$

Hit & stick collisions only occur for low masses and low collision velocities. Various experiments exist proving high dependencies on above-mentioned parameters and others like porosity, material, e.t.c. (see e.g. Weidling et al., 2012; Kothe et al., 2013; Jankowski et al., 2012). Due to the variety of parameters and the fact that every collision partner has its unique inner structure, experiments can only give statistics for the collisional outcome, simplifying the parameter set significantly to allow for theoretical computations and simulations of particle growth in PPDs. This leads to a dependency of the upper limit of the collision velocity where particle collisions always result in hit & stick on the mass of the impactor and the material properties. Weidling et al. (2012) calculated the sticking threshold for dust particles to

$$\Delta v_\mathrm{s} = \left(\frac{m_\mathrm{p}}{m_\mathrm{s}}\right)^{-5/18} \frac{\mathrm{m}}{\mathrm{s}} \quad , \tag{3.2}$$

where $m_\mathrm{s} = 1.9 \times 10^{-22}$ kg is the normalising constant from their experimental results. Material properties are very important and the transition from this formula which is valid for silicate material to other materials like H_2O or CO_n cannot be done directly.
Once the collision velocity is higher than Δv_s, collisions can lead to both, hit & stick or bouncing with increasing probability of bouncing for increasing collisional velocities. Weidling et al. (2012) also determined a maximum collision velocity for bouncing collisions following

$$\Delta v_\mathrm{b} = \left(\frac{m_\mathrm{p}}{m_\mathrm{b}}\right)^{-5/18} \frac{\mathrm{m}}{\mathrm{s}} \quad , \tag{3.3}$$

where $m_\mathrm{b} = 2.1 \times 10^{-13}$ kg is the normalising constant.

In the transition regime both collisional outcomes are possible: hit & stick and bouncing. Weidling et al. (2012) introduced a formula to calculate the bouncing probability by assuming a logarithmic distribution following

$$p_\mathrm{b} = \frac{18/5 \cdot \log_{10}(\Delta v)}{\log_{10}(m_\mathrm{b}/m_\mathrm{s})} + \frac{\log_{10}(m_\mathrm{p}/m_\mathrm{s})}{\log_{10}(m_\mathrm{b}/m_\mathrm{s})} \quad . \tag{3.4}$$

Other models exist e.g. by Kothe et al. (2013) who used the data from Weidling et al. (2012) and extended it with further experimental data. This leads to a formula for the collision velocity where 50 % of the collisions result in sticking (so called 50/50 transition):

$$\Delta v_{50/50} = \left(\frac{m_\mathrm{p}}{m_{50/50}} \right)^{-20/27} \frac{\mathrm{m}}{\mathrm{s}} \quad , \tag{3.5}$$

where $m_{50/50} = 1.0 \times 10^{-10}$ kg. The bouncing probability is described via

$$p_\mathrm{b} = 0.5 + 0.73 \log_{10} \left(\frac{\Delta v}{\Delta v_{50/50}} \right) \quad . \tag{3.6}$$

Recent studies showed that bouncing collisions can lead to mass transfer from one collision partner to the other, mostly from the target to the impactor (Jankowski et al., 2012; Langkowski et al., 2008). Since a detailed description is missing until now and the amount of transferred mass is low, most collisional outcome models do not include this abrasion (e.g. Windmark et al., 2012a). Nonetheless, research is in progress (Kothe and Blum, 2016).

3.1.2 Hit & Stick via Penetration

Fluffy target bodies can be penetrated by impactors in high-velocity collisions, leading to mass gain of the target equalling eq. 3.1 (Langkowski et al., 2008; Blum and Wurm, 2008; Güttler et al., 2009). Since most collisional outcome models do not include porosities, hit & stick via penetration is seldomly included in these models (e.g. the model by Windmark et al. (2012a)).

3.1.3 Fragmentation

Windmark et al. (2012a) introduced a model for the collisional behaviour of dust particles by calculating the center-of-mass velocity for each collision partner via

$$v_{\mathrm{com,p}} = \frac{\Delta v}{1 + m_{\mathrm{p}}/m_{\mathrm{t}}} \tag{3.7a}$$

$$v_{\mathrm{com,t}} = \frac{\Delta v}{1 + m_{\mathrm{t}}/m_{\mathrm{p}}} \tag{3.7b}$$

and determining the fragmentation degree (the relative size of the largest remnant) individually via

$$\mu_{\mathrm{frag}}(m_{\mathrm{p/t}}, v_{\mathrm{com,p/com,t}}) = 1.38 \times 10^{-1} \left(\frac{m}{m_{1.0}}\right)^{\alpha_{\mathrm{frag}}} \cdot \left(\frac{v_{\mathrm{com,p/com,t}}}{\mathrm{m\,s^{-1}}}\right)^{\beta_{\mathrm{frag}}} \tag{3.8a}$$

$$\alpha_{\mathrm{frag}} = \frac{\log_{10}(2)}{\log_{10}(m_{1.0}/m_{0.5})} = -0.068 \tag{3.8b}$$

$$\beta_{\mathrm{frag}} = \frac{\alpha_{\mathrm{frag}}}{\gamma_{\mathrm{frag}}} = -0.43 \tag{3.8c}$$

$$\gamma_{\mathrm{frag}} = 0.16 \quad . \tag{3.8d}$$

The threshold masses $m_{1.0} = 3.67 \times 10^{-4}$ kg and $m_{0.5} = 9.49 \times 10^{-8}$ kg are interpolated values from experimental data by Blum and Muench (1993) and Beitz et al. (2011). The first value represents the onset of fragmentation and the second one the case where the largest fragment is half the size of the original one (Windmark et al., 2012a). Using this model one can differ between the case where only the impacting body shatters ($\mu_{\mathrm{frag,p}} < 1$, $\mu_{\mathrm{frag,t}} \geq 1$) and the one where both bodies shatter (($\mu_{\mathrm{frag,p}} < 1$, $\mu_{\mathrm{frag,t}} < 1$). Besides a largest fragment, lots of small fragments are created in such collisions. The number distribution follows a power law index (see for example Deckers and Teiser, 2013, 2014; MacGregor et al., 2016). A more detailed analysis of the particles produced in collisions between large target bodies and small impactors is elaborated in sec. 4.2.

3.1.4 Mass Transfer and Erosion

Once the collision velocity increases, mass transfer and erosion can occur if the particle sizes differ sufficiently. This is directly linked with eq. 3.7 as mentioned there. Experimental studies by Beitz et al. (2011) show that the disruption of the impacting particle sets in once the collision velocity is larger than a threshold velocity v_{thr} which was determined to be 1.3×10^{-1} m s^{-1} for particles with a mass 4.1×10^{-3} kg.

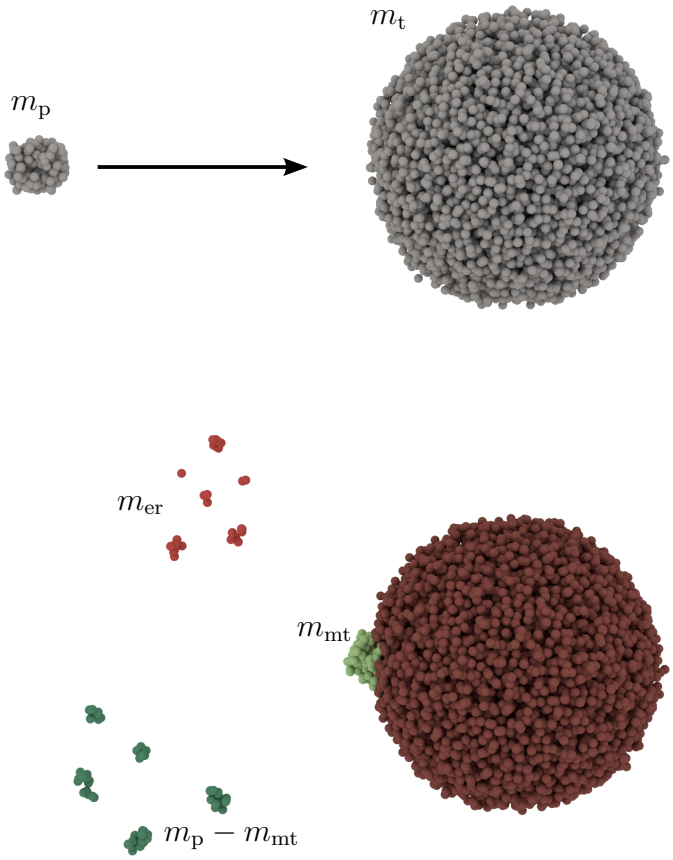

Figure 3.1: Mass balance in collisions of a small impactor m_p with a large target m_t at high collision velocities. The target mass after the collision m'_t is the target mass before the collision m_t minus the eroded mass m_er (light red) plus the transferred mass m_mt (light green). The total ejected mass m_ej equals the eroded mass m_er (light red) plus the mass of the remnants of the impactor $m_\mathrm{p} - m_\mathrm{mt}$ (dark green).

As depicted in fig. 3.1, the change in the target mass can be described via

$$\Delta m_\mathrm{t} = m'_\mathrm{t} - m_\mathrm{t} = m_\mathrm{mt} - m_\mathrm{er} \tag{3.9a}$$

$$m_\mathrm{mt} = \epsilon_\mathrm{mt} \cdot m_\mathrm{p} \quad , \tag{3.9b}$$

where m_mt is the mass which is transferred from the impactor to the target body and m_er is the mass which is eroded from the target body. Windmark et al. (2012a) introduced a model for the transferred mass according to the experimental results by Beitz et al. (2011) resulting in

$$\epsilon_\mathrm{mt} = -6.8 \times 10^{-3} + 2.8 \times 10^{-2} \cdot \frac{v_\mathrm{thr}}{\mathrm{m\,s^{-1}}} \cdot \frac{\Delta v}{\mathrm{m\,s^{-1}}} \left(\frac{m_{1.0}}{m} \right)^{-\gamma_\mathrm{frag}} \quad . \tag{3.10}$$

The eroded mass was calculated using experimental data by Teiser and Wurm (2009) and interpolated assuming a power-law dependency via

$$m_{\mathrm{er}} = m_{\mathrm{p}} \cdot \left(9.3 \times 10^{-4} \left(\frac{m_{\mathrm{p}}}{m_0} \right)^{0.15} \cdot \frac{\Delta v}{\mathrm{m\,s^{-1}}} - 0.4 \right) \quad , \tag{3.11}$$

where m_0 is the monomer mass. Recent theoretical studies of monomers impacting a larger body show erosion instead of growth (Seizinger et al., 2013). The model by Windmark et al. (2012a) as presented here does not include this erosion. The development of more sophisticated models is still in progress (e.g. by Kothe and Blum (2016)), but not published yet.
As shown later, gas drag can have a significant impact on the transferred mass in such collisions. The model described here is therefore expanded in chapter 4.

3.2 Material dependencies

Another important parameter determining the collisional outcome is the physical property of the particle's material since not only silicates are present in PPDs but water ice and other types of ices as well. One value crucial for the collisional outcome is the equilibrium contact force F_{contact} which characterises the strength of the connection of two solid spheres with radii r_1 and r_2. As shown by Derjaguin et al. (1975), F_{contact} increases linearly with increasing surface energy γ_{surf}:

$$F_{\mathrm{contact}} = 4\,\pi\,\gamma_{\mathrm{surf}} \frac{r_1\,r_2}{r_1 + r_2} \quad . \tag{3.12}$$

Blum and Wurm (2000) determined the surface energy for silicate material to $\gamma_{\mathrm{surf}}^{\mathrm{sil}} = 2 \times 10^{-2}$ J m^{-2} while for water ice the surface energy $\gamma_{\mathrm{surf}}^{\mathrm{H_2O}}$ was determined to be between 0.15 J m^{-2} (Gundlach and Blum, 2015) and 0.37 J m^{-2} (Aumatell and Wurm, 2014). Since the contact force can be interpreted as the stickiness of particles one can assume that water ice particles and aggregates are therefore much stickier than silicates. Experimental data (e.g. Gundlach and Blum, 2015) as well as simulations (e.g. Wada et al., 2007, 2008) give first approval to this theory. In the experiments by Gundlach and Blum (2015) the determined sticking and erosion threshold velocities for water ice particles is eight times higher than the ones found for silicate aggregates. Applying this to the collisional outcome model as presented in sec. 3.1 leads to a significant change and shifts the transitions between the different regimes to higher particle masses since in general the collision velocities increases with increasing particle mass. A collisional outcome model

for water ice is still subject to research since experiments investigating ice collisions do not cover the complete parameter range yet.

3.2.1 The role of carbon dioxide ice

Another point of interest is icy material beside water ice like for example carbon oxides. Especially carbon dioxide may play a crucial role in the outer disk. Using the calculated CO_2 surface energies of $\gamma_{\mathrm{surf}}^{CO_2} \approx 9 \times 10^{-2}$ J m^{-2} by Wood (1999) one could conclude that CO_2-ice would stick much less efficiently than H_2O-ice. Experimental collision studies of CO_2-ice (as well as for H_2O-ice) are still ongoing. Recent experiments by Musiolik et al. (2016a) and Musiolik et al. (2016b) provide first results in the collision behaviour of CO_2 ices. In the first paper, the collision behaviour of μm sized CO_2-ice aggregates with a CO_2-ice covered wall were investigated at an ambient pressure of ~ 0.5 mbar and a temperature of ~ 80 K (see fig. 3.2).

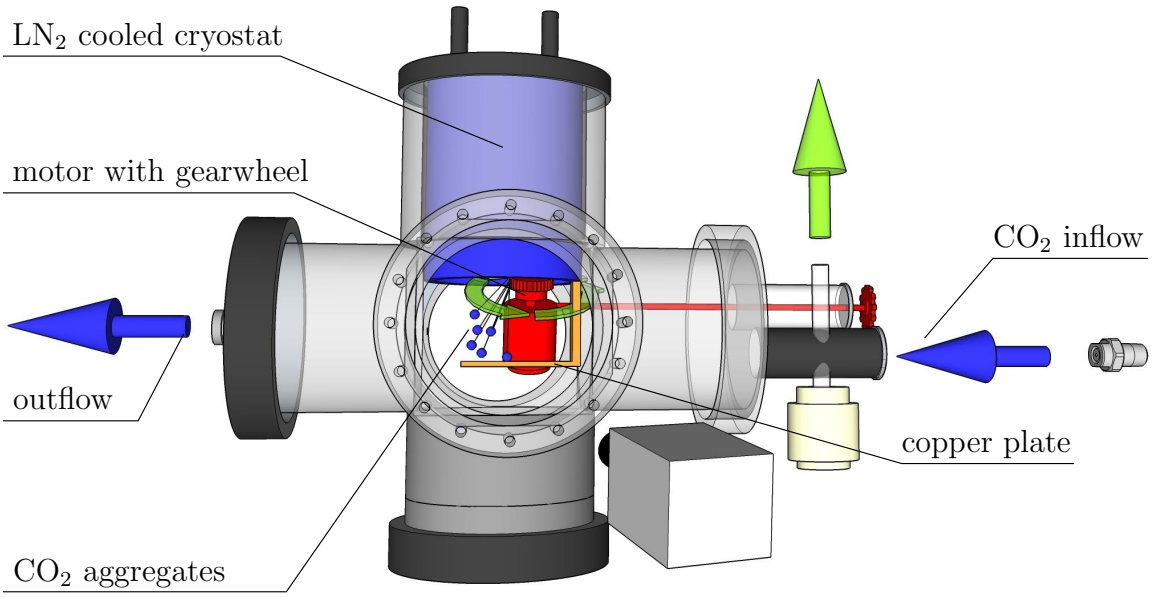

Figure 3.2: Experimental setup from Musiolik et al. (2016a). A vacuum chamber is flooded with CO_2 gas which is freezing out at the cooled cryostat and the copper plate. The CO_2-ice is beveled off from the cryostat and accelerated towards the copper plate where it collides with the CO_2-ice.

Depending on the initial velocity, the collisional outcome was either sticking (lowest velocities), bouncing or fragmentation (highest velocities). The dataset of the collisions is plotted in fig. 3.3, showing the coefficient of restitution (the ratio between the impinging velocity and the rebound velocity) and the fragmentation degree (see eq. 3.8).

For a median grain size of 60 μm, a sticking velocity of $v_{\mathrm{stick}} = (0.04 \pm 0.02)$ m s^{-1} was found. The fragmentation velocity was determined to $v_{\mathrm{frag}} = (0.75 \pm 0.05)$ m s^{-1} with a

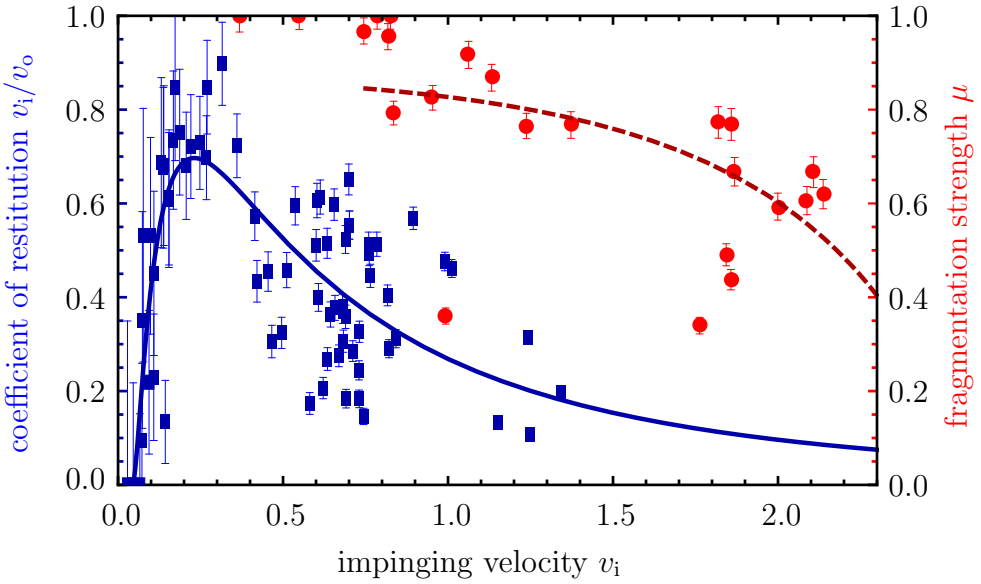

Figure 3.3: Coefficient of restitution (blue) and fragmentation strength (red) for a total of 96 collisions. The models for the fit functions are described in Musiolik et al. (2016a).

median grain size of 80 μm. Using the dependency of the sticking velocity on the particle size r_p (Dominik and Tielens, 1997),

$$v_{stick}(r_p) \propto r_p^{-\frac{6}{5}} \cdot \gamma_{surf}^{\frac{5}{6}} \quad , \tag{3.13}$$

the results are scaleable. This allows for comparison with experimental studies of silicate material (Poppe et al., 2000) and water ice (Gundlach and Blum, 2015), showing that CO_2-ice behaves more like silicate material. Although the experimentally determined surface energy for CO_2 quals more or less the water-ice values found by Gundlach and Blum (2015) and Aumatell and Wurm (2014), a direct comparison of pure CO_2-ice with an ice-mixture of 50 % H_2O-ice and 50 % CO_2-ice showed a clear tendency towards low sticking velocities. This study was performed in Musiolik et al. (2016b) where different sticking velocities v_{stick} were found depending on the H_2O-fraction (see fig. 3.4). Implications of the different sticking velocities to the growth regimes in protoplanetary disks and their zonal structure as already indicated in fig. 1.2 are discussed in the following section.

3.2.2 CO_2 dominated regions in protoplanetary disks

As already indicated in fig. 1.2, different sticking velocities might have a significant impact on the growth of particles in different parts of PPDs. Due to the disks properties, different sublimation radii exist depending on the material properties. As mentioned earlier, in the context of protoplanetary disks the sublimation radius r_{sub} is often linked

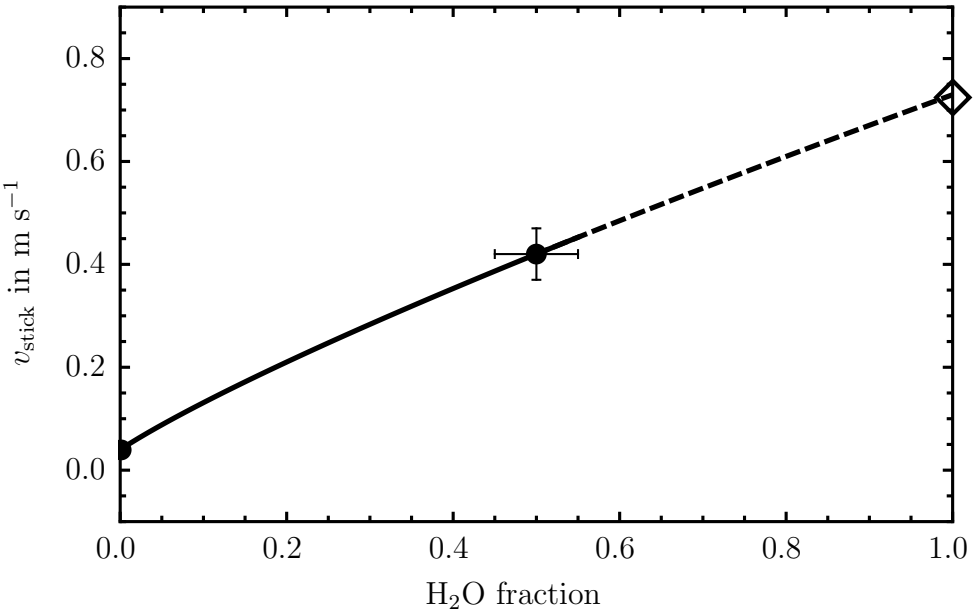

Figure 3.4: Sticking velocity v_{stick} over the H_2O fraction, from Musiolik et al. (2016b). The black dots represent measured values, the diamond is an extrapolated value using the dependency of the sticking velocity on the surface energy following eq. 3.13.

to the sublimation of silicates. Since silicate is the least volatile material which is present in significant amounts in PPDs, their sublimation radius is the closest one to the star. Often the radius is calculated setting the sublimation temperature of silicates to 1500 K (see for example van der Marel et al., 2015). Other more volatile materials exist within the disk in gaseous form in the inner part and in solid form in the outer part. Their sublimation radii can be calculated using for example a modified sublimation pressure curve from Span and Wagner (1996):

$$\ln\left(\frac{P_{\mathrm{sub}}}{P_{\mathrm{c}}}\right) = \frac{T_{\mathrm{c}}}{T}\left[k_1\left(1-\frac{T}{T_{\mathrm{c}}}\right)^{l_1} + k_2\left(1-\frac{T}{T_{\mathrm{c}}}\right)^{l_2}\right] \quad . \tag{3.14}$$

Using the experimental sublimation pressure data from Bryson et al. (1974) and the minimum mass solar nebular (MMSN) from Hayashi et al. (1985) with P_{sub} equalling the disk pressure P_{disk}, the sublimation radii for H_2O and CO_2 could be calculated to be at 2.0 AU and 9.3 AU respectively. Since H_2O and CO_2 are common in protoplanetary disks (Öberg et al., 2011; Pontoppidan et al., 2014), a zonal structure might exist in disks following fig. 3.5. Using the data obtained from Musiolik et al. (2016a,b); Gundlach and Blum (2015); Aumatell and Wurm (2014); Poppe et al. (2000), one can determine a zone wherein growth is favoured over other regions. Assuming an onion like grain structure (see fig. 3.6) where material had frozen out on the outer layer according to their volatility (see

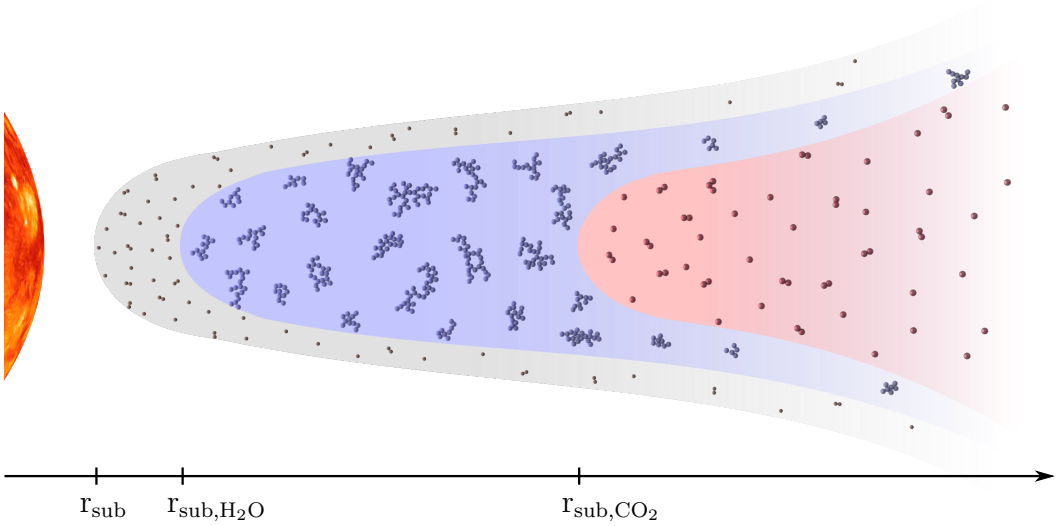

Figure 3.5: Possible zonal structure in a protoplanetary disk. In the hottest regions (gray) only silicate material exists in solid form. In colder regions, H_2O can freeze out (blue) while even further outwards (or/and closer to the midplane) CO_2-ice exists (red).

e.g. Fayolle et al., 2011; Sirono, 2013) and simultaneously assuming that the collisional outcome is not depending on the overall grain material but only on the one of the outer shell, growth should be favoured in the zone between $r_{\mathrm{sub,H_2O}}$ and $r_{\mathrm{sub,CO_2}}$ (Musiolik et al., 2016a).

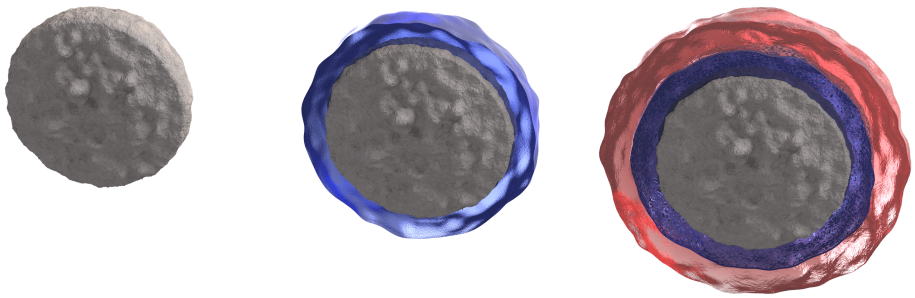

Figure 3.6: Illustration of differently coated material (cut-through), starting from the left: in the innermost zone (see fig. 3.5) only silicate material exists in solid form. Further outwards, silicate is coated with H_2O-ice while even further outwards another layer of CO_2-ice encloses the particle.

3.3 Light induced erosion effects

Besides collisions, illumination of dusty bodies consisting of granular matter in a gaseous environment can lead to erosion where particles are ejected from the body (Wurm and Krauss, 2006b; Kelling and Wurm, 2011; Kelling et al., 2011; de Beule et al., 2013). The effect can be explained as follows: Due to the illumination of the surface, a temperature gradient is established with a constant (hot) temperature in the first particle layers and decreasing temperature in deeper layers (see fig. 3.7). This temperature gradient leads

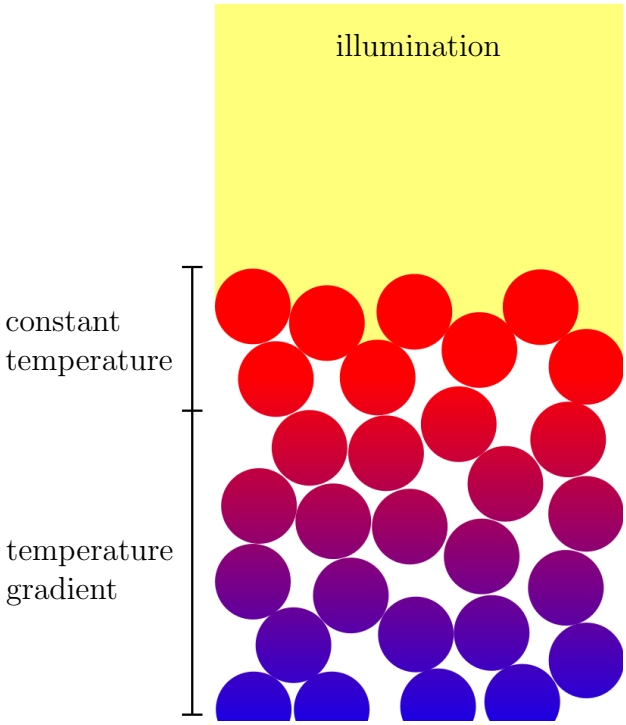

Figure 3.7: Temperature distribution of an illuminated surface consisting of single grains. The top layers have the same temperature while a temperature gradient is established with decreasing temperature with increasing depth.

to a multiplicity of effects (de Beule, 2016): First of all, a temperature gradient on a particle in a gaseous environment leads to a photophoretic force in negative gradient direction as shown in sec. 2.4.4. Furthermore, the temperature gradient inside the gas leads to an effect which is similar to photophoresis but independent on the particles temperature gradient: thermophoresis. While photophoresis describes gas particles with equal temperatures accommodating and leaving the surface with different temperatures, thermophoresis is vice versa: if the gas is hot near the top of the particle and cool near the bottom, the momentum transfer due to the impinging hot gas particles is higher than the one due to the cold impinging gas particles which causes a net force acting in negative gradient direction. The third and most important effect is a gas flow due to thermal

creep inside the capillaries: As discovered by Maxwell (1879) and Knudsen (1909), a net gas flow along a wall opposing a temperature gradient exists within a small layer with a thickness of half of the mean free path λ_{mfp}. This effect can have significant influence on the pressure difference of connected gas reservoirs: Assuming a setup where two gas reservoirs with temperature T_1 and T_2 are connected with a capillary with diameter λ_{mfp} (assuming the capillary is subject to the same temperature gradient), thermal creep would lead to a gas flow opposing the temperature gradient. This leads to an overpressure on the hotter side which is only partly levelled due to the pressure driven back-flow. The resulting overpressure in equilibrium where the pressure driven back-flow equals the gas flow due to thermal creep can be expressed via

$$\frac{P_2}{P_1} = \sqrt{\frac{T_2}{T_1}} \quad . \tag{3.15}$$

This effect has been observed and used e.g. for particle levitation (Kelling and Wurm, 2009; Jankowski et al., 2012). The same effect induces a pressure gradient which is established inside the granular matter as well, leading to a force even large enough to eject particles from the surface of granular bodies (de Beule, 2016). Furthermore, this pressure gradient produces a gas flow in the inside of the porous body (de Beule et al., 2014). While this effect plays only a subordinary role in the explanation of the light-induced erosion of granular bodies, the gas flow can be important on cometary or planetary surfaces like Mars where on global scales gaseous CO_2 can be transported into deeper, cooler layers where it deposits (de Beule et al., 2014).

The amount of eroded mass from illuminated bodies is highly dependent on the illumination strength and the material properties (de Beule, 2016). As shown by Wurm and Krauss (2006b), the erosion process sets in once the illumination intensity is above at least 10^3 W m^{-2}. Due to this dependency, erosion of bodies in PPDs is often limited to areas near the sublimation radius or at significant heights over the midplane where disk opacity and the resulting intensity drop is low. Kelling and Wurm (2011) calculated surface erosion rates of $N_{\mathrm{mer}} = 10^{-5}$ kg s^{-1} m^{-2} assuming an illumination intensity of 1.3×10^4 W m^{-2} and laboratory conditions which include normal gravitational acceleration in direction of illumination. Especially in pre-transitional disks and close to the star where the intensity of the stellar radiation is high, small bodies might get eroded quickly (see tab. 3.1).

Even when assuming the erosion rate to be overestimated for spherical particles, centimetre sized particles will easily loose significant amounts of their mass in timescales much lower than one year. Investigations of light-induced erosion by de Beule et al. (2013) in

low-gravity environment show a dependency of the surface erosion rate $N_{\mathrm{mer}} = \frac{\Delta m}{\Delta t}$ following

$$N_{\mathrm{mer}} = \frac{\omega_{\mathrm{s}}}{g_{\mathrm{env}} + \frac{F_{\mathrm{c}}}{\Delta m}} \quad , \tag{3.16}$$

where $\frac{F_{\mathrm{c}}}{\Delta m}$ is linked to the cohesion force of the material, g_{env} is the gravitational acceleration, and ω_{s} is a scaleable factor accounting for the environmental variables like for example the illumination strength. Fig. 3.8 shows the gravitational dependency of the normalised mass ejection rate ($N_{\mathrm{mer}} = 1$ for $g_{\mathrm{env}} = 9.81$ m s^{-2}) for basalt powder with grain sized between 0 and 1.25×10^{-4} m.

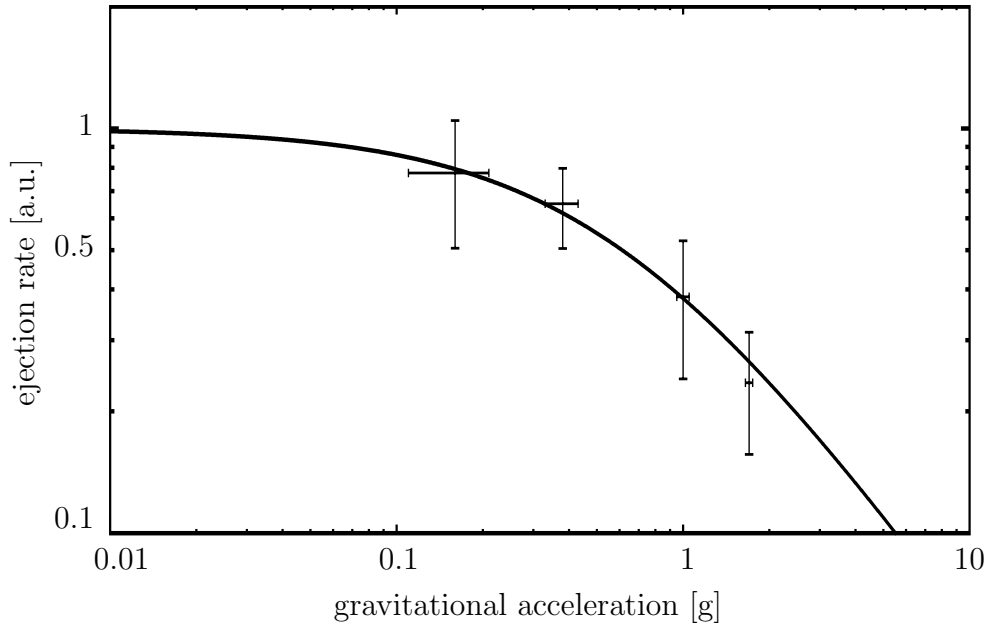

Figure 3.8: Normalised mass ejection rate for different gravitational accelerations, figure adopted from de Beule et al. (2013).

The mass loss rate can therefore be higher in low-gravity environment compared to the laboratory experiments by Kelling and Wurm (2011) (see tab. 3.1), especially when the cohesion force and therefore $\frac{F_{\mathrm{c}}}{\Delta m}$ is small.

Table 3.1: Surface erosion rate N_{mer} caused by light induced erosion as estimated from Kelling and Wurm (2011) modified with the gravitation dependency as described by de Beule et al. (2013). Displayed are the values for 1 g and 0 g.

size (m)	mass (kg)	$N_{\mathrm{mer,1\,g}}$ (kg yr^{-1} m^{-2})	$N_{\mathrm{mer,0\,g}}$ (kg yr^{-1} m^{-2})
1.0×10^{0}	5.24×10^{2}	2.48×10^{2}	6.53×10^{2}
1.0×10^{-2}	5.24×10^{-4}	2.48×10^{-2}	6.53×10^{-2}
1.0×10^{-4}	5.24×10^{-10}	2.48×10^{-6}	6.53×10^{-6}

Since in the early stages of PPD evolution the dusty bodies are small and gravitational effects are negligible when considering two-body interaction, the effect of light-induced erosion might influence heavily the growth behaviour in optically thin disks. Therefore, as shown later this erosion process might aid the recycling process in pre-transitional disks.

4

Reaccreting Ejecta in Small-Impactor Large-Target collisions

As shown in chapter 3, collisions of particles at high relative velocities can lead to erosion of the larger and disruption of the smaller body. The fragments which are produced in these collisions are often assumed to be "lost", not taking into account the effect of "reaccretion": considering the gas motion not only as source for the relative velocity between the bodies but furthermore interacting with the produced ejecta as well, it was experimentally shown that these particles can be pushed back onto the targets surface due to this drag force (Wurm et al., 2001a,b). Nonetheless, a quantification of how much influence this effect might have on particle growth in protoplanetary disks is missing. Therefore, within this chapter a model for the properties and velocities of ejected particles in small-impactor large-target collisions is presented based upon experimental data. Using Monte-Carlo methods, this model is applied to quantify the amount of reaccreted mass. Furthermore, the influence of reaccretion on the growth of particles in the MMSN is investigated.

4.1 Erosion and reaccretion in collisions

If the relative velocity of two colliding particles is high, the smaller body (in the following referred to as impactor) is destroyed, leading to mass transfer onto the larger body (in the following referred to as target) while simultaneously small particles are ejected. Besides destruction of the impactor, the target body is eroded as well. A scheme on this process

is depicted in fig. 3.1. As shown there, monomers and aggregates get ejected from the impact position with a total mass of

$$m_{\mathrm{ej}} = \sum_{\mathrm{i}} m_{\mathrm{i,ej}} = m_{\mathrm{er}} + m_{\mathrm{p}} - m_{\mathrm{mt}} \tag{4.1}$$

while the mass transferred onto the body can be expressed by

$$m'_{\mathrm{t}} - m_{\mathrm{t}} = m_{\mathrm{p}} - m_{\mathrm{ej}} \quad , \tag{4.2}$$

where m_{p} is the mass of the impactor.
Most collision models treat the ejected mass as mass loss, which lowers the growth rate (e.g. Windmark et al., 2012a). Experiments by Wurm et al. (2001a,b) as well as simulations by Sekiya and Takeda (2003) show that ejected particles can be pushed back to the surface by gas drag. Therefore, if gas drag is treated not only as source for relative velocities between impactor and target but also as drag which influences the motion of the ejecta, reaccretion might lead to much higher net growth rates.
Eq. 4.2 can then be modified that latter that a factor

$$\eta_{\mathrm{re}} = \frac{m_{\mathrm{re}}}{m_{\mathrm{ej}}} \tag{4.3}$$

is included which modifies the mass balance to

$$m'_{\mathrm{t}} - m_{\mathrm{t}} = m_{\mathrm{p}} + (\eta_{\mathrm{re}} - 1) m_{\mathrm{ej}} \quad . \tag{4.4}$$

A scheme on how reaccretion works is depicted in fig. 4.1 and fig. 4.2. In the target body's reference frame, the head-wind affecting the target body influences the ejecta as well. Their gas-grain coupling time τ_{fric} is much smaller compared to the target body's. Assuming free molecular flow, the particles are therefore accelerated back in the direction of the head-wind. Ejecta can partly be pushed back to the surface and get reaccreted by the target body.

To calculate η_{re}, Monte-Carlo simulation techniques are used including a model for the ejection of particles in collisions and the ejecta trajectories in vicinity of a gas flow.

4.2 Model for Particle Ejection

As mentioned earlier, the collision of an impactor with a target body results in mass transfer onto the latter and erosion of the larger body as well as destruction of the impactor.

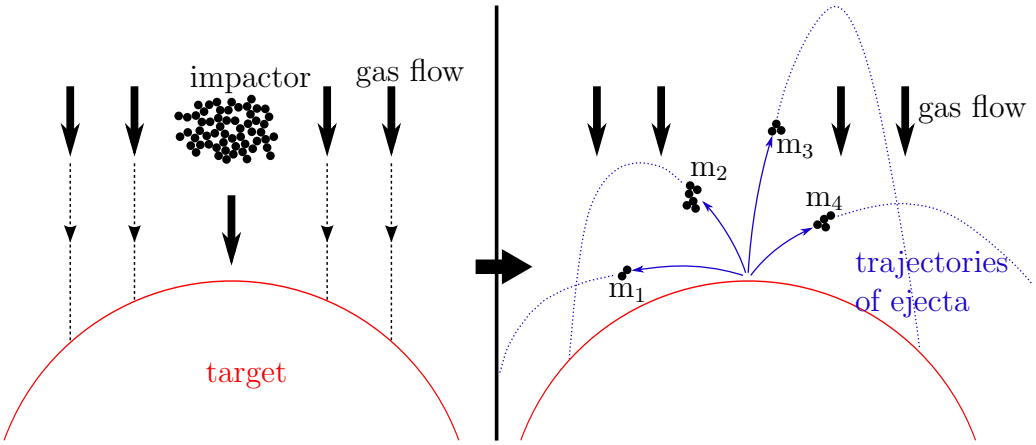

Figure 4.1: Principle of reaccretion: Due to the relative velocity of the target body and the gas, the target is affected by a head-wind. If a smaller particle – which in general is coupled to the gas much more effectively – impacts, even smaller ejecta are produced which can be pushed back to the target's surface due to the gas flow. These reaccreted particles increase the net growth of the target body in a collision. In this basic picture it is assumed that the Knudsen Number for the target body is larger or on the order of unity ($Kn \gtrsim 1$).

Besides the environmental parameters, the collisional outcome depends on the following set of parameters:

- impact velocity,
- size of the projectile,
- size of the target,
- impact location which includes
  - absolute position on the surface
  - inclination of the impact with the target surface.

Every collision produces ejecta with a specified

- size distribution
- velocity distribution
- ejecta direction.

Using experimental data by Teiser and Wurm (2009), Teiser et al. (2011a,b), and Meisner et al. (2013), a model was build to determine these values. The ejecta size and velocity are treated independently for simplicity reasons.

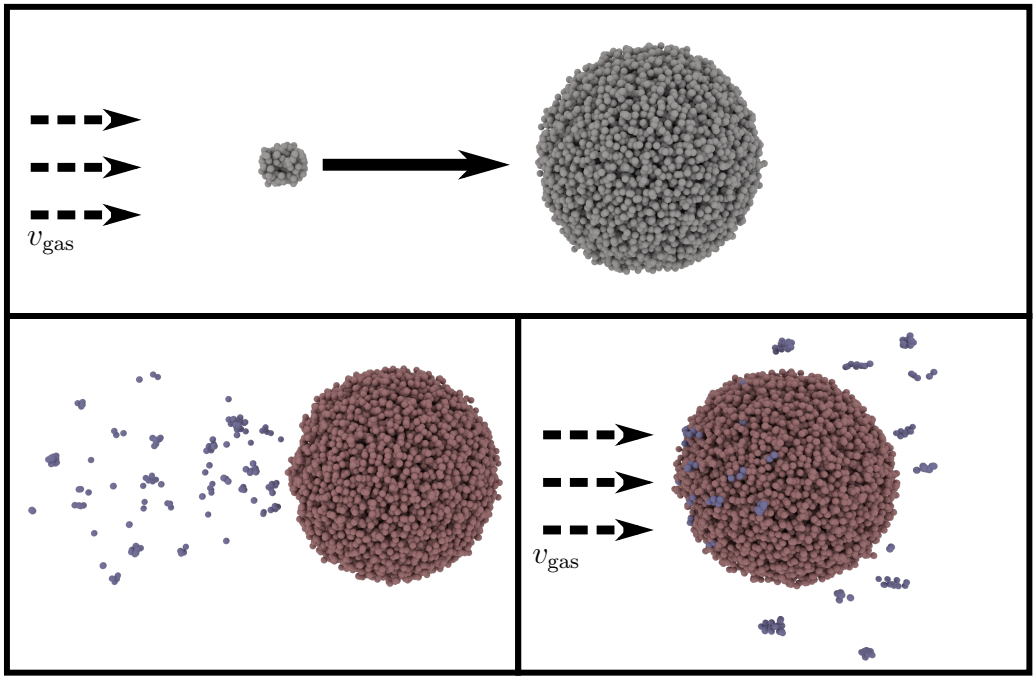

Figure 4.2: Visualisation of re-accreted mass: If a small particle impacts a larger one with a collision velocity equalling the gas velocity v_{gas} (top), particles are released (bottom left, blue: ejecta, red: target). These ejecta suffer from gas drag and are (partly) being pushed back onto the target (bottom right).

Ejecta mass – The dependency of the number density on the ejecta size s_{ej} is described by a power law

$$N(s_{\mathrm{ej}}) \propto s_{\mathrm{ej}}^{-2.1} \tag{4.5}$$

with N as the probability density (see Fig. 3 and Eq. 2 in Teiser et al. (2011b)).
One model for the distribution of ejecta was introduced by Windmark et al. (2012b), who proposed a dependency on the impact velocity with a largest remnant and a distribution of the smaller fragments following eq. 4.5. For the simulations presented within this chapter, another model is introduced, based on the data from Teiser and Wurm (2009), Teiser et al. (2011a,b), and Meisner et al. (2013).
The size distribution as well follows the power law (eq. 4.5) but in comparison to Windmark et al. (2012b) two cut-offs are applied. The higher the impact velocity is, the larger the number of small fragments gets which reduces the cut-off size at the small ejecta end. On the other side the smallest fragment must not be smaller than the monomer size which is $s_{\mathrm{mon}} = 5 \times 10^{-8}$ m.

The cut-offs are parameterised by the maximum ejecta radius $s_{\max} = s_\mathrm{p} \cdot l_\mathrm{upper}(s_\mathrm{p}, v_\mathrm{p})$ and the minimum ejecta radius $s_{\min} = s_\mathrm{p} \cdot l_\mathrm{lower}(s_\mathrm{p}, v_\mathrm{p})$ with

$$l_\mathrm{upper} = \min\left(4.24 \times 10^{-2} \cdot \left(\frac{s_\mathrm{p}}{\mathrm{m}}\right)^{-0.5} \left(v_\mathrm{p}\frac{\mathrm{s}}{\mathrm{m}}\right)^{-0.43} , \; 1.0\right) \tag{4.6}$$

$$l_\mathrm{lower} = \max\left(6.94 \times 10^{-5} \cdot \left(\frac{s_\mathrm{p}}{\mathrm{m}}\right)^{-0.95} \left(v_\mathrm{p}\frac{\mathrm{s}}{\mathrm{m}}\right)^{-0.5} , \; 5 \times 10^{-8}\frac{\mathrm{m}}{r_\mathrm{p}}\right) \tag{4.7}$$

These functions are constructed in a way that the size distribution found by Teiser et al. (2011a) as well as the total amount of ejecta for other conditions (Teiser and Wurm, 2009; Teiser et al., 2011b; Meisner et al., 2013) are matched adequately.

Ejecta velocities – the ejecta velocities in terms of impact velocity $v_\mathrm{ej}/v_\mathrm{p}$ are determined by fitting the velocity distribution from impact experiments with an impactor size of 1×10^{-4} m using a distribution function following

$$f\left(\frac{v_\mathrm{ej}}{v_\mathrm{p}}\right) = c \cdot a_\mathrm{fit} \cdot \frac{v_\mathrm{ej}}{v_\mathrm{p}} \exp\left(-\frac{a_\mathrm{fit}}{2}\left(\frac{v_\mathrm{ej}}{v_\mathrm{p}}\right)^2\right) \quad , \tag{4.8}$$

where c is the scale parameter and a_fit is the shape parameter. The fits are shown in fig. 4.3. The dependency of the shape parameter a_fit on six impact velocities $v_\mathrm{gas} = \{1.5$ m/s, 3.3 m/s, 5.2 m/s, 6.7 m/s, 27.1 m/s, 48.7 m/s $\}$ is fitted linearly to model the general dependence on all impact velocities (see fig. 4.4), resulting in

$$a_\mathrm{fit}\,(v_\mathrm{p}) = -146.5 + 176.9\,v_\mathrm{p} \quad . \tag{4.9}$$

Ejecta directions – The direction of ejecta can be specified by two angles. If the velocity vector of the impacting particle is perpendicular to the surface, the azimuth is evenly distributed for symmetry reasons and only the inclination β needs to be considered. Fitting the experimental data by Teiser and Wurm (2009) for collisions at $5.2\,\mathrm{ms}^{-1}$, the inclination can be described using a modified Weibull distribution (Eq. 4.10 and Fig. 4.5):

$$f(\delta) = a \cdot \frac{k}{l}\left(\frac{0.5\,\pi - \delta}{l}\right)^{k-1} \cdot \exp\left(\frac{0.5\,\pi - \delta}{l}\right)^{k} \tag{4.10}$$

However, most impacts on a spherical particle are not perpendicular but inclined with an impact angle ϑ (see fig. 4.6, left hand side). Following fig. 4.6, right hand side, the ejecta directions can be described using the angles γ and δ.

There is no accessible experimental data for ejecta trajectories in non-perpendicular collisions for dust projectiles in the relevant parameter range. However, it is often observed

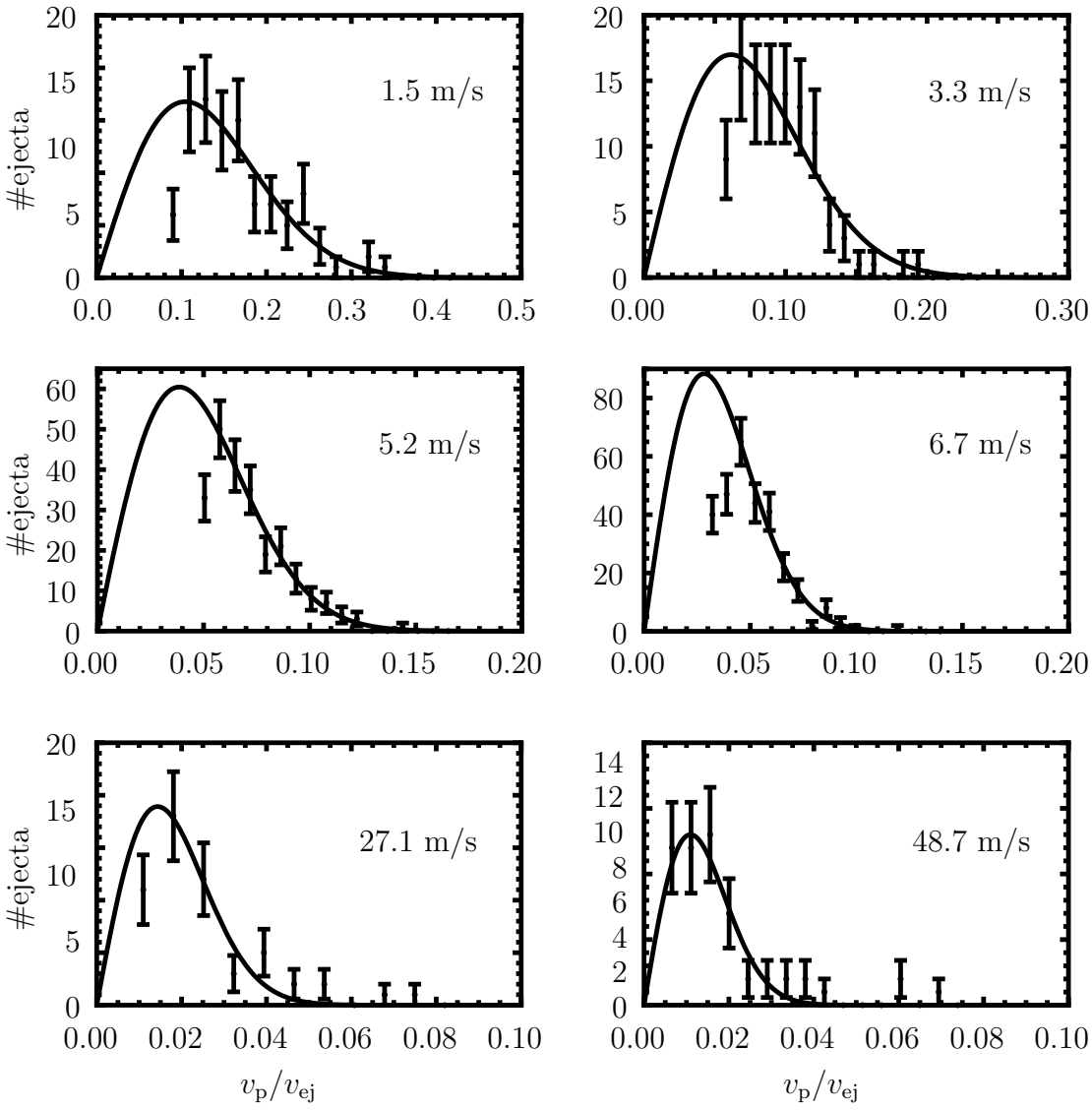

Figure 4.3: Amount of ejecta dependent on the ejecta velocities for different impactor velocities v_p, starting from 1.5 m/s (top, left) to 48.7 m/s (bottom, right). Due to the limitations of the observation and the experimental setup (gravitational acceleration), the amount of ejecta with low velocities might be highly uncertain.

qualitatively (Teiser et al., 2011a) that ejecta directions in inclined collisions are biased along the impact direction. Grazing collisions for example will not result in frequent ejecta travelling backwards. This will decrease the number of ejecta that can be accreted in secondary collisions. To account for this the projectile is considered to have a component of its momentum which is tangential to the surface. The experimentally deduced ejecta velocity $\vec{v}_u$ as described via the velocity and the ejecta angle is modified by a projection term $\vec{v}_{||} = \sin(\vartheta) \cdot \vec{e}_\vartheta \cdot v_p \cdot r_{||}$. Here, $\vec{e}_\vartheta$ is the unit vector in spherical coordinates, v_{gas} is

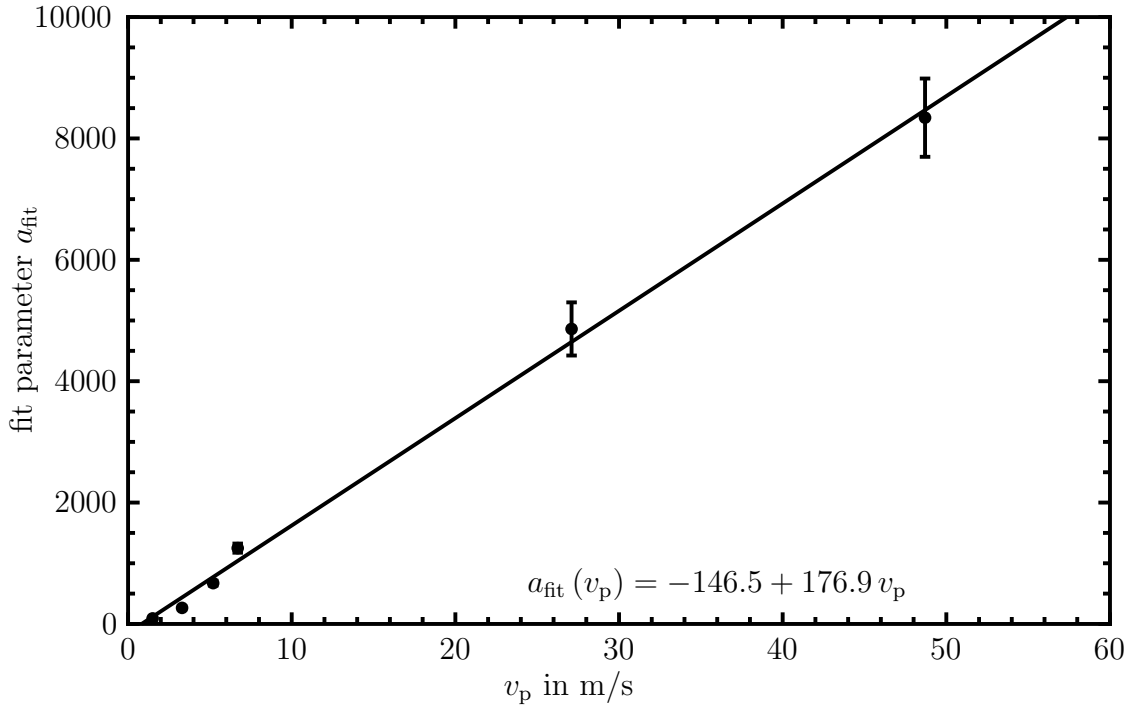

Figure 4.4: The fit paramter a_{fit} (see eq. 4.8) on different impactor velocities v_{p}, fitted with eq. 4.9

the impactor velocity which equals the gas velocity and $r_{||} = v_{\mathrm{u}} \cdot v_{\mathrm{p}}^{-1}$. The final equation for the ejecta velocity $\vec{v}_{\mathrm{ej}}$ is therefore

$$\begin{aligned} \vec{v}_{\mathrm{ej}} &= \vec{v}_{\mathrm{u}}(v_{\mathrm{p}}) + \vec{v}_{||}(\vartheta, v_{\mathrm{p}}) \\ &= v_{\mathrm{wb}} \cdot [\cos(\delta)\vec{e}_{\mathrm{r}} + \sin(\delta)\,(\cos(\gamma)\vec{e}_{\vartheta} + \sin(\gamma)\vec{e}_{\varphi})] \\ &\quad + \sin(\vartheta) \cdot \vec{e}_{\vartheta} \cdot v_{\mathrm{p}} \cdot r_{||} \quad . \end{aligned} \tag{4.11}$$

Note here that this model implies rather compact, spherical targets since inclined collisions with porous or irregular shaped bodies might more often behave like non-inclined collisions. This might be caused by either higher energy dissipation and/or by the fact that the surface element where the small particle impacts can be much less inclined than previously assumed according to the impact position for spherical targets.

4.3 Forces on Ejected Particles

Ejected particles are subjected to a gas drag force, resulting from the relative velocity between the gas and the particle. Depending on the Knudsen Number Kn (see eq. 2.18) the drag force can be calculated using e.g. eq. 2.25. Although the exact gas flow is unknown (influenced by the bodies present), the drag forces can be approximated in free

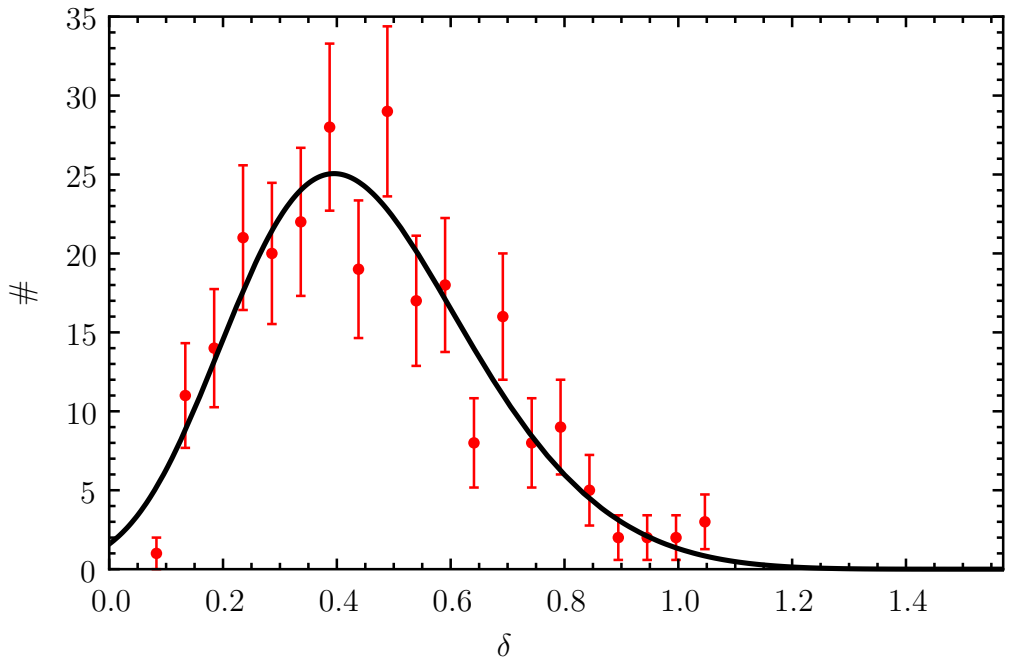

Figure 4.5: Measured ejecta angles δ from data by Teiser and Wurm (2009) ($5.2\,\mathrm{ms}^{-1}$) and fitted Weibull distribution (Eq. 4.10) with $k = 6.2$ and $l = 1.21$.

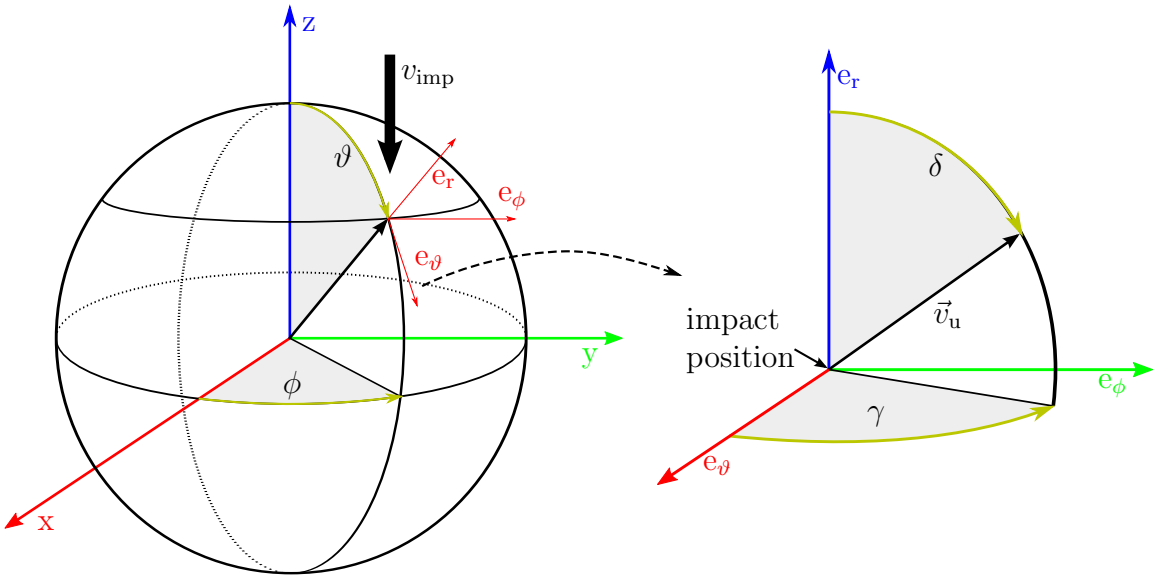

Figure 4.6: Spherical coordinates used for the description of impact position and ejecta angles. The unmodified ejecta direction $\vec{v}_{\mathrm{u}}$ is based on fitted experimental data for normal impacts. A modification factor is applied for inclined collisions (see Eq. 4.11) and the ejecta direction becomes steeper, depending on the impact angle ϑ.

molecular flow by assuming an undisturbed gas flow leading to an analytic solution of the equation of motion (see next section). Nonetheless, the validity of this approximation has to be proven. Experiments by Wurm et al. (2001a,b) showed first consistency. A more detailed theoretical examination is presented in section 4.3.2.

4.3.1 Simplified treatment of drag force acting on ejected particles

In free molecular flow, an ejecta can be treated as a single object subjected to an undisturbed gas flow. The resulting particle movement is described by the equation of motion

$$m_{\rm ej}\,\vec{a} = \frac{m_{\rm ej}}{\tau_{\rm f}}\,\vec{v}_{\rm rel} \quad , \tag{4.12}$$

with $\vec{v}_{\rm rel} = \vec{v}_{\rm gas} - \vec{v}_{\rm ej}$ and $\tau_{\rm f} = \dfrac{m_{\rm ej}}{F_{\rm D}}\,\|\vec{v_{\rm rel}}\|$ is the gas-grain friction time. Note here that the impact velocity of the particle is set to be the gas velocity. This approximation is valid in PPDs since the relative velocity between particles is directly linked to the different gas grain coupling times. Therefore, the relative velocity between the small particle and the gas is much lower than the relative velocity between the large particle and the gas and can be neglected. The solution to eq. 4.12 can analytically be determined to

$$\vec{r}(t) = \vec{r}_{\rm init} + [\vec{v}_{\rm ej} - \vec{v}_{\rm gas}]\tau_{\rm f}\left(1 - \exp\left(-\frac{t}{\tau_{\rm f}}\right)\right) + \vec{v}_{\rm gas}\,t \quad , \tag{4.13}$$

where $\vec{r}_{\rm init}$ is the (initial) impact position. This formula is given by Wurm et al. (2001a,b) who experimentally verified the condition by observing ejecta trajectories from collisions of suspended particles with a dusty surface assuming Epstein Drag. The treatment of the gas flow as undisturbed is somewhat simplified since the presence of the target body is neglected completely. Nonetheless, Wurm et al. (2001a) showed that - within the error range - ejecta behave like objects in an undisturbed gas flow even if the targets Knudsen Number $Kn_{\rm t}$ is as low as ~ 0.15.

4.3.2 Detailed treatment of drag forces acting on ejected particles

To determine the force acting on an ejected particle in presence of a target body in the free molecular flow regime, 3-D Monte Carlo simulations have been performed. The basic idea of these simulations is to calculate the momentum transfer from the surrounding gas to an ejected particle. To evaluate the results where the ejecta are in vicinity of a target

body, simulations without a target body present have been performed as well.
The simulation procedure is as follows:

- an ejecta is placed in the centre of a sufficiently large simulation sphere either with a target body present in a specified distance to the particle or without a target body
- gas particles are randomly generated on the surface of the simulation sphere with random velocities according to the thermal velocity together with the macroscopic gas velocity
- the trajectories of all gas molecules are calculated, using a gas-surface interaction model without self-interaction (free molecular flow regime)
- the number of hits and the momentum transfer per gas molecule who hit the ejecta at least once are determined.

Simulation settings

In fig. 4.7 the simulation settings are depicted. The ejecta is treated as spherical with size s_{ej} and its center of mass is at the origin ($\vec{r}_{\mathrm{ej}} = \vec{0}$). The target body with size s_{t} is placed at the position $\vec{r}_{\mathrm{t}}$ with $\mathrm{z_t} = 0$, the macroscopic gas velocity points in positive y-direction. Gas particles are uniformly distributed at the surface of a sphere with size s_{s} using pseudo-random number generators with high stability. Every gas particle is assigned a velocity corresponding to the thermal velocity distribution in all three directions plus the macroscopic gas velocity $\vec{v}_{\mathrm{gas}}$ which leads to

$$f(v_i) = \sqrt{\frac{m_{\mathrm{gas}}}{2\,\pi\,k_{\mathrm{B}}\,T}}\exp\left(\frac{-m_{\mathrm{gas}}\,v_i^2}{2\,k_{\mathrm{B}}\,T}\right) \tag{4.14}$$

$$\Rightarrow v_i(X) = \sqrt{\frac{2\,k_{\mathrm{B}}\,T}{m_{\mathrm{gas}}}}\mathrm{Erf}^{-1}(X) + \delta_{i\mathrm{y}}v_{\mathrm{gas}} \quad , X \in (-1,1) \tag{4.15}$$

for the i-th component of the gas molecule's velocity. Therefore, *ab initio* only half of the simulated gas molecules enter the simulation sphere, with a slight asymmetry towards the -y direction.
The interaction of gas molecules with the surface is calculated while the gas-gas interaction is neglected (assuming a rarified gas).

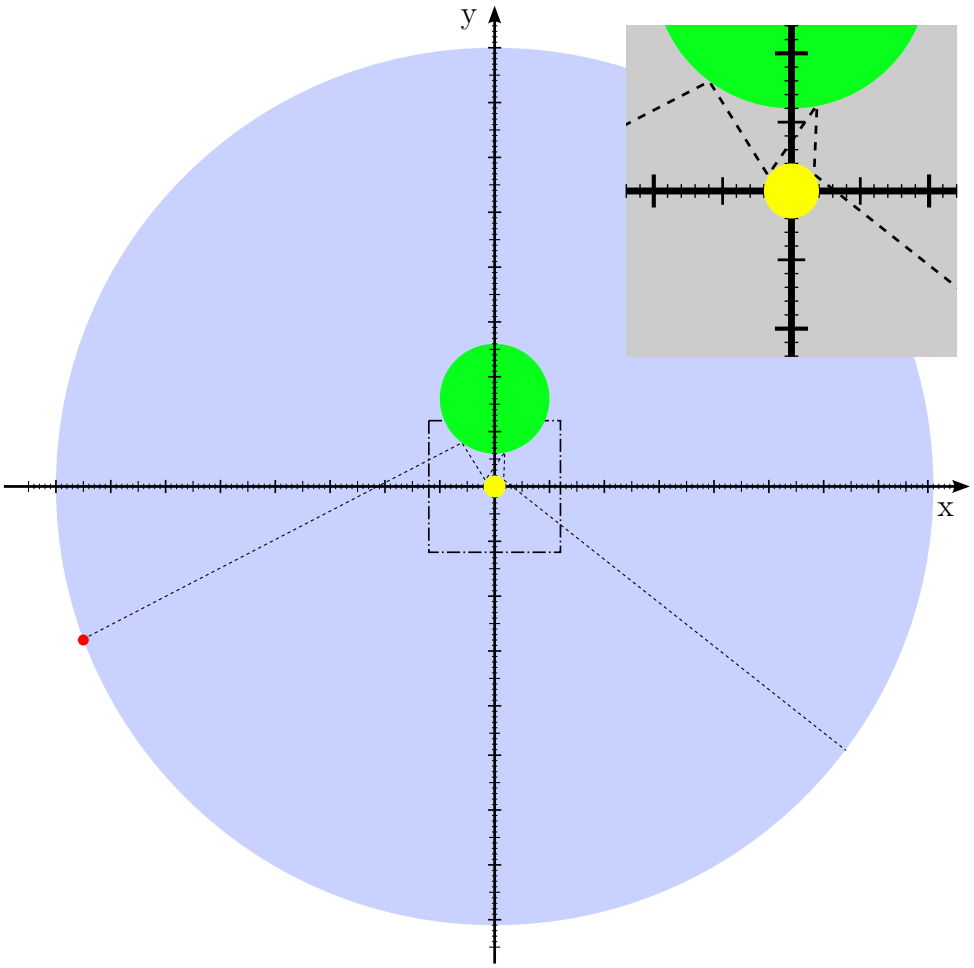

Figure 4.7: 2-D projected simulation setup (x-y-plane): The ejecta (yellow) is placed in the middle of the simulation sphere (blue), the target body (green) is placed at $\vec{r}_\mathrm{t}$ in the x-y-plane. Gas molecules (red) are uniformly placed on the simulation-spheres surface (3-D) and a velocity is assigned to them according to eq. 4.15. If a molecule collides with a surface, the resulting change in motion is calculated and the trajectory is simulated until the molecule has left the simulation sphere. A detailed view on a possible interaction of a gas molecule with both bodies is depicted in the upper right inlay.

Gas-Surface interaction

Once a gas molecule hits a solid surface with an impinging velocity $\vec{v}_\mathrm{i}$, the emergent velocity $\vec{v}_\mathrm{e}$ has to be calculated taking into account the thermal accommodation coefficient α. Generally, this can be done via

$$\vec{v}_\mathrm{e} = \alpha\,\vec{v}_\mathrm{th} + (1-\alpha)\,\vec{v}_\mathrm{i}' \quad , \tag{4.16}$$

where $\vec{v}_\mathrm{th}$ is the random thermal velocity component and $\vec{v}_\mathrm{i}'$ is the specular reflected component of $\vec{v}_\mathrm{i}$. The random thermal velocity component can be described via a parallel and a normal component $\vec{v}_\mathrm{th} = \vec{v}_\parallel + \vec{v}_\perp$. While the distribution function for the parallel

component equals eq. 4.15, the normal component can be described via (Tenenbaum et al., 1982)

$$f(\vec{v}_\perp) = \frac{m_{\mathrm{gas}}}{k_{\mathrm{B}}T}\, v_\perp \, \exp\left(-\frac{m_{\mathrm{gas}}\, v_\perp^2}{2\, k_{\mathrm{B}}\, T}\right) . \tag{4.17}$$

As mentioned in section 2.4.4, α depends on the material properties. Furthermore, the incident angle of the impacting gas molecule influences α as well. Referring to the modified Baule equation (Baule, 1914), Goodman and Wachman (1967) described the thermal accommodation coefficient via

$$\alpha = \cos(\vartheta) \cdot \alpha' \quad , \tag{4.18}$$

where ϑ is the incident angle and α' is a material constant.
Goodman and Wachman (1967) propagated a dependency of α' on the ratio between the mass of the incident molecule m_{gas} and the mass of the surface molecule m_{surf}:

$$\alpha'(m_{\mathrm{gas}}, m_{\mathrm{surf}}) = 3.6 \frac{m_{\mathrm{gas}}\, m_{\mathrm{surf}}}{(m_{\mathrm{gas}} + m_{\mathrm{surf}})^2} \quad . \tag{4.19}$$

Using SiO_2 as surface material with a molecular mass of $m_{\mathrm{surf}} = 30$ u and gas of cosmic composition with $m_{\mathrm{gas}} = 2.34$ u, the resulting α' is 0.24. The formula given by Goodman and Wachman (1967) is only valid for clean and smooth surfaces. Due to the fact that bodies in protoplanetary disks are porous but the surface topology is not taken into account in the simulations, α' is adopted to simulate rough surfaces. Besides that, the surface material can be highly contaminated with other molecules as e.g. mentioned in Kimura et al. (2015).
Considering a rough surface on micrometer scale (see fig. 4.8), multiple collisions of the gas molecules with the surface can occur, leading to larger energy exchanges and therefore to higher thermal accommodation coefficients.

On nanometer scale, the surface can be rough as well since polycrystalline and amorphous structures occur which result in higher accommodation coefficients as well (e.g. Thomas and Lord, 1974).
The exact value of α' for dust particles in PPDs is not known. Therefore, the simulations were performed estimating α' to be 0.45.

Simulation performance

Using a setup with a sphere radius s_{s} of 6 cm, a particle radius s_{p} of 0.1 cm and no larger body, the probability of a single gas molecule to hit the particle can be calculated geometrically to

$$P = 0.5 \left[1 - \cos\left(\arcsin\frac{s_{\mathrm{p}}}{s_{\mathrm{s}}}\right)\right] = 6.9 \times 10^{-5} \tag{4.20}$$

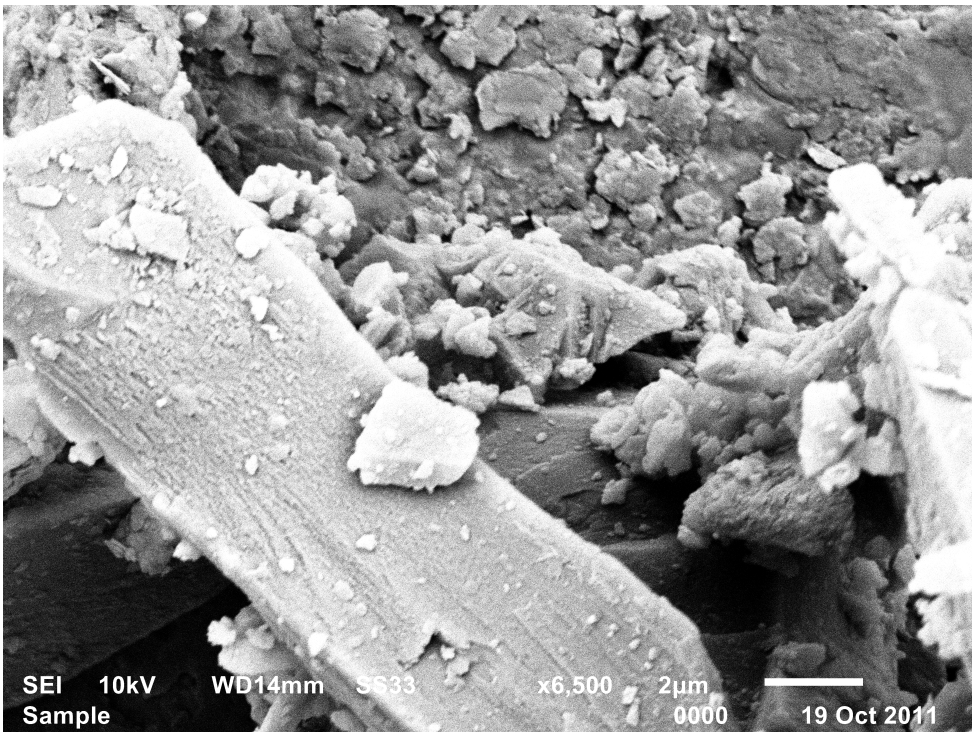

Figure 4.8: EM-Picture of a basalt surface, showing the roughness caused by the granular structure.

or via the integration method to

$$P = \int_{-\infty}^{0} p(v_r) \int_{0}^{-v_r\sqrt{s_\mathrm{p}^2 s_\mathrm{s}^{-2} - s_\mathrm{p}^4 s_\mathrm{s}^{-4}}} p(v_{\phi\vartheta}) dv_{\phi\vartheta} dv_r \tag{4.21}$$

$$= 0.5 \; - 0.5 \left(\frac{s_\mathrm{p}^2 \left(s_\mathrm{s}^2 - s_\mathrm{p}^2 \right)}{s_\mathrm{s}^4} + 1 \right)^{-0.5} \tag{4.22}$$

$$= 6.9 \times 10^{-5} \quad , \tag{4.23}$$

with

$$p(v_{\phi\vartheta}) = \frac{m_\mathrm{gas}}{k_\mathrm{B}\, T} \, v_{\phi\vartheta} \exp\left(\frac{-m\, v_{\phi\vartheta}^2}{2\, k_\mathrm{B}\, T} \right) \quad . \tag{4.24}$$

This probability is equally valid if one considers a setup with a second body and macroscopic gas velocity if gas molecules could hit the particle only once. Since this is clearly not the case, eq. 4.23 gives only a lower limit for the amount of collisions with the particle per simulated gas molecule, since it describes the probability of a gas molecule to hit the particle at least once. Nevertheless, simulations show that multiple hits occur rarely so that the probability of hitting is more or less independent from the actual setup. An example is shown in fig. 4.9. Around 3×10^5 gas molecules had to be simulated to generate 10 trajectories of gas molecules which hit the particle.

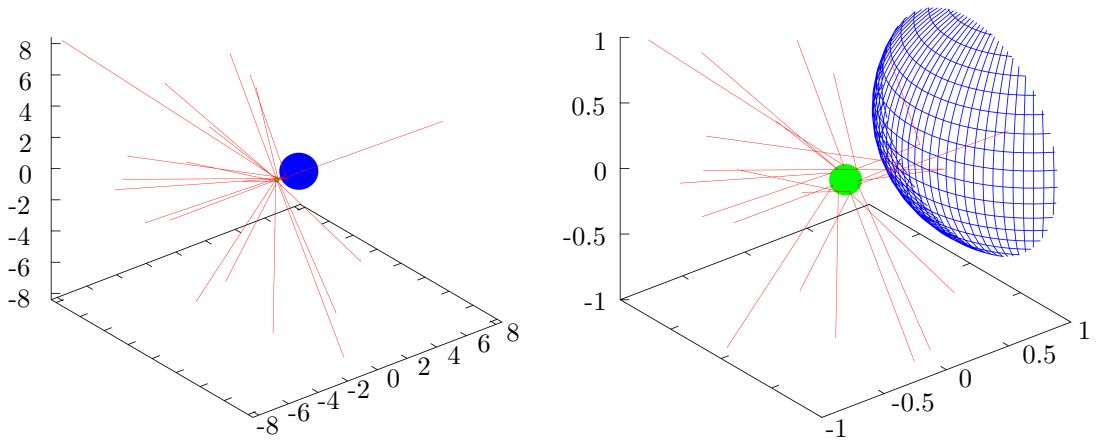

Figure 4.9: Simulated gas molecule trajectories for $v_{\mathrm{gas}} = 20$ m s^{-1}, $s_{\mathrm{ej}} = 0.1$ cm, $s_{\mathrm{t}} = 1$ cm, $\Delta y = 1.3$ cm, $\Delta x = 0$, and $T = 200$ K. Ten trajectories were chosen who all involve an interaction with the ejecta body.

Taking eq. 4.23 into account, for sufficient statistics – especially if one considers that $v_{\mathrm{th}} \gg v_{\mathrm{gas}}$ – around 10^{10} gas molecules were simulated for each specific setup with a sphere radius s_{s} of 6.0 cm. Using optimized algorithms and sorting techniques, the performance per thread (Xeon E5-2687 @ 3.1 GHz) is around 6×10^6 simulations per hour, leading to a calculation time of around $\frac{400}{\#\mathrm{threads}}$ hours.

Results

The momentum transfer onto the ejecta in y-direction is calculated by summing up the individual momentum transfer from every collision of a gas molecule with the ejecta's surface $\Delta p_{\mathrm{i,j}}$ and dividing it by the amount of simulated gas molecules #hit who are hitting the ejecta at least once (note that the second sum represents multiple hits of one gas molecule with the ejecta):

$$\frac{\Delta p}{m_{\mathrm{gas}}} = \frac{1}{\#\mathrm{hit}} \sum_{\mathrm{i}=1}^{\#\mathrm{hit}} \sum_{\mathrm{j}=1}^{\#\mathrm{col}} \Delta p_{\mathrm{i,j}} \quad . \tag{4.25}$$

The value without a target body being present is calculated from 2.25×10^{10} simulated gas molecules – with a total amount of gas molecules who hit the ejecta at least once of 1.56×10^6 – to

$$\frac{\Delta p_{\mathrm{notarget}}}{m_{\mathrm{gas}}} = 21.5 \pm 1.0\,\mathrm{m\,s^{-1}} \tag{4.26}$$

Fig. 4.10 shows the simulated data for different centre-of-gravity distances Δy between the 1 cm target body and the 0.1 cm ejecta in direction of the gas flow ($\Delta x = 0$). Except for very large distances where asymmetry effects might play a role due to the spherical

simulation space (the expectation value for $\Delta y \to \infty$ should be $\frac{\Delta p_{\text{notarget}}}{m_{\text{gas}}}$) and very small distances where shadowing effects might lead to larger forces pointing towards the target, the values resemble the simulated data point for no target present. This shows that the formula for a force acting on a particle in free molecular flow is capable of describing the accelerations due to gas drag acting on the ejecta and might even underestimate the force for small distances. Note here that in general this is only true for small gas velocities compared to the thermal randomly directed velocity.

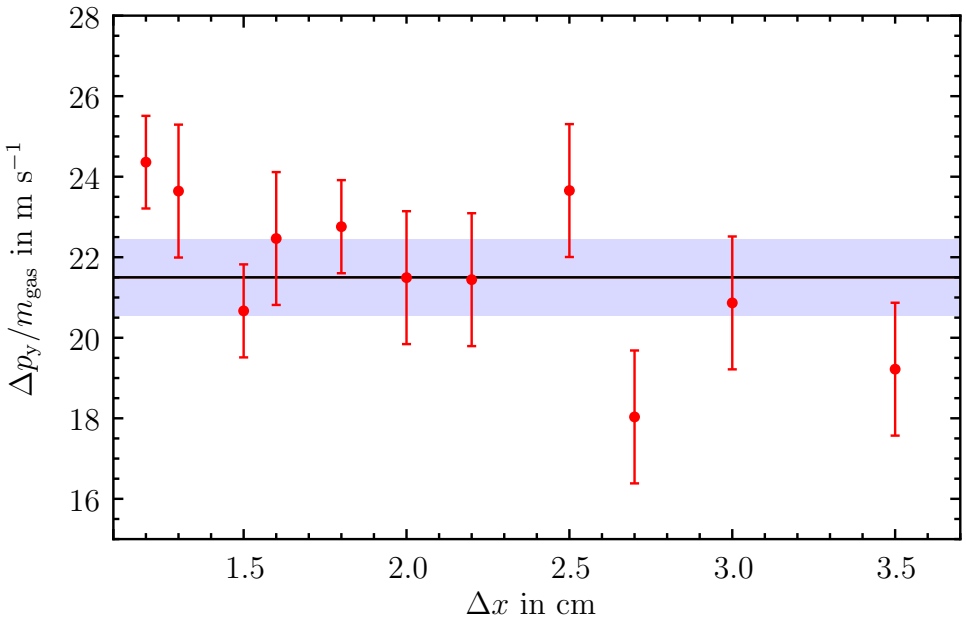

Figure 4.10: Momentum transfer $\Delta p_y/m_{\text{gas}}$ in y-direction against the center of gravity distance of ejecta and target Δy (with $(\Delta x = 0)$, see fig. 4.7) for 7.5×10^9 simulated gas molecules (distance 1.2, 1.5 and 1.8 cm: 1.5×10^{10} simulated gas molecules), $s_t = 1.0$ cm, $s_{ej} = 0.1$ cm, $s_s = 6.0$ cm, and $v_{\text{gas}} = 20$ m s^{-1}. The black line denotes the calculated momentum transfer onto the ejecta without a target body being present (the blue box denotes the error, note here that this value is determined from 2.25×10^{10} simulated gas molecules, leading to a total amount of gas molecules who hit the ejecta at least once of 1.56×10^6).

In fig. 4.11 the dependency of $\Delta p/m_{\text{gas}}$ in y- and x- direction is shown against the x-shift of ejecta and target Δx with a fixed $\Delta y = 2.5$ cm. The simulation setup equals the one described above.

4.3.3 Comparison

As can be seen from fig. 4.10 and 4.11, the simulated momentum transfers per gas molecule which hits the ejecta at least once equal each other within the range of errors for both cases, with and without a secondary body present. Although a slight dependency

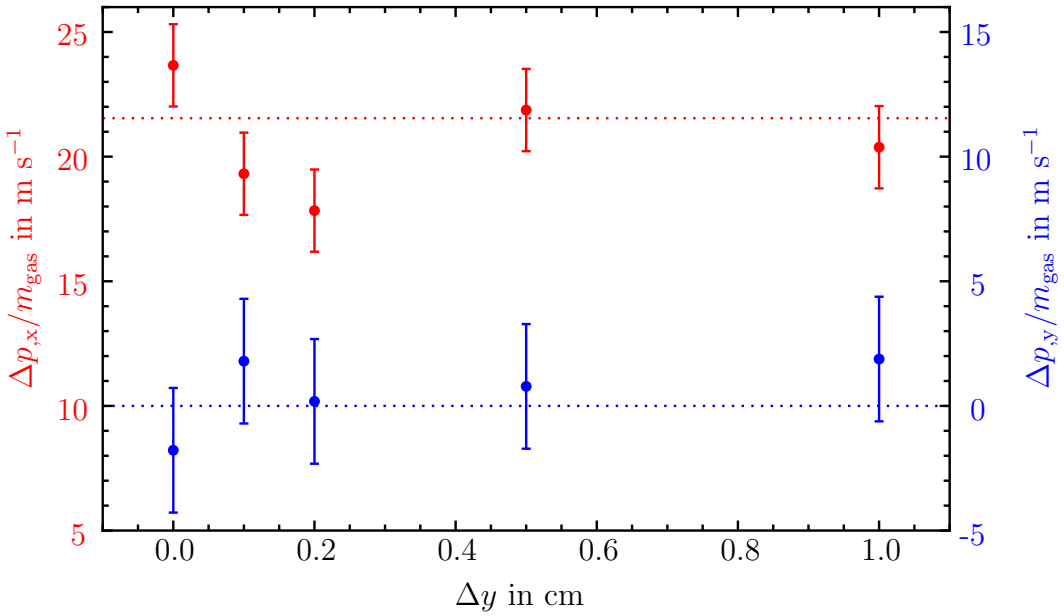

Figure 4.11: Momentum transfer $\Delta p/m_{\rm gas}$ (blue in x direction, red in y direction) against the x-shift of ejecta and target Δx (with ($\Delta y = 2.5$ cm), see fig. 4.7) for 7.5×10^9 simulated gas molecules, $s_{\rm t} = 1.0$ cm, $s_{\rm ej} = 0.1$ cm, $s_{\rm s} = 6.0$ cm, and $v_{\rm gas} = 20$ m s^{-1}. The blue dotted line denotes the zero-line (expected value for undisturbed gas flow), the red dotted line denotes the calculated momentum transfer onto the ejecta without a target body being present (see fig. 4.10).

on the distance Δy can be seen in fig. 4.10, the difference between the undisturbed and the disturbed case is less than 20 %. Furthermore, for small distances the acceleration given by eq. 4.12 might even be underestimated. This leads to the assumption that for general purposes the solution given by Wurm et al. (2001a,b) adequately describs the force on the ejecta. One has to note that the simulations presented here and the solution given by Wurm et al. (2001a,b) are in physical terms only valid in the free molecular flow regime with high (target-) Knudsen numbers. Nonetheless, since Wurm et al. (2001a,b) experimentally showed the validity down to at least $Kn_{\rm t} = 0.15$ with ejecta sizes of 1.2 μm, the simulations of reaccretion were performed for small Knudsen numbers as low as 0.1 while using Epstein Drag.

4.4 Dependencies of Reaccretion

Since the analytic solution of the particle movement as given in eq. 4.13 is directly proportional to τ_{fric}^{-1} and therefore $\propto \rho_{\text{gas}} \cdot \overline{v}_{\text{th}}$, increasing $\rho_{\text{gas}} \cdot \overline{v}_{\text{th}}$ lead to an increase in reaccreted mass and therefore to increasing η_{re}. This is shown in fig. 4.12 for the parameter set $s_{\text{t}} = 2 \times 10^{-2}$ m, $s_{\text{p}} = 2 \times 10^{-4}$ m, and $v_{\text{p}} = 50$ m s^{-1}.

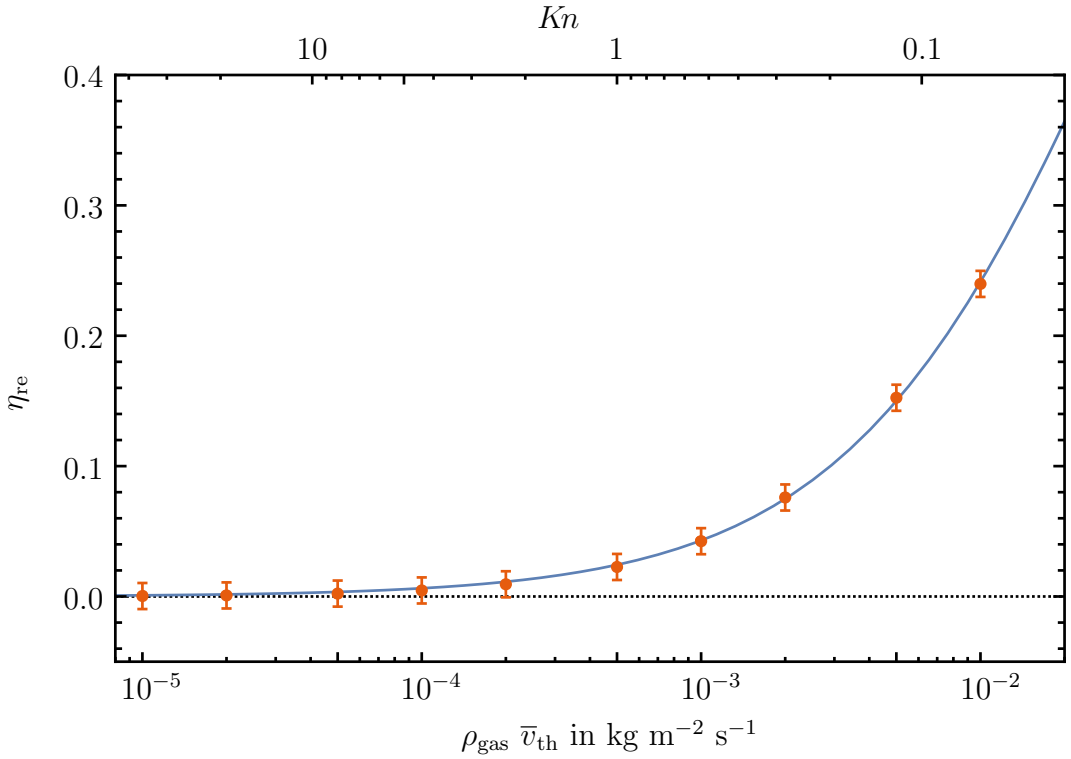

Figure 4.12: Reaccreted mass ratio η_{re} over $\rho_{\text{gas}} \cdot \overline{v}_{\text{th}}$ (bottom abscissa) and Kn (top abscissa) for $s_{\text{t}} = 2 \times 10^{-2}$ m, $s_{\text{p}} = 2 \times 10^{-4}$ m, $v_{\text{p}} = 50$ m s^{-1}.

The dependency of η_{re} on $\rho_{\text{gas}}\,\overline{v}_{\text{th}}$ can be described via

$$\eta_{\text{re}}(\rho_{\text{gas}}\,\overline{v}_{\text{th}}) = \frac{1}{2} + \frac{1}{2}\tanh\left(a(s_{\text{p}}) \cdot \log_{10}\left(\frac{\rho_{\text{gas}}\,\overline{v}_{\text{th}}}{\text{kg m}^{-2}\,\text{s}^{-1}}\right) + b(s_{\text{t}}, s_{\text{p}})\right) \quad . \tag{4.27}$$

The fit parameter a is only dependent on the impactor's size while b is dependent on both sizes. Using 22 different combinations of impactor and target sizes, the parameters can be described using log-linear functions via

$$a(s_{\text{p}}) = 1.10 + 3.12 \times 10^{-2} \log_{10}\left(\frac{s_{\text{p}}}{\text{m}}\right) \tag{4.28a}$$

$$b(s_{\text{t}}, s_{\text{p}}) = 1.77 - 3.42 \times 10^{-1} \log_{10}\left(\frac{s_{\text{p}}}{\text{m}}\right) + 9.93 \times 10^{-1} \log_{10}\left(\frac{s_{\text{t}}}{\text{m}}\right) \quad . \tag{4.28b}$$

The detailed fit function parameters as well as the data used for the fits are shown in the appendix, tab. A.1 and tab. A.2.

Furthermore, higher impact velocities (and therefore higher gas velocities) lead to an increase in η_{re} as well (see fig. 4.13). This is caused by the increase of $\frac{v_{\mathrm{p}}}{v_{\mathrm{ej}}}$ with increasing v_{p}. Since not only the ejecta velocity but also the amount and size of the ejecta is changing, the increase is nonlinear especially for small impactors.

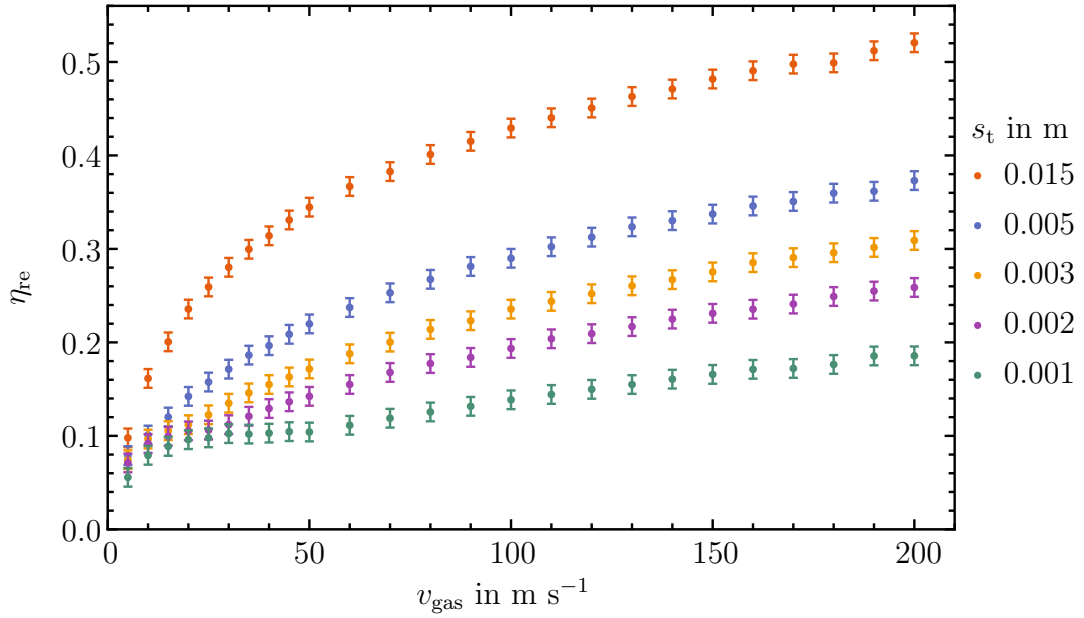

Figure 4.13: Reaccreted mass ratio η_{re} over gas velocity v_{gas} for different sized targets s_{t}, a fixed size ratio of $s_{\mathrm{t}}/s_{\mathrm{p}} = 100$ and $\rho_{\mathrm{gas}}\,\overline{v}_{\mathrm{th}} = 10^{-2}$ kg m^{-2} s^{-1}.

4.5 Reaccretion in the MMSN

By using specific disk models, a close form expression for the amount of reaccreted mass η_{re} can be found via fitting. For the MMSN, at first the dependency of η_{re} on the impactor size and target size (s_{p}, s_{t}) is determined for several distances to the central star r and after that the parameters are fitted in dependency on r.
In general the dependency of η_{re} on s_{p} and s_{t} can be described via

$$\eta_{\mathrm{re}}(s_{\mathrm{p}}, s_{\mathrm{t}}, r) = \frac{1}{2} + \frac{1}{2}\tanh\left(-a(r)\cdot\log_{10}(s_{\mathrm{p}}) - b(r) + c(r)\cdot\log_{10}(s_{\mathrm{t}})\right) \quad . \tag{4.29}$$

In fig. 4.14 the relative reaccreted mass η_{re} is plotted for different impactor and target sizes s_{p} and s_{t} for $r = 1$ AU. The fit for the data follows eq. 4.29.

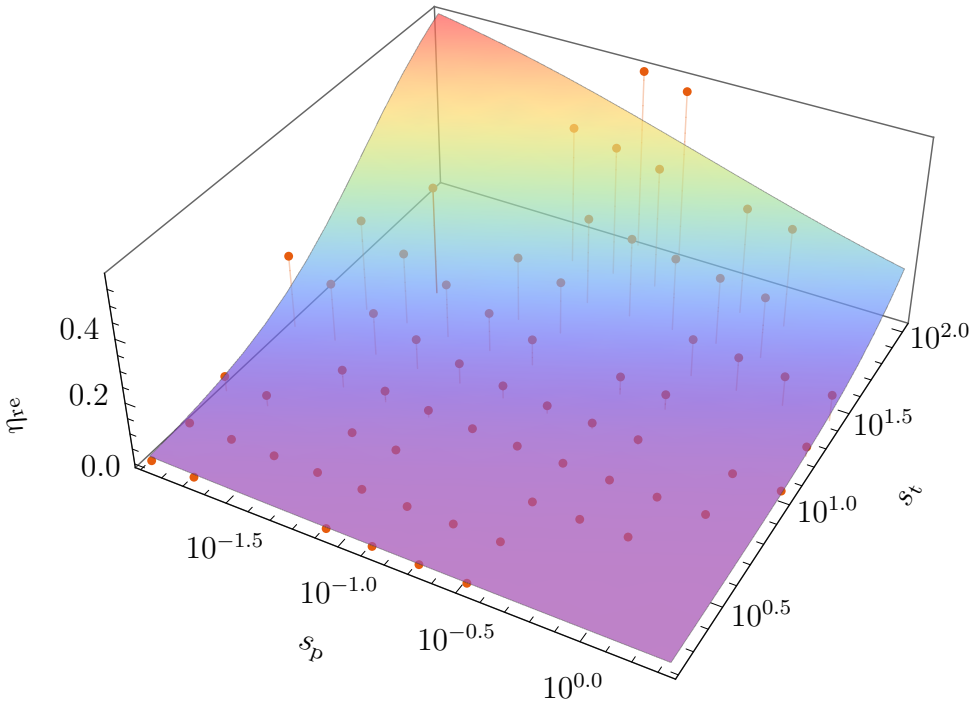

Figure 4.14: Reaccreted mass ratio η_{re} for different sized targets s_{t} and impactors s_{p} in the MMSN at a distance to the central star of $r = 1$ AU. The simulated data points in red are overlaid by the fit function following eq. 4.29.

This fit is performed for nine different distances to the central star. The resulting parameters $a(r)$, $b(r)$ and $c(r)$ (see fig. 4.15 - 4.17) can be described using simple functions, resulting in

$$a(r) = 0.34 + 0.62 \cdot \exp(-\frac{r}{\mathrm{AU}}) \tag{4.30a}$$

$$b(r) = 6.87 + 0.47 \left(\frac{r}{\mathrm{AU}}\right)^{-2} - 10.7 \cdot \exp\left(-\sqrt{\frac{r}{\mathrm{AU}}}\right) \tag{4.30b}$$

$$c(r) = 1.89 - 0.67 \left(\frac{r}{\mathrm{AU}}\right)^{-1} + 0.28 \left(\frac{r}{\mathrm{AU}}\right)^{-3} \quad . \tag{4.30c}$$

The detailed fit function parameters are shown in the appendix, tab. A.3.

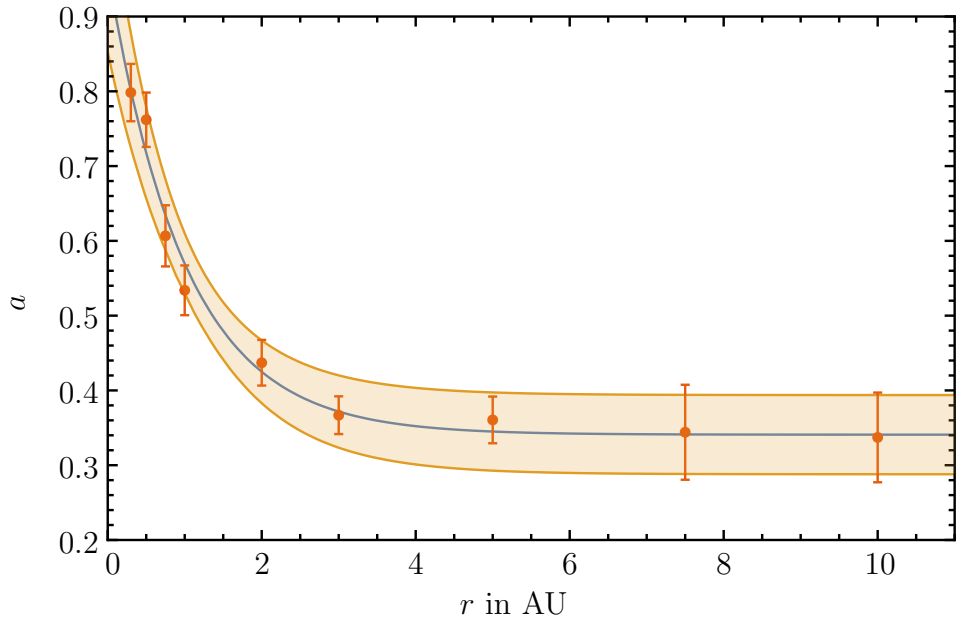

Figure 4.15: Fit for $a(r)$ (see eq. 4.29) following the fit function shown in eq. 4.30 , with $3\,\sigma$ confidence interval.

Eq. 4.29 together with eq. 4.30 can be applied to the collisional outcome model by Windmark et al. (2012a) (sec. 3.1) using the MMSN disk parameters (sec. 2.1.1) and the model for relative velocities between particles as described in sec. 2.5. Taking a turbulence value of $\alpha_t = 10^{-2}$ and a distance to the central star $r = 1$ AU, fig. 4.18 shows the growth rate as predicted by Windmark et al. (2012a) compared to the growth rate including reaccretion. Fig. 4.19 shows the relative increase in growth due to reaccretion in impactor masses

$$\frac{\text{growthrate with reaccretion}}{\text{growthrate without reaccretion}} - 1 \quad . \tag{4.31}$$

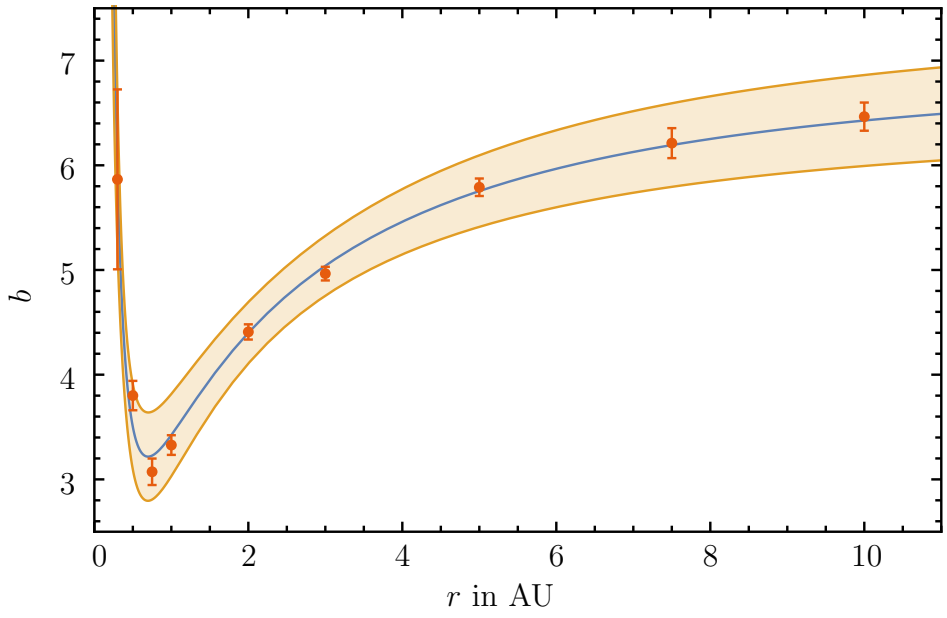

Figure 4.16: Fit for $b(r)$ (see eq. 4.29) following the fit function shown in eq. 4.30 , with $3\,\sigma$ confidence interval.

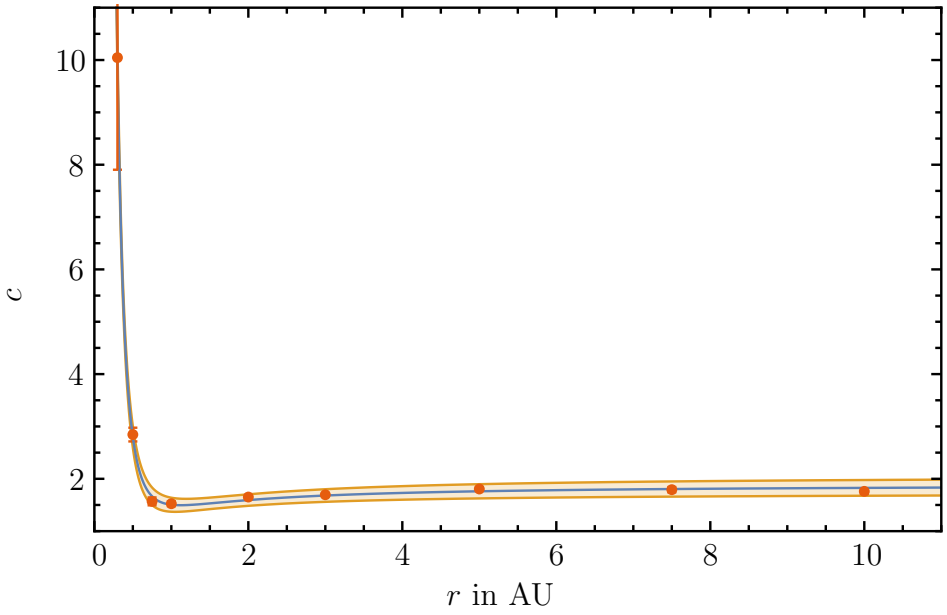

Figure 4.17: Fit for $c(r)$ (see eq. 4.29) following the fit function shown in eq. 4.30 , with $3\,\sigma$ confidence interval.

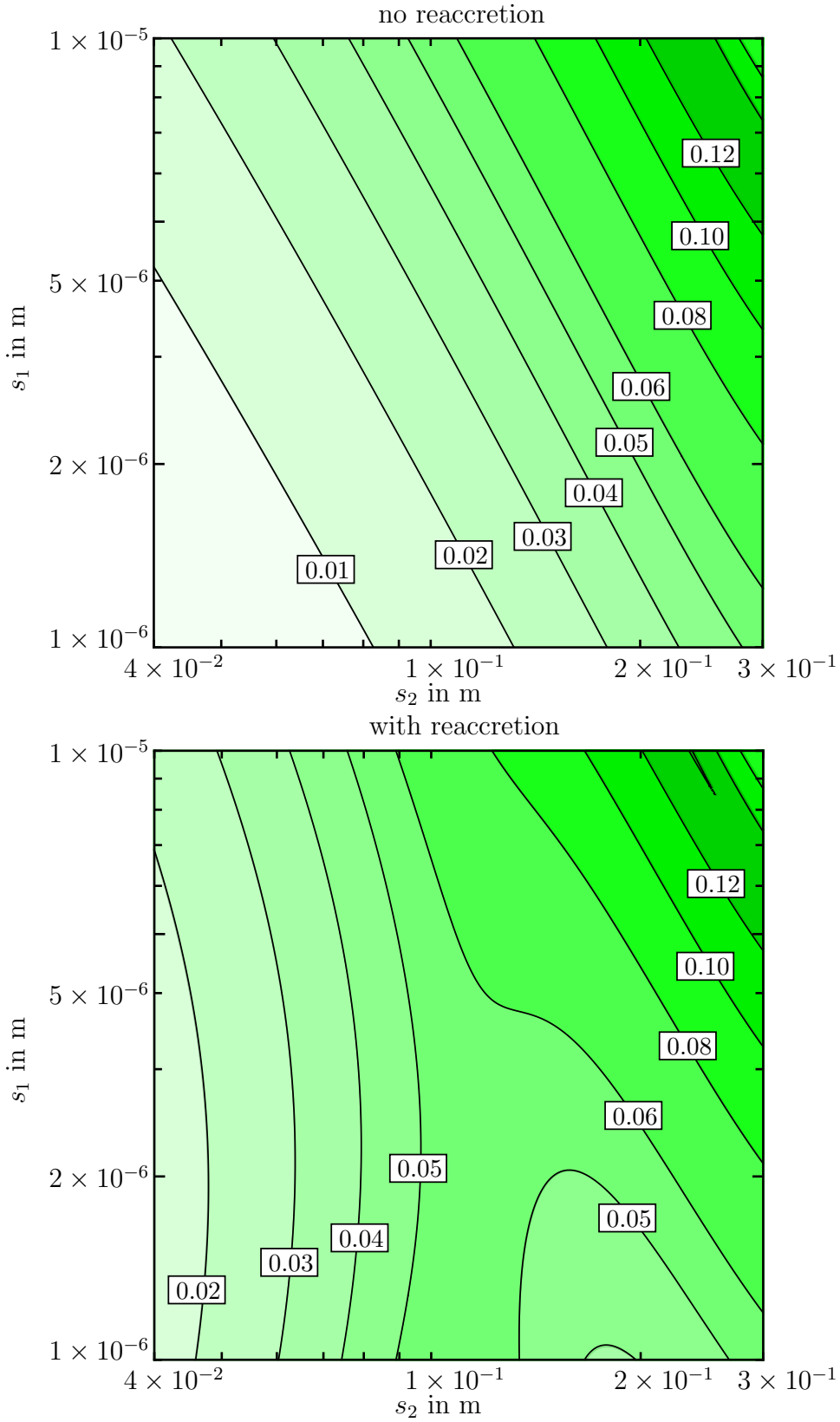

Figure 4.18: Collisional outcome of two particles in the MMSN at 1.0 AU, following the collisional outcome model (Windmark et al., 2012a) in sec. 3.1 and the collision velocities as described in sec. 2.5 with $\alpha_t = 10^{-2}$. Top: without reaccretion included, bottom: with reaccretion. Collisions of particles with the sizes shown here always result in growth, the contours depict the growth of the target body in impactor masses. A smooth cutoff for reaccretion was chosen at $Kn = 0.1$ which equals a particle size of $\sim 1.5 \times 10^{-1}$ m at 1 AU.

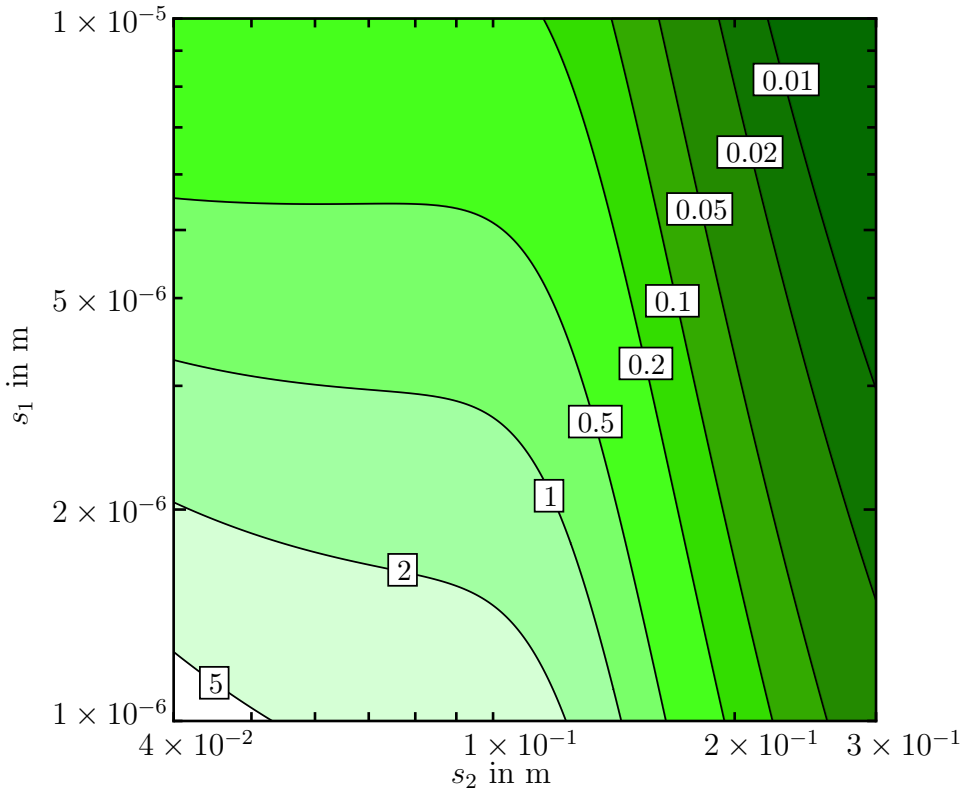

Figure 4.19: Increase in mass gain due to reaccretion compared to the mass gain without reaccretion for two particles in the MMSN at 1.0 AU following eq. 4.31 (see fig. 4.18 for details). The model including reaccretion can lead to more than 5 times higher growth rates than the model without reaccretion.

Following fig. 4.18 and 4.19, the increasing growth rates should decrease the growth timescales as well. To quantify that, the following scenario is elaborated: using the MMSN disk parameters and a fixed distance to the central star of 3 AU, the growth of a 3.2×10^{-2} m sized particle to a size of 10^{-1} m was simulated assuming only growth via mass gain in collisions with smaller particles (omitting fragmentation and mass loss in collisions with larger particles). Without reaccretion included, the growth time is about 1200 years. Including reaccretion, the growth time decreases to 190 years.
The growth times differ even more if the initial particle size is lower (1.6×10^{-2} m): without reaccretion about 55000 years are necessary, including reaccretion this time is reduced to $\sim$ 600 years.

4.6 Discussion and Caveats

As shown in this chapter, reaccretion of particles influence the growth rate significantly in certain parameter constellations. This is especially the case in collisions where only little mass is transferred directly onto the target body. Since the total ejected mass is very high, even small amounts of reaccreted material can lead to a significant relative increase in mass gain, in the MMSN by a factor of five or higher (see fig. 4.19). This decreases the timescales of runaway growth of "lucky particles": Windmark et al. (2012a) showed that if particles had overcome the bouncing-barrier, they might grow to significant sizes in timescales comparable to the disks lifetime. Nonetheless, since Windmark et al. (2012a) use a collisional outcome model which does not include erosion in collisions of larger particles with monomer sized particles as proposed by Seizinger et al. (2013), the calculated growth timescales might be somewhat underestimated. Comparing the growth of a 3.2×10^{-2} m sized particle to a size of 10^{-1} m (omitting destruction) for the "classical" model by Windmark et al. (2012a) to the same model including reaccretion leads to a decrease in the timescales of a factor of ~ 5. This value is even higher (up to a factor of ~ 100) when comparing the growth of a 1.6×10^{-2} m sized particle to a size of 10^{-1} m. Including reaccretion in this model could therefore be important to re-attain values comparable to the disk lifetime.

One major benefit of the model for reaccretion presented here is the independency on the specific collisional outcome model: although implying a distribution of the ejecta sizes, the amount of reaccreted mass is calculated in terms of impactor masses, leading to a non-dimensional factor for the efficiency. Therefore, eq. 4.29 is applicable to multiple collisional outcome models for the MMSN.

A crucial variable for reaccretion is the Knudsen number. Although reaccretion might work even for small Knudsen numbers as shown by Wurm et al. (2001a,b), the validity of this assumption has to be verified in future studies. Since the gas-grain friction time τ_{fric} is highly dependent on the particle size, large particles might still be reaccreted due to gas drag even if the Knudsen number is much smaller than unity.

The efficiency of reaccretion within the model given here depends on four variables: gas velocity v_{gas} (which equals the impact velocity), gas density times mean thermal velocity $\rho_{\mathrm{gas}}\overline{v}_{\mathrm{th}}$, impactor size s_{p} and target size s_{t}. Although the variables $\rho_{\mathrm{gas}}\overline{v}_{\mathrm{th}}$, s_{p} and s_{t} do not correlate, the gas velocity v_{gas} is at least correlated to the target size as shown in fig. 4.13.

5

Self-sustained recycling process in the inner dust ring of pre-tansitional disks

In this chapter recent investigations on dust motion in the inner part of pre-transitional disks are presented, following the publication by Husmann et al. (2016). Using the PDM as depicted in sec. 2.1.2, the force balance and the resulting radial drift velocities of differently sized dust particles are calculated. With the help of these results and using the collisional outcome model by Windmark et al. (2012b), single particle evolution simulations are performed investigating the growth and destruction processes of moving sample particles in two different pre-transitional disks. In total three different model parameters are used, one set of parameters for HD135344B and two different sets for LkCa15 showing that a self-sustained recycling process can be established in the inner parts of pre-transitional disks.

5.1 Introduction to pre-transitional disks

The observation of pre-transitional disks has been evolving in the past years from simple unresolved spectral energy distributions (e.g. Calvet et al., 2002; Najita et al., 2007; Sicilia-Aguilar et al., 2008) to high-resolution images in sub-mm and mm bands (Andrews et al., 2011b; Bruderer et al., 2014; van der Marel et al., 2015). An image showing the disk LkCa15 in 870 μm continuum emission as well as a spectral energy distribution (deprojected from that image), taken from Andrews et al. (2011a), is shown in fig. 5.1. The general disk structure of pre-transitional disks is described in fig. 1.5 and sec. 2.1.2. Summarised, these disk types contain an optically thin inner dust disk between the sublimation radius of silicate r_{sub} and a gap opening radius r_{gap} as well as an optically thick

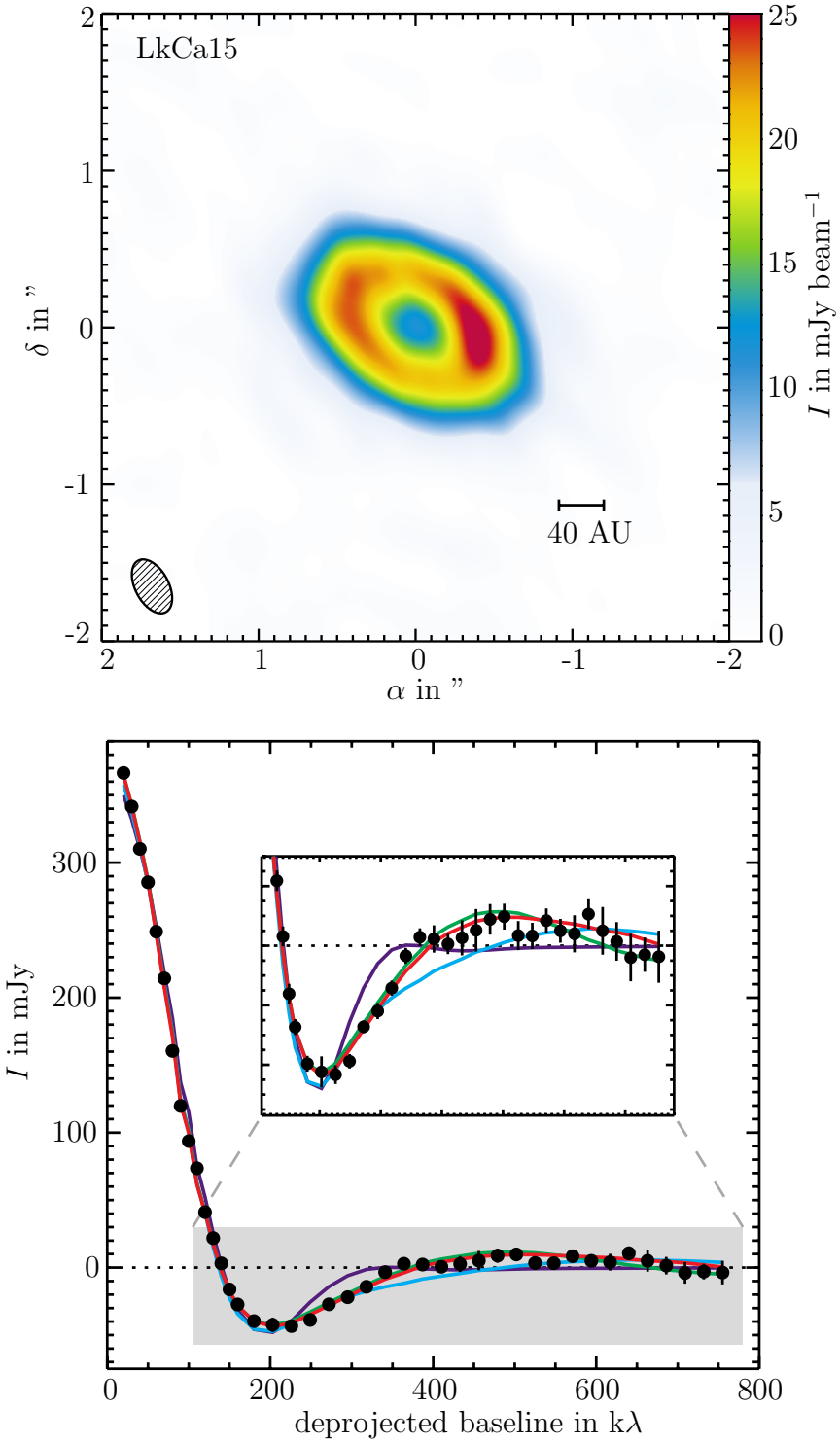

Figure 5.1: Image of the disk LkCa15 in 870 μm continuum emission (top) and spectral energy distribution (deprojected) with fits for different models (bottom), taken from Andrews et al. (2011a). The PDM as described in sec. 2.1.2 is visualised by the red line, showing a suitable solution for the disks spectral energy distribution.

outer dust ring from r_{cav} to the disk edge. In between these sub-disks, observations show that only very little dust is present. Besides the dust characteristics, pre-transitional disks contain gas whilst the gas surface density within r_{cav} is significantly reduced. The disks' characteristics can be computed from observations by fitting modelled spectral energy distributions which depend on the disk model's parameters to the observational data. As shown in fig. 5.1, Andrews et al. (2011b) compared fits for different models for the disk LkCa15, showing that the model described in sec. 2.1.2 is suitable to explain the spectral energy distribution (red line). Recent publications by van der Marel et al. (2015) show that the PDM presented in sec. 2.1.2 fits well even for other disks.

5.2 Motion of particles in pre-transitional disks

The inner parts of pre-transitional disks are considered to be optically thin in radial direction. Therefore the motion of particles can significantly be influenced by radiation-related forces. Nonetheless, the intensity of the radiation at a given distance to the central star is crucial since the photophoretic forces can be large enough to dominate the force balance. In this section the global motion of differently sized particles in different pre-transitional disks is depicted in detail.
For an appropriate calculation of the forces and the resulting motion of the particles it is essential to know in detail the disk's opacity κ_{med}, the thermal conductivity of the particles k_{th} as well as the dust scale height parameter χ_{dust} which influence the radiation-related forces notably.

5.2.1 Opacity of pre-transitional disks

Using eq. 2.12 the intensity at a given distance to the central star can be calculated. A crucial aspect in this calculation is the mean opacity κ_{med}, described by eq. 2.13 while assuming κ_{med} to be constant in r.
For the estimation of κ_{med}, data from Semenov et al. (2003) was used. They were offering values for κ_λ for five different temperature regimes, different particle types as well as different particle mineralogy (iron-rich, iron-poor, normal) with a distinct dust to gas ratio and a distinct size distribution. Since this dust distribution (see Pollack et al., 1985, for details) is different from the dust distribution (eq. 4.5) used for the calculations presented here and the exact dust properties are unknown, the values calculated give only a brief estimation of κ_{med}. For the disks LkCa15 and HD135344B, the calculated values differ between 1.8 and 5.5 $\mathrm{m^2\ kg^{-1}}$. Therefore a value of $\kappa_{\mathrm{med}} = 2.5\ \mathrm{m^2\ kg^{-1}}$ was chosen for the disk HD135344B and $\kappa_{\mathrm{med}} = 3.0\ \mathrm{m^2\ kg^{-1}}$ was chosen for the disk LkCa15.

5.2.2 Thermal conductivity of dust aggregates

The rate of heat flow $\frac{\delta Q}{\delta t}$ through a body for a given area A and a given temperature gradient $\frac{\Delta T}{l}$ can be described via

$$\frac{\delta Q}{\delta t} = k_{\mathrm{th}}\, A\, \frac{\Delta T}{l} \quad . \tag{5.1}$$

The constant of proportionality k_{th} is referred to as the thermal conductivity of the body. Whilst the thermal conductivity of solid materials or fluids can be determined easily, the one of porous dust aggregates consisting of multiple grains is not trivial to determine (Krause et al., 2011). It depends not only on the bulk material itself but on other aspects like temperature, grain size distribution, shape of the grains, number of contacts between the grains, the contact area distribution, the volume filling factor, and externally applied forces like e.g. gravity. The latter describes the ratio between the volume filled with particles and the aggregate volume. Krause et al. (2011) presented first experimental results for aggregates consisting of 1.5 μm sized SiO_2 particles with volume filling factors between 0.15 and 0.54. Their setup consisted of a laser-illuminated dust sample in a vacuum chamber observed by an infrared camera. Fitting the time dependent temperature distribution they determined values between 1.6×10^{-3} and 2.1×10^{-2} W m^{-1} K^{-1}.
Theoretical studies on thermal conductivity are still ongoing (e.g. by Kamp, 2016), but the values presented by Krause et al. (2011) give a first estimation which is comparable to measurements from Groussin et al. (2007) for the Comet 9P/Temple 1.
Since the temperature dependency of the thermal conductivity is not treated in Krause et al. (2011) and other values are missing, the thermal conductivities in the model used here were set to 10^{-2} W m^{-1} K^{-1} for the disk HD135344B and LkCa15 Model 1, and 10^{-3} W m^{-1} K^{-1} for the disk LkCa15 Model 2.

5.2.3 Dust scale height parameter

The dust scale height ($\chi_{\mathrm{dust}} \cdot h$) can be estimated from the turbulence parameter α_{t} and is limited to a maximum of the gas disk scale height (h). Therefore, χ_{dust} can range from 0 to 1. According to Dubrulle et al. (1995), χ_{dust} can be expressed via

$$\chi_{\mathrm{dust}} = \sqrt{\frac{\delta_{\mathrm{diff}}}{\mathrm{St} + \delta_{\mathrm{diff}}}} \quad , \tag{5.2}$$

where δ_{diff} is a measure of the diffusion coefficient for which in general in turbulence disks it is $\delta_{\mathrm{diff}} = \alpha_{\mathrm{t}}$ (Johansen and Klahr, 2005; Turner et al., 2006). Nonetheless, this is not

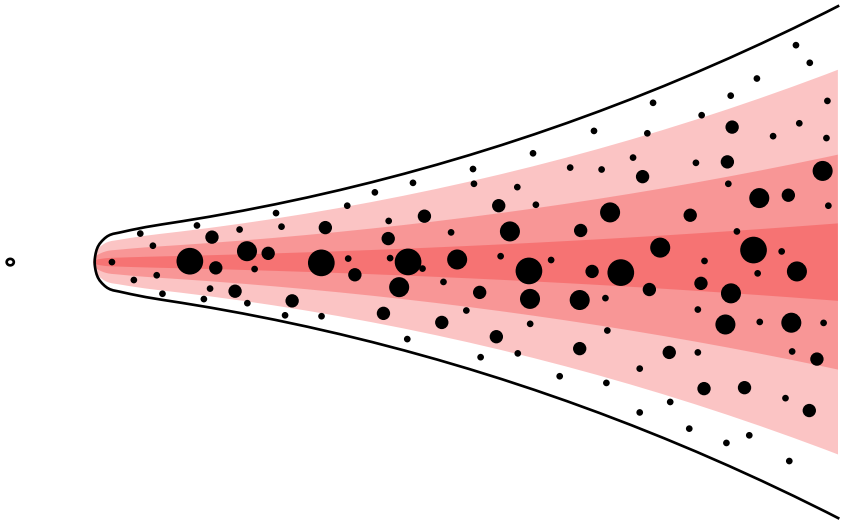

Figure 5.2: Schematic cut through a protoplanetary disk, showing the vertical dust size distribution. The largest particles are in the innermost zone (darkest red) while the smallest particles can be found throughout the entire disk.

entirely true if accretion is still taking place (Johansen et al., 2014). As can be seen from eq. 5.2, the scale height parameter depends on the particles' Stokes Numbers (see eq. 2.48) and therefore on the particles' sizes. This leads to a layered disk structure in vertical direction with the larger particles only to be found in the midplane and the smaller particles be found throughout the entire disk. Here, the Stokes Number for the large particles $\mathrm{St}_{\mathrm{large}}$ is assumed to be large compared to the turbulence parameter α_{t} while for small particles it is assumed to be $\alpha_{\mathrm{t}} \gg \mathrm{St}_{\mathrm{small}}$. A scheme of a layered disk structure is depicted in fig. 5.2. For the motion of particles near the midplane the dust density at the midplane is important since the radiation related forces (radiation pressure and photophoresis) depend on the intensity I (see eq. 2.12). While the inner dust disks in pre-transitional disks are in relative terms thin and hot, the disks are assumed to be highly turbulent due to magneto-rotational instabilities (Johansen et al., 2014). Dzyurkevich et al. (2010) estimated α_{t} values of 10^{-3} near the dead zones of MRI turbulent disks. Nonetheless, at the edge of transitional disks higher values are predicted e.g. by Chiang and Murray-Clay (2007). For an exact calculation of the midplane density of the dust one has to integrate over the size-dependent dust densities using a size distribution function as mentioned in eq. 4.5 with a cutoff at a maximum and minimum particle size. Since firstly, the mean disk opacity κ_{med} shows significant uncertainties, secondly, the turbulence value is not known exactly and thirdly, eq. 5.2 might not be fulfilled completely, the dust scale height parameter for the calculation of the midplane motion of particles was simplified by choosing it to be equal for all particle sizes and set to 0.5 for the inner disk of LkCa15 and 0.85 for the (generally hotter and smaller) inner disk of HD135344B.

Table 5.1: Disk parameters for HD135344B and LkCa15 adopted from van der Marel et al. (2015). Two different model parameters were used for LkCa15, M1 denotes the first model, M2 the second one. Values marked with an asterisk are modified from respectively not given by van der Marel et al. (2015).

Disk	r_c (AU)	Σ_c $\left(\frac{g}{cm^2}\right)$	h_c (rad)	ϕ	δ^*_{gas}	δ^*_{dust}	κ^*_{med} $\left(\frac{m^2}{kg}\right)$
HD135344B	25	300	0.15	0.05	10^{-2}	10^{-3}	2.5
LkCa15 M1	85	34	0.06	0.04	10^{-2}	$2 \cdot 10^{-5}$	3.0
LkCa15 M2	85	34	0.06	0.04	$5 \cdot 10^{-3}$	$3 \cdot 10^{-5}$	3.0

Disk	r_{sub} (AU)	r_{gap} (AU)	r_{cav} (AU)	M ($M_\odot$)	L ($L_\odot$)	T_{eff} (K)	k^*_{th} $\left(\frac{W}{m\,K}\right)$	χ^*_{dust}
HD135344B	0.18	0.25	40	1.6	7.8	6590	10^{-2}	0.85
LkCa15 M1	0.08	1	45	1.0	1.2	4730	10^{-2}	0.5
LkCa15 M2	0.08	1	45	1.0	1.2	4730	10^{-3}	0.5

5.2.4 Disk and dust parameters

To describe pre-transitional disks, the PDM was used (see section 2.1.2) with the disk and dust parameters listed in tab. 5.1. The values are adopted from van der Marel et al. (2015) with changes in δ_{gas} and δ_{dust} within the uncertainty range of the model parameters given by van der Marel et al. (2015). As mentioned, the values for the mean disk opacity κ_{med}, the thermal conductivity of the particles k_{th} and the dust scale hight χ_{dust} are described in sec. 5.2.1 to 5.2.3.

5.2.5 Forces on particles in pre-transitional disks

The forces in radial direction for non-moving particles (assuming the gas to have no radial velocity component) can be calculated using the given formulas for photophoresis (see sec. 2.4.4), radiation pressure (see sec. 2.4.3 and eq. 2.30) and the residual gravity (see sec. 2.4.2 and eq. 2.28). In fig. 5.3 the strength of the accelerations due to residual gravity a_{res}, photophoresis a_{phot}, and radiation pressure a_{rp} are plotted against the distance to the central star for different particle sizes for the disk LkCa15 (Model 1 and Model 2). Fig. 5.4 displays the force balance in radial direction. As shown in these plots, one can distinguish between three different curve progressions (assuming the radial distance r always to be larger than the sublimation radius r_{sub}):

a) $a_{\text{total}} < 0$ for all distances to the central star: If the particles are large, the accelerations pointing outwards $a_{\text{rp}} + a_{\text{phot}}$ are insufficient to overcome a_{res}.

b) $a_{\text{total}} > 0$ for $r_{\text{min}} < r < r_{\text{max}}$: Since the acceleration due to photophoresis a_{phot} peaks at $P = \hat{P}$ and decreases for lower or higher pressures, regions exist where photophoresis dominates the force balance. A critical maximum particle size s_{crit} can be calculated for the transition between case a) and case b). As shown later, this turnover point is of great interest in the simulation of the evolution of single particles.

c) $a_{\text{total}} > 0$ for $r < r_{\text{max}}$: For small particles (or special disk configurations with large amounts of dust and gas) the forces pointing outwards dominate the force balance until a certain distance r_{max} is reached.

The force characteristics might deviate significantly from the ones presented if the disk properties change, for example due to very low opacities and/or very little gas. An example for a disk with force characteristics deviating from fig. 5.3 and 5.4 is HD135344B, where the force balance is either negative throughout the entire disk (large particles) or positive close to the star and negative further outwards (small particles, see fig. 5.5).

5.2.6 Solution to particle drifts in pre-transitional disks

Using eq. 2.45, the radial drift velocities of differently sized particles in the disk LkCa15 and HD135344B can be calculated for particles moving in the midplane. This is achieved - assuming τ_{fric} to be small - by deriving the steady-state solutions $\frac{\mathrm{d}v}{\mathrm{d}t} = 0$:

$$\frac{\mathrm{d}(rv_\phi)}{\mathrm{d}t} = \frac{\mathrm{d}r}{\mathrm{d}t}v_\phi + r\underbrace{\frac{\mathrm{d}v_\phi}{\mathrm{d}t}}_{\stackrel{!}{=}0} = -\frac{r}{\tau_{\text{fric}}}(v_\phi - v_{\phi,\text{gas}}) \tag{5.3a}$$

$$\underbrace{\frac{\mathrm{d}v_\text{r}}{\mathrm{d}t}}_{\stackrel{!}{=}0} = \frac{v_\phi^2}{r} - \frac{GM_*}{r^2} - \frac{(v_r - v_{r,\text{gas}})}{\tau_{\text{fric}}} + \frac{F_{\text{radial}}}{m} \quad . \tag{5.3b}$$

Combining these equations yields (with $v_\text{r} = \frac{\mathrm{d}r}{\mathrm{d}t}$):

$$v_\phi^3 + \underbrace{\left(\frac{r^2}{\tau_{\text{fric}}^2} + \frac{r}{m}F_{\text{radial}} - \Omega^2 r^2 + \frac{r}{\tau_{\text{fric}}}v_{\text{r,gas}}\right)}_{=3b} v_\phi - \underbrace{\frac{r^2}{\tau_{\text{fric}}^2}v_{\phi,\text{gas}}}_{=2c} = 0 \tag{5.4}$$

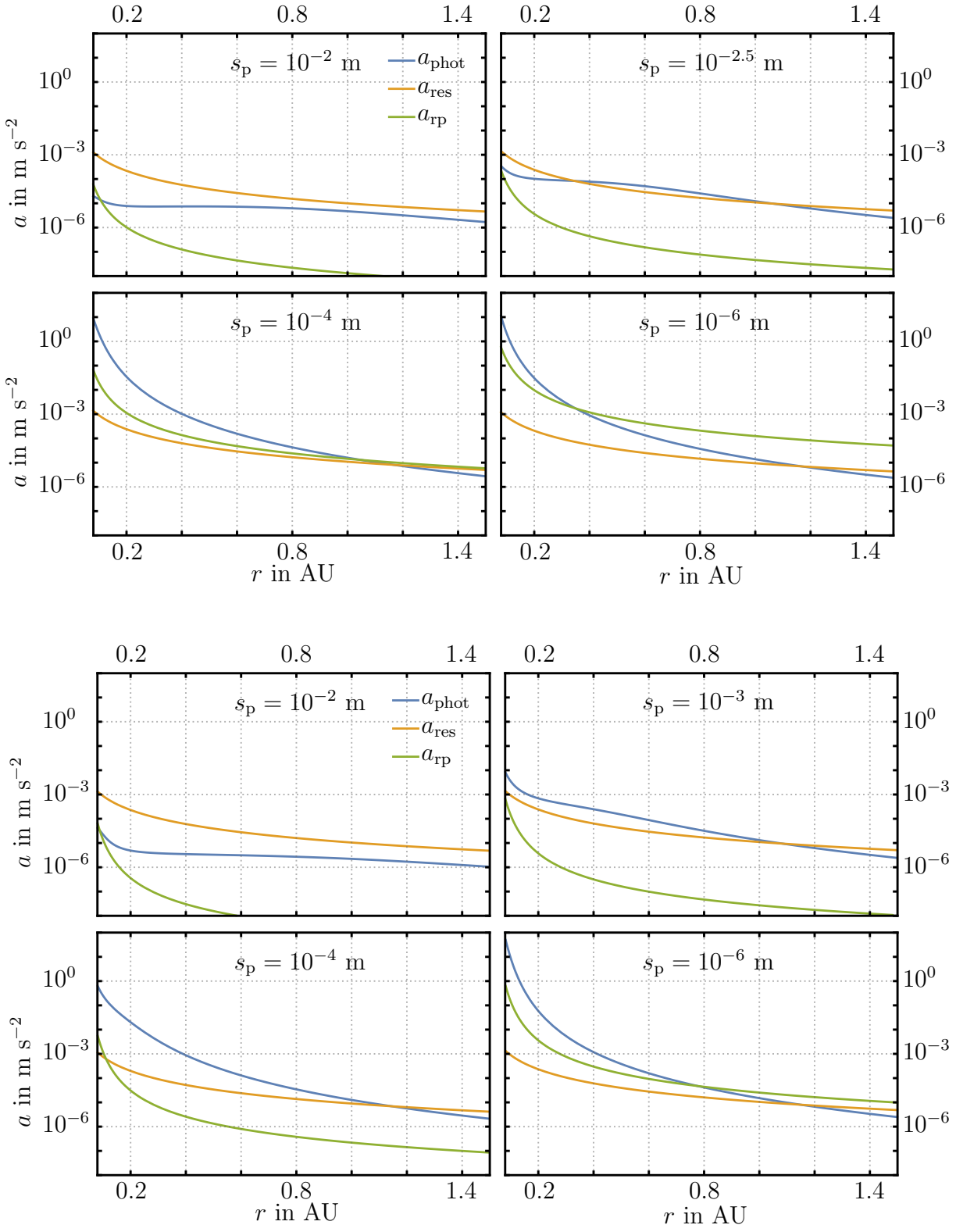

Figure 5.3: The norm of the accelerations of differently sized particles in the disk LkCa15 caused by the forces mentioned, Model 1 at the top, Model 2 at the bottom. As shown in the plot, blue denotes acceleration due to photophoresis, green due to radiation pressure and orange due to the residual gravity. Partially from (Husmann et al., 2016).

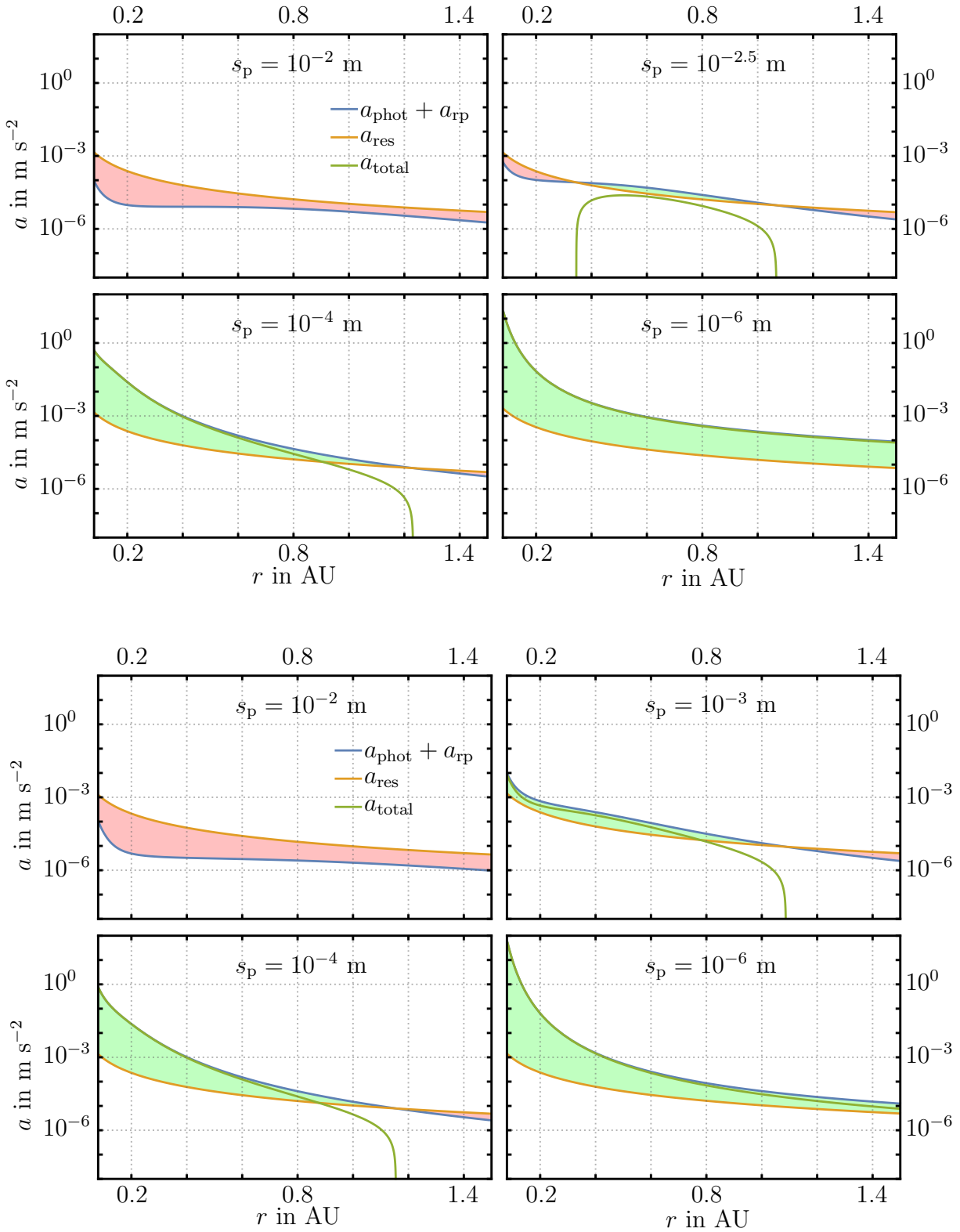

Figure 5.4: Comparison of acceleration directed outwards due to photophoresis and radiation pressure $a_{rp} + a_{phot}$ (blue) with the residual acceleration a_{res} (orange) of differently sized particles in the disk LkCa15, Model 1 at the top, Model 2 at the bottom. The total acceleration in radial direction a_{total} is plotted with a green line. Red filling between a_{radial} and a_{res} denotes a total acceleration directed inwards, green filling a total acceleration directed outwards. Partially from (Husmann et al., 2016).

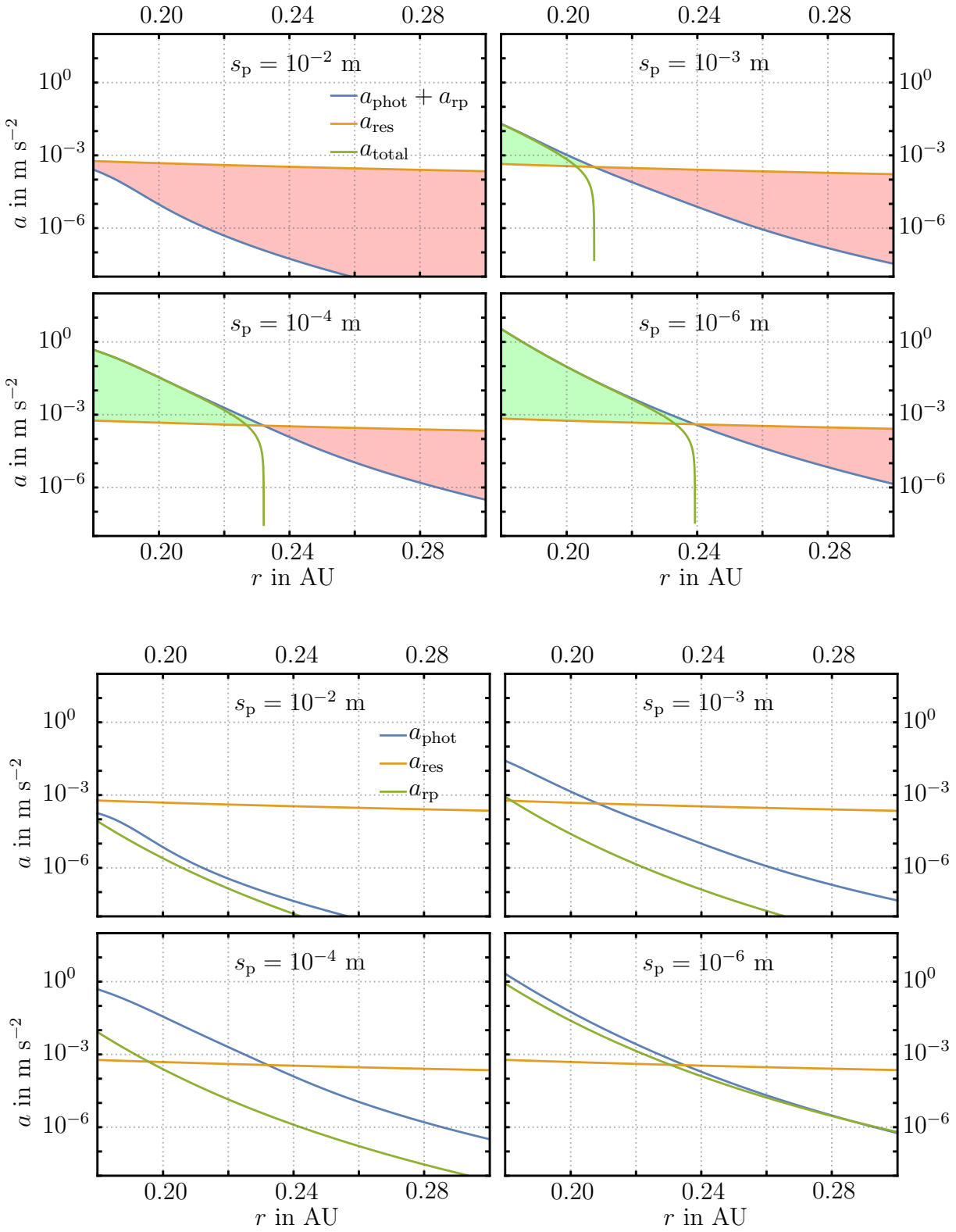

Figure 5.5: Forces in the disk HD135344B. Top: comparison of the accelerations due to photophoresis and radiation pressure a_{radial} (blue) to the residual acceleration a_{res} (orange) of differently sized particles. Bottom: norm of the accelerations in radial direction of differently sized particles, due photophoresis in blue, radiation pressure in green and the residual gravity in orange.

Using the cubic polynomial theorem (trigonometric/hyperbolic solutions), the three solutions $v_{\phi,\mathrm{k}}$, $k \in \{-1, 0, 1\}$ can be computed analytically by a case by case analysis.

$$\text{CASE I} : b > 0$$

$$v_{\phi,\mathrm{k}} = -2\sqrt{b}\sinh\left(\frac{1}{3}\left(2\pi ki + \sinh^{-1}\left(\frac{c}{\sqrt{b^3}}\right)\right)\right) \tag{5.5a}$$

$$\text{CASE II} : -c^{2/3} < b < 0$$

$$v_{\phi,\mathrm{k}} = -2\sqrt{-b}\cosh\left(\frac{1}{3}\left(2\pi ki + \cosh^{-1}\left(\frac{c}{\sqrt{-b^3}}\right)\right)\right) \tag{5.5b}$$

$$\text{CASE III} : b < -c^{2/3}$$

$$v_{\phi,\mathrm{k}} = -2\sqrt{-b}\cos\left(\frac{1}{3}\left(2\pi k + \cos^{-1}\left(\frac{c}{\sqrt{-b^3}}\right)\right)\right) \tag{5.5c}$$

Up to all three roots can be real solutions to the problem (trigonometric solution). According to the physical model of a protoplanetary disk, negative solutions can be excluded, reducing the amount of possible logic solutions to two. One is much lower than the orbital velocity of the gas $v_{\phi,\mathrm{gas}}$ and one is of the same order of $v_{\phi,\mathrm{gas}}$ leaving this as only possible solution. The latter results from the physical expectation that small τ_{fric} lead to quick coupling of the motion of dust to the one of the gas.
Using tab. 5.1, a profile of particle motion can be created showing the drift velocity depending on the distance to the central star r and the particle size s. In fig. 5.6 this plot is shown for the disk LkCa15 (Model 1 and Model 2), in fig. 5.7 the one for the disk HD135344B is depicted.

Solving the equations of motion (eq. 2.45) numerically, the drift timescales can be computed. In fig. 5.8 the particle drift over time is shown for particles starting at the sublimation radius r_{sub} in the disk LkCa15 Model 1 and in the disk HD135344B.

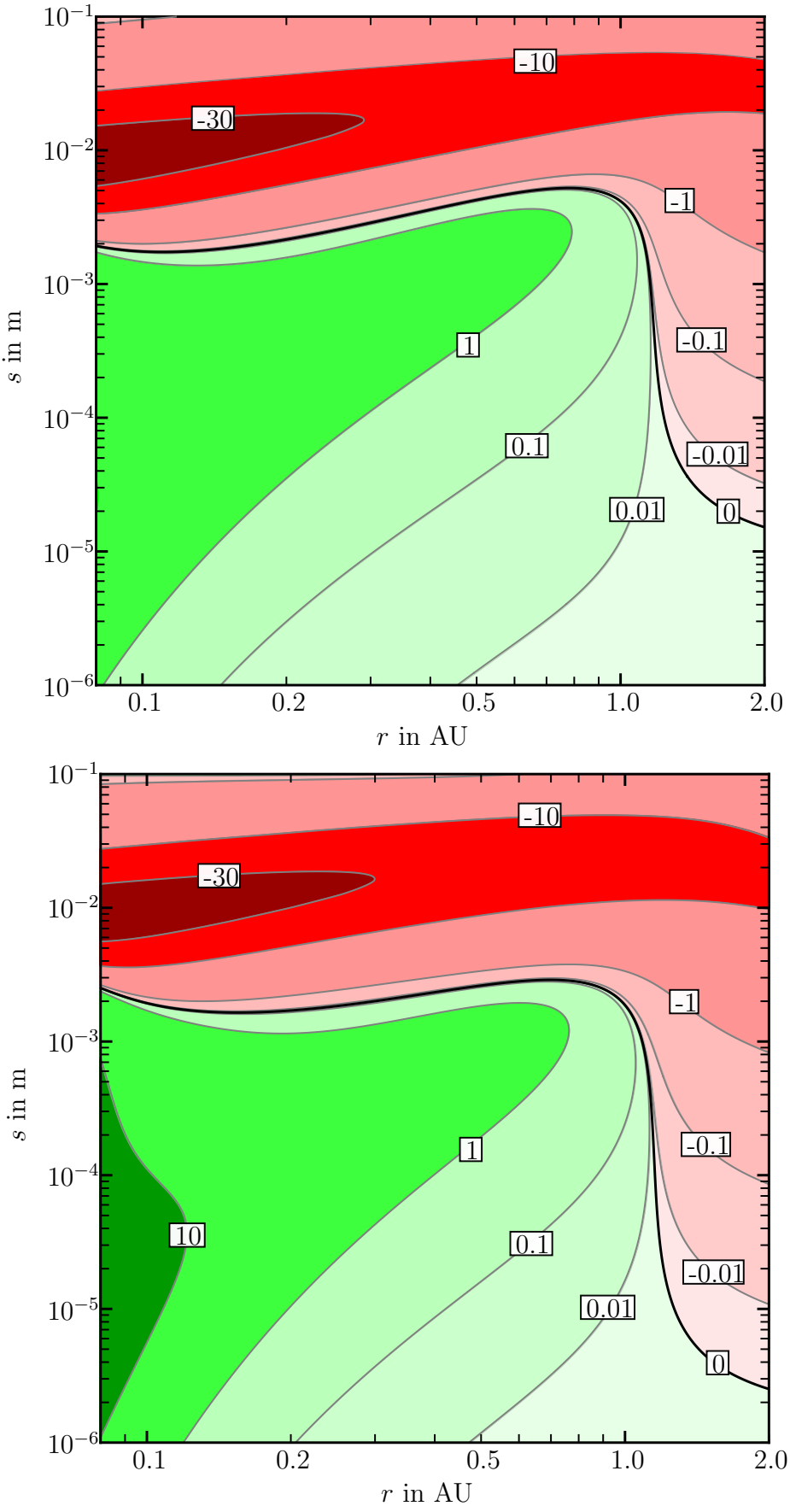

Figure 5.6: Drift velocities in m/s depending on the particle size s and the distance to the central star r for the disk LkCa15 (Model 1 top, Model 2 bottom). Red denotes inwards directed drift (towards the star), green vice versa. The black line (zero-velocity line) denotes $v_{\mathrm{r}}(s, r) = 0$. Its function is uniquely defined in the disk LkCa15.

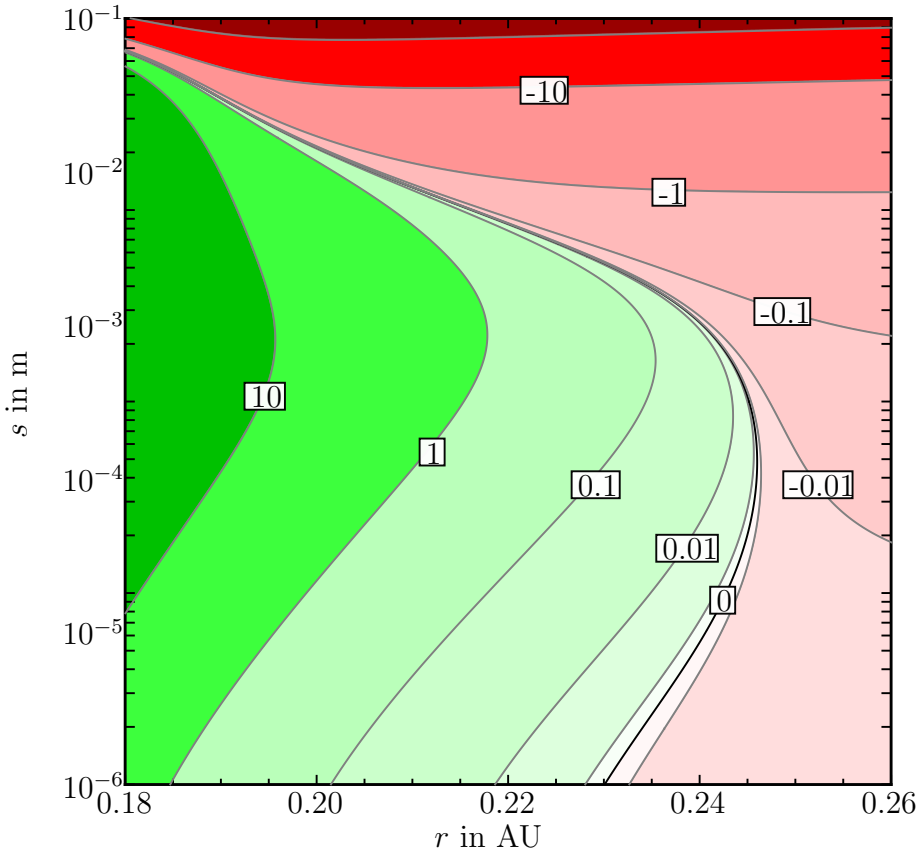

Figure 5.7: Drift velocities in m/s depending on the particle size s and the distance to the central star r for the disk HD135344B. Red denotes inwards directed drift (towards the star), green vice versa. The black line (zero-velocity line) denotes $v_{\mathrm{r}}(s, r) = 0$. In contrast to the disk LkCa15, its function is not defined uniquely over the full interval.

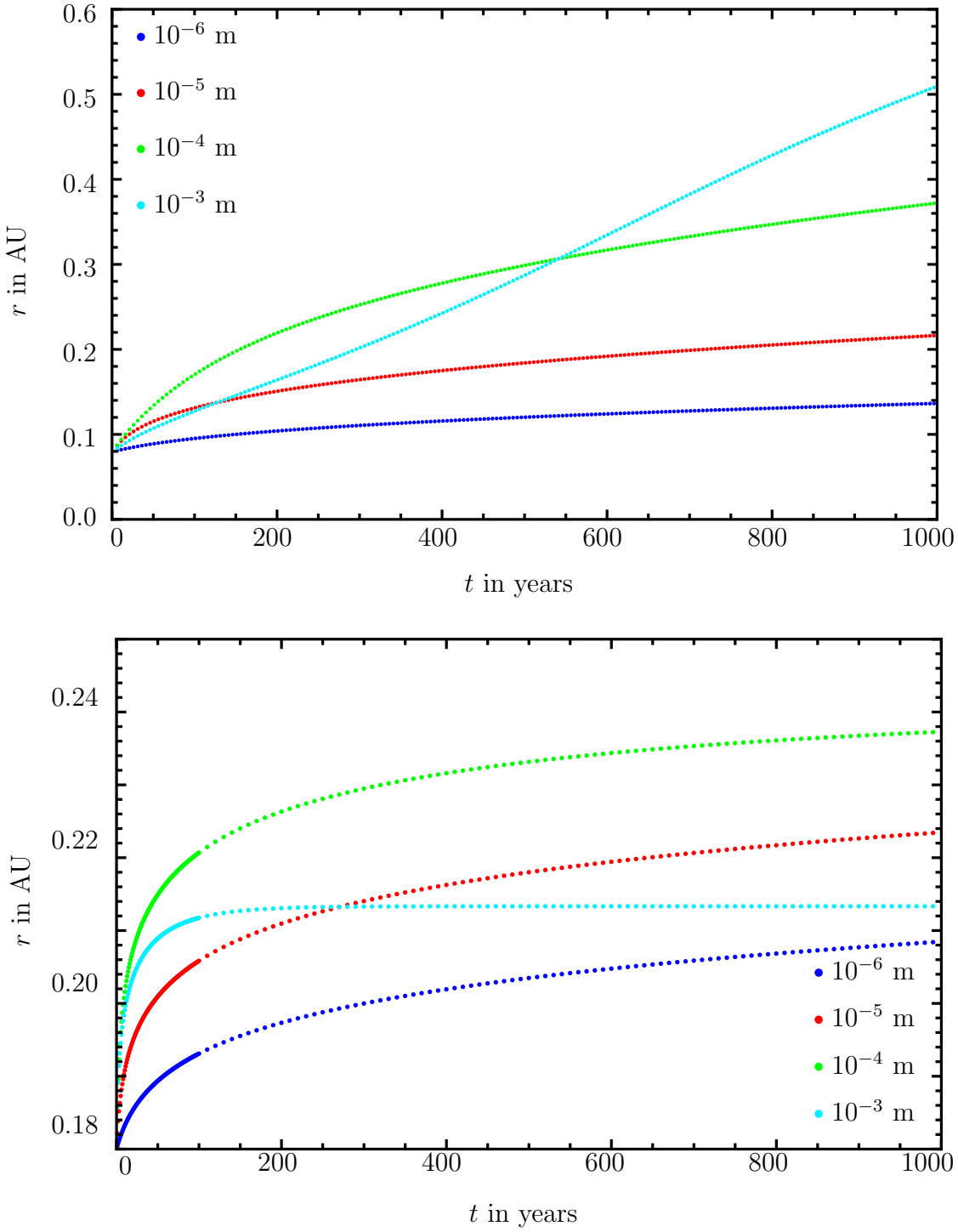

Figure 5.8: Particle drift over time. Top: LkCa15, Model 1. Bottom: HD135344B. The solution was found by solving eq. 2.45 numerically.

5.3 Implications on the disk: self-sustained recycling mechanism

As shown in the previous section, especially fig. 5.6 and fig. 5.7, particles tend to drift outwards until they reach their "stability point" (except for very small particles in the disk LkCa15). At this point the particles are in a stable state of equilibrium at a distance r to the star. This implies a radial drift velocity of zero. Simultaneously, any excursion in radial direction leads to a restoring momentum pointing towards the stability point. Anyhow, the particles do not oscillate on macroscopic scales due to overdamping (τ_{fric} small). The stability point is linked to the gap opening radius r_{gap} and equals the values given by van der Marel et al. (2015). Therefore, the dust cannot leave the inner disk and drift outwards into the gap. As published by Husmann et al. (2016), the following mechanism for a self-sustained recycling procedure is presented:

- starting at the sublimation radius r_{sub}, particles drift outwards due to radiation pressure and photophoresis
- while drifting outwards, the larger particles overtake the smaller ones and can grow in collisions due to mass transfer
- once they reach their stability point, the larger particles grow even further and follow the "zero-velocity" line as depicted in fig. 5.6 and fig. 5.7
- while drifting inwards, the particles grow further until they collide with equally sized particles near the sublimation radius. This results in smaller particles being produced and the whole procedure starts again

A scheme on this proposed recycling mechanism in the inner dust disk is shown in fig. 5.9.
As discussed later, one has to distinguish between both disk types since the inwards drift of large particles differ. While in the disk LkCa15 the size-dependent drift velocity shows a turning point at approximately 1 AU with a maximum particle size for which the drift is still directed outwards, in the disk HD135344B it is vice versa with a bump at a particle size of about 5×10^{-5} m. Therefore, particles in the disk LkCa15 have a significant inwards directed drift once they reach a certain size and overcome the turning point. Particles in the disk HD135344B only drift inwards when they simultaneously grow.

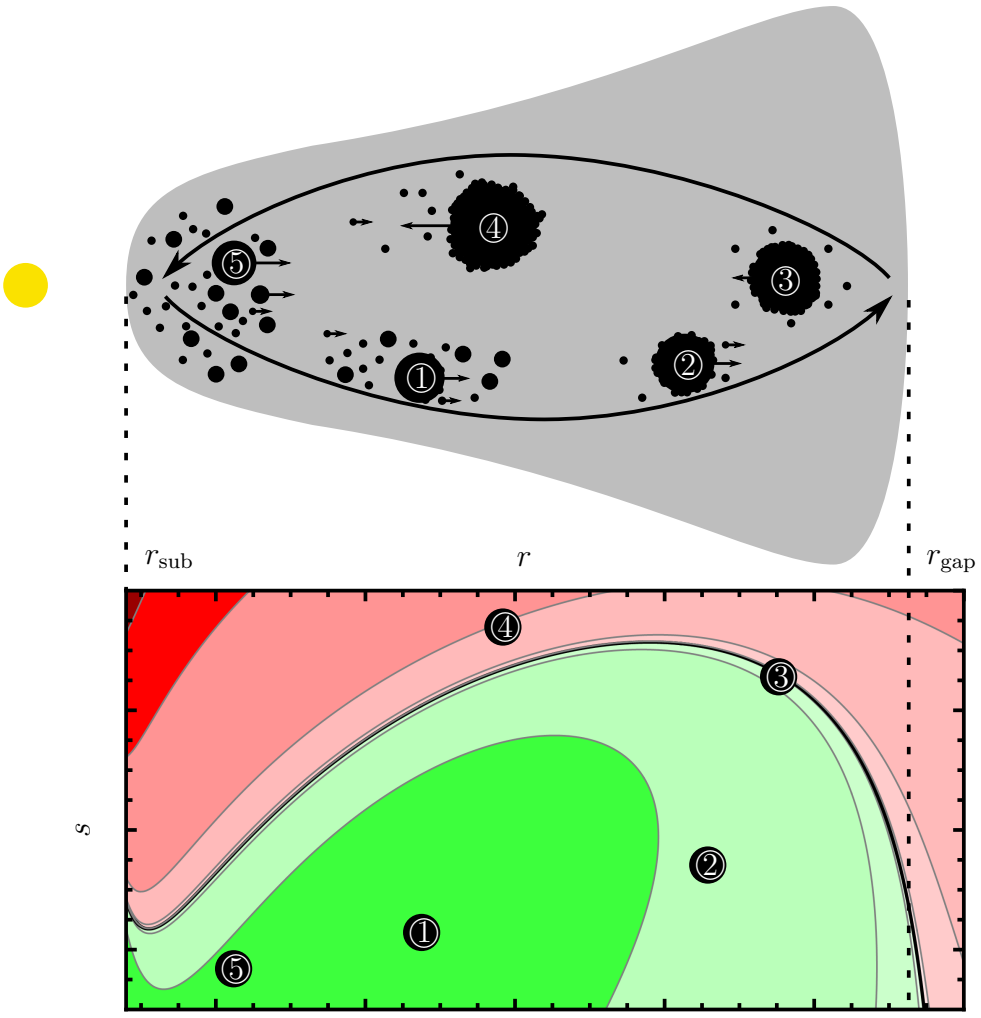

Figure 5.9: Scheme of the proposed recycling mechanism (top) with corresponding drift velocities (bottom, red denotes drift towards the star, red *vice versa*). Inside the disk, small particles drift outwards (1). During the drift, they grow in collisions with smaller particles via mass transfer (2). Once they reach a critical size, the drift direction switches and an inwards directed motion sets in (3). While drifting inwards, the particles grow even further (4) until they eventually get destroyed in collisions with (more or less) equally sized particles (5) and the process starts again.

To prove the viability of this model, several aspects have to be investigated:

- what is the overall growth behaviour of large particles while drifting outwards?
- once they reach their stability point, what are the time scales at which they overcome the turning point (only in the disk LkCa15) and how long does it take to drift inwards again?
- do the particles get destroyed further inwards?

To cope with these questions, the following considerations and calculations have to be taken into account:

- calculating collision velocities for different distances to the star and different particle sizes according to sec. 2.5.2
- calculating the collisional outcome for different distances to the star and different particle sizes according to sec. 3.1
- estimating collision probabilities.

In the following section an investigation using a single particle evolution simulation is presented to validate the model including above mentioned aspects and the calculated drift velocities.

5.4 Single particle evolution - Simulation settings

The question to deal with, resulting from the previous section, is if particles follow the denoted growth/destruction path in the different disks. Therefore, the collision velocities and the collisional outcome for different distances to the star and different particle sizes are calculated, followed by the simulation description.

5.4.1 Collision velocities and collisional outcome

The collision velocities for different sized particles can be calculated for every distance r to the central star by using eq. 2.52a for the relative radial component, eq. 2.52b for the relative azimuthal component, the solutions for the relative turbulent velocities (see sec. 2.5.2), and eq. 2.56 for the relative velocity due to Brownian motion of gas particles. The different components influencing the total collision velocity at 0.25 AU are exemplarily plotted in fig. 5.10 for the disk LkCa15, Model 1. The resulting total collision velocities Δv for the disk LkCa15 Model 1 and HD135344B at different distances to the central star are plotted in fig. 5.11 and fig. 5.12. Plots showing the collision velocities for the disk model 2 LkCa15 as well as additional ones for the disk HD135344B may be found in the appendix, fig. A.1 to A.6.

As shown in fig. 5.10, the influence of Brownian motion on the collision velocities is negligible since the turbulence parameter is large and therefore turbulent relative motion dominates even for small particles. This leads to collision velocities at 0.25 AU of at least 8×10^{-2} m s^{-1} for similar sized particles of $s_{1,2} = 10^{-6}$ m with a peak velocity of 316 m s^{-1} for different sized particles of $s_1 = 1.84 \times 10^{-2}$ m and $s_2 = 4.63 \times 10^{-4}$ m as shown in fig. 5.11. For 1.0 AU, the minimum collision velocity is 8×10^{-2} m s^{-1} for

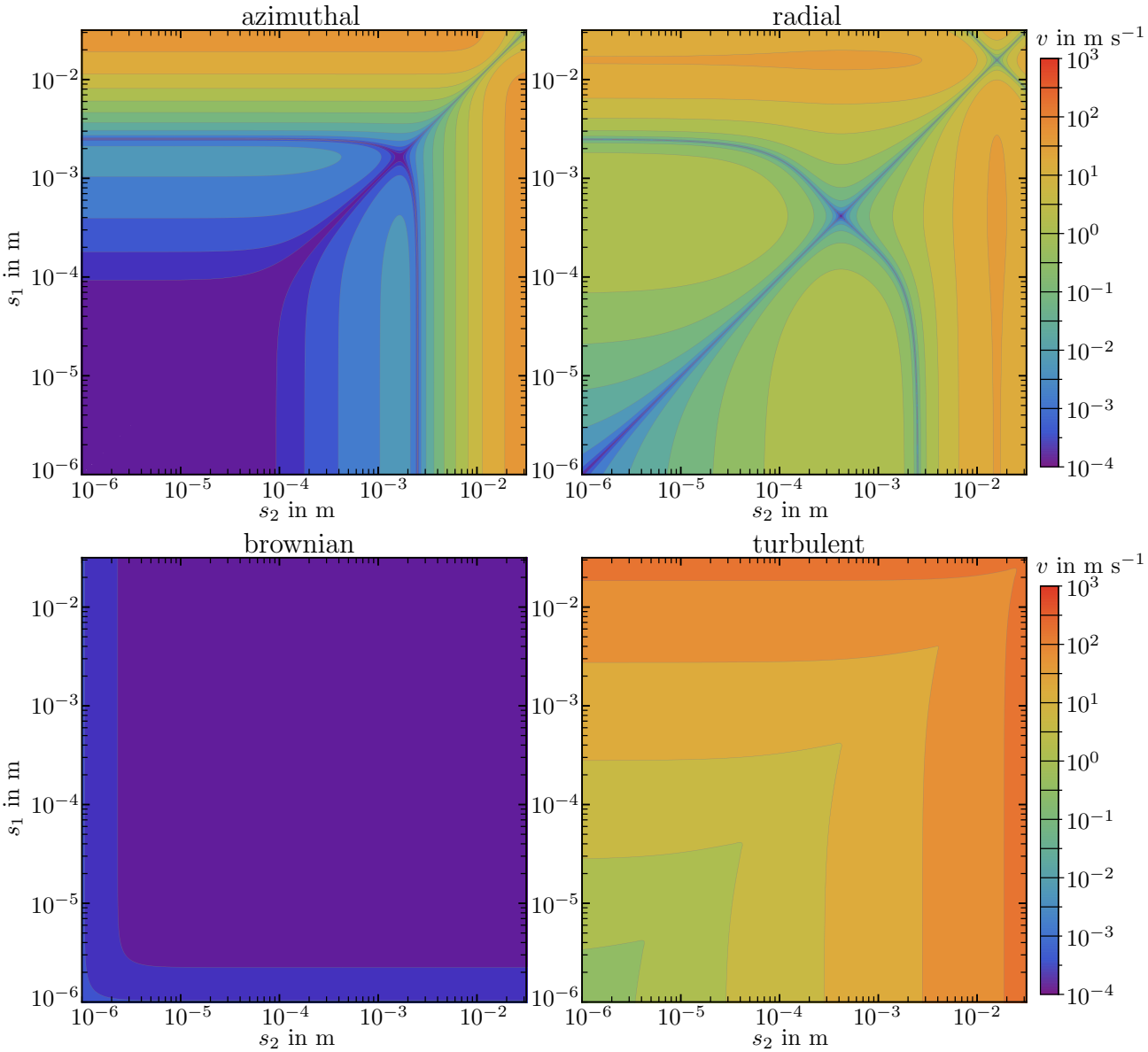

Figure 5.10: Comparison of different sources for the collision velocities in the disk LkCa15 Model 1 for a distance of 0.25 AU to the central star. Top left: relative velocity due to azimuthal motion, top right: due to radial motion, bottom left: due to Brownian motion, bottom right: due to turbulent motion. The contours are in logarithmic intervals with an increase in power of 0.5.

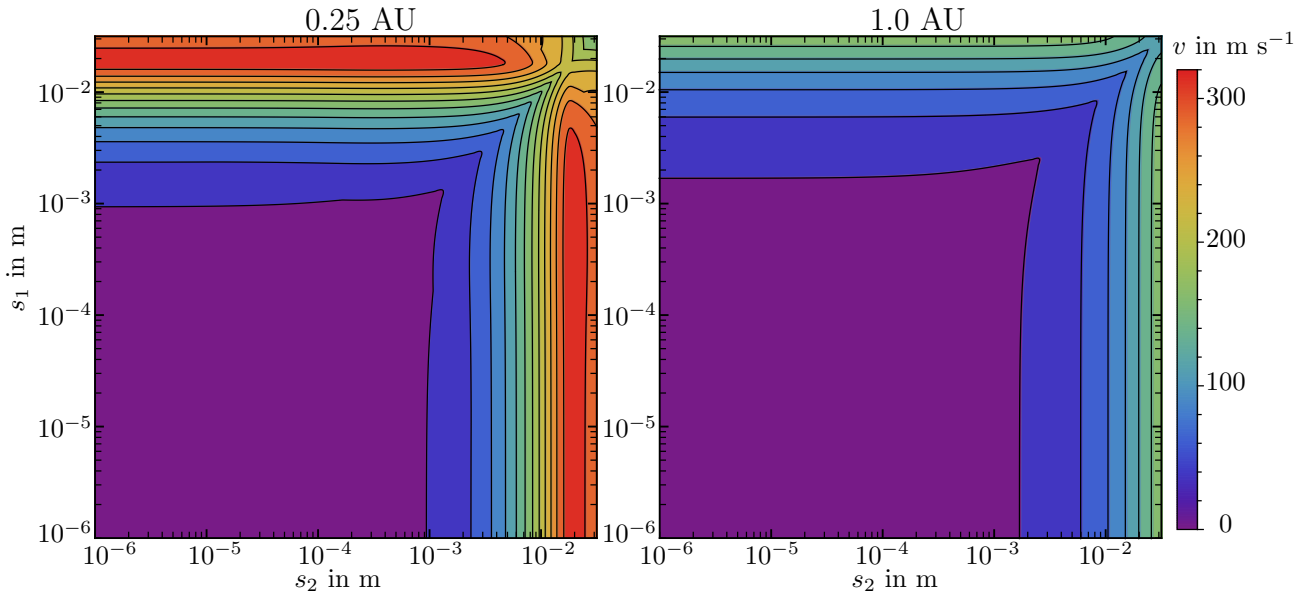

Figure 5.11: Collision velocities in the disk LkCa15 Model 1 for a distance of 0.25 AU (left) and 1.0 AU (right) to the central star. The contours are in intervals of 25 m s^{-1}. The maximum collision velocity can be up to 300 m s^{-1}.

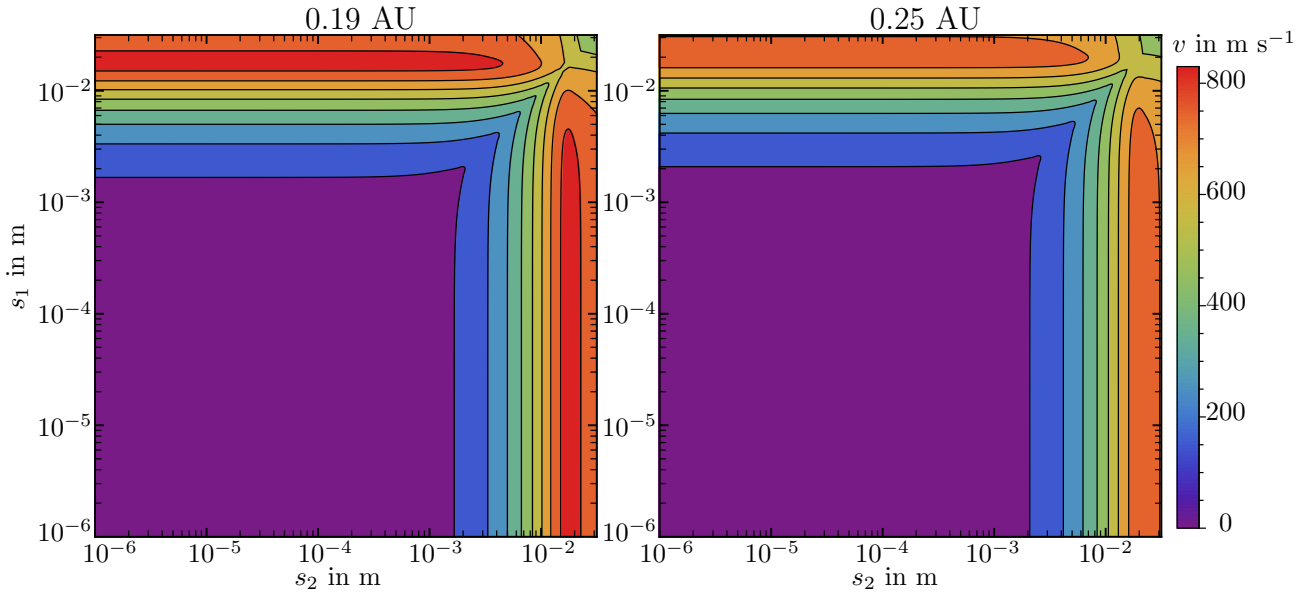

Figure 5.12: Collision velocities in the disk HD135344B for a distance of 0.19 AU (left) and 0.24 AU (right) to the central star. The contours are in intervals of 100 m s^{-1}.

similar sized particles of $s_{1,2} = 10^{-6}$ while the maximum collision velocity (in the given size range) decreases compared to 0.25 AU to 166 m s^{-1} for different sized particles of $s_1 = 3.16 \times 10^{-2}$ m and $s_2 = 10^{-6}$ m. The collision velocities in the disk HD135344B can get significantly higher than in the disk LkCa15 which is caused by higher α_{turb} value as well as by increased pressure which is about 15 times higher.

Using collision velocities stated above, the collisional outcome can be calculated following the model by Windmark et al. (2012a) (see sec. 3.1). The collisional outcome for different sized particles in the disk LkCa15 Model 1 and HD135344B for two distances to the central star are plotted in fig. 5.14 and fig. 5.15. A plot of the disk LkCa15 Model 2 can be seen in the appendix (fig. A.7). In fig. 5.13 the collisional outcome for the disk with included contour lines for the collision velocities are plotted. As shown there, the outcome is not directly linked to the collision velocity though some relations can be seen for example in the bouncing regime (yellow).

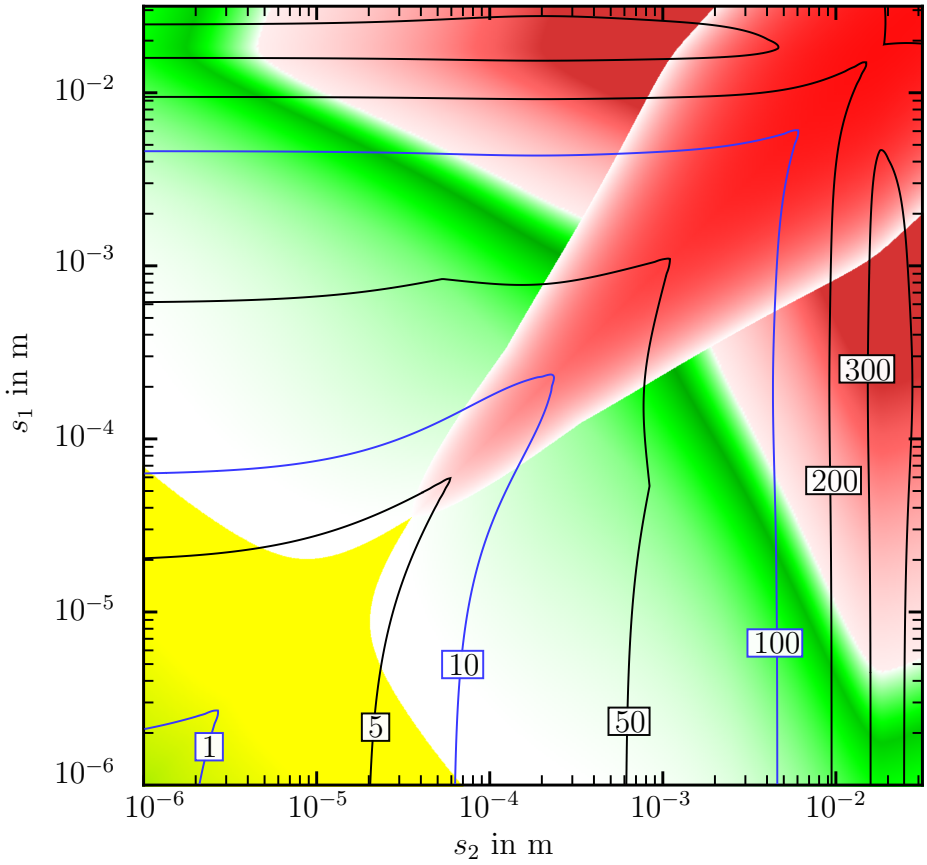

Figure 5.13: Collisional outcome in the disk LkCa15 Model 2 for a distance of 0.25 AU to the central star. Starting from the bottom left: low velocity collision of small particles lead to hit & stick (green). With increasing size, the collision velocities increase as well (see fig. 5.11) and transition into the bouncing regime occurs (yellow). Distinguishing between (nearly) equally sized collision partners and differently sized ones, either partial fragmentation takes place (with either net mass gain of the larger body or net mass loss) or complete fragmentation (both bodies) occurs. The strength of mass transfer is colour-coded from 0 m_p (white) to 0.16 m_p (dark green), erosion is colour-coded from 0 m_p (white) to 4 m_p (dark red) and the fragmentation strength μ_frag (see eq. 3.8) is colour-coded from 1.0 (white) to 0.05 (red). Here, m_p is always the mass of the smaller collision partner. The pure sticking regime is not visible in this plot. The contour lines denote the collision velocities. A more detailed view of the collision velocities in LkCa15 Model 1 as well as the collisional outcome for 1.0 AU are depicted in the appendix, fig. A.6 and A.3 respectively.

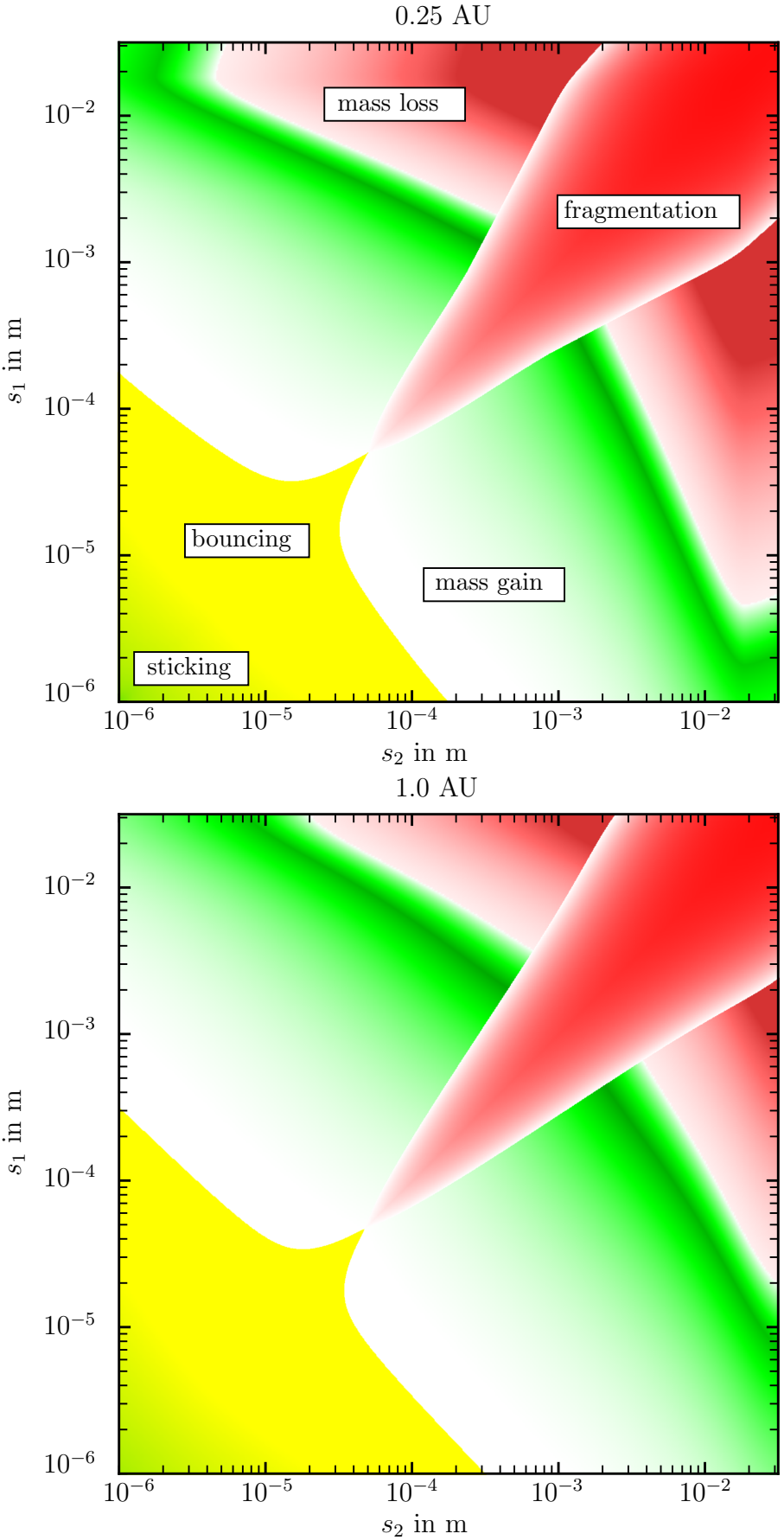

Figure 5.14: Collisional outcome in the disk LkCa15 Model 1 for a distance of 0.25 AU (top) and 1.0 AU (bottom) to the central star. See fig. 5.13 for an explanation of the colour codings.

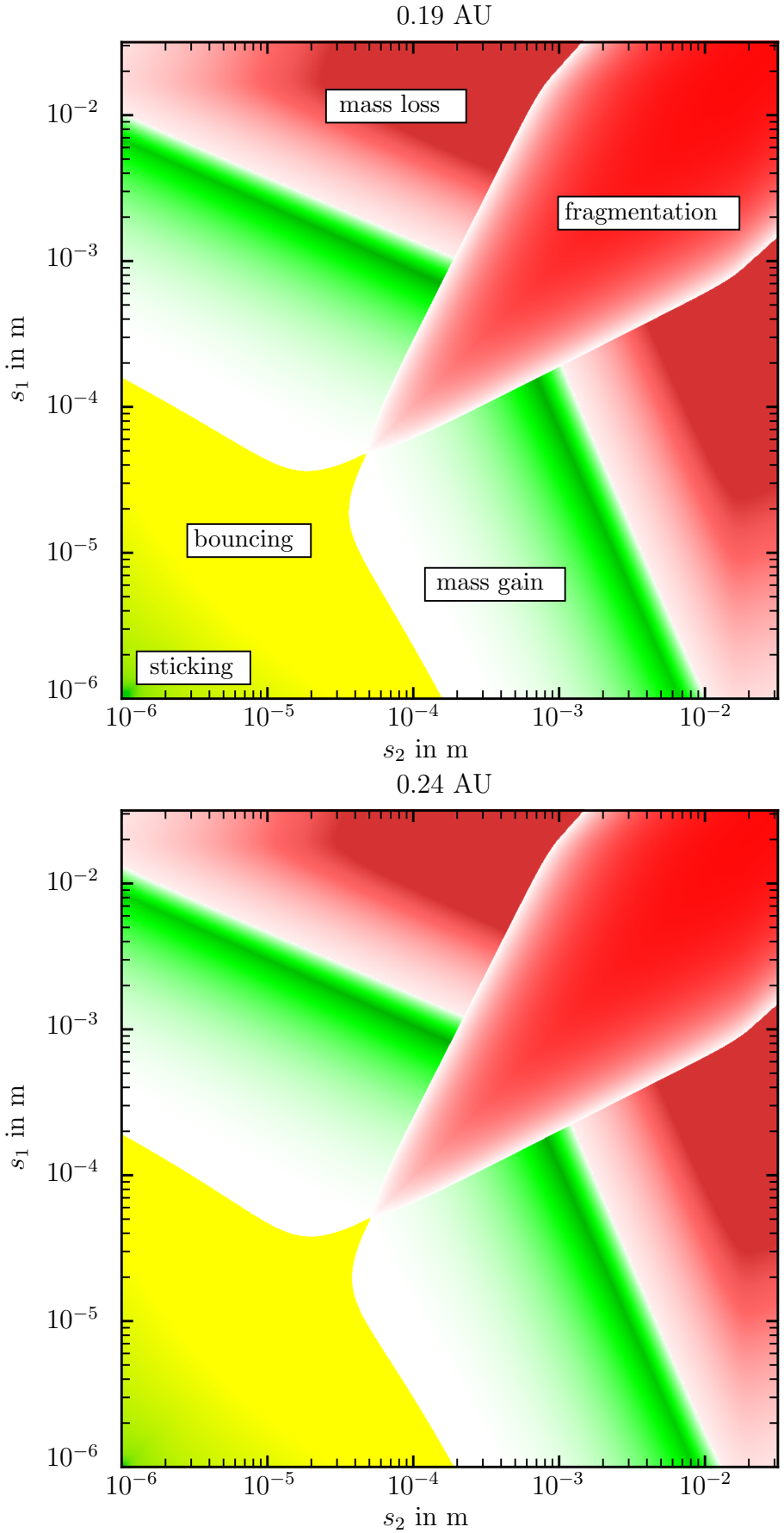

Figure 5.15: Collisional outcome in the disk HD135344B for a distance of 0.19 AU (top) and 0.24 AU (bottom) to the central star. See fig. 5.13 for an explanation of the colour codings.

Several conclusions can be drawn according to the collisional outcome plots:

- First of all, the minimum particle size existing in the disks can be assumed to be $\sim 10^{-6}$ m. This results from the transition between the hit & stick and the bouncing regime. In fig. 5.16 the sticking probability for equally sized particles in the disk LkCa15 Model 2 at 0.25 AU is plotted and fig. 5.17 shows the sticking probability for a 10^{-6} m large particle with particles of different sizes. Assuming reproduction of small particles due to collisions where at least one partner is destroyed, the maximum possible particle size due to growth of monomers is 9×10^{-6} m for the disk LkCa15 Model 2. Since growth to this maximum size needs lots of collisions and therefore time, a limit was set to a sticking probability equalling the inverse of the Euler Number e^{-1}. In the case of LkCa15 Model 2, the resulting size is slightly below 10^{-6} m. For simplicity reasons, the value was therefore put to 10^{-6} m which is simultaneously assumed to be the smallest particle size in the disks.

- Secondly, collisions of equally sized particles result in either sticking, bouncing or critical fragmentation. Furthermore (as shown in later sections) for a given particle size, the vertical dimension of the fragmentation regime determines how quickly larger particles can be destroyed: the higher the collision velocity, the more often collisions of differently sized particles result in fragmentation.

- Thirdly, collisions differently sized particles lead either to sticking, bouncing or mass gain/loss due to partial fragmentation. Small particles ($s < 2 \times 10^{-5}$ m) cannot grow in collisions unless they get swept up by larger ones. Even when crossing this value, growth is still very limited. For example: a 2×10^{-5} m sized particle can only grow in collisions with particles of 2×10^{-5} m or smaller, but not smaller than 3×10^{-6}. Therefore these particles exist very long unless – as mentioned – they are swept up by larger particles being partially destroyed. On the other hand, particles which are already large can grow more efficiently in collisions with small partners. For example, a 10^{-2} m sized target body colliding with impactors smaller than 10^{-5} m can grow with mass transfer coefficients ϵ_{mt} of up to 0.16. On the other hand, they might loose mass more easily. This is caused by collisions with impactors larger than 10^{-5} m who erode the target efficiently or even lead to fragmentation.

It is therefore not directly visible from the collisional outcome plot If particles grow over time, loose mass or even get fragmented.

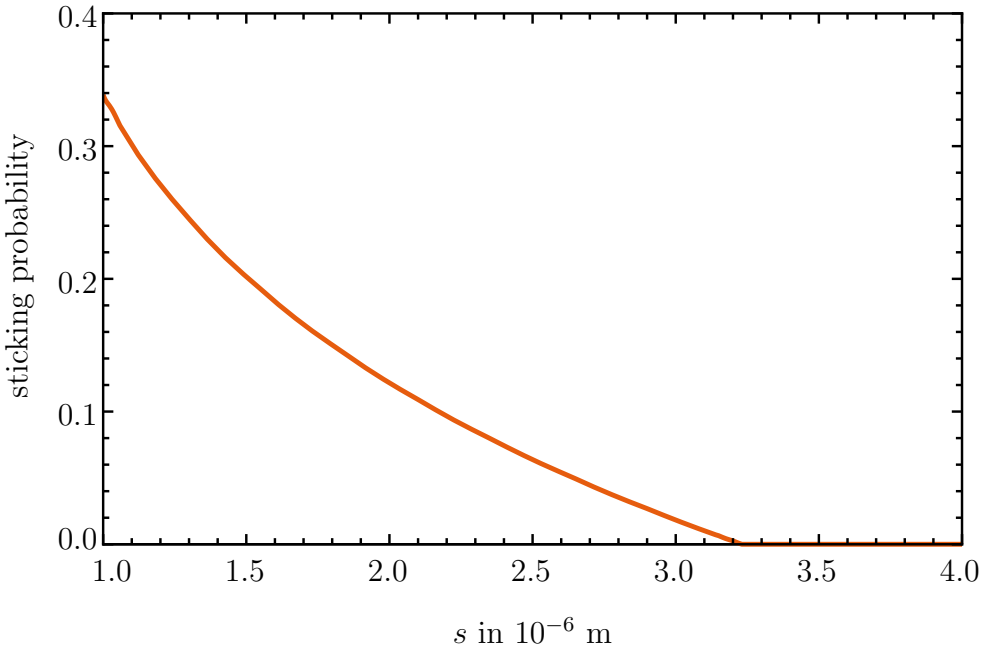

Figure 5.16: Sticking probability for equally sized particles in the disk LkCa15 Model 2 for a distance of 0.25 AU to the central star.

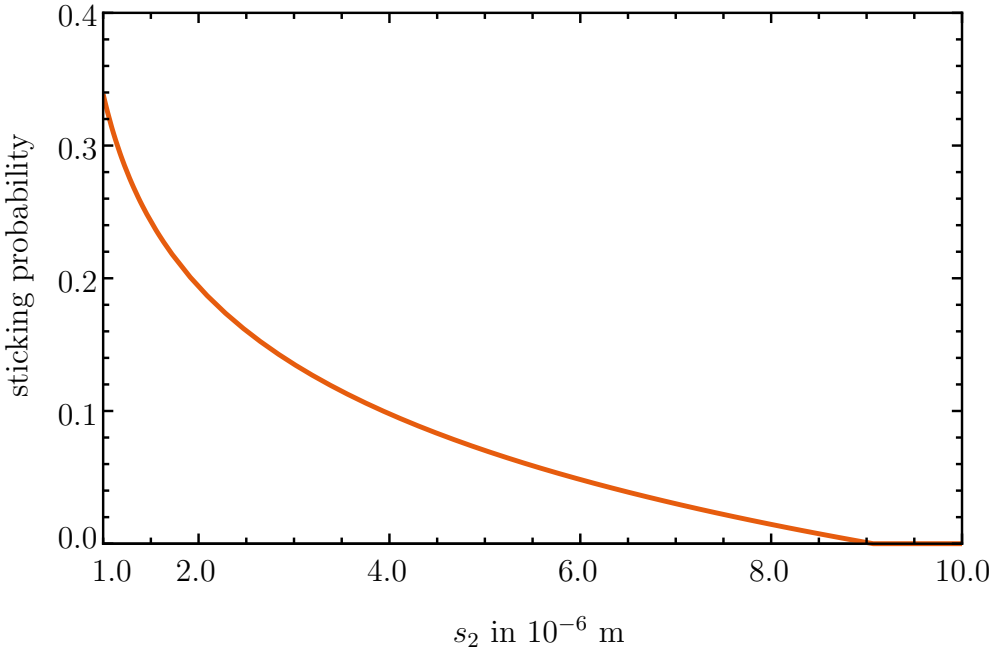

Figure 5.17: Sticking probability for a 10^{-6} m particle with particles of different sizes s_2 in the disk LkCa15 Model 2 for a distance of 0.25 AU to the central star.

Several model boundaries and issues can be concluded from the collisional outcome plots: The two transitions on the one hand between the regimes bouncing and mass gain/fragmentation and on the other hand between the regimes mass gain/mass loss and fragmentation are sharp. As mentioned in chapter 3, the collisional outcome models are always approximations and simplifications assuming idealised collision partners leading to a specific outcome for given particle sizes and collision velocities. Even using just one specific collision velocity is somewhat simplified when taking into account that the collision velocity due to turbulence and Brownian motion follows a statistical distribution. Windmark et al. (2012b) showed that this velocity distribution influence significantly the dust evolution in a protoplanetary disk. Nonetheless, for the mechanism and simulations proposed in sec. 5.3, the model is sufficient since only the evolution of single particles will be simulated.

5.4.2 Collision probabilities

The amount of collisions per time interval between two particles with sizes s_1 and s_2 can be derived via (note here that $p_{\mathrm{col},1\to2} \neq p_{\mathrm{col},2\to1}$)

$$p_{\mathrm{col},1\to2} = N_2 \cdot \Delta v_{1,2} \cdot \sigma_{s_1,s_2} \quad , \tag{5.6}$$

where N_2 is the Number Density of particles of size s_2, $\Delta v_{1,2}$ is the relative velocity (see previous section) and σ_{s_1,s_2} is the collisional cross-section which is

$$\sigma_{s_1,s_2} = \pi \left(s_1 + s_2\right)^2 \quad . \tag{5.7}$$

The latter follows from the maximum lateral distance two particles of size s_1 and s_2 can have while still hitting each other. Note here that the collision probability does not represent the amount of collision between two particles with sizes s_1 and s_2 but is the probability that the observed particle s_1 hits a particle of size s_2. Moreover, the equation stated above results from the mean-field approach for the change of the amount of particles over time given by von Smoluchowski (1916). As can be concluded from that, the amount of collisions of two particles with sizes s_1 and s_2 per second and per volume ($\#_{\mathrm{col}}$ s^{-1} m^{-3}) can be computed via

$$\frac{\#_{\mathrm{col}}}{\mathrm{s} \cdot \mathrm{m}^3} = N_1 \, N_2 \, \Delta v_{1,2} \sigma_{s_1,s_2} \quad . \tag{5.8}$$

Note here that strictly speaking $p_{\mathrm{col},1\to2}$ describes a probability density since $N_2 \to 0$ for an infinite small size interval. Therefore the calculations have been carried out with finite size intervals set to 30 bins per size decade.

5.4.3 Additional disk and simulation parameters

For the calculation of a single particle evolution using the collision probabilities (eq. 5.6), the collision velocities and the collisional outcome (sec. 5.4.1) more parameters have to be determined. First of all, the dust distribution used in the disk (see eq. 4.5) has to be described in detail. Using a number density depending on the particle size s_i it is

$$N_i = N_0 \cdot s_i^{-\kappa_{\text{size}}} \quad , \tag{5.9}$$

where N_0 is a normalising constant in such way that $\int N_i \, \mathrm{d}m_i = \rho_{\text{dust}}$. The exponent κ_{size} is assumed to be constant in the disk HD135344B since the inner dust disk is small and – as shown later – particles do not necessarily drift the whole inner disk. For the disk LkCa15 (both models) κ_{size} is assumed to be dependent on the distance to the central star. This results from the fact that the outwards directed drift of small particles depends on the distance to the central star: the further away, the lower the drift velocity. Taking this into account, small particles will be concentrated further outwards leading to an increased slope in the size distribution.
Other parameters are the maximum and minimum particle size. While in the disk LkCa15 the minimum particle size is always assumed to be 10^{-6} m and the maximum particle size is 10^{-2}, in the disk HD135344B the minimum and maximum particle size has to be determined dynamically according to the particle drift profile as shown in fig. 5.7.
With a given particle of size s_1, the change in mass ΔM can be calculated via

$$\Delta M(s_1, r, \Delta t) = \int_{s_{\min}}^{s_{\max}} \Delta t \, p_{\text{col}}(s_1, s_2, r) \, \Delta m(s_1, s_2, r) \, \mathrm{d}s_2 \quad . \tag{5.10}$$

Within this equation, $\Delta m(s_1, s_2, r)$ is the mean mass change of particle 1 due to collisions with particles of size s_2 at a given distance to the central star r which is given by the collisional outcome model. $\Delta t \, p_{\text{col}}(s_1, s_2, r)$ describes the amount of collisions in a given time interval Δt of two particles at a given distance to the central star r. As likewise mentioned above, this equation is a simplification from the coagulation equation given by von Smoluchowski (1916). The additional disk parameters necessary for the simulations are shown in tab. 5.2.

5.4.4 Simulation settings

Using the collision probabilities from eq. 5.6, Monte-Carlo Simulations have been performed for the three disks with different particle sizes and positions. A visualisation of the full parameter set necessary for the calculation of particle evolution in the disk LkCa15 Model 2 at 0.25 AU is displayed in fig. 5.18. Performing single particle evolution

Table 5.2: Simulation/Disk parameters

Disk	$\alpha_{\rm turb}$	$\kappa_{\rm size}$	$s_{\rm min}$ (m)	$s_{\rm max}$ (m)	bins / size decade
LkCa15 Model 1	10^{-2}	$3.1 + \left(2\frac{r-r_{\rm sub}}{\rm AU}\right)^{0.4}$	10^{-6}	10^{-2}	30
LkCa15 Model 2	10^{-2}	$3.1 + \left(2\frac{r-r_{\rm sub}}{\rm AU}\right)^{0.4}$	10^{-6}	10^{-2}	30
HD134355B	10^{-2}	4.0	dyn.	dyn.	30

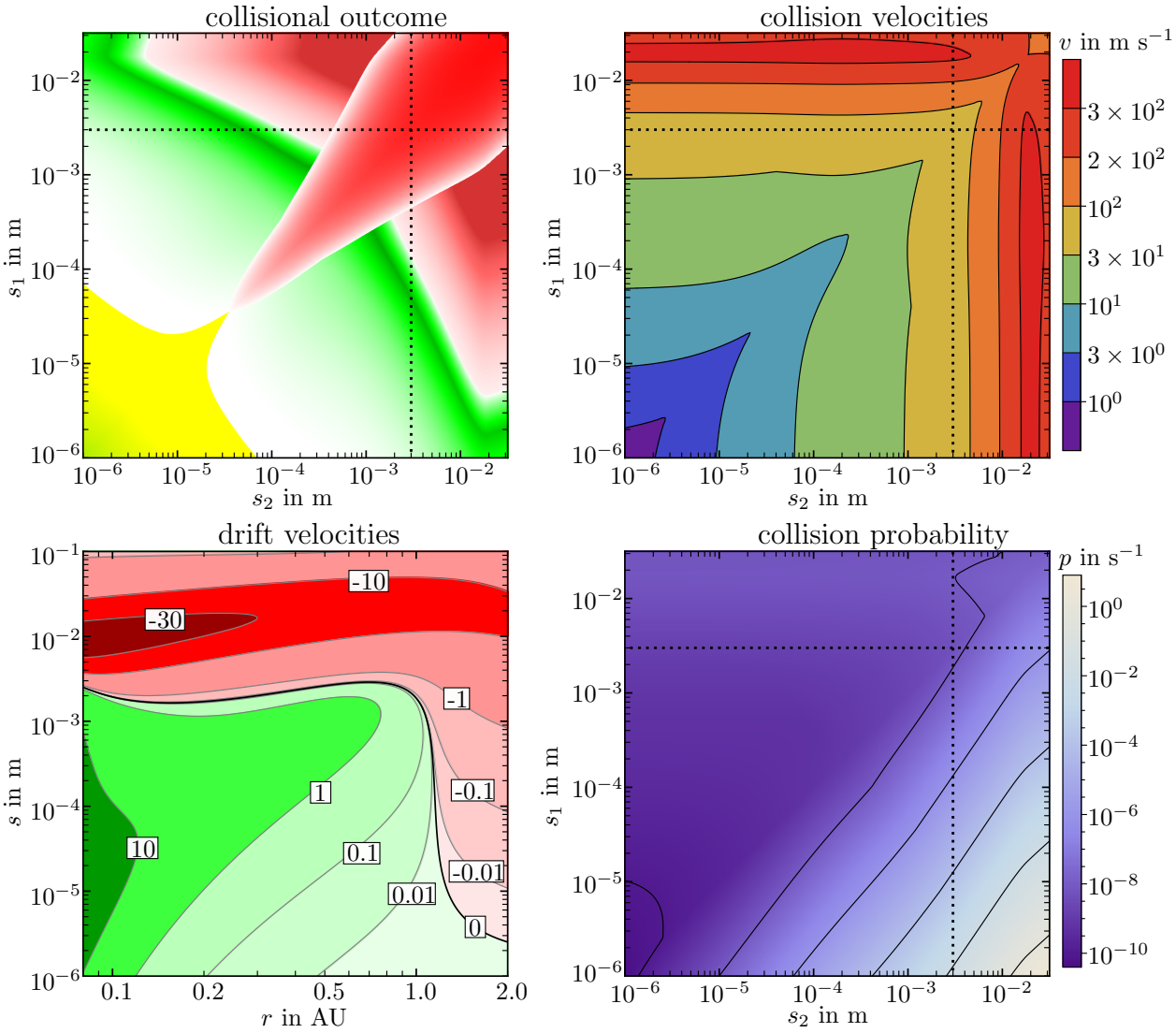

Figure 5.18: Full parameter set for calculation of particle evolution in the disk LkCa15 Model 2 at 0.25 AU. Displayed is the collisional outcome (top left), collision velocity (top right), radial drift velocity (bottom left) and collision probability for particle 1 hitting particle 2 (bottom right). The dotted lines represent the maximum particle size where radial drift can still be directed outwards. The collision probability is not symmetric due to the fact that $p_{\rm col,1\to2} \neq p_{\rm col,2\to1}$.

simulations includes the following steps:

- position the test particle of size s at a distance r to the central star
- calculate the drift for the time interval Δt
- calculate the collision probabilities
- check for fragmentation and if necessary calculate the new particle mass/size (largest fragment)
- calculate the change in mass for all other collisions

Step 2 to 5 are repeated and the evolution is tracked (size $s(t)$ and position $r(t)$).

5.5 Single particle evolution - Results

The simulated particle trajectories in the two-dimensional r – s space are compliant with a disk where a self-sustained recycling process exists. Within this sections the results are presented in detail differencing between the two disk types of LkCa15 and HD135344B.

5.5.1 LkCa15

Model 1 - An example of a particle trajectory in r – s – space is plotted in fig. 5.19 (see caption for details). As can be seen there, a particle with a size of 1.58×10^{-3} m inserted at ~ 1.12 AU grows while following the zero-velocity line until it reaches the "peak" (see fig. 5.21 for a description of the terminology) and starts to drift inwards while leaving the steady state. Although the particle suffers from several destructive events, the time necessary for growth is $\sim 3 \times 10^6$ years.

Model 2 - An example of a possible trajectory in the second disk model is plotted in fig. 5.20 (see caption for details). The time to grow from the initial size to the size at which the inwards drift sets in is about 3×10^5 years while the inwards drift (from 0.8 AU to 0.2 AU) happens quickly in less than 2×10^4 years.

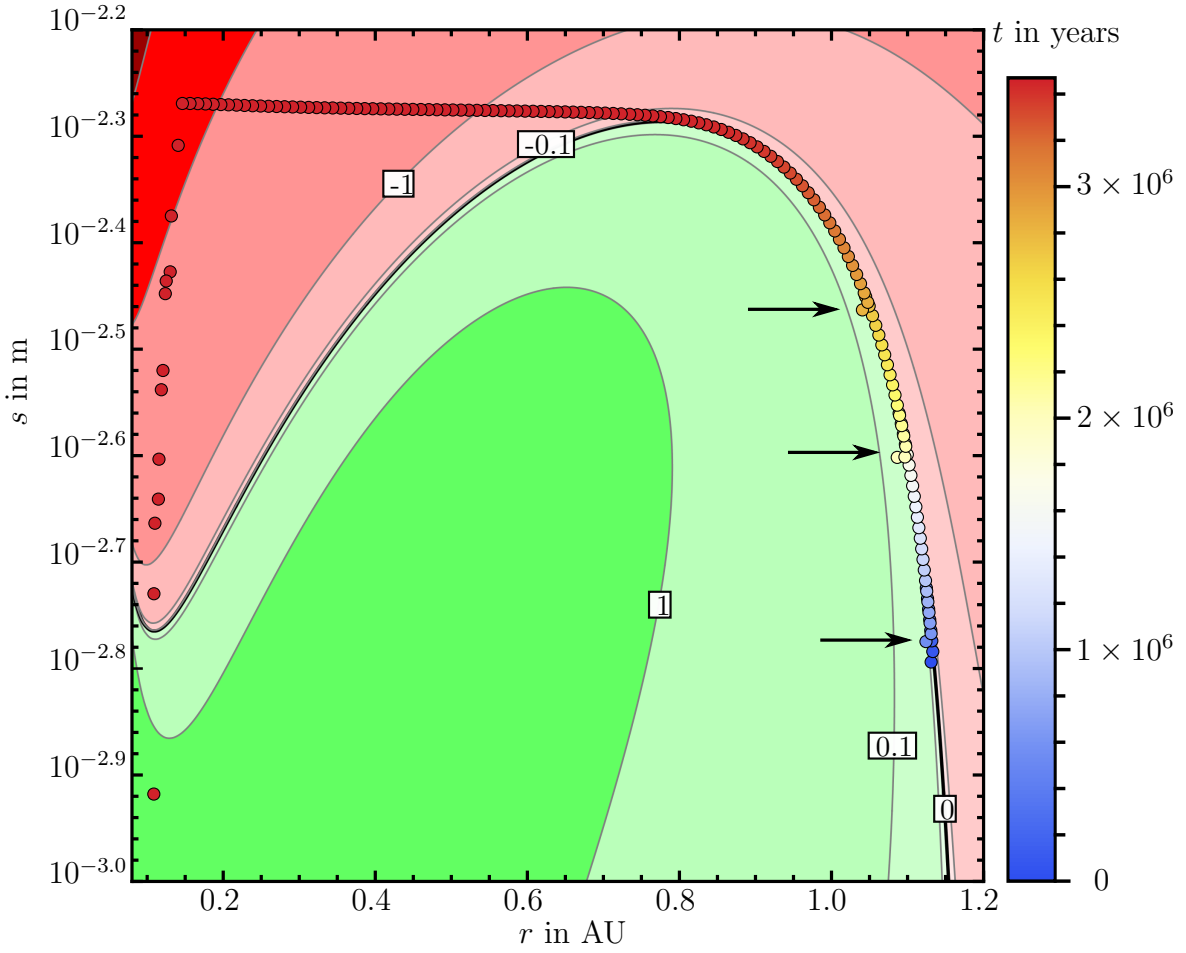

Figure 5.19: Example of a simulated particle in the disk LkCa15 Model 1, inserted at 1.12 AU with a size of 1.58×10^{-3} m. The datapoints are colour coded according to time, the size of the time steps is dynamic. The arrows denote destructive events. The growth of the particle needs about 3×10^6 years, starting from a size of about 1.7×10^{-3} m and growing a factor of 3 to a size of about 5×10^{-3} m. Only merely visible are the delays in the growth due to fragmentation events. For this particle, the delay is negligible compared to the total growth timescale. Once the particle reaches the top of the bump, the inwards drift sets in resulting in a drift of around 0.6 AU in less than 10^{-5} years. Once the particle reaches $\sim$ 0.15 AU, a fragmentation cascade sets in leading to quick destruction of the particle. (Husmann et al., 2016)

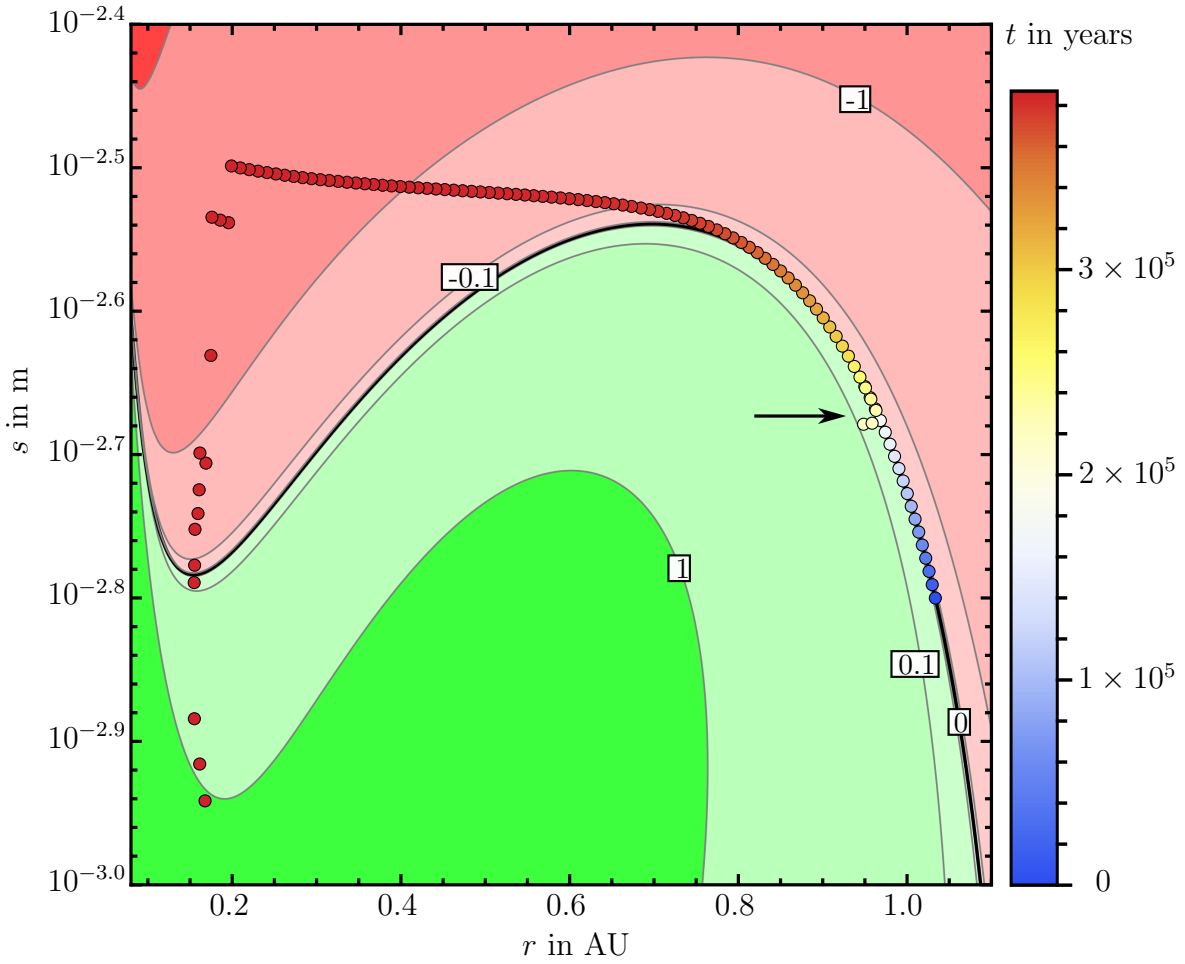

Figure 5.20: Example of a simulated particle in the disk LkCa15 Model 2, inserted at 1.12 AU with a size of 1.58×10^{-3} m. The datapoints are colour coded according to time, the time steps are not fixed. The arrows denote destructive events. The particle grow while simultaneously drifting inwards following the zero-velocity line. When it reaches the peak (see fig. 5.21) the velocity increases and the particle drifts inwards in less than 2×10^4 years. While drifting inwards, the particle still grows until it is fragmented for the first time at ~ 0.2 AU, where it has a size of about 3.2×10^{-3} m. The fragmentation cascade happens in less then 10^3 years. Note that not every simulated point in the particle trajectory is plotted for visibility reasons.(Husmann et al., 2016)

Comparison - Although the trajectories resemble each other in appearance, the growth timescale is significantly smaller for the second model. The latter can be explained by comparing the differences between the maximum particle size for which drift can still be directed outwards s_{peak} (see fig. 5.21) to the minimum particle size (between r_{sub} and r_{peak}) for which drift can still be directed inwards s_{valley} (see fig. 5.21). This difference is higher by a factor of three for model 1. Therefore, particles in the second model do not have to grow as much as particles in the first model have to. The resulting growth timescales for the second model are about one order of magnitude lower than the ones in the first model.

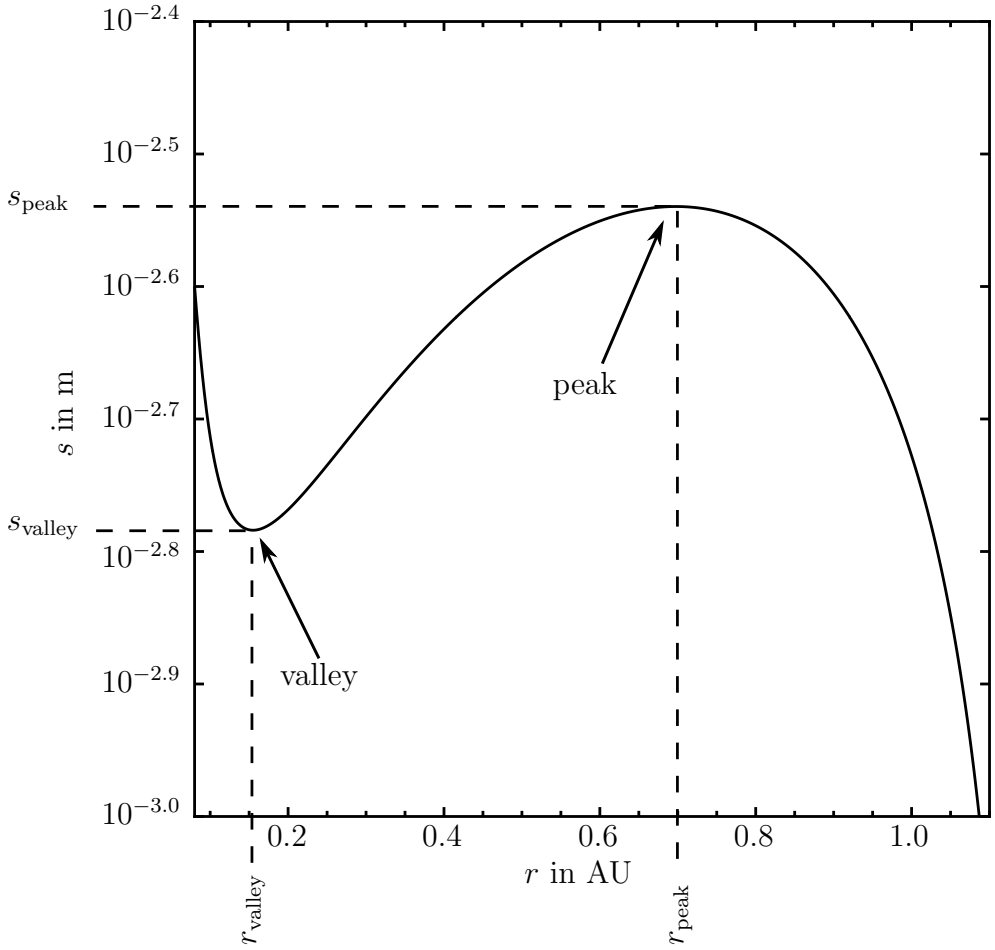

Figure 5.21: Zero-velocity line ($v_{\mathrm{r}}(s, r) = 0$) for the disk LkCa15, Model 1: explanation of "valley" and "peak" used in the description of particle movement. The corresponding particle sizes are s_{valley} and s_{peak}.

5.5.2 HD135344B

Two example trajectories of particles inserted at different distances with different size are plotted in fig. 5.22 (see caption for details). As can be seen there, both particles describe separate, closed circles with growth and fragmentation events taking place regularly. Therefore particles in the disk do not necessarily have to drift through the complete disk for growth and destruction but can stay localised within a few tens of AU while mass is still transported from the outer part into the inner one.
As can be drawn from 5.7, small particles are lacking in the outer regions of the inner dust disk. To account for this, the maximum and minimum particle sizes are determined dynamically. Therefore, for a given distance to the central star r the corresponding $s_{\max}$ and $s_{\min}$ are calculated following the zero-velocity line. For a distance of 0.24 AU, for example, the minimum and maximum particle sizes are approximately 8×10^{-6} m and 3×10^{-4} m respectively.

5.6 Discussion

As can be drawn from the velocity calculations shown in sec. 5.2, the inner dust disk in pre-transitional disks can be in steady state. The concept of small particles drifting outwards and larger ones drifting inwards may lead to a self-sustained recycling mechanism as described in sec. 5.3.
As mentioned in sec. 3.3, other effects might strengthen this picture even more: If larger particles drift inwards, light-induced erosion will excavate material or even destroy them, leading to smaller particles which tend to drift outwards again (de Beule et al., 2013). As can be drawn from the erosion rates presented in tab. 3.1, particles with sizes below 10^{-1} m will quickly enough loose significant amounts of mass. Therefore, the vast majority of particles pass the zero-velocity line and start drifting outwards again instead of getting lost due to evaporation while drifting inwards too far. Including light-induced erosion would therefore benefit the model of self-sustained recycling and might strengthen the model against unfavourable parameter constellations e.g. minimum and maximum particle size and size distributions. Since this erosion effect is not quantified in detail for the setup depicted here, it is not implemented in the model but mentioned as additional possible extension.
While in the disk HD135344B particles – regardless of their size – have a maximum distance to the central star up to which the drift is still directed outwards (see fig. 5.7), in the disk LkCa15 the smallest particles drift even further outwards (see fig. 5.6). These small particles might explain the observations of the dust inside the cavity (e.g. van der Marel et al., 2015).

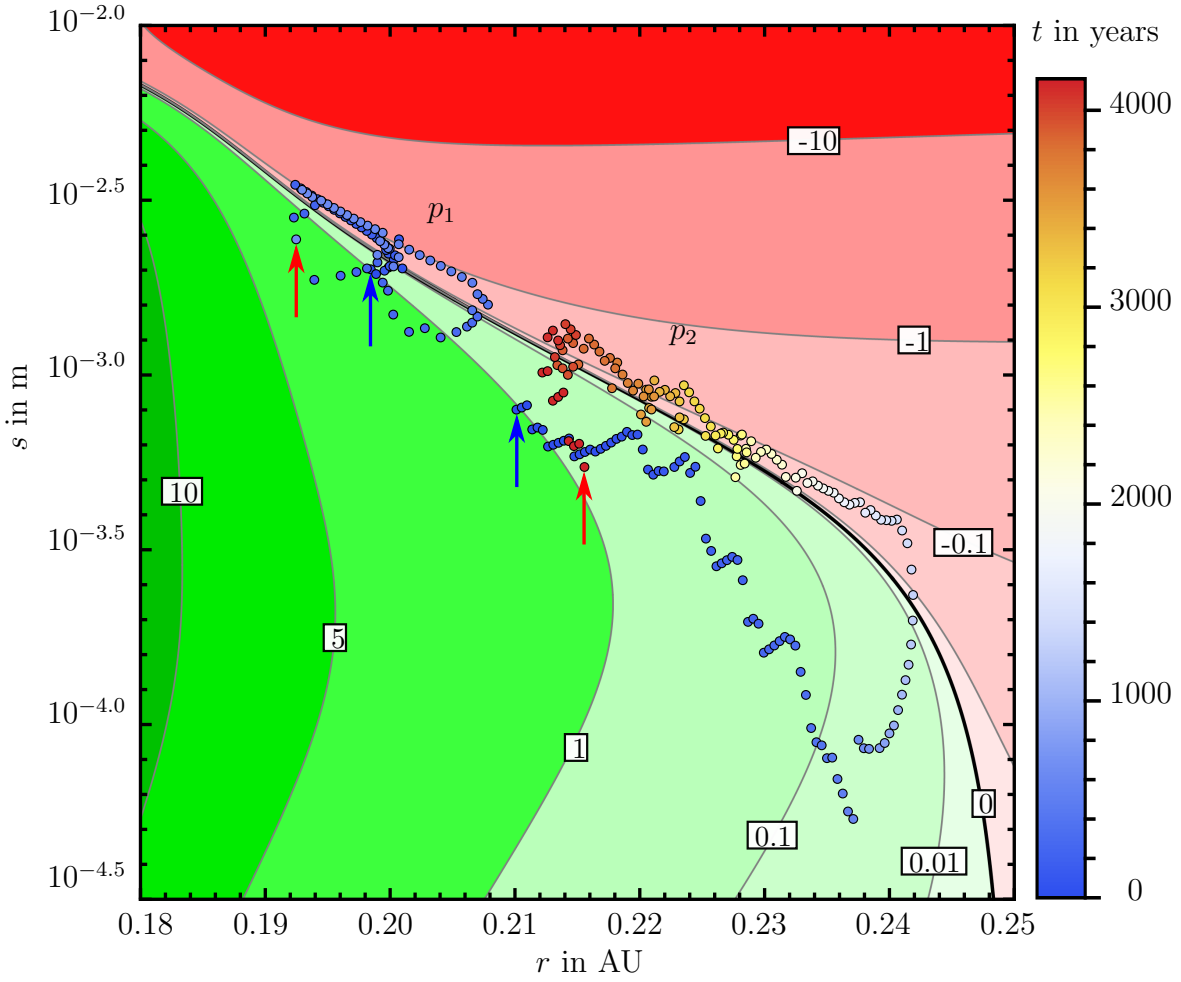

Figure 5.22: Example of two simulated particles in the disk HD135344B, inserted at 0.210 AU with a size of 8.0×10^{-4} m (p_1) and 0.198 AU with a size of 2.0×10^{-3} m (p_2). The datapoints are colour coded according to time, the time steps are not fixed. Note here that for visualisation reasons particle p_1 is plotted only for the first $\sim$ 450 years while particle p_2 is plotted for $\sim$ 4100 years. Start and end points are marked with arrows, blue denotes the starting point and red the end point. In general, the trajectories seem more chaotic than for the disk LkCa15 since fragmentation events happen far more often. Especially particle p_2 (right side) has multiple fragmenting events at the beginning while drifting outwards. Once it reaches about 0.24 AU, growth begins to dominate. The particle starts to drift inwards again while once more multiple fragmentation events take place peaking in a fragmentation cascade at 0.215 AU. Particle p_1 describes two circles in the s–r–space, one smaller circle (only the left part of the trajectory) and one larger circle. (Husmann et al., 2016)

5.6.1 LkCa15

As shown in the previous sections, it is possible to establish a self-sustained recycling mechanism in in both investigated models of the disk LkCa15 (see fig. 5.6 as well as the single particle evolution calculations fig. 5.19 and 5.20). Particles can follow the zero-velocity line and grow simultaneously even beyond the peak (see fig. 5.21, e.g. 0.8 AU / 5.1×10^{-3} m in Model 1). Parameter sweeps for k_{th}, χ_{dust}, δ_{gas}, δ_{dust} as well as κ_{med} show that self-sustained recycling might be possible for several parameters and no fine tuning of the parameters is necessary (see Appendix, table A.4).
A comparison of the simulated particle drifts in Model 1 and Model 2 shows significant differences in the time particles need to grow from s_{valley} to s_{peak} (see fig. 5.21), in the following referred to as "growth timescale". An optimum growth timescale is in the order of the time particles need to drift from the sublimation radius to the stability point, in the following referred to as "drift timescale". This guarantees a steady state of the dust-disk since the mass which is transported outwards (in terms of small particles) is replenished by the grown bodies which drift inwards. In both disk models, the drift timescales are on the order of 10^5 yr with small particles generally tend to drift slower than bigger ones. A detailed tabular on the drift timescales for differently sized particles in both disk models is presented in tab. 5.3.

Table 5.3: Drift timescales in years from r_{sub} to 0.95 AU for differently sized particles in the disk LkCa15, Model 1 and Model 2

Size	1×10^{-6} m	2×10^{-6} m	5×10^{-6} m	1×10^{-5} m	1×10^{-4} m
Model 1	2.4×10^5 yr	1.9×10^5 yr	1.3×10^5 yr	8.4×10^4 yr	1.2×10^4 yr
Model 2	2.4×10^5 yr	1.6×10^5 yr	7.6×10^4 yr	4.1×10^4 yr	4.8×10^3 yr

The growth timescales on the other hand differ, with $\sim 3.2 \times 10^6$ yr in the first model and $\sim 3.6 \times 10^5$ yr in the second model. A steady-state is therefore preferably possible in the second disk model where drift and growth timescale are approximately the same. Even if the growth and drift timescales differed, the general idea of a self sustained recycling process would still be valid: If the drift timescale is higher than the growth timescale, more mass will be accumulated at the outer edge of the inner dust ring. This would affect the growth timescale, since in general more mass would lead to a more efficient growth and to a higher mass flow pointing towards the star. The dust surface density might therefore oscillate in time and the system will be robust against perturbations. A more detailed analysis of the change in surface density and of the exact growth and drift behaviour would need a size- and distance dependent Smoluchowski or Monte-Carlo growth simulation with sufficient spatial-, temporal- and volumetric resolution. As illustrated in section 5.7.2, not

only the radial but also the vertical position of particles highly influence the drift and collision behaviour. Thus for an extensive simulation, a two-dimensional calculation of the dust density as well as a more sophisticated temperature model (with temperatures depending on the actual dust distribution) has to be included, leading to an enormous requirement of computing capacity.
The drift and growth timescales are comparable to the disk's viscous timescale which for Model 2 at 1.0 AU is

$$t_{\nu,\mathrm{turb}} = \frac{r^2}{\alpha_{\mathrm{turb}}\, c_\mathrm{s}\, h} \approx 10^5\,\mathrm{yr} \quad . \tag{5.11}$$

Therefore, the recycling process should be independent of the gas behaviour as the radial gas motion is already implemented in the model. Nonetheless, gas has to be replenished from the cavity since otherwise the photophoretic force will drop and the dust disk starts to collapse. This process can explain the evolution from pre-transitional to transitional disks with somewhat complex intermediate steps as can be seen for example in the disk SR21 (see tab. 2.1). This disk is dust- and gas-free from the sublimation radius to a distance of approximately 7.0 AU and only little (but visible) dust ($\delta_\mathrm{dust} = 10^{-6}$) and gas ($\delta_\mathrm{gas} = 10^{-2}$) from 7.0 AU to r_cav at around 25 AU.

5.6.2 HD135344B

The results for the disk HD135344B show significant differences compared to the ones for the disk LkCa15. As the disk's opacity is much higher in the disk HD135344B, the maximum distance particles can drift is only about 0.07 AU. The increased dust density leads to significantly higher collision rates resulting in localised "recycling circles": instead of drifting the whole disk in order to return to their starting point and size as they do in the disk LkCa15, particles only drift much smaller parts of the disk. As shown in fig. 5.12, particles with sizes in the range of $\sim 8 \times 10^{-5}$ m drift the furthest. Larger ones as well as smaller ones cannot drift as far. For large particles this is intuitive, for small particles the limit is caused by the drag due to the gas motion in radial direction. Particles at r_gap are not trapped at this position since collisions – either causing growth or destruction – both lead to an inwards directed drift. Otherwise those particles were very unlikely to overcome the bouncing barrier following the ideas by Windmark et al. (2012a) and Windmark et al. (2012b). The drift simulations show as well that the very small amount of particles observed in the cavity cannot have been released from the inner dust disk.

5.7 Caveats

Several variables and models used for the simulation of the particle evolution contain uncertainties. Whilst a few parameters are – either directly or within the given uncertainties – adopted from van der Marel et al. (2015), the values for the mean opacity κ_{med}, the heat conductivity k_{th}, the dust scale height parameter χ_{dust}, as well as the turbulence parameter α_{t} had to be estimated using given models and experiments. Three aspects influencing the particle drift, the collisional outcome and therefore the complete recycling mechanism are the size distribution of the dust, the strength of photophoresis and turbulence.

5.7.1 The size distribution of the dust

Besides other factors, the size distribution of the dust as described in eq. 5.9 determines the growth timescales and is therefore important for the efficiency of the recycling process. Especially the value chosen for the exponent κ_{size} has the highest impact. Generally, high κ_{size}-values decrease the growth timescales but simultaneously decrease the probability of destroying the large, inwards drifting particles. Low values behave vice versa. Following the "lucky particles" theory by Windmark et al. (2012a) (sec. 4.6), one would expect high κ_{size}-values since only few particles can evolve and grow beyond the typical size of particles at the bouncing barrier.
The model for κ_{size} – especially in the disk LkCa15 – is only a rough estimation as explained earlier. Even if κ_{size} was much higher, the effect of light-induced erosion as shown in sec. 3.3 would efficiently erode large bodies close to r_{sub}. Fragmentation due to collisions would therefore not necessarily be required to prevent bodies from passing the sublimation radius and being lost for the recycling process. One has to note here that since the exact amount of eroded mass is not known for the specific setup, a model for light-induced erosion is not implemented in the simulations and is therefore dedicated to future work.

5.7.2 The role of photophoresis

Radiation related forces like photophoresis and radiation pressure can dominate the force balance as shown in fig. 5.3. Especially the photophoretic force depends highly on the temperature gradient on the particle which itself is highly dependent on the radiation field. In the approximations used here, the temperature gradient is calculated using only the star as radiation source and a background radiation field. In a pre-transitional disk this setting is somewhat simplified. Since the mean opacity κ_{med} can deviate significantly from zero, the thermal radiation of the dust had to be considered as well for an exact calculation of the photophoretic force. Though, in general, the opacity for infrared radiation is much

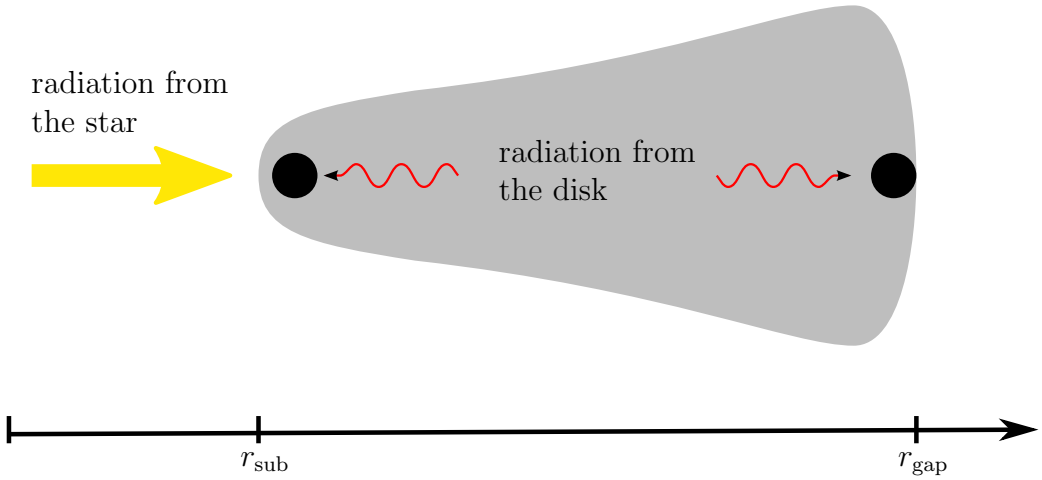

Figure 5.23: Radiation on particles inside a pre-transitional disk. The particle's front close to the sublimation radius is irradiated by the sun while the back is irradiated by the hot dust in the disk itself, the temperature gradient is therefore not as high as the one of a particle which is illuminated only by the sun. The particle near the gap radius is irradiated by both sources in radial direction, the temperature gradient should therefore be higher than the one of a particle irradiated only by the solar radiation (reduced due to the disk opacity).

higher than the opacity for the visible spectrum (e.g. Semenov et al., 2003). The resulting temperature distribution on the surface of a particle inside the inner dust disk would be asymmetric since the radiation from the azimuthal disk direction would be significantly higher than the radiation from the vertical direction. Furthermore, the side of the particle which points away from the star would be heated due to thermal radiation of the outer dust as well. The temperature gradient calculated within the formulae given in sec. 2.4.4 might therefore be overestimated, especially for particles close to the sublimation radius. Particles further outwards (e.g. at the disk edge) on the other hand might have an increased gradient since the side facing the sun is irradiated not only by the solar radiation but by thermal radiation from the dust disk itself. A visualisation of the scenarios depicted here is given in fig. 5.23.

Other variables and effects influencing the photophoretic forces are the disk height and the turbulent motion of particles inside the disk. The intensity at a distance r depends on the integrated dust density as shown in eq. 2.12. The calculations presented are carried out for the midplane only and therefore only the midplane intensity is used. Dust motion in vertical direction might lead to higher drift velocities in radial direction since the disk is much more opaque in the midplane compared to the higher disk layers. The intensity due to solar irradiation for different distances to the central star r and different heights

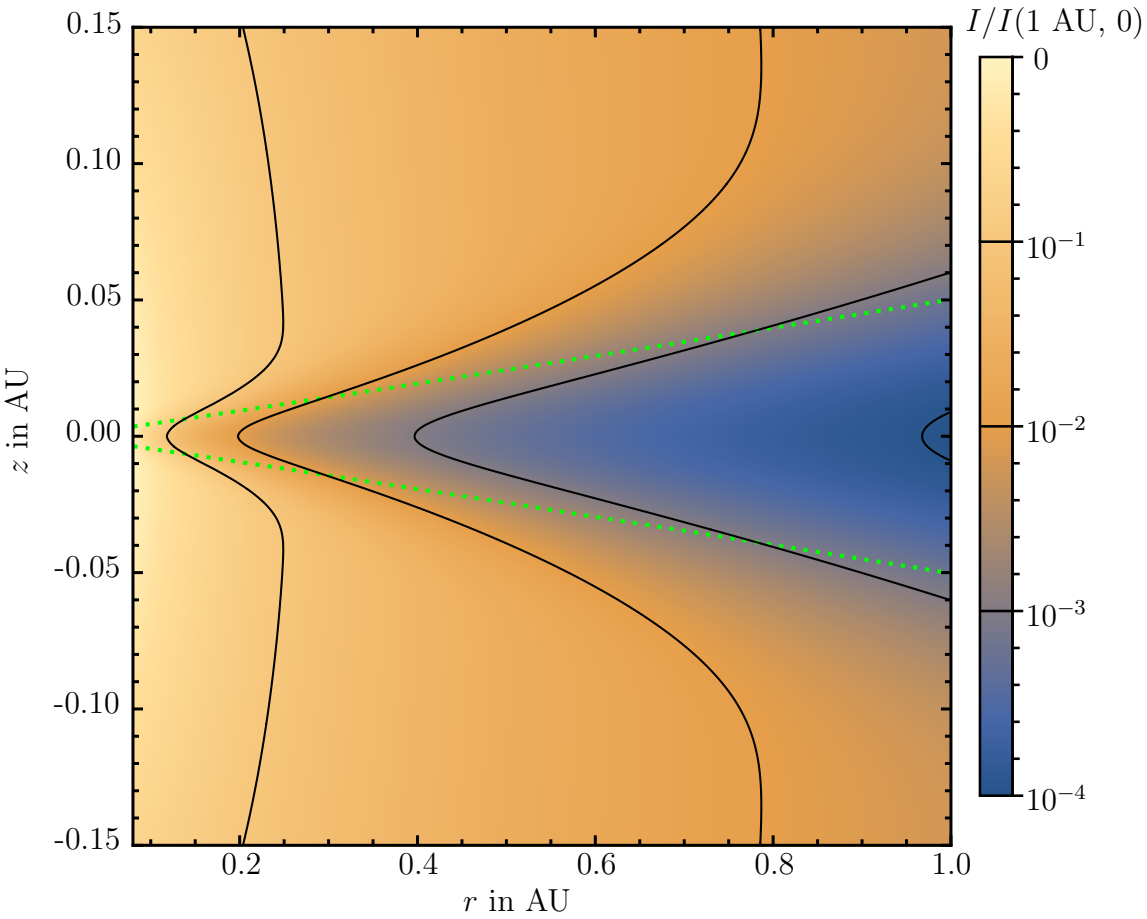

Figure 5.24: Relative intensity $I(r, z)/I(1.0\text{ AU}, 0.0\text{ AU})$ for different distances to the central star r and different heights above the midplane z in the disk LkCa15, Model 2. The contours are in decades, starting from 10^{-1} on the left to 10^{-4} on the right. The green dashed line denotes the disks scale height h.

above midplane z can be calculated using eq. 1.7 for the dust density $\rho_{\text{dust}}(r', z')$ and integrating the mean opacity along the path of radiation, resulting in

$$I(r, h) = I_0(r, z) \cdot \exp\left[-\int_{r_{\text{sub}}}^{r} \kappa_{\text{med}}(r')\rho_{\text{dust}}\left(r', r' \tan\left\{\frac{z}{r}\right\}\right) \text{dr}'\right] \tag{5.12a}$$

$$I_0(r, z) = \frac{L_\star}{4\,\pi\,(r^2 + z^2)} \quad . \tag{5.12b}$$

For the disk LkCa15 Model 2 the intensity dependent on the distance to the central star r and the height above midplane z is plotted in fig 5.24. Following eq. 5.12 it can be concluded that the ratio of the intensity of the solar radiation at the midplane at 1.0 AU and the intensity at the disk scale height at 1.0 AU is

$$\frac{I(1.0\,\text{AU}, 0.0\,\text{AU})}{I(1.0\,\text{AU}, h(1.0\,\text{AU}))} \approx 0.16 \quad . \tag{5.13}$$

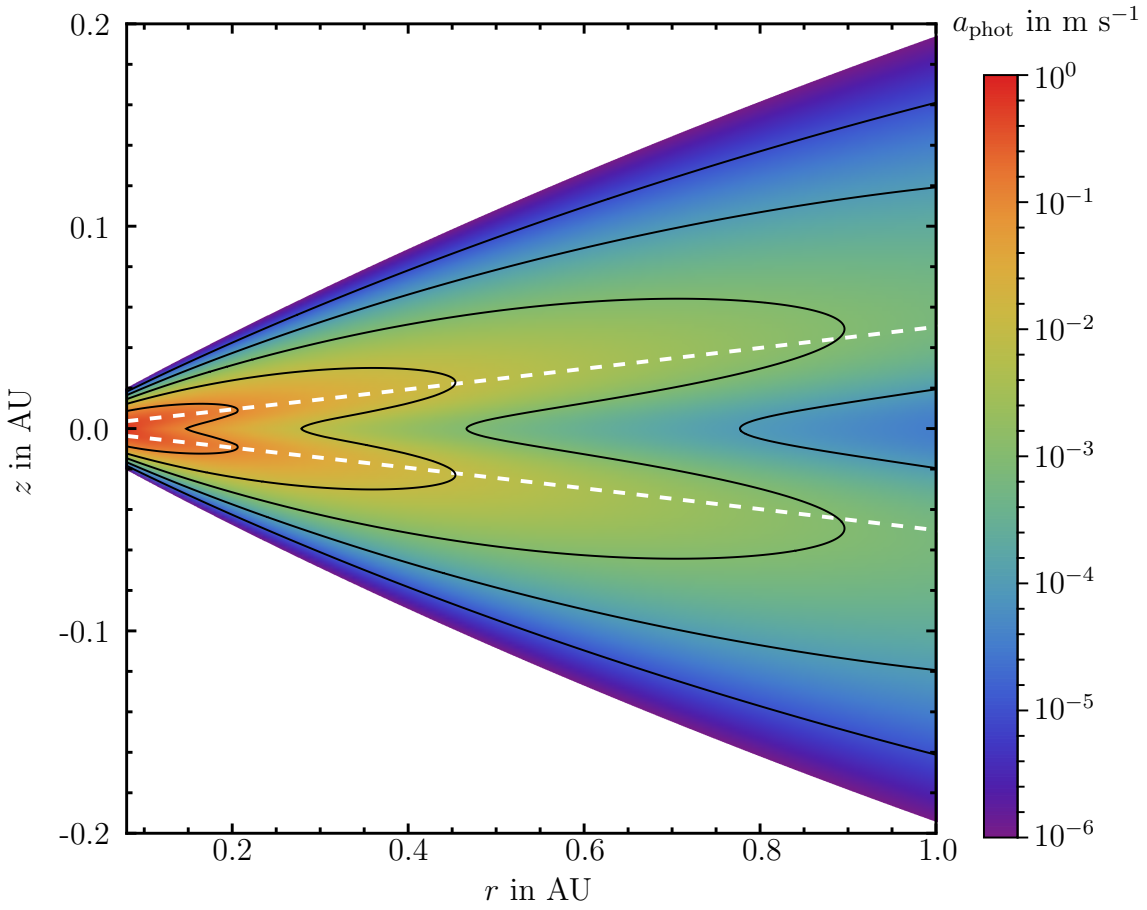

Figure 5.25: Acceleration due to photophoresis for different distances to the central star r and different heights above the midplane z in the disk LkCa15, Model 2 for a particle with a size of 10^{-4} m. The contours are in decades, starting from 10^{-1} in the mid-left to 10^{-5}. The white dashed line denotes the disks scale height h.

Since for large thermal conductivities, photophoresis is linearly dependent on the intensity in a first approximation, the resulting force on dust particles can get about six times higher at the disk height h at 1.0 AU than at the midplane. The ratio $I(r,0)/I(r,h(r))$ can be described in first order with a logarithm following

$$I(r,0)/I(r,h(r)) \approx a\log[r] + b \quad , \tag{5.14}$$

where $a = 2.1$ and $b = 6.5$ for the disk LkCa15 Model 2. The acceleration due to photophoresis for a 10^{-4} m sized particle is depicted in fig. 5.25. As can be seen, the photophoretic force in certain heights above the midplane can be a factor 10 higher than in the inner part. Since the gas density decreases for increasing distances to the midplane as well, the resulting net force on a non-moving particle with included drag due to the gas flow towards the star can differ as well. The total acceleration on a particle with a size of 5×10^{-4} m is depicted in fig. 5.25. Note here that additional effects like Poynting-

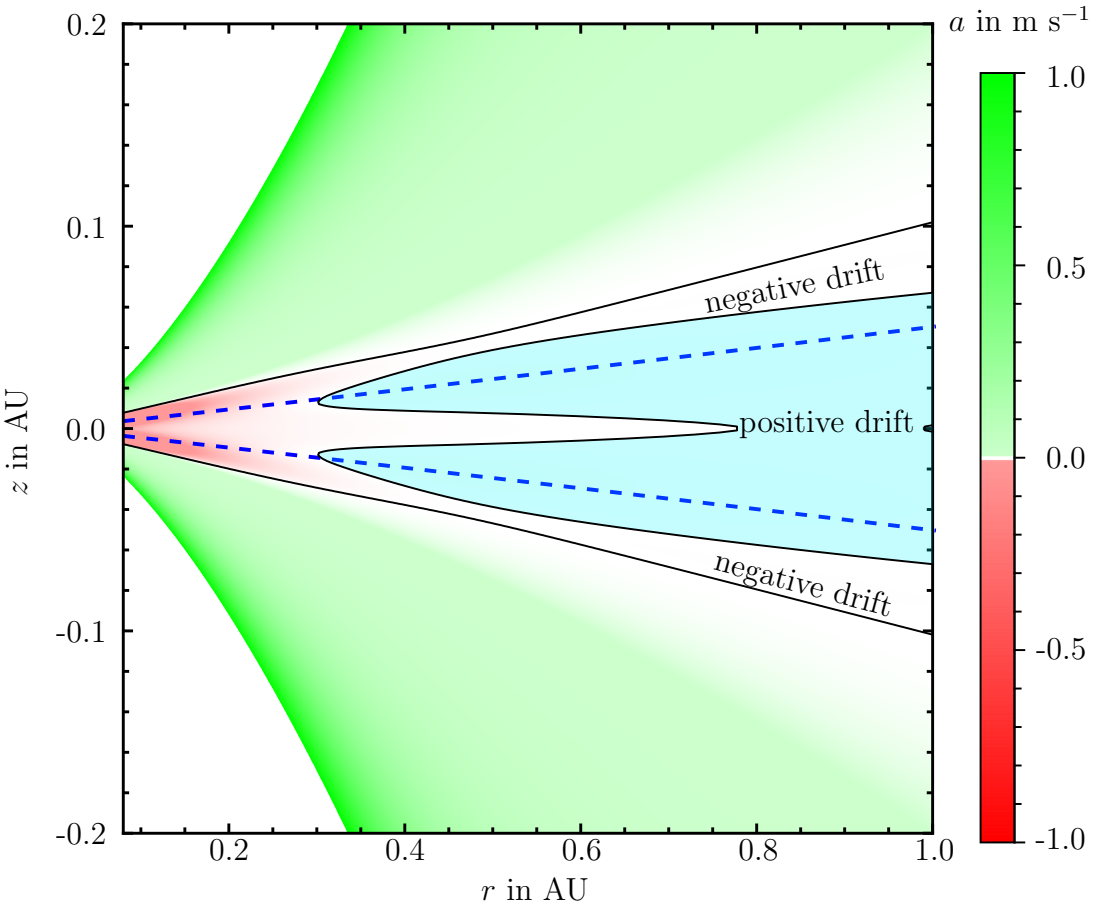

Figure 5.26: Total acceleration in radial direction assuming a non-moving, 5×10^{-4} m particle due to photophoresis, radiation pressure, residual gravity, and gas drag due to the gas flow towards the star for different distances to the central star r and different heights above the midplane z in the disk LkCa15, Model 2. The contours differ the zones with outwards directed drift (green) from those with inwards directed drift (red). Since the accelerations in the inner disk is only very small, a blueish background color emphasizes the outwards directed drift. The blue dashed line denotes the disks scale height h. Note here that only a simplified gas flow is used following eq. 2.46 and assuming the independency on the height above the midplane.

Robertson drag are not included and the accelerations for vanishing gas pressures are therefore not calculated correctly.

Furthermore, for an explicit calculation of the forces acting on particles depending not only on the distance to the central star but also on the height above the midplane, a vertical temperature profile of the gas has to be estimated. Since a model for radiative heat transfer is lacking for the disks LkCa15 and HD135344B, the temperature distribution

has to be assumed and is therefore only a rough estimation. In fig. 5.25 and 5.26, the temperature distribution was assumed to be

$$T(r,z) = T(r) \cdot \left(1 + \frac{3}{2}\left(\frac{z}{H}\right)^2\right) \quad . \tag{5.15}$$

Using this approximation, the general picture of a hotter upper disk is reproduced as for example calculated by Akimkin et al. (2013). Again, it should be pointed out that this assumption is very rough, especially for large heights above the midplane. Using more sophisticated models including dust motion and radiative heat transfer might lead to values which could extremely differ from the values stated here.

5.7.3 The role of turbulence

In general, the collisional outcome as depicted for example in fig. 5.14 depends significantly on the collision velocities which are dominated by the relative turbulent velocities as can be seen in fig. 5.10. Hence, in fig. 5.27 the impact on different α_{turb} values on the collisional outcome in the disk LkCa15, Model 2 at 0.5 AU is depicted.

As can be seen, decreasing α_{turb} values lead to a shift in the transition between bouncing and mass gain as well as in the transition between mass gain and mass loss. For Model 2 with a maximum initial growth size of 1.58×10^{-3} m, higher turbulence values are beneficial since the growth rate increases with increasing α_{turb}. On the other hand, even small turbulence values would not prevent a self-sustained recycling process in the inner dust disk of LkCa15. Even though small turbulence velocities would reduce mass gain in collisions of large targets with small particles, small particles would more efficiently grow via hit and stick and would therefore partially compensate the reduced mass gain. In fig. 5.27 this can be seen as the dark green area at the bottom left corners of the collisional outcome plots increase for decreasing α_{turb}.

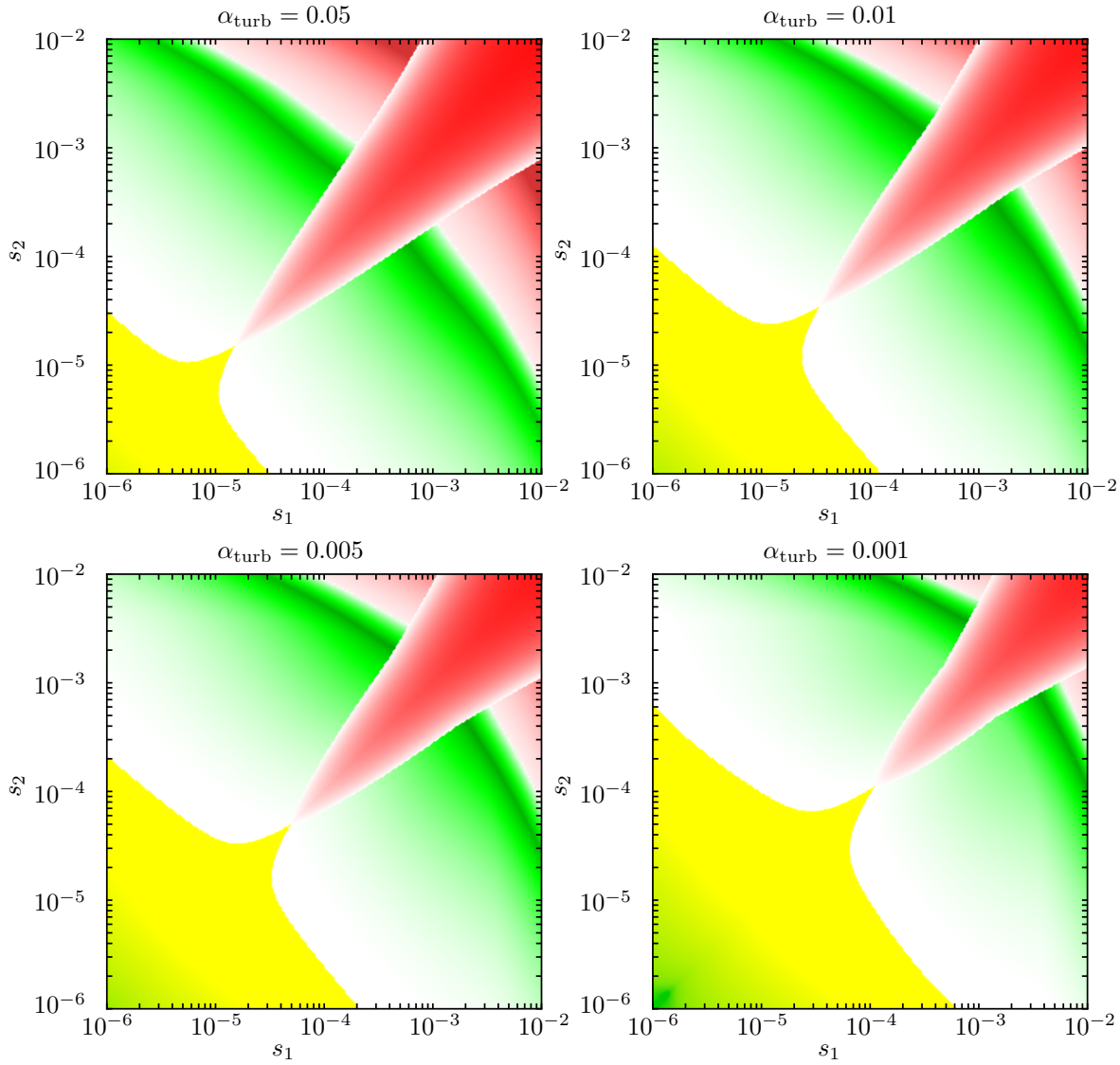

Figure 5.27: Comparison of different $\alpha_{\rm turb}$ values and their impact on the collisional outcome in the disk LkCa15, Model 2 at 0.5 AU.

6

Conclusion and Outlook

The evolution of protoplanetary disks is highly complex and object of research in multiple fields. Within this work, the motion and evolution of dust particles are focused. Since disks – especially in later stages – can be optically thin, radiation related forces like radiation pressure (sec. 2.4.3) and photophoresis (sec. 2.4.4) influence the dust motion significantly. A new formalism for calculating photophoretic forces on particles embedded in a gaseous environment with gas temperatures differing from the particle temperature is therefore introduced (Loesche et al. (2016), Loesche and Husmann (2016), and sec. 2.4.4). By including this aspect and linearising the temperature gradient along the particle's surface, the given approximations enhance the calculations significantly as shown in Loesche et al. (2016) and Loesche and Husmann (2016). Though the given formula is an improvement for particles in protoplanetary disks, more sophisticated models would require exactly calculated gas temperatures and disk opacities as well as the consideration of radiation from the hot dust itself. These calculations can therefore only be performed individually for a specific disk setup.

Other aspects which are treated within this work and which are important for the understanding of the dust evolution in protoplanetary disks are the influences on the growth of particles. On this occasion collision processes and the outcome of these collisions take first place. Although experimental and theoretical investigations have proceeded far, an extensive, precise model is still lacking. Beside other causes, one issue is the treatment of collisions which cannot be done straight forwards. This means that there exist plenty collision parameters (e.g. collision velocity, collision angle, mass, porosity, material, particles shape) which influence the collisional outcome significantly. In collisional outcome models this parameter range is therefore reduced to only a few parameters. In the model by Windmark et al. (2012a) which is used in this work the decisive parameters are the collision velocity and the particles' masses. Since collision velocities are calculated for a

specific disk and a specific distance to the central star, the transition between the different outcome regimes is strict (as can be seen for example in fig. 5.14). Improvements to the collision velocities by implementing e.g. a velocity distribution influence the transitions and the dust evolution (Windmark et al., 2012b). Nonetheless, more input for the modelling of the collisional outcome is necessary to cope with the high amount of different parameters: The case of different materials is of high interest, especially H_2O ice and CO_2 ice. As shown within this work and the publications by Musiolik et al. (2016a) and Musiolik et al. (2016b) as well as Gundlach and Blum (2015), particles consisting of H_2O ice are much stickier than silicates while on the other hand those consisting of CO_2 ice might behave like silicates. Future studies on dust evolution in different parts of the disk have to cope for the different properties of the materials present. They should therefore test for the viability of the theory of regions in PPDs where growth of particles occurs preferentially (see. sec. 3.2).

Additional effects can play a crucial role in the collisional outcome as well. As shown in chapter 4, gas drag due to headwind can lead to higher growth rates in collisions between small impactors and larger targets. This is caused by the reaccretion of ejecta produced in such collisions which are pushed back onto the target's surface due to the gas drag. The effect can significantly influence the timescales necessary for growth of particles to larger sizes. With eq. 4.29 an analytical formula is given for the amount of reaccreted mass in the minimum mass solar nebula. By inlcuding a cut-off value for small Knudsen Numbers this formula can be used for all kinds of collisional outcome models for the MMSN. Although experimental studies on this effect have already been published (Wurm et al., 2001a,b), a quantitative experimental investigation – especially in the transition regime between free molecular flow and slip flow – is lacking. Therefore the results presented in section 4.1 are only upper limits for the amount of re-accreted material. Besides experimental studies on the reaccretion itself, the forces on the ejecta in vicinity of a second, larger body have to be studied in detail for different drag regimes. With a more sophisticated model, the actual trajectories of the ejecta could be calculated more precisely and the results could be improved.

Furthermore, in optically thin disks or at the inner edge of the dust disk, another effect can lead to erosion of bodies and particles. This is caused by light induced effects (de Beule et al., 2011, 2013). Experimental investigations show that erosion rates in low gravitation environment can be significantly larger (sec. 3.3). Especially in pre-transitional disks this effect might therefore aid the disruption of large particles near the sublimation radius.

By including photophoresis and radiation pressure in the equation of motion of particles in the inner parts of pre-transitional disks it is shown in chapter 5 that a self-sustained recycling process can be established (Husmann et al., 2016). Although some simplifications are applied, the general picture of small particles being transported outwards, growing bigger, drifting inwards again and getting destroyed is verified. These results are capable of explaining the stability of the inner dust ring: Although observations suggest that no material is replenished from the outer dust disk due to the nearly dust-free gap, the inner dust disk can be stable against significant mass loss due to inwards or outwards directed particle drift. Nonetheless, more sophisticated two-dimensional disk models with inclusion of radiative heat transfer and dust density evolution could improve the understanding of the dust evolution in the inner dust ring of pre-transitional disks. Since these studies would imply temporal and spacial evolution, the required computational capacity would be very high. Even a one-dimensional dust surface density evolution including photophoresis, radiation pressure and radial gas drift would require high spacial and temporal resolution while lots of optimisations and simplifications had to be made. Nonetheless, by using these computational methods, the disk evolution from the pre-transitional disk towards the transitional disk (the loss of the inner dust ring) as a pre-step to debris disk could be investigated as well. Since calculations show that the dust recycling process is stable for several viscous timescales, the proposed reduction of the resupplied gas from the outer disk over time has to be investigated in detail for the determination of the inner dust disk's lifetime.

The results presented within this work include further important steps for the understanding of the physical processes involved in dust evolution and dust motion in protoplanetary disks. The collisional outcome models can be extended by including the material properties as well as the effect of reaccretion. By taking into account radiation related forces in non-opaque disks, the motion of particles can be influenced significantly leading to a recycling mechanism in the inner parts of pre-transitional disks. All investigated aspects show the complexity of the formation of planets starting with small dust particles but are moreover aiding the understanding and developments towards a full-featured model of protoplanetary disks and their evolution.

Appendix A

Appendix

A.1 Additional fit parameter data

A.2 Dependencies of Reaccretion

Fit data for parameters $a(s_\mathrm{p})$ and $b(s_\mathrm{t}, (s_\mathrm{p}))$ from eq. 4.27:

$$a(s_\mathrm{p}) = a_1 + a_2 \log_{10}\left(\frac{s_\mathrm{p}}{\mathrm{cm}}\right) \tag{A.1a}$$

$$b(s_\mathrm{t}, s_\mathrm{p}) = -b_1 + b_2 \log_{10}\left(\frac{s_\mathrm{t}}{\mathrm{cm}}\right) - b_3 \log_{10}\left(\frac{s_\mathrm{p}}{\mathrm{cm}}\right) \quad . \tag{A.1b}$$

Table A.1: Fit data for $a(s_\mathrm{p})$ and $b(s_\mathrm{t}, s_\mathrm{p})$ from eq. A.1

fit parameter	value	error
a_1	1.005	4.7×10^{-3}
a_2	3.12×10^{-2}	3.1×10^{-3}
b_1	1.77×10^{-1}	5.9×10^{-2}
b_2	9.93×10^{-1}	2.9×10^{-2}
b_3	3.42×10^{-1}	2.8×10^{-2}

Table A.2: Fit data for dependency of η_{re} on $\rho_{\mathrm{gas}}\,\overline{v}_{\mathrm{th}}$ (see eq. 4.27)

s_{t}	s_{p}	a	a_{error}	b	b_{error}
0.01	0.00002	0.916056	0.0115934	0.854907	0.0138995
0.01	0.00005	0.922466	0.0115867	0.656983	0.0126007
0.01	0.0002	0.948135	0.0093184	0.351003	0.00886158
0.01	0.0004	0.957047	0.009488	0.271433	0.00876274
0.02	0.00004	0.939447	0.0115839	1.01519	0.0159054
0.02	0.0001	0.935948	0.0127463	0.732203	0.0162592
0.02	0.0004	0.948418	0.0112147	0.554827	0.0137253
0.02	0.0008	0.956051	0.0111226	0.482623	0.013407
0.03	0.00006	0.944401	0.00903747	1.08149	0.0141826
0.03	0.00015	0.963938	0.007195	0.868562	0.0107267
0.03	0.0006	0.974789	0.0125272	0.71436	0.0182082
0.03	0.0012	0.987909	0.0100492	0.649172	0.0144382
0.15	0.0003	0.957275	0.0119339	1.43168	0.0251116
0.15	0.00075	0.964155	0.0117101	1.34015	0.0243838
0.15	0.003	0.986112	0.0110249	1.22716	0.0226412
0.2	0.0004	0.956093	0.0134369	1.51502	0.0303993
0.2	0.001	0.968545	0.0116477	1.43999	0.0261087
0.2	0.004	0.985194	0.0119709	1.31429	0.0265241
0.3	0.0006	0.965981	0.0118173	1.65862	0.0288726
0.3	0.0015	0.980562	0.0118103	1.59131	0.0286347
0.5	0.001	0.984832	0.0115446	1.86984	0.0313497
0.5	0.0025	0.996764	0.0106179	1.79577	0.028684

A.2.1 Reaccretion in the MMSN

Fit data for parameters $a(r)$, $b(r)$, and $c(r)$ from eq. 4.29.

$$a(r) = a_1 + a_2 \cdot \exp(-\frac{r}{\mathrm{AU}}) \tag{A.2a}$$

$$b(r) = b_1 + b_2 \left(\frac{r}{\mathrm{AU}}\right)^{-2} - b_3 \cdot \exp\left(-\sqrt{\frac{r}{\mathrm{AU}}}\right) \tag{A.2b}$$

$$c(r) = c_1 - c_2 \left(\frac{r}{\mathrm{AU}}\right)^{-1} + c_3 \left(\frac{r}{\mathrm{AU}}\right)^{-3} \tag{A.2c}$$

Table A.3: Fit data for $a(r)$, $b(r)$, and $c(r)$ from eq. A.2

fit parameter	value	error
a_1	3.41×10^{-1}	1.2×10^{-2}
a_2	6.21×10^{-1}	3.1×10^{-2}
b_1	6.87	1.0×10^{-1}
b_2	4.71×10^{-1}	2.4×10^{-2}
b_3	1.07×10^{1}	4.4×10^{-1}
c_1	1.893	3.4×10^{-2}
c_2	2.804×10^{-1}	5.1×10^{-3}
c_3	6.69×10^{-1}	4.6×10^{-2}

A.3 Collision Velocities and Outcome - Additional figures

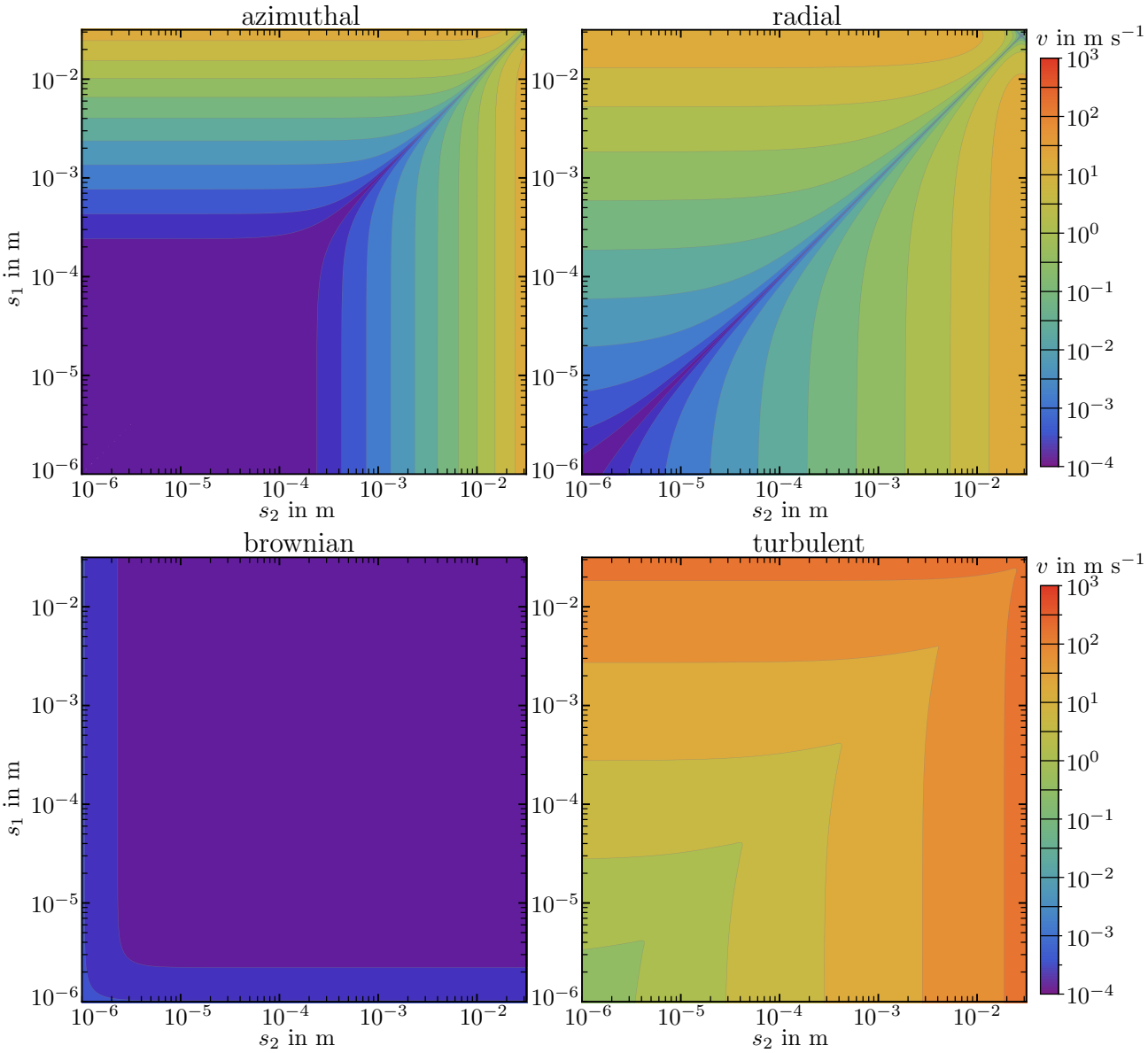

Figure A.1: Comparison of different sources for the collision velocities in the disk LkCa15 Model 1 for a distances of 1.0 AU to the central star. Top left: relative velocity due to azimuthal motion, top right: due to radial motion, bottom left: due to brownian motion, bottom right: due to turbulent motion.

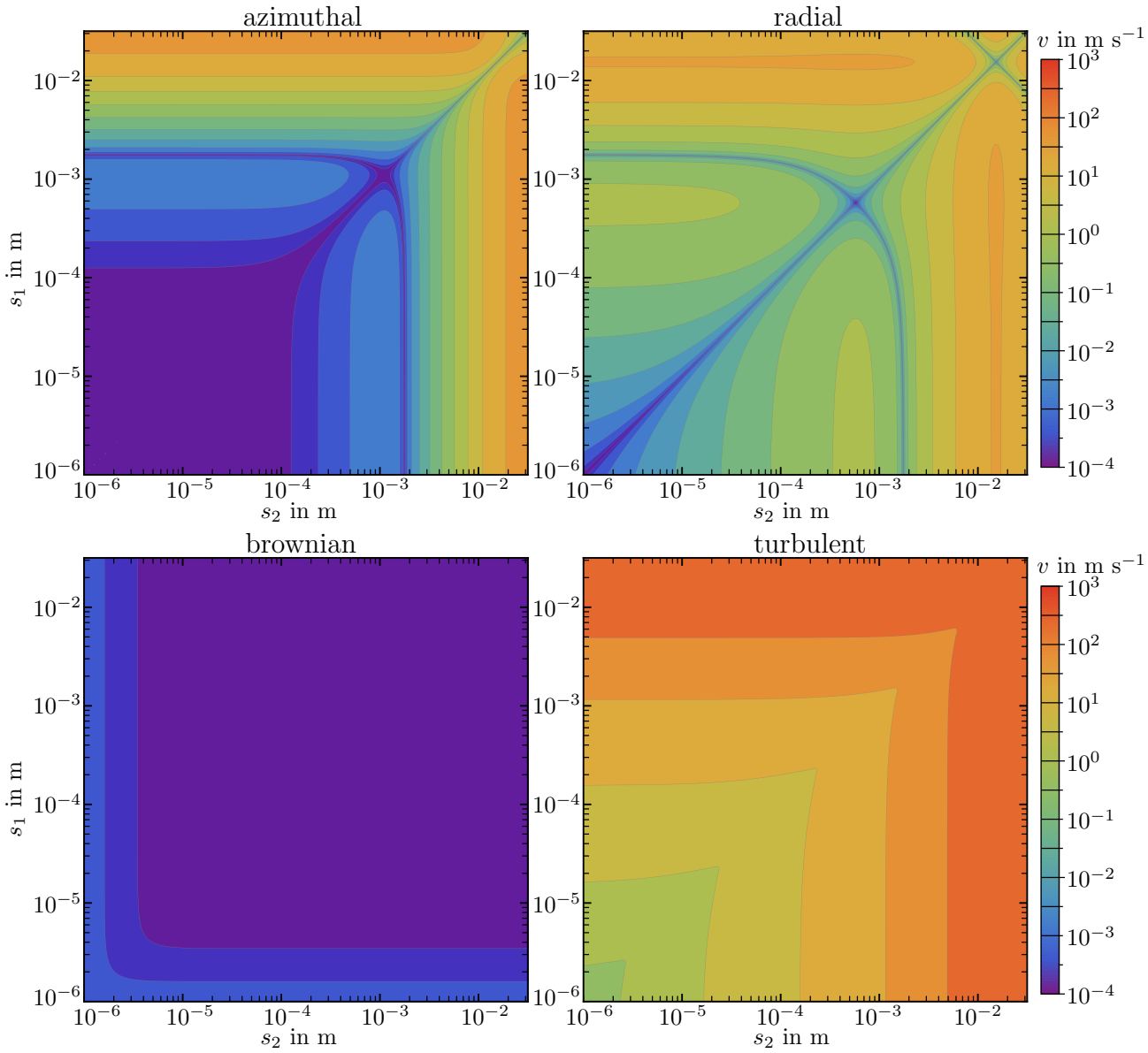

Figure A.2: Comparison of different sources for the collision velocities in the disk LkCa15 Model 2 for a distances of 0.25 AU to the central star. Top left: relative velocity due to azimuthal motion, top right: due to radial motion, bottom left: due to brownian motion, bottom right: due to turbulent motion.

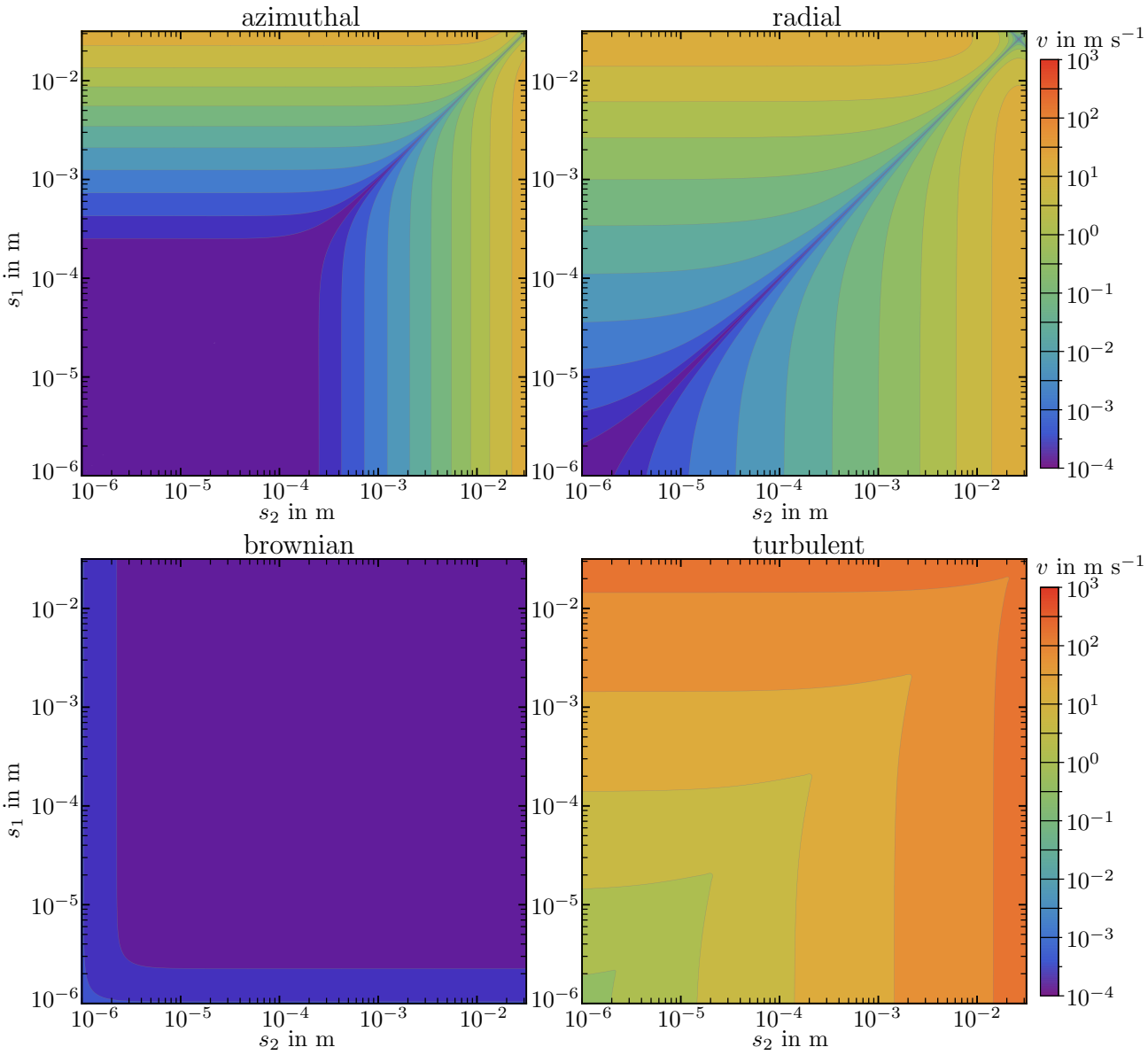

Figure A.3: Comparison of different sources for the collision velocities in the disk LkCa15 Model 2 for a distances of 1.0 AU to the central star. Top left: relative velocity due to azimuthal motion, top right: due to radial motion, bottom left: due to brownian motion, bottom right: due to turbulent motion.

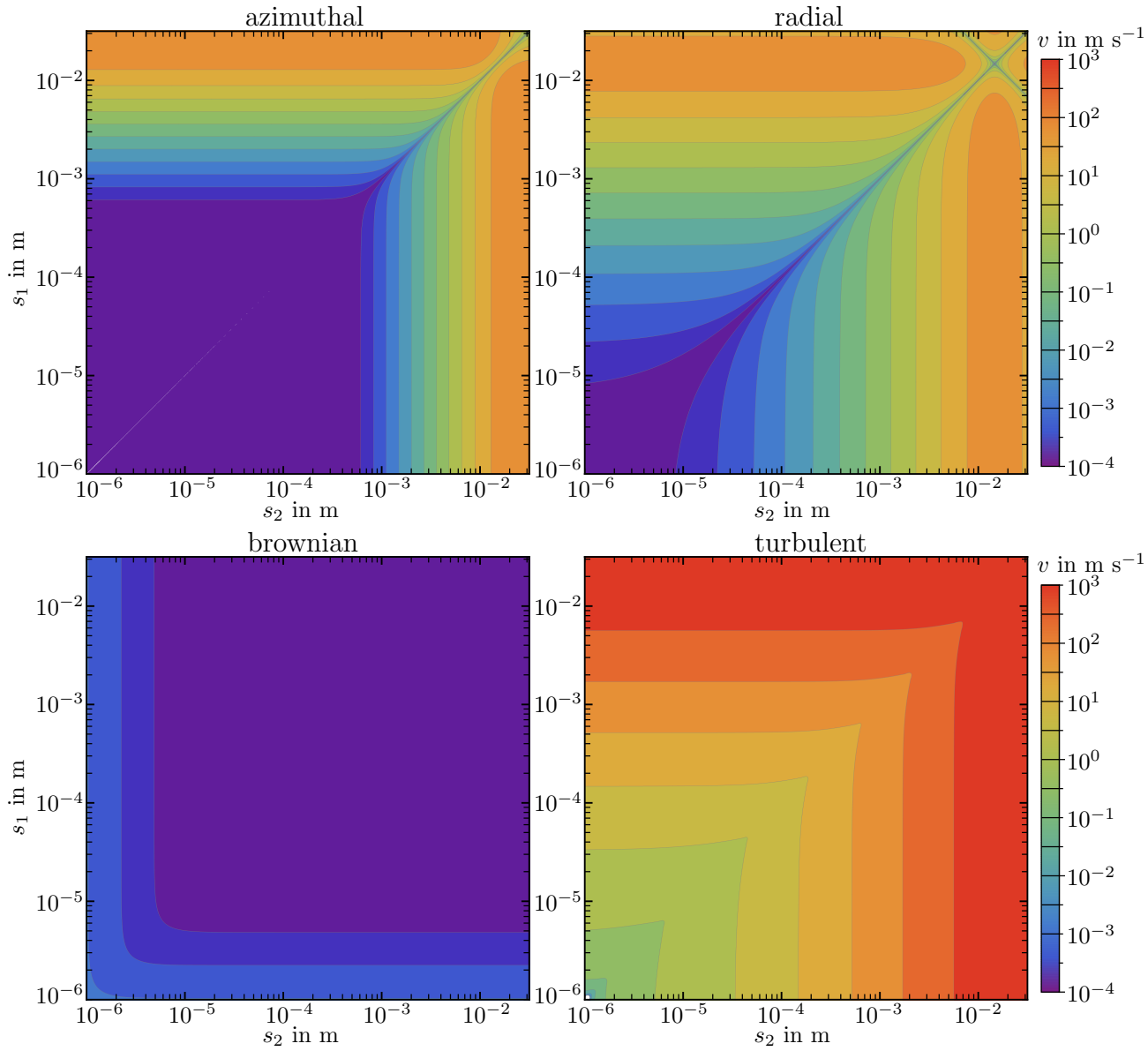

Figure A.4: Comparison of different sources for the collision velocities in the disk HD135344B for a distances of 0.19 AU to the central star. Top left: relative velocity due to azimuthal motion, top right: due to radial motion, bottom left: due to brownian motion, bottom right: due to turbulent motion.

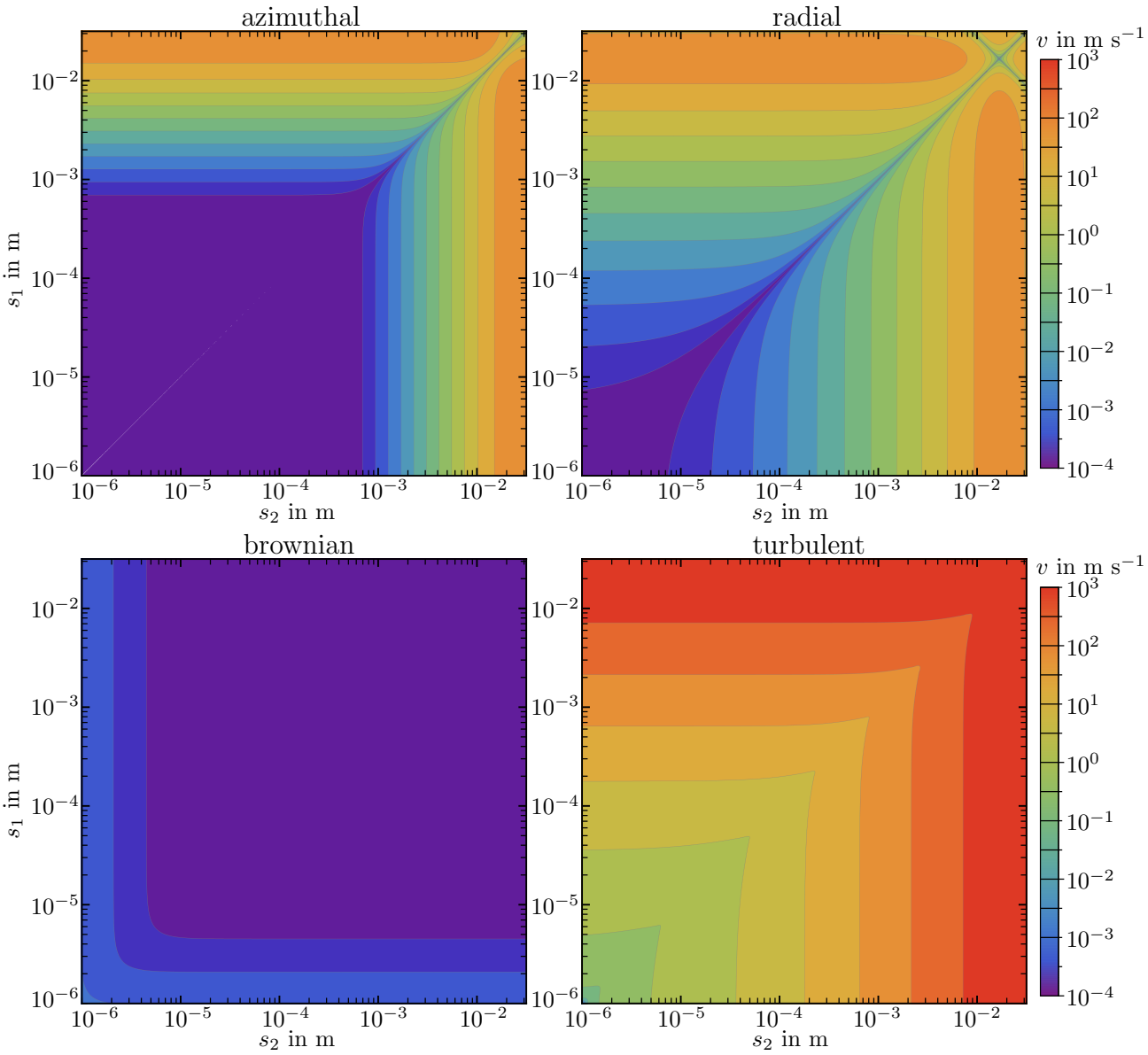

Figure A.5: Comparison of different sources for the collision velocities in the disk HD135344B for a distances of 0.24 AU to the central star. Top left: relative velocity due to azimuthal motion, top right: due to radial motion, bottom left: due to brownian motion, bottom right: due to turbulent motion.

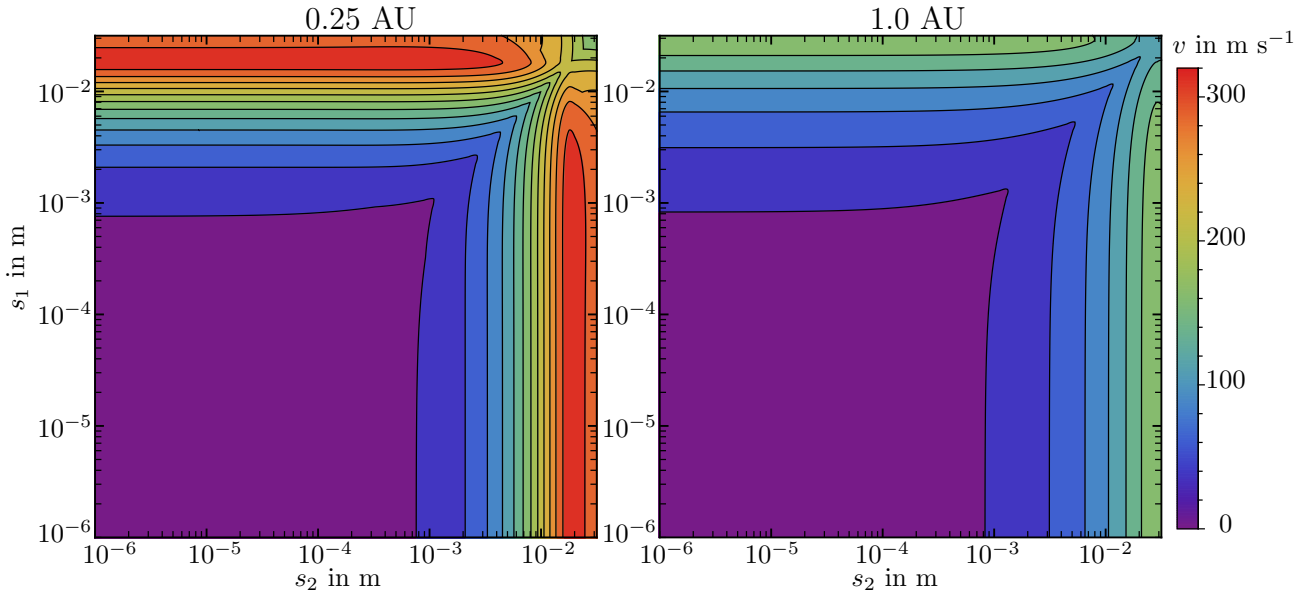

Figure A.6: Collision velocities in the disk LkCa15 Model 2 for a distances of 0.25 AU (left) and 1.0 AU (right) to the central star. The contours are in intervals of 25 m s^{-1}.

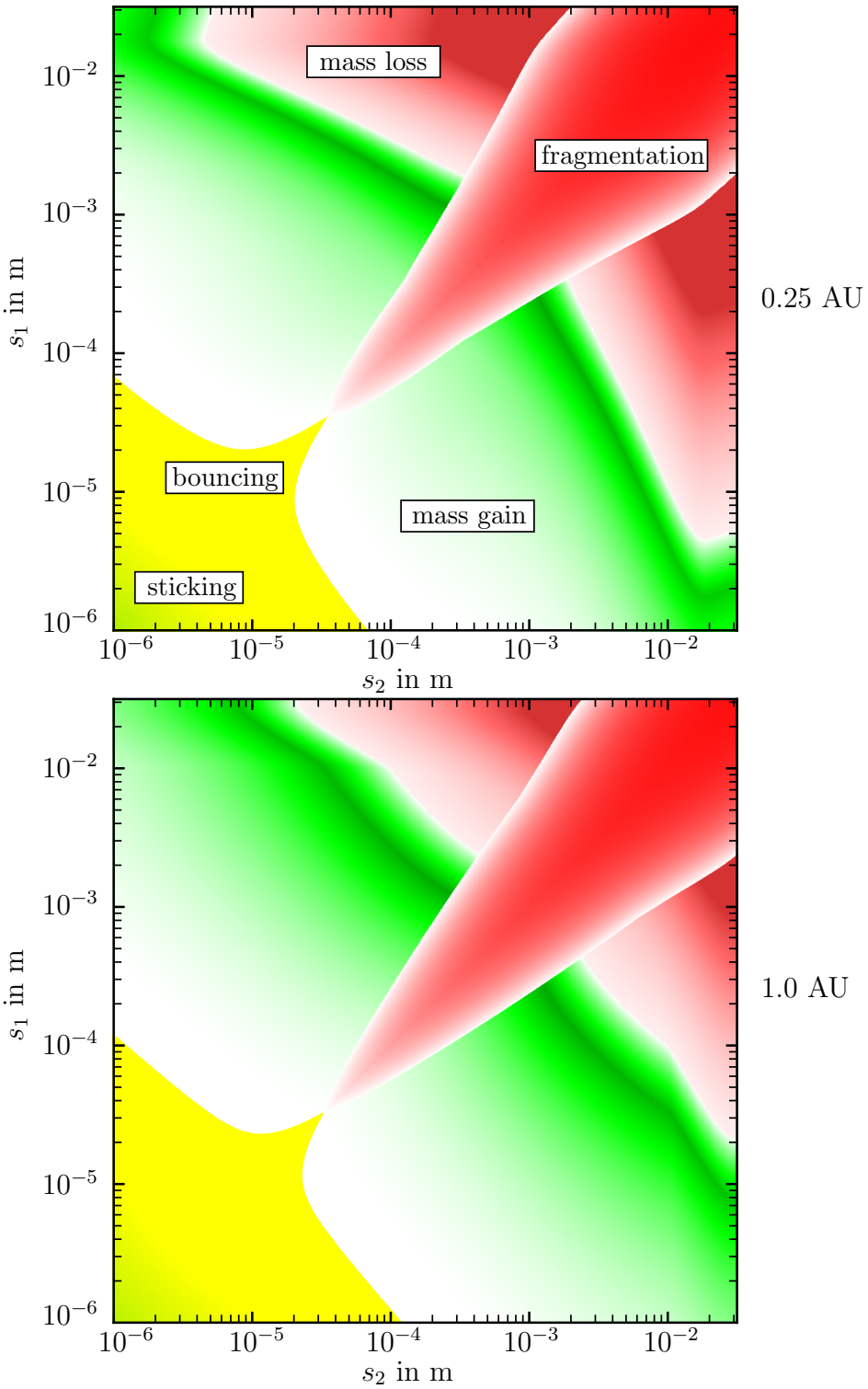

Figure A.7: Collisional outcome in the disk LkCa15 Model 2 for a distances of 0.25 AU (top) and 1.0 AU (bottom) to the central star. See fig. 5.14 for an explanation of the color codings.

A.4 Parameter sweep for the disk LkCa15

Table A.4: Parameter sweep for the disk LkCa15, r_{stop} marks the calculated maximum outward drift of a 10^{-4} m particle, $r_{\mathrm{p,max}}$ denotes the calculated maximum size where drift can still be positive.

δ_{dust}	δ_{gas}	χ_{dust}	k_{th} W/m · K	κ_ν	r_{stop} AU	$r_{\mathrm{p,max}}$ $\log(r_p/\mathrm{m})$
0.00001	0.005	0.3	0.01	2.5	1.2	-2
0.00001	0.005	0.3	0.01	3	1	-2.2
0.00001	0.005	0.3	0.01	3.5	0.8	-2.4
0.00001	0.005	0.4	0.01	2.5	1.5	-1.9
0.00001	0.005	0.4	0.01	2.5	1.6	-1.9
0.00001	0.005	0.4	0.01	3	1.2	-2
0.00001	0.005	0.4	0.01	3.5	1.2	-2
0.00001	0.005	0.5	0.01	2.5	1.7	-1.8
0.00001	0.005	0.5	0.01	3	1.7	-2
0.00001	0.005	0.5	0.01	3.5	1.5	-2
0.00001	0.01	0.3	0.01	2.5	1.7	-1.9
0.00001	0.01	0.3	0.01	3.5	1.2	-2.2
0.00001	0.01	0.3	0.1	3	1.5	-2
0.00001	0.01	0.4	0.01	3.5	1.8	-2
0.00001	0.01	0.4	0.1	2.5	0.8	-2.1
0.00001	0.01	0.4	0.1	3	0.8	-2.2
0.00001	0.01	0.5	0.01	3.5	2	-1.9
0.00001	0.01	0.5	0.1	2.5	1	-2
0.00001	0.01	0.5	0.1	3	0.8	-2.1
0.00001	0.05	0.3	0.1	2.5	1.2	-2.4
0.00001	0.05	0.3	0.1	3	1.2	-2.6
0.00001	0.05	0.3	0.1	3.5	0.8	-2.8
0.00001	0.05	0.4	0.1	2.5	1.7	-2.2
0.00001	0.05	0.4	0.1	3	1.5	-2.2
0.00001	0.05	0.4	0.1	3.5	1.2	-2.5
0.00001	0.05	0.5	0.1	2.5	1.8	-2
0.00001	0.05	0.5	0.1	3	1.8	-2.1
0.00001	0.05	0.5	0.1	3.5	1.7	-2.2
0.00001	0.1	0.3	0.1	2.5	1.7	-2.4
0.00001	0.1	0.3	0.1	3	1.6	-2.7
0.00001	0.1	0.3	0.1	3.5	1.2	-2.8
0.00001	0.1	0.4	0.1	3	2	-2.2
0.00001	0.1	0.5	0.1	3.5	2	-2.2
0.00002	0.005	0.3	0.001	2.5	1.3	-2.5
0.00002	0.005	0.3	0.001	3	1	-2.7
0.00002	0.005	0.4	0.001	2.5	2	-2.2
0.00002	0.005	0.4	0.001	3	1.4	-2.4

Table A.5: Parameter sweep for the disk LkCa15, r_{stop} marks the calculated maximum outward drift of a 10^{-4} m particle, $r_{\mathrm{p,max}}$ denotes the calculated maximum size where drift can still be positive (continued).

δ_{dust}	δ_{gas}	χ_{dust}	k_{th} W/m · K	κ_ν	r_{stop} AU	$r_{\mathrm{p,max}}$ $\log(r_p/\mathrm{m})$
0.00002	0.005	0.4	0.001	3.5	1.2	-2.5
0.00002	0.005	0.4	0.01	2.5	0.8	-2.5
0.00002	0.005	0.5	0.001	3.5	1.8	-2.3
0.00002	0.005	0.5	0.01	2.5	1	-2.2
0.00002	0.005	0.5	0.01	3.5	0.7	-2.5
0.00002	0.005	0.5	0.1	2.5	1	-2.2
0.00002	0.01	0.3	0.001	2.5	1.6	-2.6
0.00002	0.01	0.3	0.001	3	1	-2.8
0.00002	0.01	0.4	0.01	2.5	1	-2.5
0.00002	0.01	0.4	0.01	2.5	1	-2.4
0.00002	0.01	0.5	0.01	2.5	1.5	-2.1
0.00002	0.01	0.5	0.01	3	1.1	-2.3
0.00002	0.01	0.5	0.01	3.5	1	-2.6
0.00002	0.05	0.3	0.01	2.5	1.3	-2.8
0.00002	0.05	0.4	0.01	3	1.5	-2.7
0.00002	0.05	0.4	0.01	3.5	1.2	-2.9
0.00002	0.05	0.5	0.01	3.5	1.8	-2.4
0.00002	0.05	0.5	0.1	2.5	1	-2.8
0.00002	0.05	0.5	0.1	3	0.8	-2.8
0.00002	0.1	0.4	0.1	2.5	1	-2.9
0.00003	0.005	0.4	0.001	2.5	1	-2.6
0.00003	0.005	0.4	0.001	2.588	1	-2.6
0.00003	0.005	0.5	0.001	2.5	1.5	-2.3
0.00003	0.005	0.5	0.001	2.588	1.3	-2.4
0.00003	0.005	0.5	0.001	3	1.05	-2.5
0.00003	0.01	0.4	0.001	2.588	1.2	-2.7
0.00003	0.01	0.5	0.001	2.588	2	-2.3
0.00003	0.01	0.5	0.001	3	1.4	-2.5
0.00003	0.01	0.5	0.001	3.5	1	-2.8
0.00003	0.05	0.4	0.01	2.5	1	-3
0.00003	0.05	0.4	0.01	2.588	1	-3
0.00003	0.05	0.5	0.001	3.5	2	-3
0.00003	0.05	0.5	0.01	2.588	1.3	-2.8
0.00003	0.05	0.5	0.01	2.588	1.3	-2.7
0.00003	0.05	0.5	0.01	3	1.05	-3

Bibliography

Akimkin, V., Zhukovska, S., Wiebe, D., Semenov, D., Pavlyuchenkov, Y., Vasyunin, A., Birnstiel, T., and Henning, T. (2013). Protoplanetary Disk Structure with Grain Evolution: The ANDES Model. *ApJ*, 766:8.

André, P. (1994). Observations of protostars and protostellar stages. In Montmerle, T., Lada, C. J., Mirabel, I. F., and Tran Thanh Van, J., editors, *The Cold Universe*, page 179.

André, P. and Montmerle, T. (1994). From T Tauri stars to protostars: Circumstellar material and young stellar objects in the rho Ophiuchi cloud. *ApJ*, 420:837–862.

Andrews, S. M., Rosenfeld, K. A., Wilner, D. J., and Bremer, M. (2011a). A Closer Look at the LkCa 15 Protoplanetary Disk. *ApJ*, 742:L5.

Andrews, S. M. and Williams, J. P. (2005). Circumstellar Dust Disks in Taurus-Auriga: The Submillimeter Perspective. *ApJ*, 631:1134–1160.

Andrews, S. M., Wilner, D. J., Espaillat, C., Hughes, A. M., Dullemond, C. P., McClure, M. K., Qi, C., and Brown, J. M. (2011b). Resolved Images of Large Cavities in Protoplanetary Transition Disks. *The Astrophysical Journal*, 732:42.

Andrews, S. M., Wilner, D. J., Zhu, Z., Birnstiel, T., Carpenter, J. M., Pérez, L. M., Bai, X.-N., Öberg, K. I., Hughes, A. M., Isella, A., and Ricci, L. (2016). Ringed Substructure and a Gap at 1 au in the Nearest Protoplanetary Disk. *ApJ*, 820:L40.

Armitage, P. J. (2010). *Astrophysics of Planet Formation*. Cambridge University Press (Cambridge).

Aumatell, G. and Wurm, G. (2014). Ice aggregate contacts at the nm-scale. *MNRAS*, 437:690–702.

Baillié, K., Charnoz, S., and Pantin, E. (2015). Time evolution of snow regions and planet traps in an evolving protoplanetary disk. *A&A*, 577:A65.

Baule, B. (1914). Theoretische behandlung der erscheinungen in verdünnten gasen. *Annalen der Physik*, 349(9):145–176.

Beitz, E., Güttler, C., Blum, J., Meisner, T., Teiser, J., and Wurm, G. (2011). Low-velocity Collisions of Centimeter-sized Dust Aggregates. *The Astrophysical Journal*, 736:34.

Beresnev, S., Chernyak, V., and Fomyagin, G. (1993). Photophoresis of a spherical particle in a rarefied gas. *Physics of Fluids A: Fluid Dynamics*, 5:2043–2052.

Birnstiel, T., Dullemond, C. P., and Brauer, F. (2010). Gas- and dust evolution in protoplanetary disks. *A&A*, 513:A79.

Blum, J. and Muench, M. (1993). Experimental investigations on aggregate-aggregate collisions in the early solar nebula. *Icarus*, 106:151.

Blum, J. and Wurm, G. (2000). Experiments on Sticking, Restructuring, and Fragmentation of Preplanetary Dust Aggregates. *Icarus*, 143:138–146.

Blum, J. and Wurm, G. (2008). The Growth Mechanisms of Macroscopic Bodies in Protoplanetary Disks. *ARA&A*, 46:21–56.

Blum, J., Wurm, G., Kempf, S., and Henning, T. (1996). The Brownian Motion of Dust Particles in the Solar Nebula: an Experimental Approach to the Problem of Preplanetary Dust Aggregation. *Icarus*, 124:441–451.

Bruderer, S., van der Marel, N., van Dishoeck, E. F., and van Kempen, T. A. (2014). Gas structure inside dust cavities of transition disks: Ophiuchus IRS 48 observed by ALMA. *Astronomy and Astrophysics*, 562:A26.

Bryson, C., Cazcarra, V., and Levenson, L. L. (1974). Sublimation rates and vapor pressures of water, carbon dioxide, nitrous oxide, and xenon. *Journal of Chemical & Engineering Data*, 19(2):107–110.

Calvet, N., D'Alessio, P., Hartmann, L., Wilner, D., Walsh, A., and Sitko, M. (2002). Evidence for a developing gap in a 10 myr old protoplanetary disk. *The Astrophysical Journal*, 568:1008–1016.

Chiang, E. and Murray-Clay, R. (2007). Inside-out evacuation of transitional protoplanetary discs by the magneto-rotational instability. *Nature Physics*, 3:604–608.

Chiang, E. I. and Goldreich, P. (1997). Spectral Energy Distributions of T Tauri Stars with Passive Circumstellar Disks. *ApJ*, 490:368–376.

Cuello, N., Gonzalez, J.-F., and Pignatale, F. C. (2016). Effects of photophoresis on the dust distribution in a 3D protoplanetary disc. *MNRAS*, 458:2140–2149.

Cunningham, E. (1910). On the Velocity of Steady Fall of Spherical Particles through Fluid Medium. *Proceedings of the Royal Society of London Series A*, 83:357–365.

D'Alessio, P., Cantö, J., Calvet, N., and Lizano, S. (1998). Accretion Disks around Young Objects. I. The Detailed Vertical Structure. *ApJ*, 500:411–427.

de Beule, C. (2016). *Lifting grains from a dust bed by interaction with optical radaition and gas at low ambient pressure*. PhD thesis, University of Duisburg-Essen.

de Beule, C., Kelling, T., Wurm, G., Teiser, J., and Jankowski, T. (2011). Light induced erosion of dusty planetesimals and Mars: μg experiments. *Journal of Physics Conference Series*, 327(1):012047.

de Beule, C., Kelling, T., Wurm, G., Teiser, J., and Jankowski, T. (2013). From Planetesimals to Dust: Low-gravity Experiments on Recycling Solids at the Inner Edges of Protoplanetary Disks. *The Astrophysical Journal*, 763:11.

de Beule, C., Wurm, G., Kelling, T., Küpper, M., Jankowski, T., and Teiser, J. (2014). The martian soil as a planetary gas pump. *Nature Physics*, 10(1):17–20.

Deckers, J. and Teiser, J. (2013). Colliding Decimeter Dust. *ApJ*, 769:151.

Deckers, J. and Teiser, J. (2014). Macroscopic Dust in Protoplanetary Disks - from Growth to Destruction. *Astrophysical Journal*, 796:99.

Deckers, J. and Teiser, J. (2016). Collisions of solid ice in planetesimal formation. *MNRAS*, 456:4328–4334.

Derjaguin, B., Muller, V., and Toropov, Y. (1975). Effect of contact deformations on the adhesion of particles. *J. Colloid. Interface Sci.*

Dobbs, C. L., Krumholz, M. R., Ballesteros-Paredes, J., Bolatto, A. D., Fukui, Y., Heyer, M., Low, M.-M. M., Ostriker, E. C., and Vázquez-Semadeni, E. (2014). Formation of Molecular Clouds and Global Conditions for Star Formation. *Protostars and Planets VI*, pages 3–26.

Dominik, C. and Tielens, A. G. G. M. (1997). The Physics of Dust Coagulation and the Structure of Dust Aggregates in Space. *ApJ*, 480:647–673.

Dubrulle, B., Morfill, G., and Sterzik, M. (1995). The dust subdisk in the protoplanetary nebula. *Icarus*, 114:237–246.

Dzyurkevich, N., Flock, M., Turner, N. J., Klahr, H., and Henning, T. (2010). Trapping solids at the inner edge of the dead zone: 3-D global MHD simulations. *A&A*, 515:A70.

Fayolle, E. C., Öberg, K. I., Cuppen, H. M., Visser, R., and Linnartz, H. (2011). Laboratory H_2O:CO_2 ice desorption data: entrapment dependencies and its parameterization with an extended three-phase model. *A&A*, 529:A74.

Fukui, Y. and Kawamura, A. (2010). Molecular Clouds in Nearby Galaxies. *ARA&A*, 48:547–580.

Goodman, F. O. and Wachman, H. Y. (1967). Formula for Thermal Accommodation Coefficients. *J. Chem. Phys.*, 46(6):2376–2386.

Groussin, O., A'Hearn, M. F., Li, J.-Y., Thomas, P. C., Sunshine, J. M., Lisse, C. M., Meech, K. J., Farnham, T. L., Feaga, L. M., and Delamere, W. A. (2007). Surface temperature of the nucleus of Comet 9P/Tempel 1. *Icarus*, 187:16–25.

Gundlach, B. and Blum, J. (2015). The Stickiness of Micrometer-sized Water-ice Particles. *ApJ*, 798:34.

Güttler, C., Blum, J., Zsom, A., Ormel, C. W., and Dullemond, C. P. (2010). The outcome of protoplanetary dust growth: pebbles, boulders, or planetesimals?. I. Mapping the zoo of laboratory collision experiments. *A&A*, 513:A56.

Güttler, C., Krause, M., Geretshauser, R. J., Speith, R., and Blum, J. (2009). The Physics of Protoplanetesimal Dust Agglomerates. IV. Toward a Dynamical Collision Model. *ApJ*, 701:130–141.

Haack, H. and Wurm, G. (2007). Life on the edge - formation of cais and chondrules at the inner edge of the dust disk. In *Meteoritics and Planetary Science Supplement*, volume 42, page 5157.

Haisch, K. E., Lada, E. A., and Lada, C. J. (2001). Disk Frequencies and Lifetimes in Young Clusters. *ApJ*, 553:L153–L156.

Hartmann, L., Calvet, N., Gullbring, E., and D'Alessio, P. (1998). Accretion and the Evolution of T Tauri Disks. *ApJ*, 495:385–400.

Hartmann, W. K. (1978). Planet formation - Mechanism of early growth. *Icarus*, 33:50–61.

Hayashi, C. (1981). Structure of the Solar Nebula, Growth and Decay of Magnetic Fields and Effects of Magnetic and Turbulent Viscosities on the Nebula. *Progress of Theoretical Physics Supplement*, 70:35–53.

Hayashi, C., Nakazawa, K., and Nakagawa, Y. (1985). Formation of the solar system. *Protostars and Planets II*, pages 1100–1153.

Hettner, G. (1928). Neuere experimentelle und theoretische Untersuchungen über die Radiometerkräfte. *Ergebnisse der exakten Naturwissenschaften*, 7:209–237.

Husmann, T., Loesche, C., and Wurm, G. (2016). Self-sustained recycling in the inner dust ring of pre-transitional disks. *ApJ*, accepted.

Hutchins, D., Harper, M., and Felder, R. (1995). Slip correction measurements for solid spherical particles by modulated dynamic light scattering. *Aerosol Science and Technology*, 22(2):202–218.

Jankowski, T., Wurm, G., Kelling, T., Teiser, J., Sabolo, W., Gutiérrez, P. J., and Bertini, I. (2012). Crossing barriers in planetesimal formation: The growth of mm-dust aggregates with large constituent grains. *A&A*, 542:A80.

Johansen, A., Blum, J., Tanaka, H., Ormel, C., Bizzarro, M., and Rickman, H. (2014). The Multifaceted Planetesimal Formation Process. *Protostars and Planets VI*, pages 547–570.

Johansen, A. and Klahr, H. (2005). Dust Diffusion in Protoplanetary Disks by Magnetorotational Turbulence. *ApJ*, 634:1353–1371.

Kamp, M. (2016). Theroetical studies on thermal conductivity of porous dust aggregates. Master's thesis, University Duisburg-Essen.

Kelling, T. and Wurm, G. (2009). Self-Sustained Levitation of Dust Aggregate Ensembles by Temperature-Gradient-Induced Overpressures. *Phys. Rev. Lett.*, 103:215502–1–215502–4.

Kelling, T. and Wurm, G. (2011). A Mechanism to Produce the Small Dust Observed in Protoplanetary Disks. *ApJ*, 733:120–125.

Kelling, T., Wurm, G., Kocifaj, M., Klačka, J., and Reiss, D. (2011). Dust ejection from planetary bodies by temperature gradients: Laboratory experiments. *Icarus*, 212:935–940.

Kimura, H., Wada, K., Senshu, H., and Kobayashi, H. (2015). Cohesion of Amorphous Silica Spheres: Toward a Better Understanding of The Coagulation Growth of Silicate Dust Aggregates. *ApJ*, 812:67.

Knudsen, M. (1909). Thermischer Molekulardruck der Gase in Röhren and porösen Körpern. *Annalen der Physik*, 336:633–640.

Kothe, S. and Blum, J. (2016). A collision model for protoplanetary dust. In *Planet Formation and Evolution*.

Kothe, S., Blum, J., Weidling, R., and Güttler, C. (2013). Free collisions in a microgravity many-particle experiment. III. The collision behavior of sub-millimeter-sized dust aggregates. *Icarus*, 225:75–85.

Krause, M., Blum, J., Skorov, Y., and Trieloff, M. (2011). Thermal conductivity measurements of porous dust aggregates: I. technique, model and first results. *Icarus*. Im Druck.

Krauss, O. and Wurm, G. (2005). Photophoresis and the pile-up of dust in young circumstellar disks. *The Astrophysical Journal*, 630:1088–1092.

Kruss, M., Demirci, T., Koester, M., Kelling, T., and Wurm, G. (2016). Failed Growth at the Bouncing Barrier in Planetesimal Formation. *ApJ*, 827:110.

Kuepper, M., de Beule, C., Wurm, G., Matthews, L. S., Kimery, J. S., and Hyde, T. W. (2014). Photophoresis on polydisperse basalt microparticles under microgravity. *Journal of Aerosol Science*, 76:126–137.

Kutner, M. L., Tucker, K. D., Chin, G., and Thaddeus, P. (1977). The molecular complexes in Orion. *ApJ*, 215:521–528.

Lada, C. J. (1976). Detailed observations of the M17 molecular cloud complex. *ApJS*, 32:603–629.

Lada, C. J. and Wilking, B. A. (1984). The nature of the embedded population in the Rho Ophiuchi dark cloud - Mid-infrared observations. *ApJ*, 287:610–621.

Langkowski, D., Teiser, J., and Blum, J. (2008). The Physics of Protoplanetesimal Dust Agglomerates. II. Low-Velocity Collision Properties. *ApJ*, 675:764–776.

Loesche, C. (2015). *On the photophoretic force exerted on mm- and sub–mm–sized particles*. PhD thesis, Universität Duisburg-Essen.

Loesche, C. and Husmann, T. (2016). Photophoresis on particles hotter/colder than the ambient gas for the entire range of pressures. *Journal of Aerosol Science*, 102:55–71.

Loesche, C., Teiser, J., Wurm, G., Hesse, A., Friedrich, J. M., and Bischoff, A. (2014). Photophoretic Strength on Chondrules. 2. Experiment. *The Astrophysical Journal*, 792(1):73.

Loesche, C. and Wurm, G. (2012). Thermal and photophoretic properties of dust mantled chondrules and sorting in the solar nebula. *A&A*, 545:A36.

Loesche, C., Wurm, G., Jankowski, T., and Kuepper, M. (2016). Photophoresis on particles hotter/colder than the ambient gas in the free molecular flow. *Journal of Aerosol Science*, 97:22 – 33.

Loesche, C., Wurm, G., Teiser, J., Friedrich, J. M., and Bischoff, A. (2013). Photophoretic Strength on Chondrules. 1. Modeling. *The Astrophysical Journal*, 778(2):101.

Loth, E. (2008). Drag of non-spherical solid particles of regular and irregular shape. *Powder Technology*, 182:342–353.

Lynden-Bell, D. and Pringle, J. E. (1974). The evolution of viscous discs and the origin of the nebular variables. *MNRAS*, 168:603–637.

MacGregor, M. A., Wilner, D. J., Chandler, C., Ricci, L., Maddison, S. T., Cranmer, S. R., Andrews, S. M., Hughes, A. M., and Steele, A. (2016). Constraints on Planetesimal Collision Models in Debris Disks. *ApJ*, 823:79.

Markiewicz, W. J., Mizuno, H., and Voelk, H. J. (1991). Turbulence induced relative velocity between two grains. *A&A*, 242:286–289.

Matthews, L. S., Kimery, J. B., Wurm, G., de Beule, C., Kuepper, M., and Hyde, T. W. (2016). Photophoretic force on aggregate grains. *MNRAS*, 455:2582–2591.

Maxwell, J. C. (1879). On stresses in rarified gases arising from inequalities of temperature. *Philosophical Transactions of the Royal Society of London*, 170:231–256.

McKee, C. F. and Ostriker, E. C. (2007). Theory of Star Formation. *ARA&A*, 45:565–687.

Meakin, P., Donn, B., and Mulholland, G. W. (1989). Collisions between point masses and fractal aggregates. *Langmuir*, 5(2):510–518.

Meisner, T., Wurm, G., Teiser, J., and Schywek, M. (2013). Preplanetary scavengers: Growing tall in dust collisions. *A&A*, 559:A123.

Min, M., Dullemond, C. P., Kama, M., and Dominik, C. (2011). The thermal structure and the location of the snow line in the protosolar nebula: Axisymmetric models with full 3-D radiative transfer. *Icarus*, 212:416–426.

Murray, N. (2011). Star Formation Efficiencies and Lifetimes of Giant Molecular Clouds in the Milky Way. *ApJ*, 729:133.

Musiolik, G., Teiser, J., Jankowski, T., and Wurm, G. (2016a). Collisions of CO2 Ice Grains in Planet Formation. *ApJ*, 818:16.

Musiolik, G., Teiser, J., Jankowski, T., and Wurm, G. (2016b). Ice Grain Collisions in Comparison: CO2, H20, and Their Mixtures. *ApJ*, 827(1):63.

Najita, J. R., Carr, J. S., Glassgold, A. E., and Valenti, J. A. (2007). Gaseous inner disks. In Reipurth, B., Jewitt, D., and Keil, K., editors, *Protostars and Planets V*, pages 507–522. University of Arizona Press, Tucson, AZ.

Öberg, K. I., Murray-Clay, R., and Bergin, E. A. (2011). The Effects of Snowlines on C/O in Planetary Atmospheres. *ApJ*, 743:L16.

Oka, T., Hasegawa, T., Sato, F., Tsuboi, M., Miyazaki, A., and Sugimoto, M. (2001). Statistical Properties of Molecular Clouds in the Galactic Center. *ApJ*, 562:348–362.

Ormel, C. W. and Cuzzi, J. N. (2007). Closed-form expressions for particle relative velocities induced by turbulence. *A&A*, 466:413–420.

Pollack, J. B., McKay, C. P., and Christofferson, B. M. (1985). A calculation of the Rosseland mean opacity of dust grains in primordial solar system nebulae. *Icarus*, 64:471–492.

Pontoppidan, K. M., Salyk, C., Bergin, E. A., Brittain, S., Marty, B., Mousis, O., and Öberg, K. I. (2014). Volatiles in Protoplanetary Disks. *Protostars and Planets VI*, pages 363–385.

Poppe, T., Blum, J., and Henning, T. (2000). Analogous Experiments on the Stickiness of Micron-sized Preplanetary Dust. *ApJ*, 533:454–471.

Rader, D. J. (1990). Momentum slip correction factor for small particles in nine common gases. *Journal of aerosol science*, 21(2):161–168.

Reed, L. D. (1977). Low knudsen number photophoresis. *Journal of Aerosol Science*, 8(2):123–131.

Reipurth, B., Jewitt, D., and Keil, K. (2007). Protostars and Planets V. *Protostars and Planets V*.

Rohatschek, H. (1995). Semi-empirical model of photophoretic forces for the entire range of pressures. *Journal of Aerosol Science*, 26(5):717–734.

Roman-Duval, J., Jackson, J. M., Heyer, M., Rathborne, J., and Simon, R. (2010). Physical Properties and Galactic Distribution of Molecular Clouds Identified in the Galactic Ring Survey. *ApJ*, 723:492–507.

Sanders, D. B., Solomon, P. M., and Scoville, N. Z. (1984). Giant molecular clouds in the Galaxy. I - The axisymmetric distribution of H2. *ApJ*, 276:182–203.

Seizinger, A., Krijt, S., and Kley, W. (2013). Erosion of dust aggregates. *A&A*, 560:A45.

Sekiya, M. and Takeda, H. (2003). Were planetesimals formed by dust accretion in the solar nebula? *Earth, Planets, and Space*, 55:263–269.

Semenov, D., Henning, T., Helling, C., Ilgner, M., and Sedlmayr, E. (2003). Rosseland and Planck mean opacities for protoplanetary discs. *A&A*, 410:611–621.

Shakura, N. I. and Sunyaev, R. A. (1973). Black holes in binary systems. Observational appearance. *A&A*, 24:337–355.

Sicilia-Aguilar, A., Henning, T., Juhász, A., Bouwman, J., Garmire, G., and Garmire, A. (2008). Very low mass objects in the coronet cluster: The realm of the transition disks. *The Astrophysical Journal*, 687:1145–1167.

Sirono, S.-i. (2013). Size and Surface Area of Icy Dust Aggregates after a Heating Event at a Protoplanetary Nebula. *ApJ*, 765:50.

Solomon, P. M., Rivolo, A. R., Barrett, J., and Yahil, A. (1987). Mass, luminosity, and line width relations of Galactic molecular clouds. *ApJ*, 319:730–741.

Span, R. and Wagner, W. (1996). A New Equation of State for Carbon Dioxide Covering the Fluid Region from the Triple-Point Temperature to 1100 K at Pressures up to 800 MPa. *Journal of Physical and Chemical Reference Data*, 25:1509–1596.

Teiser, J., Engelhardt, I., and Wurm, G. (2011a). Porosities of Protoplanetary Dust Agglomerates from Collision Experiments. *ApJ*, 742:5.

Teiser, J., Küpper, M., and Wurm, G. (2011b). Impact angle influence in high velocity dust collisions during planetesimal formation. *Icarus*, 215:596–598.

Teiser, J. and Wurm, G. (2009). High-velocity dust collisions: forming planetesimals in a fragmentation cascade with final accretion. *MNRAS*, 393:1584–1594.

Tenenbaum, A., Ciccotti, G., and Gallico, R. (1982). Stationary nonequilibrium states by molecular dynamics. Fourier's law. *Phys. Rev. A*, 25:2778–2787.

Thomas, L. B. and Lord, R. (1974). Comparative measurements of tangential momentum and thermal accommodations on polished and on roughened steel spheres. *Rarefied gas dynamics*, 8:405–412.

Turner, N. J., Willacy, K., Bryden, G., and Yorke, H. W. (2006). Turbulent Mixing in the Outer Solar Nebula. *ApJ*, 639:1218–1226.

van der Marel, N., van Dishoeck, E. F., Bruderer, S., Pérez, L., and Isella, A. (2015). Gas density drops inside dust cavities of transitional disks around young stars observed with ALMA. *Astronomy and Astrophysics*, 579:A106.

van Eymeren, J. and Wurm, G. (2012). The implications of particle rotation on the effect of photophoresis. *MNRAS*, 420:183–186.

Voelk, H. J., Jones, F. C., Morfill, G. E., and Roeser, S. (1980). Collisions between grains in a turbulent gas. *A&A*, 85:316–325.

von Borstel, I. and Blum, J. (2012). Photophoresis of dust aggregates in protoplanetary disks. *A&A*, 548:A96.

von Smoluchowski, M. (1916). Drei Vortrage uber Diffusion, Brownsche Bewegung und Koagulation von Kolloidteilchen. *Zeitschrift fur Physik*, 17:557–585.

Wada, K., Tanaka, H., Suyama, T., Kimura, H., and Yamamoto, T. (2007). Numerical Simulation of Dust Aggregate Collisions. I. Compression and Disruption of Two-Dimensional Aggregates. *ApJ*, 661:320–333.

Wada, K., Tanaka, H., Suyama, T., Kimura, H., and Yamamoto, T. (2008). Numerical Simulation of Dust Aggregate Collisions. II. Compression and Disruption of Three-Dimensional Aggregates in Head-on Collisions. *ApJ*, 677:1296–1308.

Weidenschilling, S. J. (1977a). Aerodynamics of solid bodies in the solar nebula. *MNRAS*, 180:57–70.

Weidenschilling, S. J. (1977b). The distribution of mass in the planetary system and solar nebula. *Ap&SS*, 51:153–158.

Weidling, R., Güttler, C., and Blum, J. (2012). Free collisions in a microgravity many-particle experiment. I. Dust aggregate sticking at low velocities. *Icarus*, 218:688–700.

Whipple, F. L. (1972). On certain aerodynamic processes for asteroids and comets. In Elvius, A., editor, *From Plasma to Planet*, page 211.

Windmark, F., Birnstiel, T., Güttler, C., Blum, J., Dullemond, C. P., and Henning, T. (2012a). Planetesimal formation by sweep-up: how the bouncing barrier can be beneficial to growth. *A&A*, 540:A73.

Windmark, F., Birnstiel, T., Ormel, C. W., and Dullemond, C. P. (2012b). Breaking through: The effects of a velocity distribution on barriers to dust growth. *A&A*, 544:L16.

Wood, S. E. (1999). *Nucleation and growth of CO2 ice crystals in the Martian atmosphere*. PhD thesis, Univ. of California, Dept. of Earth and Space Sciences Los Angeles.

Wurm, G., Blum, J., and Colwell, J. E. (2001a). Aerodynamical sticking of dust aggregates. *Phys. Rev. E*, 64(4):046301.

Wurm, G., Blum, J., and Colwell, J. E. (2001b). NOTE: A New Mechanism Relevant to the Formation of Planetesimals in the Solar Nebula. *Icarus*, 151:318–321.

Wurm, G. and Krauss, O. (2006a). Dust Eruptions by Photophoresis and Solid State Greenhouse Effects. *Phys. Rev. Lett.*, 96:134301–+.

Wurm, G. and Krauss, O. (2006b). Dust Eruptions by Photophoresis and Solid State Greenhouse Effects. *Phys. Rev. Lett.*, 96:134301.

Wurm, G. and Krauss, O. (2008). Experiments on negative photophoresis and application to the atmosphere. *Atmospheric Environment*, 42(11):2682–2690.

Wurm, G., Teiser, J., Bischoff, A., Haack, H., and Roszjar, J. (2010). Experiments on the photophoretic motion of chondrules and dust aggregates — Indications for the transport of matter in protoplanetary disks. *Icarus*, 208:482–491.

Wurm, G., Trieloff, M., and Rauer, H. (2013). Photophoretic Separation of Metals and Silicates: The Formation of Mercury-like Planets and Metal Depletion in Chondrites. *The Astrophysical Journal*, 769:78.

Wyatt, M. C. (2005). The insignificance of P-R drag in detectable extrasolar planetesimal belts. *A&A*, 433:1007–1012.

Yalamov, Y. I., Kutukov, V. B., and Shchukin, E. R. (1976a). Motion of small aerosol particle in a light field. *Journal of Engineering Physics*, 30:648–652.

Yalamov, Y. I., Kutukov, V. B., and Shchukin, E. R. (1976b). Theory of the photophoretic motion of the large-size volatile aerosol particle. *Journal of Colloid and Interface Science*, 57(3):564–571.

Appendix B

Glossary and Abbrevations

Variables - Part A

α_{t}	-	turbulence parameter
α	-	thermal accommodation coefficient
α_{m}	-	momentum accommodation coefficient
χ_{dust}	-	dust scale height factor (flaring angle)
Δ_{dust}	-	dust density drop function
Δv	m s^{-1}	relative velocity
$\delta_{\mathrm{dust/dustcav/gas}}$	-	dust (in cavity) / gas density drop values
η_{re}	-	amount of reaccreted mass in units of ejecta mass m_{ej}
ϵ	-	emissivity
γ_{surf}	J m^{-2}	surface energy
$\kappa_{\mathrm{med}/\lambda}$	m^2 kg^{-1}	mean / wavelenght dependend opacity
κ_{s}	-	thermal creep coefficient
κ_{size}	-	exponent for the dust size distribution
$\nu_{\mathrm{t/dyn/gas}}$	m^2 s^{-1}	turbulent / dynamic / gas viscosity
$\mu_{\mathrm{frag,p/t}}$	-	largest impactor / target fragment size
λ	m	wavelenght
λ_{mfp}	m	mean free path of gas molecules
ϕ	-	exponent for aspect ratio
Φ_{refl}	W	reflected energy flux
ρ_{dust}	kg m^{-2}	dust density
ρ_{gas}	kg m^{-2}	gas density
Σ_{dust}	kg m^{-2}	dust surface density
Σ_{gas}	kg m^{-2}	gas surface density
$\Sigma_{\mathrm{c/0}}$	kg m^{-2}	gas surface density at critical radius / 1.0 AU
τ_{f}	s	gas grain friction time
τ_{co}	-	scaling coefficient for photophoresis (co)
τ_{fm}	-	scaling coefficient for photophoresis (fm)
Ω	s^{-1}	orbital frequency
Ω_{k}	s^{-1}	Keplarian frequency

Variables - Part B

A_0^{co}	K	continuum temperature
A_0^{fm}	K	free molecular flow temperature
a_{res}	m s^{-2}	acceleration due to residual gravity
c_{s}	m s^{-1}	sound speed
C_{D}	-	drag coefficient
F_{contact}	kg m s^{-2}	contact force
F_{D}	kg m s^{-2}	drag force
F_{rad}	kg m s^{-2}	force due to radiation pressue regime)
F_{ph}	kg m s^{-2}	photophoretic force (superscript denotes
F_λ	W	wavelenght dependend flux
h / h_{c}	AU	scale height (gas) / at critical radius
h_{dust}	AU	dust scale height
h_{fm}	W m^{-1} K^{-1}	heat transfer coefficient for photophoresis
I	W	intensity of irradiation
k_{th}	W m^{-1} K^{-1}	thermal conductivity of particle
k_{gas}	W m^{-1} K^{-1}	thermal conductivity of gas
Kn	-	Knudsen number
L_*	W	luminosity of the (proto-)star
M_{disk}	kg	mass of the protoplanetary disk
M_*	kg	mass of the (proto-)star
m_{gas}	kg	mass of a gas molecule
m_{ej}	kg	mass of ejected particles
m_{t}	kg	mass of the target body
m_{p}	kg	mass of the impacting body
m_{s}	kg	normalizing mass for the sticking threshold
m_{b}	kg	normalizing mass for the bouncing threshold
m_{mt}	kg	mass transfered from impactor to target body
m_{er}	kg	mass eroded from target body
P / P_{disk}	N m^2	(disks) gas pressure
$\hat{P}$	N m^2	peak pressure for photophoresis
p_{s}	-	sticking probability
r	AU	distance to the central star
r_{c}	AU	critical radius
r_{cav}	AU	outer cavity radius
r_{gap}	AU	inner cavity radius
$r_{\mathrm{sub,x}}$	AU	sublimation radius (material dependend)
r_{out}	AU	outer disk radius
R_{surf}	-	surface reflectivity
Re / $\mathrm{Re_p}$	-	Reynolds number / particle Reynolds number
s	m	particle size (radius)
St	-	Stokes number
t	s	time

Variables - Part C

T	K	midplane temperature
T_{bb}	K	black body temperature
T_{gas}	K	gas temperature
T_{rad}	K	background radiation temperature
T_{∞}	K	gas temperature far away from particle
v_{com}	m s^{-1}	center of mass velocity
v_{b}	m s^{-1}	bouncing threshold velocity
v_{phi}	m s^{-1}	azimuthal velocity
$v_{\mathrm{phi,gas}}$	m s^{-1}	azimuthal gas velocity
v_{r}	m s^{-1}	radial velocity
$v_{\mathrm{r,gas}}$	m s^{-1}	radial gas velocity
v_{s} / v_{stick}	m s^{-1}	sticking threshold velocity
v_{frag}	m s^{-1}	fragmentation threshold velocity
v_{k}	m s^{-1}	Keplarian velocity
$\overline{v}_{\mathrm{th}}$	m s^{-1}	mean thermal velocity
z	AU	height above midplane (vertical direction)

Constants and units

σ_{SB}	5.671×10^{-8} W m^{-2} K^{-4}	Stefan-Boltzmann Constant
Σ_0	1.7×10^{4} kg m^{-2}	gas surface density in MMSN at 1.0 AU
AU	1.496×10^{11} m	astonomical unit
G	6.674×10^{-11} m^3 kg^{-1} s^{-2}	gravitational constant
J_1	1/2	asymmetrie parameter
J_2	1/4	asymmetrie parameter
k_{B}	1.381×10^{-23} J K^{-1}	Boltzmann constant
ly	9.461×10^{15} m ($\approx 6.3 \times 10^{4}$ AU)	lightyear
$M_{\odot}$	1.989×10^{30} kg	mass of the sun
N_{A}	6.022×10^{23} mol^{-1}	Avogadro constant
T_0	200 K / 280 K	midplane temperature in MMSN at 1.0 AU
T_{sub}	1500 K	sublimation temperature of silicates
u	1.661×10^{-27} kg	atomic mass unit

Abbrevations

ALMA	Atacama Large Millimeter/submillimeter Array
MMSN	Minimum Mass Solar Nebular
PPD	Protoplanetary Disk
PDM	Pre-transitional Disk Model

Danksagung

Vielen Dank an Prof. Dr. Gerhard Wurm für die Möglichkeit zur Promotion in seiner Arbeitsgruppe sowie für die Unterstützung und die hilfreichen Ratschläge.

Besonderen Dank an Christoph Lösche, Grzegorz Musiolik, Markus Küpper und Caroline de Beule für die ergiebige Zusammenarbeit in unterschiedlichsten Bereichen.

Vielen Dank an Jens Teiser für die Möglichkeit zur Mitarbeit in seinem Projekt sowie an Thorben Kelling als auch an den Rest der Arbeitsgruppe für eine tolle gemeinsame Zeit, geistreiche Unterhaltungen und konstruktive Fachgespräche.

Special thanks to Fredrik Windmark for fruitful discussions and his support.

Ein Dankeschön möchte ich meiner Familie für ihre Unterstützung aussprechen. Insbesondere Christina danke ich für ihrer stete Hilfe und ihre Aufmunterungen.